Title	Regulation of Molecular Topologies via Supramolecular Strategies
Author(s)	Xiao, Chunlin
Citation	大阪大学, 2025, 博士論文
Version Type	VoR
URL	https://doi.org/10.18910/103244
rights	
Note	

Regulation of Molecular Topologies via Supramolecular Strategies

A Doctor Thesis

by

Chunlin Xiao

Submitted to the Graduate school of Science, The University of Osaka

July, 2025

Contents

Chapter 1

General Introduction

1. Background

1.1 The concept of topology: from mathematics to real-world

Topology, originally developed as a branch of mathematics, deals with properties of objects that are preserved under continuous deformations such as stretching, twisting, or bending, without cutting or gluing. In essence, topology focuses on the connectivity and global arrangement of components rather than their precise geometrical dimensions or angles. This abstraction allows diverse systems to be classified and understood based on their topological features. Two objects are considered topologically equivalent (or homeomorphic) if one can be smoothly transformed into the other through such continuous deformations. For example, a coffee mug and a donut (torus) are homeomorphic, as both possess one continuous hole (Figure 1-1). In contrast, objects that cannot be transformed into each other without cutting or reconnecting are recognized to be non-homeomorphic. For instance, a sphere, a donut, and a bowknot (figure-eight ring) possess zero, one, and two holes, respectively, and are therefore topologically distinct (non-homeomorphic) from one another (Figure 1-2).

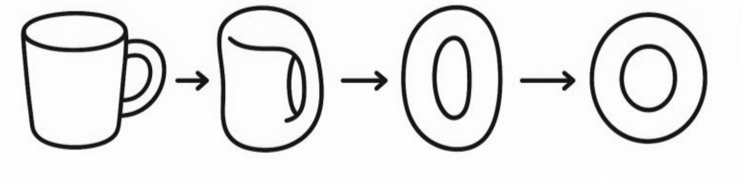

Figure 1-1. A homeomorphic transformation from a coffee mug to a torus.

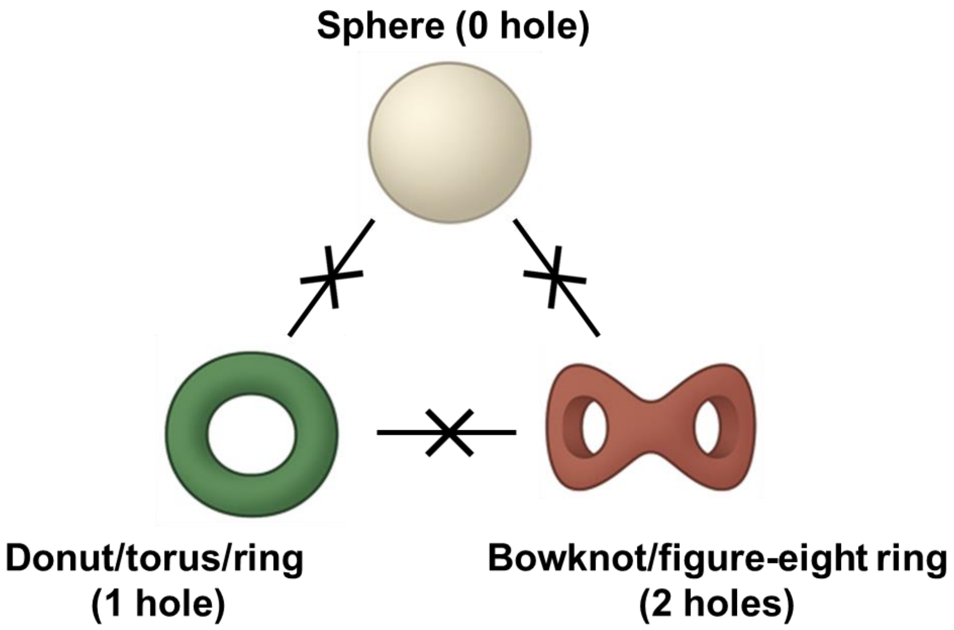

Figure 1-2. Prohibition of transformation among non-homeomorphic topologies.

Notably, distinct topological structures are not only mathematically different but also lead to diverse physical behaviors and applications in real-world systems. Their functional significance will be further discussed in the following sections.

Beyond its mathematical foundation, topological features profoundly influence the properties and functions of macroscopic objects in daily life. Even simple differences in topology—such as linear versus cyclic structures—can result in distinct mechanical and functional characteristics. For example, linear ropes are widely used due to their flexibility, ease of handling, and capacity for controlled tension. In contrast, circular or closed-loop structures, such as rings or hoops, inherently resist stretching and are often utilized in applications requiring mechanical stability, load distribution, or structural reinforcement.

Since ancient times, humans have utilized increasingly sophisticated topological designs to address functional needs. Early examples include the use of ropes and knots for hunting, transportation, and construction, exploiting their ability to transmit and hold forces reliably. The circular topology of rings has long been employed in engineering components such as pulleys, wheels, and gaskets, where the closed-loop structure enhances durability and load-bearing capacity. More complex topological forms, such as entangled or coiled configurations, are exemplified by the compact arrangement of instant noodle bricks, which maximize packing efficiency while maintaining mechanical integrity. Similarly, woven fabrics and braided structures combine multiple interlaced filaments to achieve a balance between flexibility, strength, and resistance to deformation. The diverse functional behaviors of these materials are directly rooted in their topological architectures.

1.2 Topology in chemistry: topological molecules and their applications

Similar to macroscopic objects, molecules in the microscopic world also adopt diverse topologies. Linear and circular structures represent the most fundamental topological forms for molecules. To date, numerous molecules with much more sophisticated topologies beyond simple linear and circular structures have been discovered in biological systems and constructed in artificial systems.

1.2.1 Cyclic molecules in biological systems

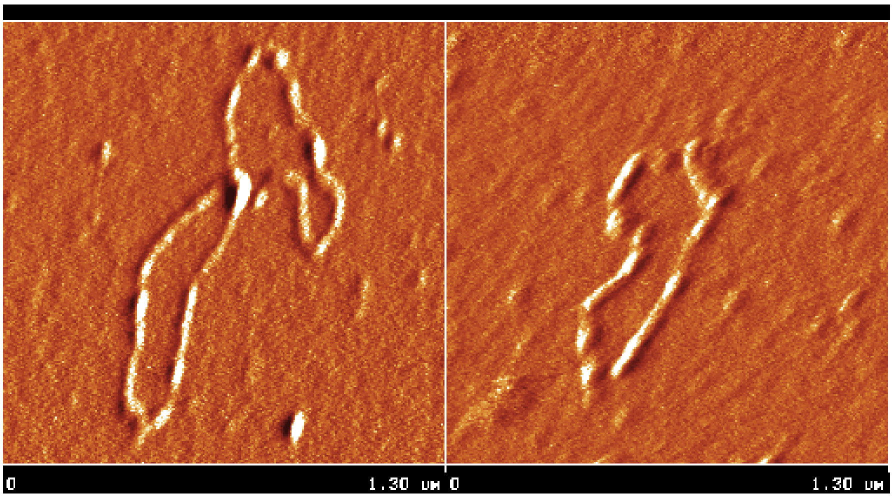

Figure 1-3. Atomic force microscope images for DNA catenane and cyclic DNA.

In biological systems, the molecules with different topologies generally exhibit distinct properties and functions. For example, circular DNA (Figure 1-3) and RNA, owing to their covalently closed structures, display enhanced stability against exonuclease degradation and adopt unique replication and regulatory mechanisms compared to linear nucleic acids.[1-14] Similarly, cyclic peptides and proteins benefit from conformational rigidity and improved metabolic stability, which often lead to enhanced receptor binding affinity and bioactivity relative to their linear analogues.[14-23]

1.2.2 Artificial molecules with various topologies

Linear molecules have been the most extensively studied and applied structures throughout the history of chemistry. In addition, cyclic molecules represent the simplest topological forms that are not homeomorphic to linear structures. They have been widely explored, synthesized, and applied in various fields such as supramolecular chemistry,[24-36] materials science,[37-43] polymer science,[44-52] and pharmaceutical science.[53-58] In particular, similar to the unique roles of circular DNA and RNA in biological systems, cyclic polymers (CPs), as a class of artificial macrocycles, exhibit distinct and intriguing properties compared to their linear counterparts. Owing to the absence of end groups, cyclic homopolymers typically display a reduced hydrodynamic volume and a slower degradation profile, while cyclic block copolymers show markedly different self-assembly behavior. Thereby, based on these unique features, CPs have been widely used in drug delivery, biomaterials and so on[44-52, 59-67].

Beyond simple cyclic molecules, the field of mechanically interlocked molecules (MIMs) has enabled the design and synthesis of much more sophisticated topological architectures. MIMs are molecular architectures in which the components are not connected via conventional covalent bonds but are interlocked through their topological arrangement. [2]Rotaxane is the most fundamental mechanically interlocked architectures.[68] Specifically, a [2]rotaxane is the structures consisting of a linear “axle” component threaded through a macrocyclic “wheel,” with bulky end groups (stoppers) at both ends of the axle to prevent the ring from dissociating (Figure 1-4a). Building on rotaxanes, higher-order mechanically interlocked systems have been developed in recent decades, which includes various poly[n]rotaxanes.[69-72]

The exploration of designing and synthesizing various MIMs with unique topologies not only pushes the synthetic capabilities of chemistry but also deepens our understanding of the relationship between molecular structure (topology) and properties, paving the way for exciting new applications based on these novel MIMs.

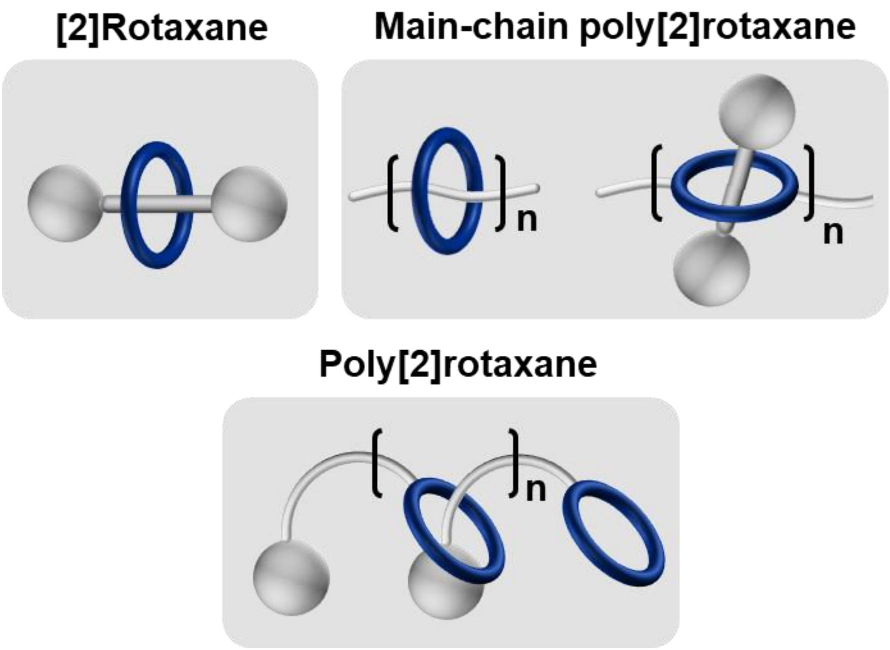

Figure 1-4. [2]Rotaxane as the most fundamental MIMs and various poly[n]rotaxanes

Additionally, the growing attention on MIMs originates not just from their aesthetically appealing molecular architectures, but more importantly from their potential in a wide range of practical applications enabled by their non-covalent (dynamic) and mechanically interlocked (movable) features. In recent years, MIMs such as rotaxanes and catenanes have been widely employed in fields including molecular recognition[73-79], supramolecular catalysis[80-83], and polymeric materials.[84-88]

1.2.3 Synthesis of molecules with various topologies

Despite the broad potential of topological molecules such as CPs and MIMs, their practical exploration is often hindered by the significant challenges associated with their synthesis and purification, which in turn limits both the fundamental understanding of their properties and their broader application in other fields.

As for the synthesis of CPs, two competitive reaction pathways are generally involved: the coupling of end groups on two different linear precursors to form an undesired high-molecular-weight linear polymer, and the intramolecular coupling of two reactive end groups on the same polymer chain to produce the desired cyclic polymer. Although technically simple, the inherent reaction competition typically leads to materials with broad dispersity, and the cyclized product is usually a minor, low-molecular-weight component within a complex mixture of linear and cyclic species. Consequently, the crude products are often poorly defined and contain significant amounts of linear impurities, even after fractionation or other purification methods. With endeavors in recent decades, three distinct approaches have been developed for preparation of cyclic polymers: bimolecular ring closure, unimolecular ring closure and the ring-expansion technique (Figure 1-5).[44-49, 59, 60]

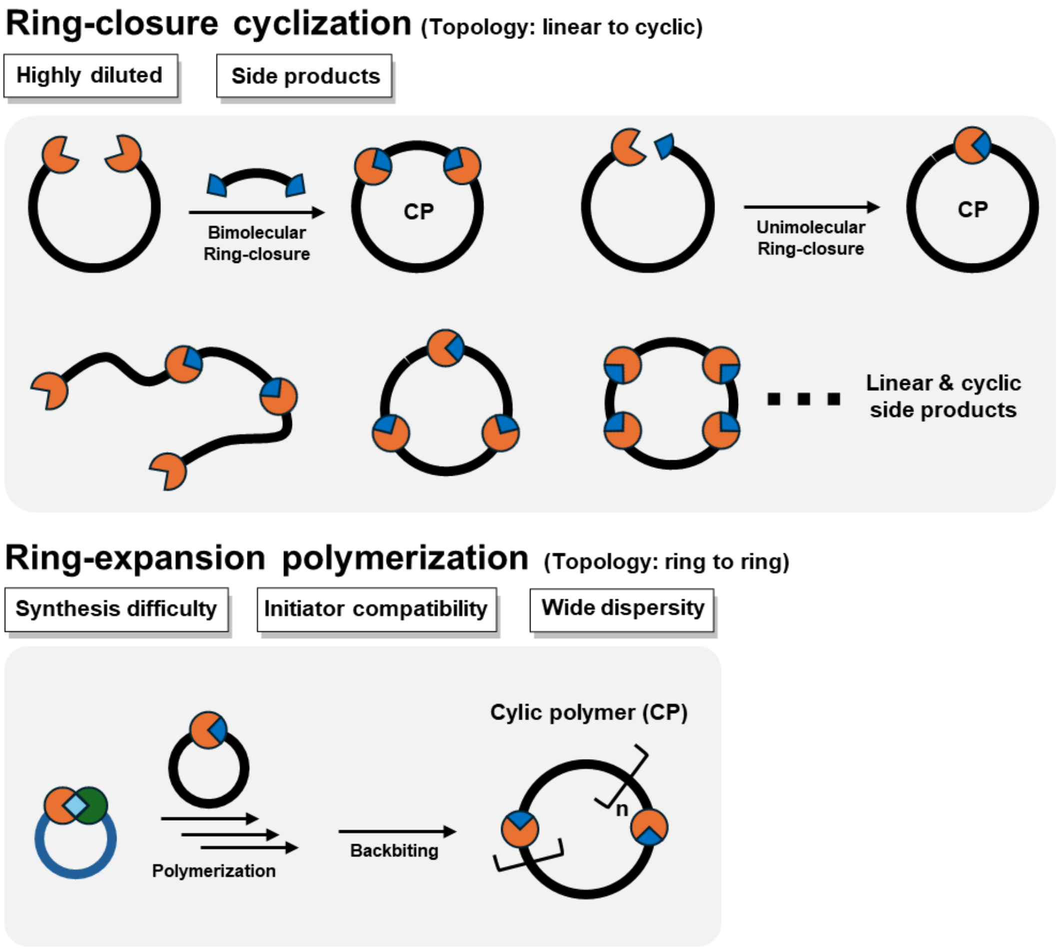

Figure 1-5 Preparation of cyclic polymers by ring-closure cyclization (upper) and ring-expansion polymerization (below).

Regarding the synthesis of MIMs, especially rotaxanes, several representative strategies have been developed since the early statistical method reported in the last century. Unlike this earliest statistical approach, the later-developed methods typically require a so-called “template,” in which the two molecular components are assembled through either noncovalent or covalent interactions—most commonly noncovalent. After fixing the template, further reactions generate the mechanical bond, thereby completing the construction of the rotaxane topology. To date, efforts to synthesize rotaxanes have consistently aimed to improve the efficiency, convenience, generality, reversibility, and functionality of synthetic methods. However, no reported strategy has successfully achieved all these criteria simultaneously (Figure 1-6).[89-93]

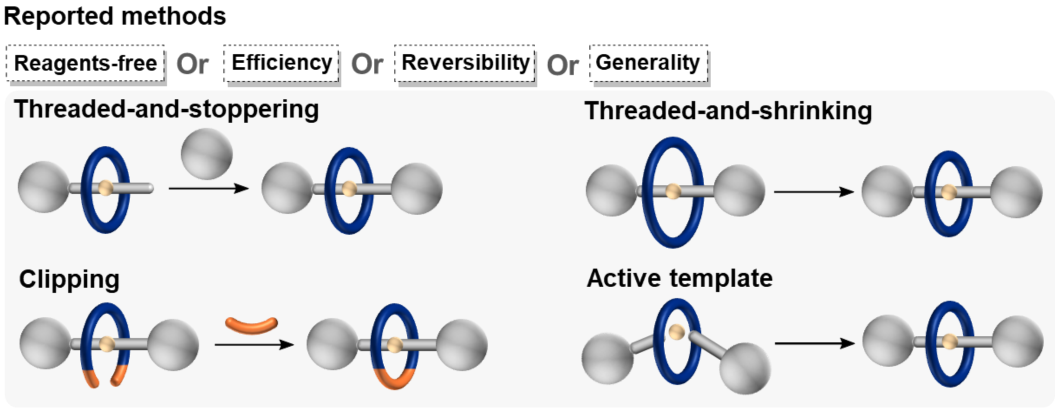

Figure 1-6 Reported methods for rotaxane synthesis

1-3. Scope and outline of this thesis

This thesis primarily focuses on developing novel strategies for tuning molecular topologies. Specifically, the catalyst-free photoreaction is applied as an important tool to regulate the topologies of polymer, macrocycle and rotaxane via the supramolecular strategies. This thesis achieves two main goals: (1) developing a method for preparation of well-defined cyclic polymers at high concentrations (~ 80 g/L), overcoming high dilution constraints of conventional methods (~ 0.1 g/L); (2) developing a rotaxane synthesis strategy that is simultaneously quantitative, reagent-free, reversible, and generally-applicable.

In chapter 2, (E)-3,4,5-trimethoxycinnamic acid (**TCA**) terminal-modified Poly(ethylene glycol) (PEG) are applied to form water-soluble double-stranded pseudo-polyrotaxane (pPRx) with hydroxypropyl-γ-cyclodextrin (HPγCD). **TCA** end groups serve as both active groups for ring-closure and the bulky groups for regulating the structure of pPRx. By assistance of pRRx, two **TCA** end groups of one PEG chain are close to each other, resulting in efficient intramolecular [2+2] photocycloaddition to produce cyclic macromonomer (**C-1mer**) as major product at high concentrations (Figure 1-7). The formation of the pPRx and the cyclization reaction at high concentrations are investigated by NMR spectra, MALDI-TOF MS spectrum, GPC measurement and so on.

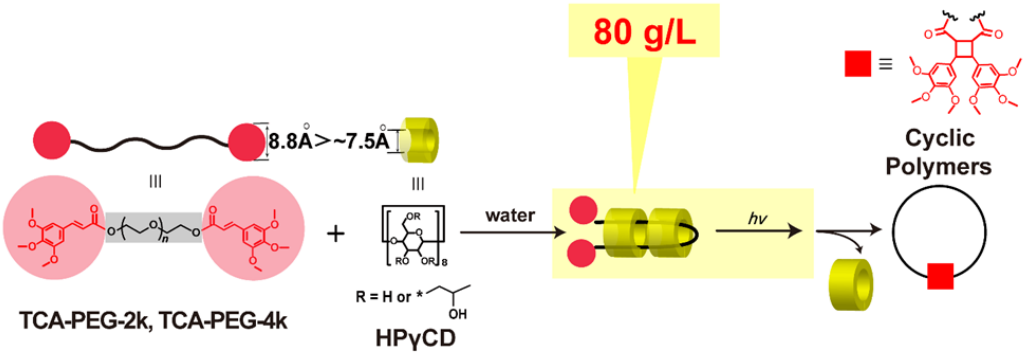

Figure 1-7. Preparation of cyclic PEGs with assistance of pPRx.

In chapter 3, first we developed a methodology to tune the topology of macrocycle. By stimuli-triggered and reversible intramolecular [2+2] photocycloaddition, a transformation between non-homeomorphic topologies (ring versus figure-eight ring) was achieved. The topology transformation is then applied to synthesize rotaxanes and tune the mechanical interlocked states in rotaxanes. With introducing rationally designed axle molecule, using the macrocycle that is capable of transforming to figure-eight ring as wheel molecule, [2]rotaxane is successfully synthesized with quantitative conversion, and [3]rotaxane is also synthesized with high conversion (91%). Similar to the geometric isomers obtained in the transformation of macrocycle in the absence of axle molecules, chair-like and orthogonal rotaxanes are obtained. Additionally, the mechanical bond in chair-like rotaxanes can be unlocked and convert back to the pseudo-rotaxane under heating, with a quantitative conversion (Figure 1-8). The rotaxanation, derotaxanation and the structure of all rotaxanes are characterized by NMR and ESI-MS spectra.

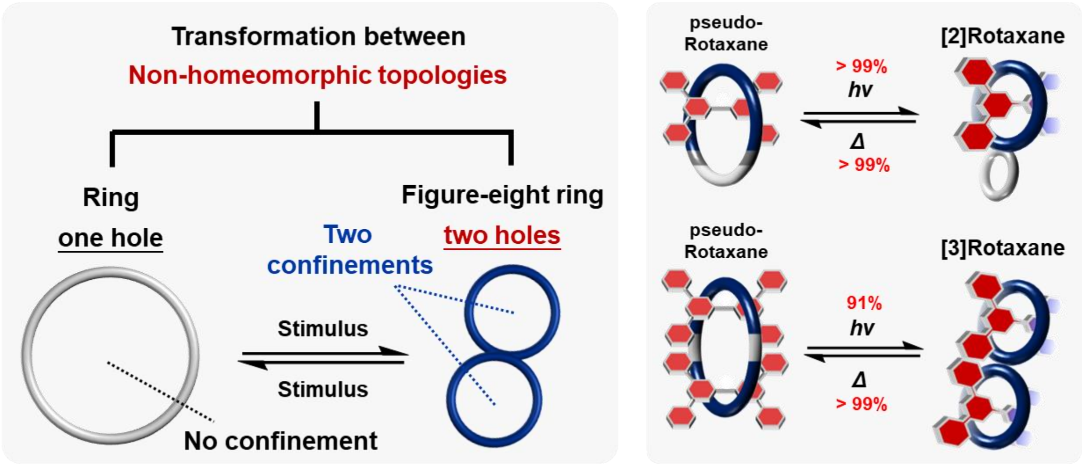

Figure 1-8. Construction and regulation of mechanical interlock in rotaxanes based on transformation between non-homeomorphic topologies.

In chapter 4, the works presented in chapters 2, 3 and 4 are summarized.

References

1. Wang, S.; Kool, E. T. *Nucleic Acids Res.* **1994**, *22*, 2326–2333.
2. Toptan, T.; Abere, B.; Nalesnik, M. A.; Swerdlow, S. H.; Ranganathan, S.; Lee, N; Shair, K.; Moore, P.; Chang, Y. *Proc. Natl. Acad. Sci. U.S.A.* **2018**, *115*, E8737–E8745.
3. Yamaguchi, H.; Kubota, K.; Harada, A. *Chem. Lett.* **2000**, *29*, 384–385.
4. Kool, E. T. *Acc. Chem. Res.* **1998**, *31*, 502.

5. Lasda, E.; Parker, R. *RNA* **2014**, *20*, 1829–1842.
6. Liu, D.; Daubendiek, S. L.; Zillman, M. A.; Ryan, K.; Kool, E. T. *J. Am. Chem. Soc.* **1996**, *118*, 1587–1594.
7. Schlacher, K.; Pham, P.; Cox, M. M.; Goodman, M. F. *Chem. Rev.* **2006**, *106*, 406–419.
8. Møller, H. D.; Mohiyuddin, M.; Prada-Luengo, I.; Sailani, M. R.; Halling, J. F.; Plomgaard, P.; Maretty, L.; Hansen, A. J.; Snyder, M. P.; Pilegaard, H.; Lam, H. Y. K.; Regenberg, B. *Nat. Commun.* **2018**, *9*, 1069.
9. Liu, C. X.; Chen, L. L. *Cell* **2022**, *185*, 2016–2034.
10. Vo, J. N.; Cieslik, M.; Zhang, Y.; Shukla, S.; Xiao, L.; Zhang, Y.; Wu, Y. M.; Dhanasekaran, S. M.; Engelke, C. G.; Cao, X.; Robinson, D. R.; Nesvizhskii, A. I.; Chinnaiyan, A. M. *Cell* **2019**, *176*, 869–881.
11. Litke, J. L.; Jaffrey, S. R. *Nat. Biotechnol.* **2019**, *37*, 667–675.
12. Bahn, J. H.; Zhang, Q.; Li, F.; Chan, T. M.; Lin, X.; Kim, Y.; Wong, D. T. W.; Xiao, X. *Clin. Chem.* **2015**, *61*, 221–230.
13. Arnberg, A. C.; Van Ommen, G. J.; Grivell, L. A.; Van Bruggen, E. F. J.; Borst, P. *Cell* **1980**, *19*, 313–319.
14. Wesselhoeft, R. A.; Kowalski, P. S.; Anderson, D. G. *Nat. Commun.* **2018**, *9*, 2629.
15. Trabi, M.; Craik, D. J. *Trends Biochem. Sci.* **2002**, *27*, 132–138.
16. Gillon, A. D.; Saska, I.; Jennings, C. V.; Guarino, R. F.; Craik, D. J.; Anderson, M. A. *Plant J.* **2008**, *53*, 505–515.
17. Joo, S. H. *Biomol. Ther.* **2012**, *20*, 19.
18. Ji, X.; Nielsen, A. L.; Heinis, C. *Angew. Chem.* **2024**, *136*, e202308251.
19. Dougherty, P. G.; Sahni, A.; Pei, D. *Chem. Rev.* **2019**, *119*, 10241–10287.
20. Jeck, W. R.; Sharpless, N. E. *Nat. Biotechnol.* **2014**, *32*, 453–461.
21. Zorzi, A.; Deyle, K.; Heinis, C. *Curr. Opin. Chem. Biol.* **2017**, *38*, 24–29.
22. Kessler, H. *Angew. Chem. Int. Ed. Engl.* **1982**, *21*, 512–523.
23. Hill, T. A.; Shepherd, N. E.; Diness, F.; Fairlie, D. P. *Angew. Chem. Int. Ed.* **2014**, *53*, 13020–13041.

24. Tashiro, S.; Shionoya, M. *Acc. Chem. Res.* **2020**, *53*, 632–643.

25. Sessler, J. L.; Davis, J. M. *Acc. Chem. Res.* **2001**, *34*, 989–997.

26. Wu, J. R.; Wu, G.; Yang, Y. W. *Acc. Chem. Res.* **2022**, *55*, 3191–3204.

27. Zhang, Z. Y.; Li, C. *Acc. Chem. Res.* **2022**, *55*, 916–929.

28. Bols, P. S.; Anderson, H. L. *Acc. Chem. Res.* **2018**, *51*, 2083–2092.

29. Jirásek, M.; Anderson, H. L.; Peeks, M. D. *Acc. Chem. Res.* **2021**, *54*, 3241–3251.

30. Golder, M. R.; Jasti, R. *Acc. Chem. Res.* **2015**, *48*, 557–566.

31. Gleiter, R.; Esser, B.; Kornmayer, S. C. *Acc. Chem. Res.* **2009**, *42*, 1108–1116.

32. Le Poul, N.; Le Mest, Y.; Jabin, I.; Reinaud, O. *Acc. Chem. Res.* **2015**, *48*, 2097–2106.

33. Chen, C. F.; Han, Y. *Acc. Chem. Res.* **2018**, *51*, 2093–2106.

34. Ghale, G.; Nau, W. M. *Acc. Chem. Res.* **2014**, *47*, 2150–2159.

35. Harada, A. *Acc. Chem. Res.* **2001**, *34*, 456–464.

36. Hu, Q. D.; Tang, G. P.; Chu, P. K. *Acc. Chem. Res.* **2014**, *47*, 2017–2025.

37. Lou, X. Y.; Zhang, S.; Wang, Y.; Yang, Y. W. *Chem. Soc. Rev.* **2023**, *52*, 6644–6663.

38. Zhou, Y.; Jie, K.; Zhao, R.; Huang, F. *Adv. Mater.* **2020**, *32*, 1904824.

39. Höger, S. *Chem. Eur. J.* **2004**, *10*, 1320–1329.

40. Yuan, Y.; Bang, K. T.; Wang, R.; Kim, Y. *Adv. Mater.* **2023**, *35*, 2210952.

41. Ji, X.; Ahmed, M.; Long, L.; Khashab, N. M.; Huang, F.; Sessler, J. L. *Chem. Soc. Rev.* **2019**, *48*, 2682–2697.

42. Qi, Z.; Schalley, C. A. *Acc. Chem. Res.* **2014**, *47*, 2222–2233.

43. Zhang, H.; Zou, R.; Zhao, Y. *Coord. Chem. Rev.* **2015**, *292*, 74–90.

44. Haque, F. M.; Grayson, S. M. *Nat. Chem.* **2020**, *12*, 433–444.

45. Bielawski, C. W.; Benitez, D.; Grubbs, R. H. *Science* **2002**, *297*, 2041–2044.

46. Jia, Z.; Monteiro, M. J. *J. Polym. Sci., Part A: Polym. Chem.* **2012**, *50*, 2085–2097.

47. Kricheldorf, H. R. *J. Polym. Sci., Part A: Polym. Chem.* **2010**, *48*, 251–284.

48. Morgese, G.; Trachsel, L.; Romio, M.; Divandari, M.; Ramakrishna, S. N.; Benetti, E. M. *Angew. Chem.* **2016**, *128*, 15812–15817.

49. Roland, C. D.; Li, H.; Abboud, K. A.; Wagener, K. B.; Veige, A. S. *Nat. Chem.* **2016**, *8*, 791–796.
50. Nasongkla, N.; Chen, B.; Macaraeg, N.; Fox, M. E.; Fréchet, J. M.; Szoka, F. C. *J. Am. Chem. Soc.* **2009**, *131*, 3842–3843.
51. Xia, Y.; Boydston, A. J.; Grubbs, R. H. *Angew. Chem. Int. Ed.* **2011**, *50*, 5882.
52. Li, B.; Yu, B.; Ye, Q.; Zhou, F. *Acc. Chem. Res.* **2015**, *48*, 229–237.
53. Newman, D. J. *Expert Opin. Drug Discov.* **2018**, *13*, 379–385.
54. Buolamwini, J. K. *Curr. Pharm. Des.* **2000**, *6*, 379–392.
55. Garcia Jimenez, D.; Poongavanam, V.; Kihlberg, J. *J. Med. Chem.* **2023**, *66*, 5377–5396.
56. Yu, X.; Sun, D. *Molecules* **2013**, *18*, 6230–6268.
57. Marsault, E.; Peterson, M. L. *J. Med. Chem.* **2011**, *54*, 1961–2004.
58. Driggers, E. M.; Hale, S. P.; Lee, J.; Terrett, N. K. *Nat. Rev. Drug Discov.* **2008**, *7*, 608–624.
59. Alberty, K. A.; Hogen-Esch, T. E.; Carlotti, S. *Macromol. Chem. Phys.* **2005**, *206*, 1035–1042.
60. Hogen-Esch, T. E. *J. Polym. Sci., Part A: Polym. Chem.* **2006**, *44*, 2139–2155.
61. Hadziioannou, G.; Cotts, P. M.; ten Brinke, G.; Han, C. C.; Lutz, P.; Strazielle, C.; Rempp, P.; Kovacs, A. J. *Macromolecules* **1987**, *20*, 493–497.
62. Kammiyada, H.; Ouchi, M.; Sawamoto, M. *Macromolecules* **2017**, *50*, 841–848.
63. Kapnistos, M.; Lang, M.; Vlassopoulos, D.; Pyckhout-Hintzen, W.; Richter, D.; Cho, D.; Chang, T.; Rubinstein, M. *Nat. Mater.* **2008**, *7*, 997–1002.
64. Halverson, J. D.; Grest, G. S.; Grosberg, A. Y.; Kremer, K. *Phys. Rev. Lett.* **2012**, *108*, 038301.
65. Marko, J. F. *Macromolecules* **1993**, *26*, 1442–1444.
66. Poelma, J. E.; Ono, K.; Miyajima, D.; Aida, T.; Satoh, K.; Hawker, C. J. *ACS Nano* **2012**, *6*, 10845–10854.
67. Zhang, B.; Zhang, H.; Li, Y.; Hoskins, J. N.; Grayson, S. M. *ACS Macro Lett.* **2013**, *2*, 845–848.

68. Stoddart, J. F. *Angew. Chem. Int. Ed.* **2017**, *56*, 11094.
69. Harada, A.; Hashidzume, A.; Yamaguchi, H.; Takashima, Y. *Chem. Rev.* **2009**, *109*, 5974–6023.
70. Wenz, G.; Han, B. H.; Müller, A. *Chem. Rev.* **2006**, *106*, 782–817.
71. Arunachalam, M.; Gibson, H. W. *Prog. Polym. Sci.* **2014**, *39*, 1043–1073.
72. Huang, F.; Gibson, H. W. *Prog. Polym. Sci.* **2005**, *30*, 982–1018.
73. Lim, J. Y.; Beer, P. D. *Chem* **2018**, *4*, 731–783.
74. Langton, M. J.; Beer, P. D. *Acc. Chem. Res.* **2014**, *47*, 1935–1949.
75. Tse, Y. C.; Docker, A.; Marques, I.; Félix, V.; Beer, P. D. *Nat. Chem.* **2025**, *in press*, 1–9.
76. Beer, P. D.; Gale, P. A. *Angew. Chem. Int. Ed.* **2001**, *40*, 486–516.
77. Gilday, L. C.; Robinson, S. W.; Barendt, T. A.; Langton, M. J.; Mullaney, B. R.; Beer, P. D. *Chem. Rev.* **2015**, *115*, 7118–7195.
78. Evans, N. H.; Beer, P. D. *Angew. Chem. Int. Ed.* **2014**, *53*, 11716–11754.
79. Arun, A.; Tay, H. M.; Beer, P. D. *Chem. Commun.* **2024**, *60*, 11849–11863.
80. Leigh, D. A.; Marcos, V.; Wilson, M. R. *ACS Catal.* **2014**, *4*, 4490–4497.
81. Wang, K.; Tian, X.; Jordan, J. H.; Velmurugan, K.; Wang, L.; Hu, X. Y. *Chin. Chem. Lett.* **2022**, *33*, 89–96.
82. Olivo, G.; Capocasa, G.; Del Giudice, D.; Lanzalunga, O.; Di Stefano, S. *Chem. Soc. Rev.* **2021**, *50*, 7681–7724.
83. Kwamen, C.; Niemeyer, J. *Chem. Eur. J.* **2021**, *27*, 175–186.
84. Harada, A.; Li, J.; Kamachi, M. *Nature* **1992**, *356*, 325–327.
85. Okumura, Y.; Ito, K. *Adv. Mater.* **2001**, *13*, 485–487.
86. Kim, K. *Chem. Soc. Rev.* **2002**, *31*, 96–107.
87. Sagara, Y.; Karman, M.; Verde-Sesto, E.; Matsuo, K.; Kim, Y.; Tamaoki, N.; Weder, C. *J. Am. Chem. Soc.* **2018**, *140*, 1584–1587.
88. Hart, L. F.; Hertzog, J. E.; Rauscher, P. M.; Rawe, B. W.; Tranquilli, M. M.; Rowan, S. J. *Nat. Rev. Mater.* **2021**, *6*, 508–530.
89. Hänni, K. D.; Leigh, D. A. *Chem. Soc. Rev.* **2010**, *39*, 1240–1251.

90. Xue, M.; Yang, Y.; Chi, X.; Yan, X.; Huang, F. *Chem. Rev.* **2015**, *115*, 7398–7501.

91. Spence, G. T.; Beer, P. D. *Acc. Chem. Res.* **2013**, *46*, 571–586.

92. Goldup, S. M. *Acc. Chem. Res.* **2024**, *57*, 1696–1708.

93. Heard, A. W.; Goldup, S. M. *ACS Cent. Sci.* **2020**, *6*, 117–128.

Chapter 2

Efficient Synthesis of Cyclic Poly(ethylene glycol)s under High Concentration Conditions by the Assistance of Pseudopolyrotaxane with Cyclodextrin Derivatives

2-1 Introduction

Cyclic polymers (CPs) have attracted increasing attention in recent decades due to their unique properties and potential applications, which arise from the absence of end groups.[1-5] However, the efficient synthesis of well-defined CPs remains a significant challenge, despite the development of several representative methods. These synthetic strategies can generally be categorized into two types based on whether a change in polymer topology is involved during the process: ring-closure cyclization (includes bimolecular and unimolecular approaches), and ring-expansion polymerization (Figure 2-1).[6-10]

Ring-closure methods construct CPs either via bimolecular coupling, in which a difunctional linear polymer reacts with a bifunctional linker, or via unimolecular cyclization, where complementary reactive groups are present at the two ends of the same polymer chain (Figure 2-1).[11] However, both approaches typically require highly dilute reaction conditions to minimize the formation of undesired linear or cyclic side products with increased molecular weight (MW) due to intermolecular reactions.

Ring-expansion polymerization generates cyclic polymers through the repeated insertion of cyclic monomers into a preformed cyclic catalyst or initiator. Although this method avoids the entropic penalty associated with conventional ring-closure by expanding an existing ring, it still suffers from considerable drawbacks, including synthetic complexity, limited initiator compatibility, and poor control over MW and

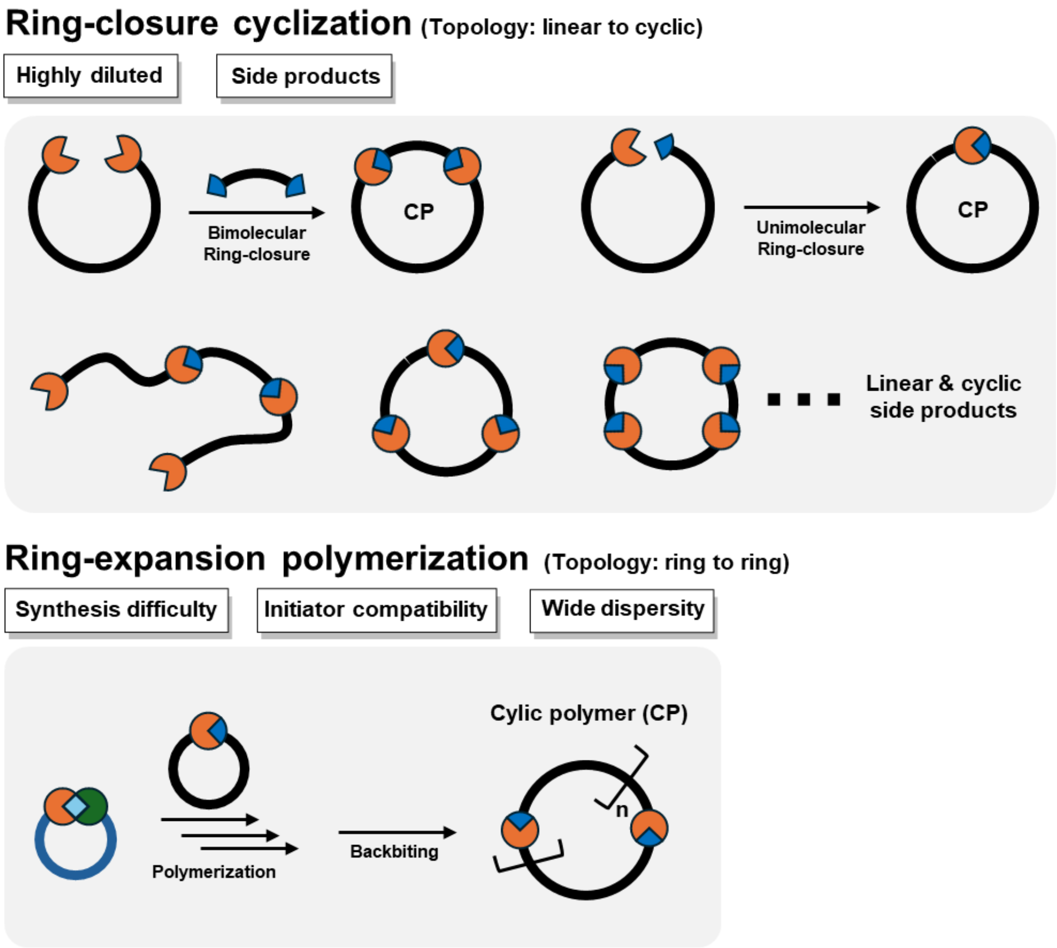

Figure 2-1 Preparation of cyclic polymers by ring-closure cyclization (upper) and ring-expansion polymerization (below).

dispersity. [12]

Ring-closure cyclization is currently the more widely used approach, primarily because of the relatively easy synthesis of precursors, particularly the preparation of telechelic polymers through end-groups-functionalization. However, the requirement for highly dilute conditions during the cyclization step remains a major limitation, which significantly reduces the synthetic efficiency and restricts the broader application of CPs. In recent years, some supramolecular strategies have been employed to facilitate the synthesis of CPs. For instance, self-assembly of telechelic polymers can be driven by π–π stacking interactions between the terminal groups, followed by reactions that yield cyclic polymers.[13-14] In another example, cucurbit[n]uril derivatives have been used to form 1:2 host–guest inclusion complexes with the end groups of telechelic polymers. Subsequent reactions between the end groups within the confined cavity of the host molecule lead to the formation of CPs.[15] Nevertheless, despite these advances, ring-closure methods still suffer from fundamental limitations, particularly the reliance on extremely dilute reaction conditions (0.1 g/L in general) and the challenge of suppressing undesired high-molecular-weight side products, both of which significantly hinder their scalability and practical applicability.

Previously, our group reported cyclization assisted by pPRx constituted of poly(ethylene glycol) (Mn = 400 g/mol) (PEG400) and γ-cyclodextrin (γCD).[16] In high concentration (60 g/L), a propenyl group-modified PEG chain formed double-stranded pPRx with γCD,[17] rendering two propenyl end groups approaching each other. Consequent ring-closure was achieved through a thiol-ene click reaction using a dithiol reagent. This method gave a 14% yield of cyclic PEG400, however, high molecular weight (MW) products were produced. To date, only the cyclization for PEG400 has been studied based on the pPRx-assisted strategy. The synthesis of cyclic PEG with a higher MW, which is widely used in biologic applications, has yet to be reported.

In this work, we apply (E)-3,4,5-trimethoxycinnamic acid (**TCA**) terminal-modified PEG to form water-soluble double-stranded pPRx with HPγCD. **TCA** serves as both the functional groups for the ring-closure and the bulky end groups for regulating the inclusion motif of pPRx. Given the larger molecular size of **TCA** compared to the cavity size of HPγCD (Figure 3-1), the pPRx formed in solution is likely derived from the inclusion of a single PEG chain folding to a U-like shape by HPγCD (Scheme 1b, Scheme S1). This favors the intramolecular cyclization of TCA-modified PEG by the [2+2] photocycloaddition of cinnamoyl terminals to yield the cyclic polymer at high concentration (80 g/L). This cyclization strategy was approved to be applicable for not only the cyclization of PEG (Mn = 2,000 g/mol) (PEG-2k), but also for PEG with relatively higher MW such as PEG (Mn = 4,000 g/mol) (PEG-4k). Without assistance of pPRx, the cyclization of modified PEG gives few C-1mer. By adding HPγCD to form pPRx, the cyclization of **TCA-PEG-2k** and **TCA-PEG-4k** both showed good selectivity to obtain C-1mer as major products at high concentration (10 g/L ~ 80g/L), of which the reaction concentration is hundreds of times higher than conventional methods.[10–15]

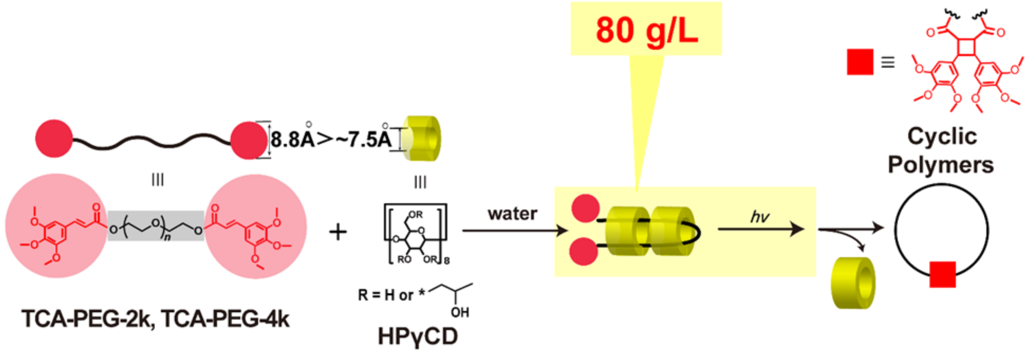

Figure 2-2. Cyclization of PEG modified by **TCA** groups by assistance of HPγCD.

2-2 Materials and Methods

Materials

All the reagents and chemicals used were obtained from commercial sources, unless otherwise noted. HPγCD is the mixture of multi-hydroxypropyl-substituted γCD, of which averaged substituted number is 0.7.

Methods

The 1H NMR spectra were acquired using a JEOL (Tokyo, Japan) JNM-ECA 500 MHz NMR spectrometer. Chemical shifts were referenced to sodium 3-(trimethylsilyl)-1 propanesulfonate ($\delta = 0.00$ ppm) and the solvent value ($\delta = 4.79$ ppm for D2O). Fluorescence spectra were recorded on a HITACHI F-2500 fluorescence spectrophotometer (Tokyo, Japan). Slit widths were both 5.0 nm for excitation and emission side and sensitivity was set to high. MALDI–TOF MS spectra were recorded in the linear positive mode on a mass spectrometer (BRUKER DALTONICS, Ultraflex

III and autoflex maX). 2,5-Dihydroxybenzoic acid was used as a matrix. ESI-MS spectra were recorded in the linear positive mode on a mass spectrometer (Thermo Fisher Scientific, Orbitrap XL). The gel permeation chromatography (GPC) was performed using chloroform or THF at 40 ºC with polystyrene columns [TSKgel GMHHR-M × 2; flow rate = 1.0 mL/min] connected to a Tosoh DP-8020 pump, a CO-8020 column oven, a UV-8020 ultraviolet detector, and an RI-8020 refractive-index detector.

Synthetic work

Synthesis of **TCA**-modified PEG

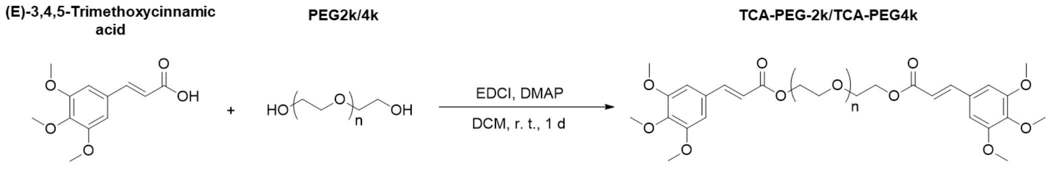

Scheme 2-1. Synthesis of **TCA**-modified PEG

TCA-PEG-2k: 4-Dimethylaminopyridine (DMAP) (73.3 mg, 0.6 mmol, 0.6 eq), (*E*)-3,4,5-trimethoxycinnamic acid (**TCA**) (1.428 g, 6 mmol, 6 eq), and poly(ethylene glycol) (PEG) (M_n = 2000 g/mol) (2 g, 1 mmol, 1 eq) were dissolved in dichloromethane (40 mL). After stirring for 10 minutes, the solution of 1-(3-dimethylaminopropyl)-3-ethylcarbodiimide hydrochloride (EDCI) (1.342 g, 7 mmol, 7 eq) in dichloromethane (20 mL) was added into the mixture dropwisely. After 1 d reaction at room temperature, the mixture was washed by 1 M HCl, saturated NaCl solution and water successively, then the organic phase was dried by $MgSO_4$. The solvent was removed by rotary evaporation to obtain crude product, and the crude product was purified by silica column chromatography (ethyl acetate, then dichloromethane : methanol = 9 : 1) to give **TCA-PEG-2k** as white wax (1.8 g, 75 %). ^{1}H NMR δ (500 MHz, Chloroform-*d*, TMS) =7.59 (d, *J* = 15.9 Hz, 1H), 6.73 (s, 2H), 6.37 (d, *J* = 15.9 Hz, 1H), 4.39 – 4.28 (t, *J* = 9.6 Hz, 2H), 3.86 (s, 6H), 3.85 (s, 3H), 3.79 – 3.71 (t, *J* = 9.6 Hz, 3H) 3.61 (m, 89H) (Figure S2).

TCA-PEG-4k: 4-Dimethylaminopyridine (DMAP) (73.3 mg, 0.6 mmol, 0.6 eq), (*E*)-3,4,5-trimethoxycinnamic acid (**TCA**) (1.428 g, 6 mmol, 6 eq), and poly(ethylene glycol) (PEG) (M_n = 4000 g/mol) (1 g, 1 mmol, 1 eq) were dissolved in dichloromethane (40 mL). After stirring for 10 minutes, the solution of 1-(3-dimethylaminopropyl)-3-ethylcarbodiimide hydrochloride (EDCI) (1.342 g, 7 mmol, 7 eq) in dichloromethane (20 mL) was added into the mixture dropwisely. After 1 d reaction at room temperature, the solvent was removed by rotary evaporation and the residues were dissolved in hot ethanol. **TCA-PEG-4k** as white solid was obtained by 3 times recrystallization from cold ethanol (0.9 g, 80%).^{1}H NMR (500 MHz, Chloroform-*d*) δ 7.59 (d, *J* = 15.9 Hz, 1H), 6.73 (s, 2H), 6.36 (d, *J* = 15.9 Hz, 1H), 4.38 – 4.26 (t, *J* = 9.6 Hz, 2H), 3.86 (s, 6H), 3.85 (s, 3H), 3.78 – 3.72 (t, *J* = 9.6 Hz, 2H), 3.61 (m, 131H) (Figure S2).

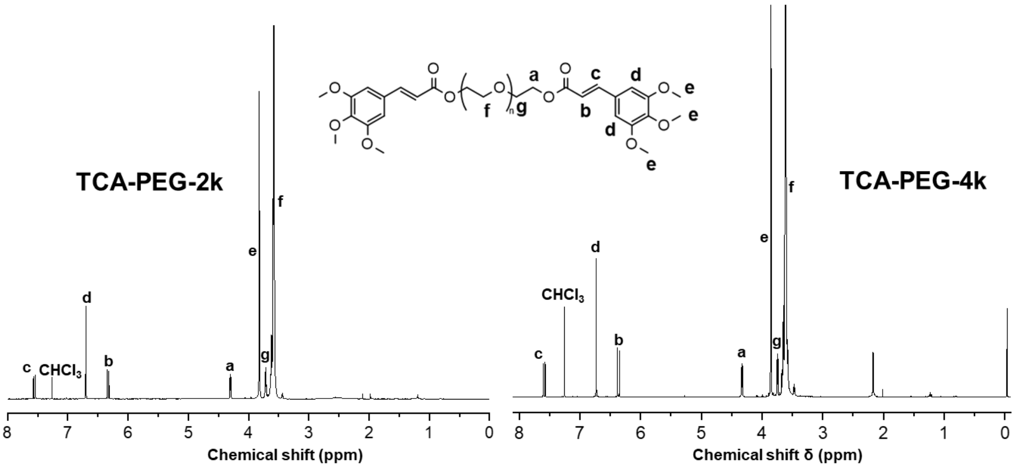

Figure 2-3. ^{1}H NMR spectra of **TCA-PEG-2k** and **TCA-PEG-4k**, CDCl$_3$, r.t.

Synthesis of model molecule (**TCA-2glyco**)

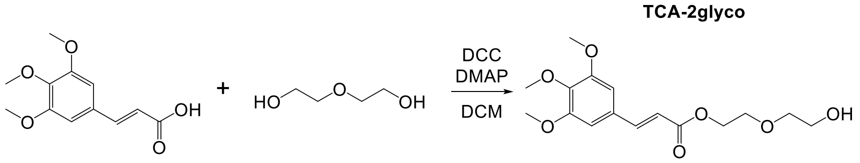

Scheme 2-2. The synthesis of **TCA-2glyco**

1 g (1 eq) (*E*)-3,4,5-trimethoxycinnamic acid, 2.67 g (6 eq) diethylene Glycol and 51.3 mg (0.1 eq) DMAP were added to the flask and dissolved by DCM. The solution of 0.86 g (1 eq) N,N'-dicyclohexylcarbodiimide in DCM was added to the mixture dropwisely. The mixture was stirred at r. t. overnight. After reaction, the mixture was washed by water (x 2) and then brine (x 1). The crude was obtained by drying the organic phase and followed by evaporation. The **TCA-2glyco** was obtained as white wax by purifying the crude through silica column chromatography (100% Ethyl acetate, yield. 66%). ^{1}H NMR (500 MHz, Chloroform-d) δ 7.62 (d, J = 15.9 Hz, 1H), 6.75 (s, 2H), 6.38 (d, J = 15.9 Hz, 1H), 4.41 – 4.35 (t, J = 9.6 Hz, 2H), 3.87 (s, 9H), 3.80 – 3.74 (m, 4H), 3.65 – 3.62 (t, J = 9.6 Hz, 2H).

2-2 Results and discussion

2-2-1 Formation of pPRx between HPγCD and TCA-modified PEG

TCA-modified PEG was synthesized from PEG by an esterification reaction with (*E*)-3,4,5-trimethoxycinnamic acid (Scheme 2-1). The structure was characterized by ^{1}H NMR and MALDI-TOF mass spectra (Figure 2-3). Given the larger molecular size of **TCA** compared to the cavity size of HPγCD (Figure 2-4), the pPRx formed in solution is likely derived from the inclusion of a single PEG chain folding to a U-like shape by HPγCDThe formation of water-soluble pPRx from **TCA-PEG-2k** and HPγCD in an aqueous solution was investigated using NOESY measurements. A correlation peak between proton a of the PEG unit on **TCA-PEG-2k** and the proton of HPγCD was observed (Figures 2-5), indicating that the PEG chain of **TCA-PEG-2k** was fully included by HPγCD. Protons b, c, and d on the C=C bond of cinnamoyl moiety showed correlation peaks with HPγCD, implying that the cinnamoyl terminals were also partially included in the HPγCD cavity.[18] Additionally, the DOSY

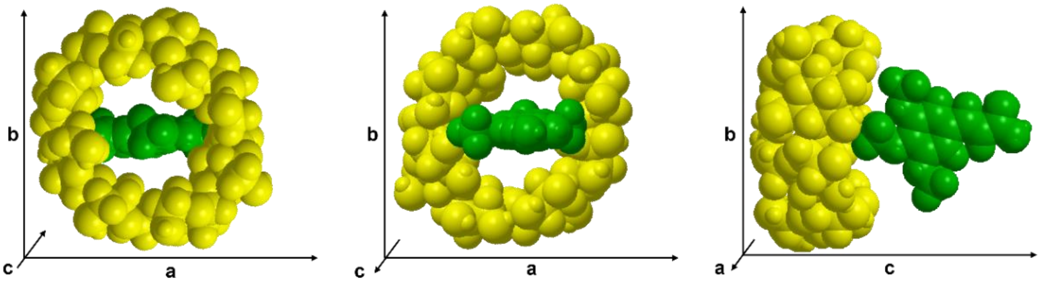

Figure 2-4. Molecular size of **TCA** (green) and cavity size of HPγCD (yellow).

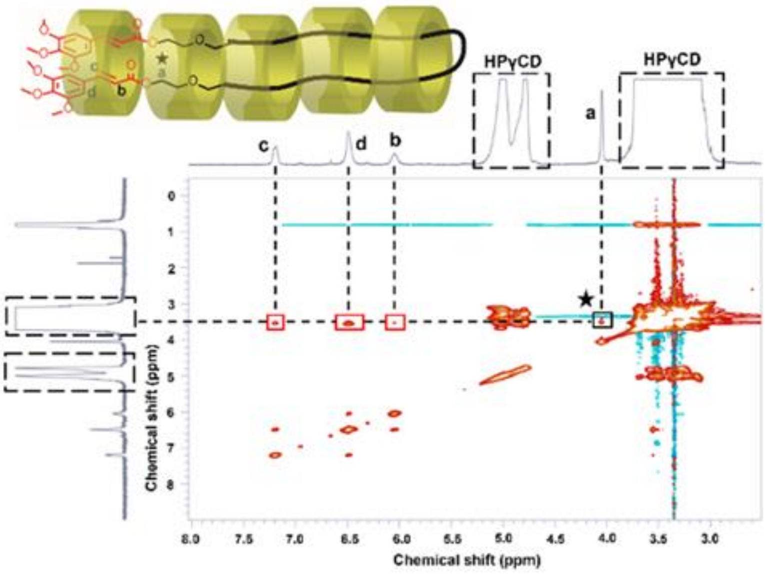

Figure 2-5. The NOESY spectrum of a solution of **TCA-PEG-2k** with HPγCD ([**TCA-PEG-2k**] = 10 g/L, **TCA-PEG-2k** : HPγCD = 1 : 12) in D_2O at 5 °C.

measurement of an aqueous solution of **TCA-PEG-2k** in the presence of HPγCD (d_0 **TCA-PEG-2k@**HPγCD = 0.94) showed a lower diffusion constant than that of the **TCA-PEG-2k** aqueous solution without HPγCD(d_0 **TCA-PEG-2k** = 1.23). This was attributed to the larger molecular size after the formation of pPRx (Figures. 2-6 and 2-7, Scheme 2-3). Based on these results, it is concluded that the **TCA-PEG-2k** formed U-like-shaped pPRx with HPγCD in an aqueous solution.

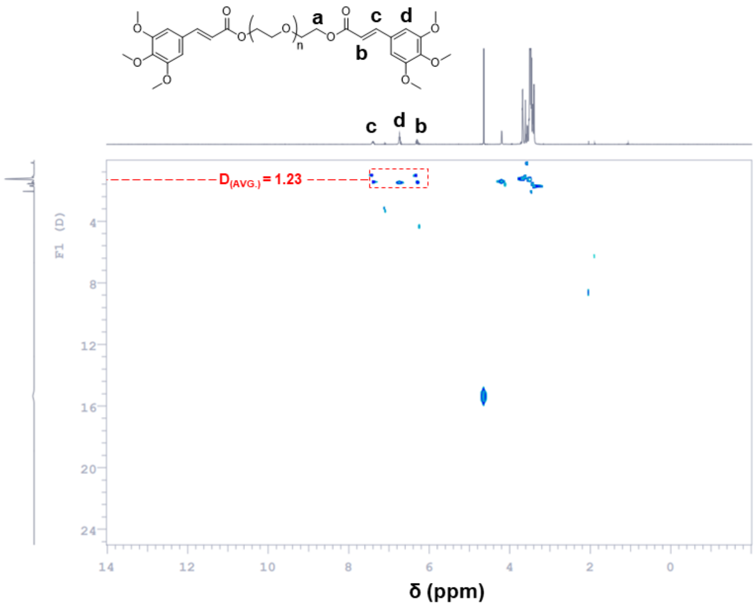

Figure 2-6. DOSY spectrum of **TCA-PEG-2k** ([**TCA-PEG-2k**] = 10 g/L), D_2O, 20 °C.

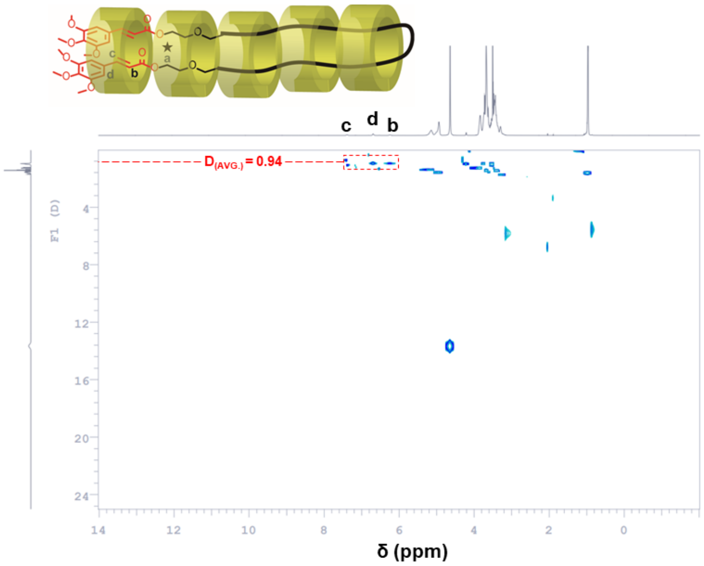

Figure 2-7. DOSY spectrum of mixture of **TCA-PEG-2k** and HPγCD ([**TCA-PEG-2k**] = 10 g/L, **TCA-PEG-2k** : HPγCD = 1 : 12), D_2O, 20 °C.

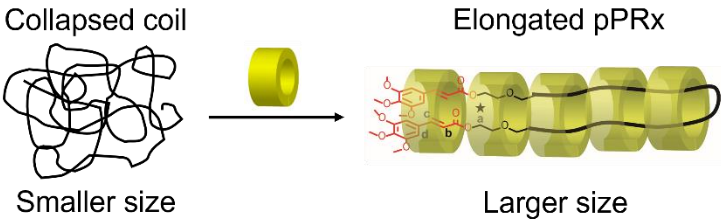

Scheme 2-3. Molecular size change after adding HPγCD

2-2-2 Cyclization of TCA-PEG-2k by assistance of pPRx

An aqueous solution of **TCA-PEG-2k** and HPγCD was irradiated for 3 h at 5 °C after bubbling N_2 for 10 min at a **TCA-PEG-2k** concentration of 80 g/L and a **TCA-PEG-2k** : HPγCD ratio of 1:12. After the reaction, water was removed by evaporation, and all residues were re-dissolved in methanol. Then the HPγCD was removed by precipitating in chloroform. The ^{1}H NMR showed all C=C bonds disappeared after irradiation (Figure 2-8), indicating the completion of the photocycloaddition of the cinnamoyl moiety. Successive gel permeation chromatograph (GPC) measurements for the irradiated product showed that the peaks of **TCA-PEG-2k** disappeared, while a fraction with a longer elution time formed. This fraction was isolated by separation GPC (Figures. 2-9a, 2-9b and 2-10). The ^{1}H NMR spectrum of the isolated products did not show C=C bonds (Figure 2-9c), and the MALDI-TOF result indicated the MW was the same as **TCA-PEG-2k** before irradiation (Figures 2-9d and 2-9e). These results showed that the major product was **C-1mer** after photoreaction in the presence of HPγCD. By calculating the peak-fitting, the ratio of the **C-1mer** in the products after photocycloaddition was only 9% in the absence of HPγCD, but increased to 66% in the presence of HPγCD (Figure 2-13). These results indicated that HPγCD assisted in the intramolecular cyclization of **TCA-PEG-2k**.

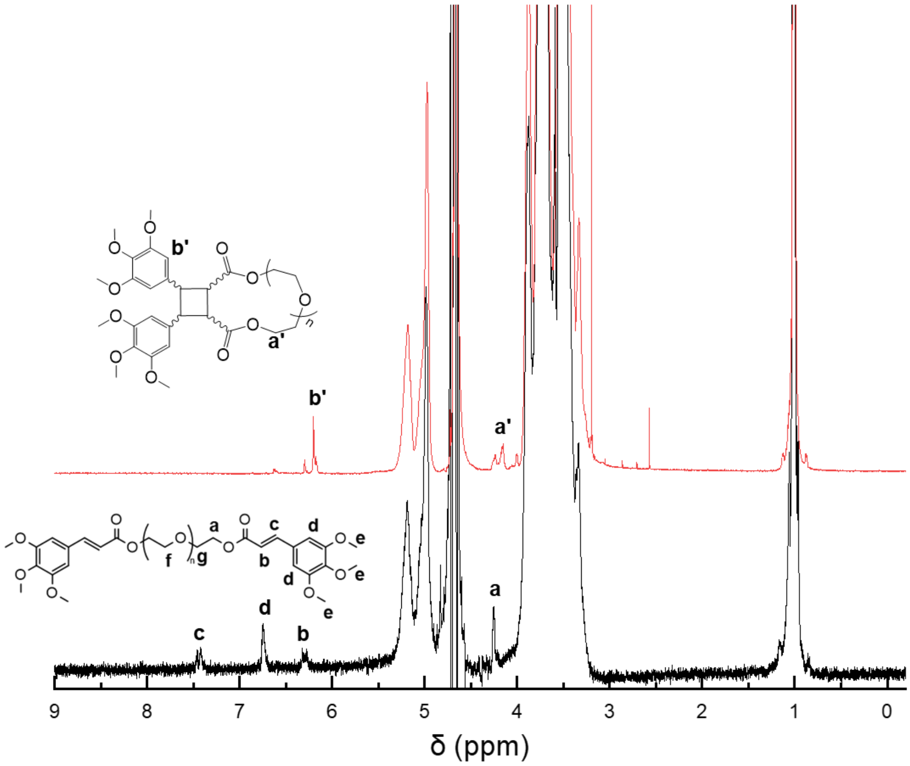

Figure 2-8. ^{1}H NMR spectra of solution of **TCA-PEG-2k** and HPγCD ([**TCA-PEG-2k**] = 80 g/L, **TCA-PEG-2k : HPγCD** = 1 : 12) before (lower) and after (upper) irradiation, D_2O, r. t.

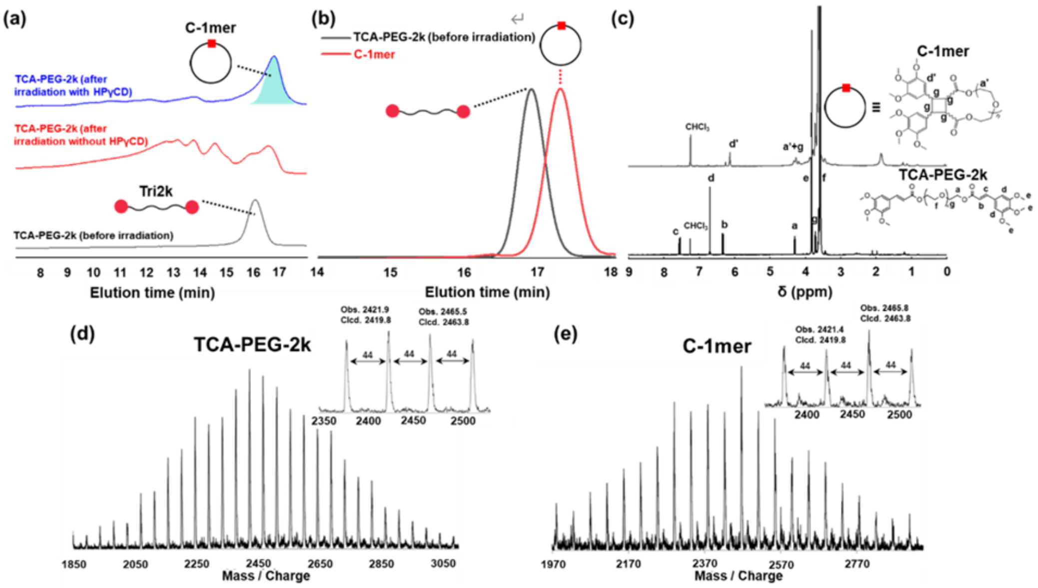

Figure 2-9. (a) GPC charts of aqueous solutions of **TCA-PEG-2k** in the presence and absence of HPγCD before/after irradiation for 3 h ([**TCA-PEG-2k**] = 80 g/L, **TCA-PEG-2k** : HPγCD = 1 : 12), eluent: chloroform. (b) GPC charts of isolated **C-1mer** and **TCA-PEG-2k**, eluent: THF. (c) ^{1}H NMR spectrum spectra of isolated **C-1mer** and **TCA-PEG-2k** before irradiation. MALDI-TOF spectra of (d) **TCA-PEG-2k** and (e) isolated **C-1mer**.

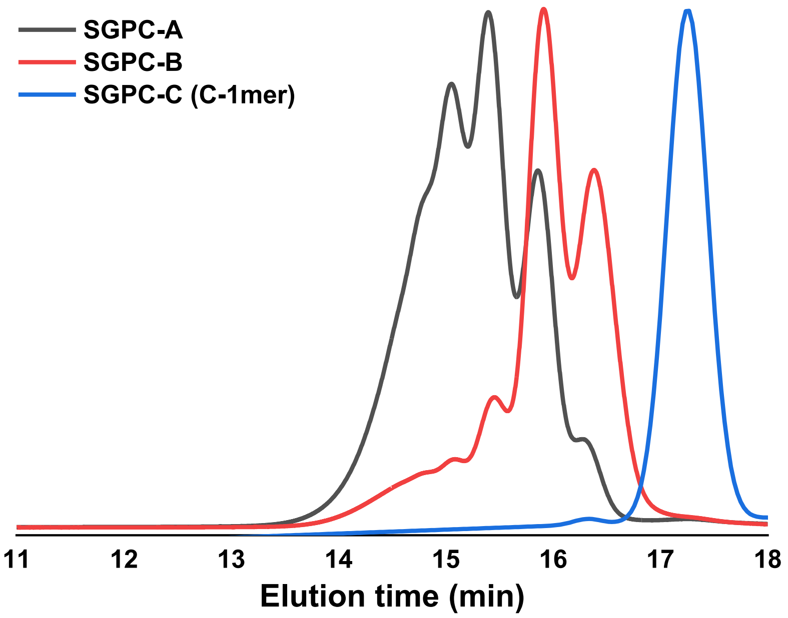

Figure 2-10. GPC charts of three fractions obtained by separation GPC (SGPC).

We investigated the concentration-dependency of yield of **C-1mer** by GPC measurements (Figure 2-11). Solution of **TCA-PEG-2k** and HPγCD with different **TCA-PEG-2k** concentrations (10 g/L, 20 g/, 40 g/L, 60 g/L and 80 g/L, **TCA-PEG-2k** : HPγCD = 1 : 12 in all samples) were irradiated for 3 h at 5 °C after bubbling N_2 for 10 min. The yield of **C-1mer** increased with decreasing the **TCA-PEG-2k** concentration (Figures 2-14 to 2-18). When the **TCA-PEG-2k** concentration was 10 g/L, the yield of **C-1mer** raised to 74%, showing good selectivity for synthesizing **C-1mer**, where the reaction concentration (10 g/L) was still 100 times higher than conventional cyclization methods (~ 0.1 g/L).

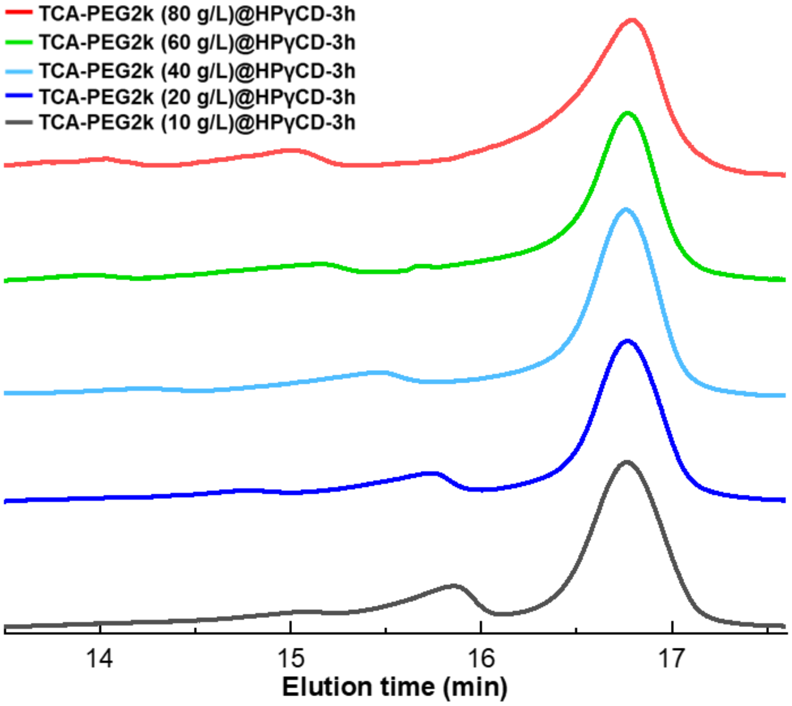

Figure 2-11. GPC charts of products after irradiating the solution of **TCA-PEG-2k** and HPγCD with different concentration of **TCA-PEG-2k**, eluent: chloroform.

Additionally, with the assistance of pPRx, the yield of **C-1mer** was higher than the case of irradiating **TCA-PEG-2k** in the absence of HPγCD. In the case of without adding HPγCD, the yield of **C-1mer** dramatically decreased as the concentration increased. In fact, the yield of **C-1mer** was less than 10% when the **TCA-PEG-2k** concentration was higher than 80 g/L (Figures 2-12 and 2-18). Therefore, adding HPγCD to form U-like-shaped pPRx effectively favored the cyclization of **TCA-PEG-2k** in high concentrations.

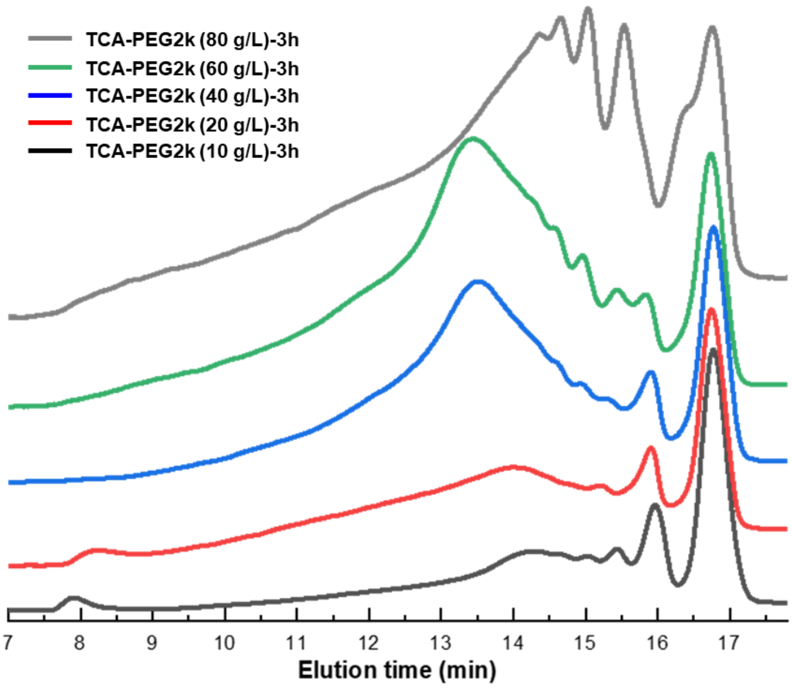

Figure 2-12. GPC charts of solution of **TCA-PEG-2k** ([**TCA-PEG-2k**] = 10 ~ 80 g/L) after 3 h irradiation, eluent: chloroform.

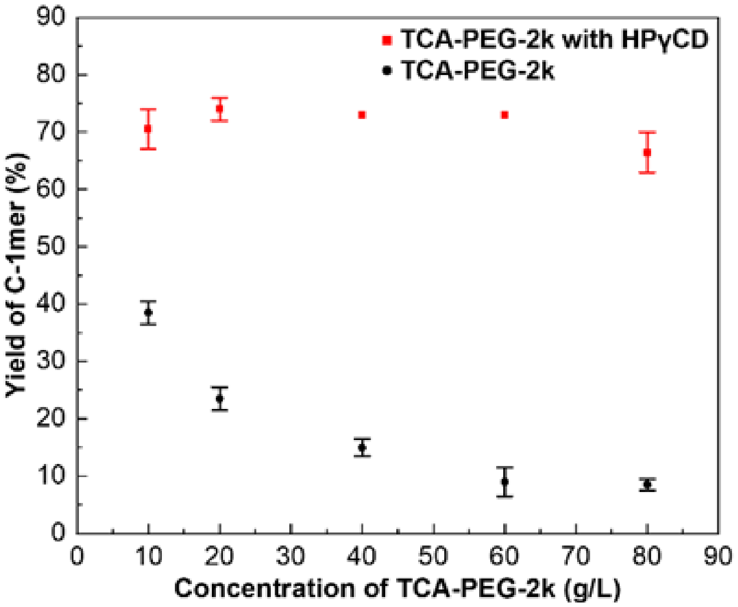

Figure 2-13. The yield of **C-1mer** verse concentration of **TCA-PEG-2k** in the presence and absence of HPγCD.

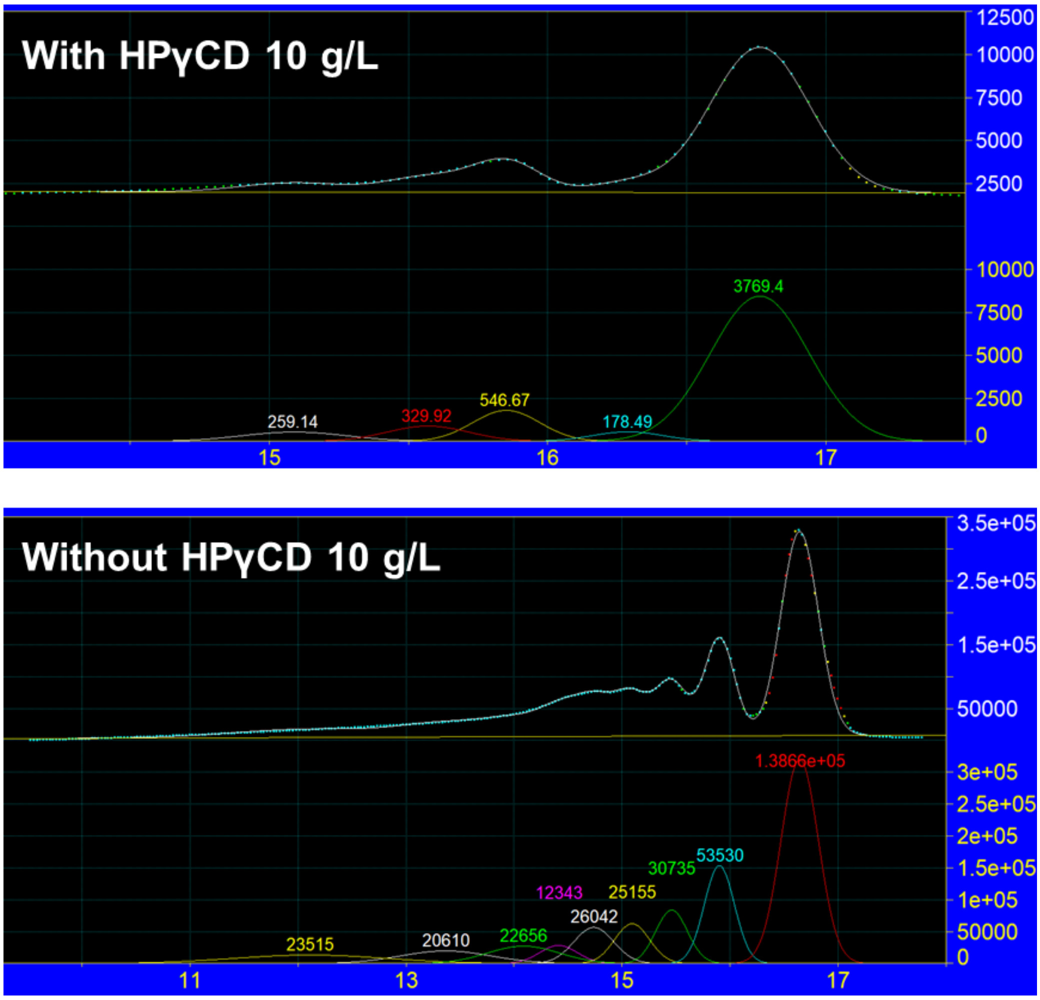

Figure 2-14. Curve fitting using the nonlinear least-squares method for GPC profiles of products of irradiating **TCA-PEG-2k** ([**TCA-PEG-2k**] = 10 g/L) in the presence and absence of HPγCD. Ratio of **C-1mer** in the obtained product is calculated from the integral ratio of the peaks. GPC profiles are shown as the signal intensity (differential refractive index) vs elution time.

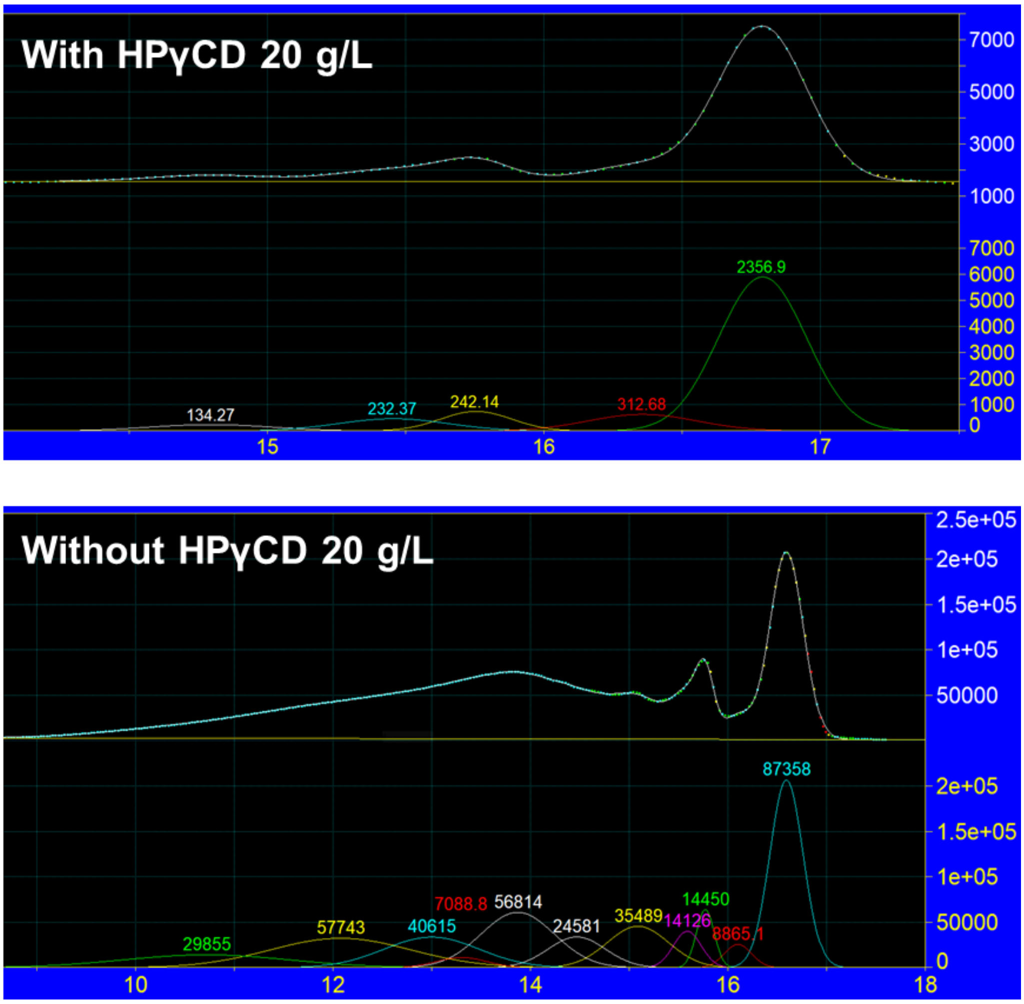

Figure 2-15. Curve fitting using the nonlinear least-squares method for GPC profiles of products of irradiating **TCA-PEG-2k** ([**TCA-PEG-2k**] = 20 g/L) in the presence and absence of HPγCD. Ratio of **C-1mer** in the obtained product is calculated from the integral ratio of the peaks. GPC profiles are shown as the signal intensity (differential refractive index) vs elution time.

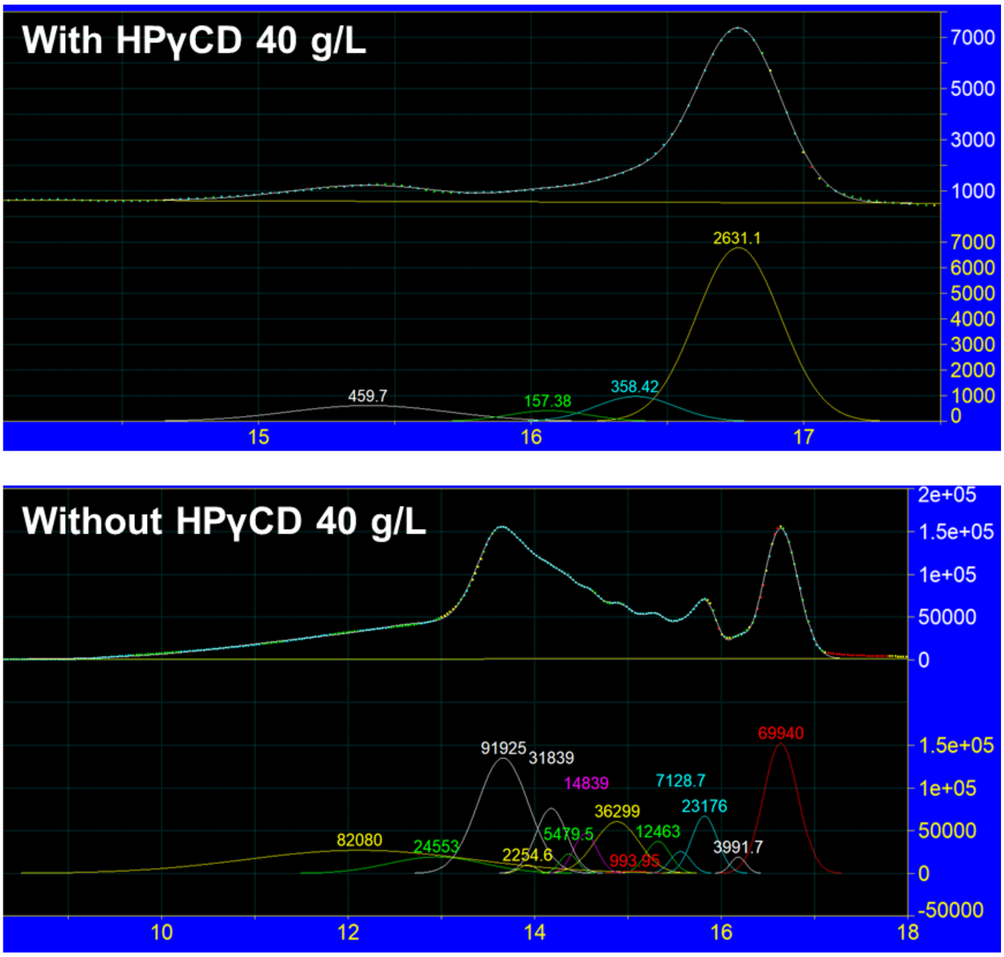

Figure 2-16. Curve fitting using the nonlinear least-squares method for GPC profiles of products of irradiating **TCA-PEG-2k** ([**TCA-PEG-2k**] = 40 g/L) in the presence and absence of HPγCD. Ratio of **C-1mer** in the obtained product is calculated from the integral ratio of the peaks. GPC profiles are shown as the signal intensity (differential refractive index) vs elution time.

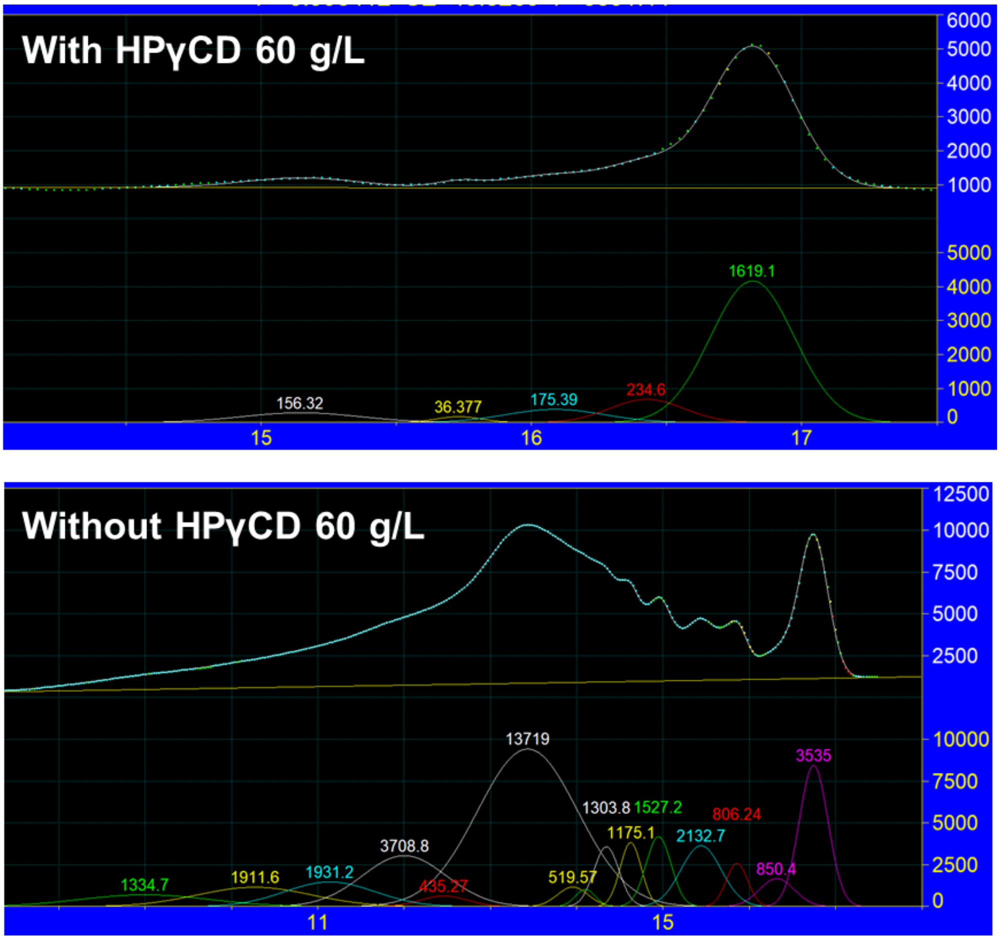

Figure 2-17. Curve fitting using the nonlinear least-squares method for GPC profiles of products of irradiating **TCA-PEG-2k** ([**TCA-PEG-2k**] = 60 g/L) in the presence and absence of HPγCD. Ratio of **C-1mer** in the obtained product is calculated from the integral ratio of the peaks. GPC profiles are shown as the signal intensity (differential refractive index) vs elution time.

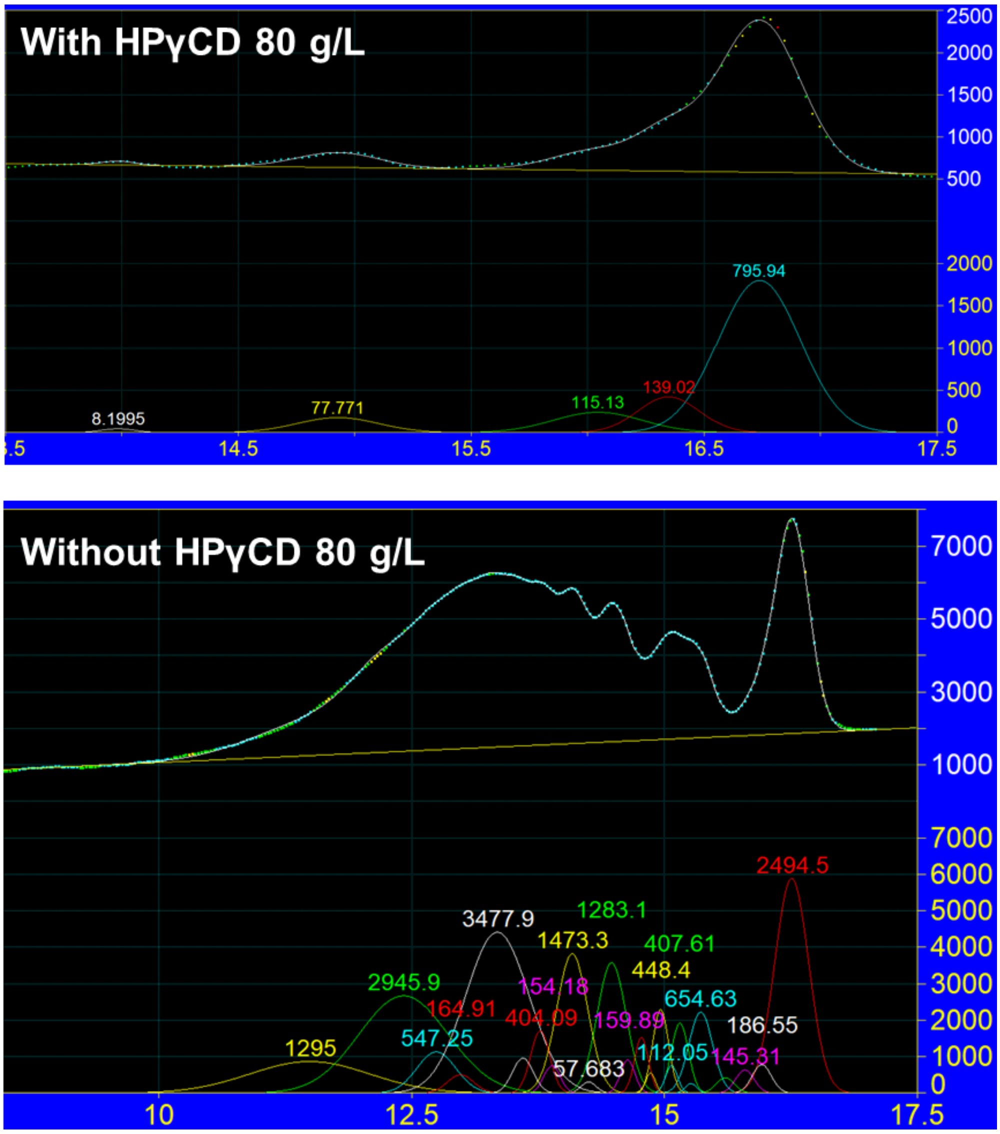

Figure 2-18. Curve fitting using the nonlinear least-squares method for GPC profiles of products of irradiating **TCA-PEG-2k** ([**TCA-PEG-2k**] = 80 g/L) in the presence and

absence of HPγCD. Ratio of **C-1mer** in the obtained product is calculated from the integral ratio of the peaks. GPC profiles are shown as the signal intensity (differential refractive index) vs elution time.

2-2-3 Cyclization of TCA-PEG-4k by assistance of pPRx

Our pPRx-assisted strategy was also applicable for the cyclization of PEG with higher MW. The pPRx-assisted cyclization of **TCA-PEG-4k** was performed by the same method at the concentration of 80 g/L. The ^{1}H NMR showed all C=C of **TCA-PEG-4k** disappeared after irradiation in the presence of HPγCD, indicating the completion of the ring-closure through the photocycloaddition of the cinnamoyl moiety (Figures 19 and 20). Besides, according to the GPC results, high MW products were the major products after irradiating **TCA-PEG-4k** in the absence of HPγCD and the ratio of **C-1mer** in products was only 5% (Figure 21). In contrast, in the pPRx-assisted cyclization of **TCA-PEG-4k** gave **C-1mer** as major products. The ratio of **C-1mer** dramatically increased to 45% compared with the cyclization without HPγCD.

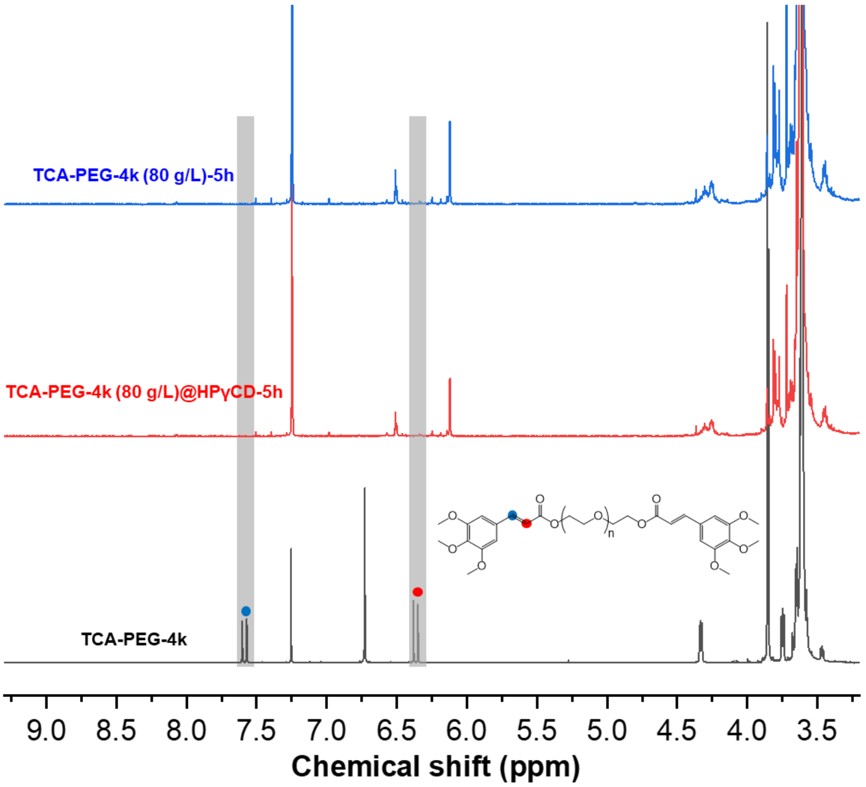

Figure 2-19. ^{1}H NMR spectra of solution of **TCA-PEG-4k** and HPγCD ([**TCA-PEG-4k**] = 80 g/L, **TCA-PEG-4k :** HPγCD = 1 : 20) before (lower) and after (upper) irradiation, D$_2$O, r. t.

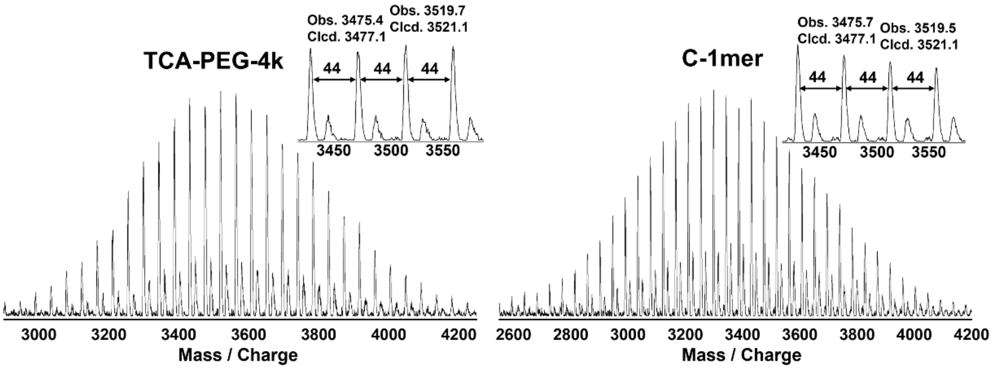

Figure 2-20. The MALDI-TOF spectra of **TCA-PEG-4k** and **C-1mer** obtained by irradiating aqueous solution of **TCA-PEG-4k** and HPγCD ([**TCA-PEG-4k**] = 80 g/L, **TCA-PEG-4k :** HPγCD = 1 : 20).

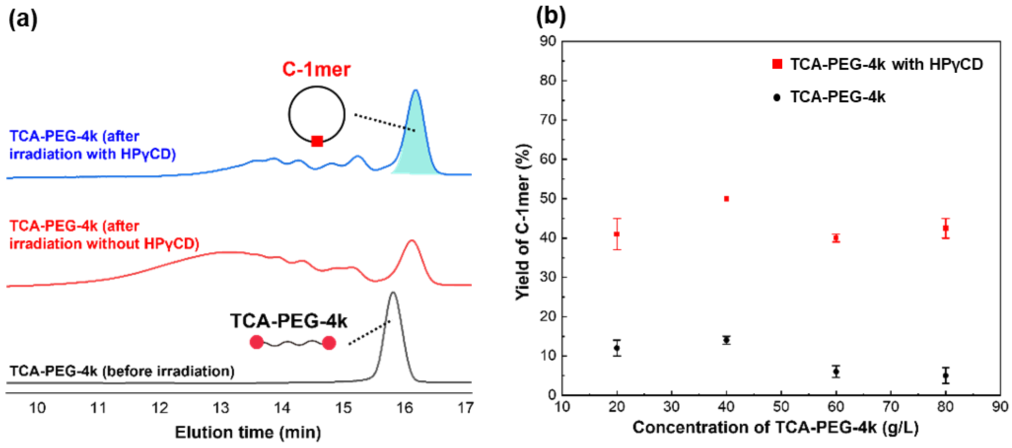

Figure 2-21. (a) GPC charts of aqueous solutions of **TCA-PEG-4k** in the presence and absence of HPγCD before/after irradiation for 5 h ([**TCA-PEG-4k**] = 80 g/L, **TCA-PEG-4k** : HPγCD = 1 : 20), eluent: chloroform. (b) The yield of **C-1mer** of cyclization of **TCA-PEG-4k** in the presence and absence of HPγCD at different concentrations.

The concentration-dependency in the pPRx-assisted cyclization of **TCA-PEG-4k** was also investigated (20 g/, 40 g/L, 60 g/L and 80 g/L, **TCA-PEG-4k** : HPγCD = 1 : 20 in all samples). The yield of **C-1mer** showed nearly no dependency on the concentration (43% at 20 g/L, 45% at 80 g/L), which is similar with the cyclization of **TCA-PEG-2k** (Figure 4b, S24-27). Without HPγCD, the yield of **C-1mer** in product was much lower than that of pPRx-assisted cyclization (11% at 20 g/L, 5% at 80 g/L) (Figs. 4b and S28-S32). This result indicated that the pPRx also assisted in the intramolecular cyclization of **TCA-PEG-4k** to obtain the **C-1mer**.

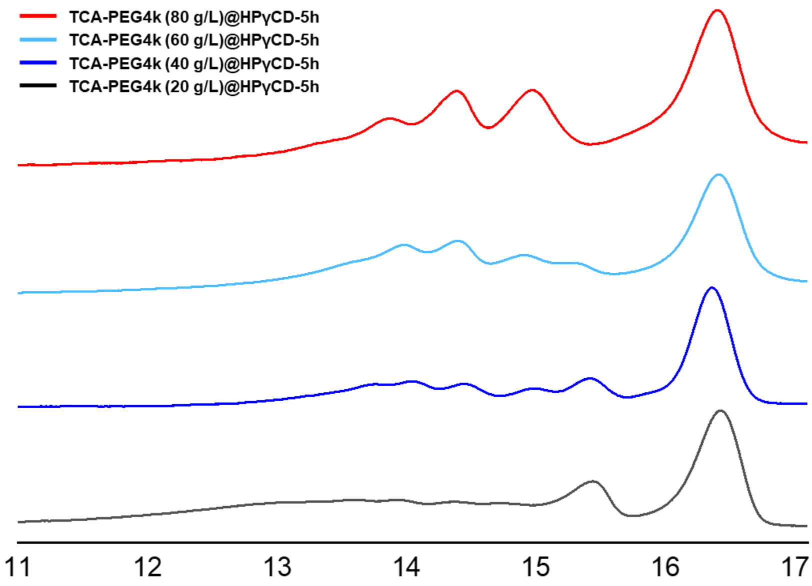

Figure 2-22. GPC charts of solution of **TCA-PEG-4k** ([**TCA-PEG-4k**] = 20 ~ 80 g/L) after 5 h irradiation in the presence of HPγCD, eluent: chloroform.

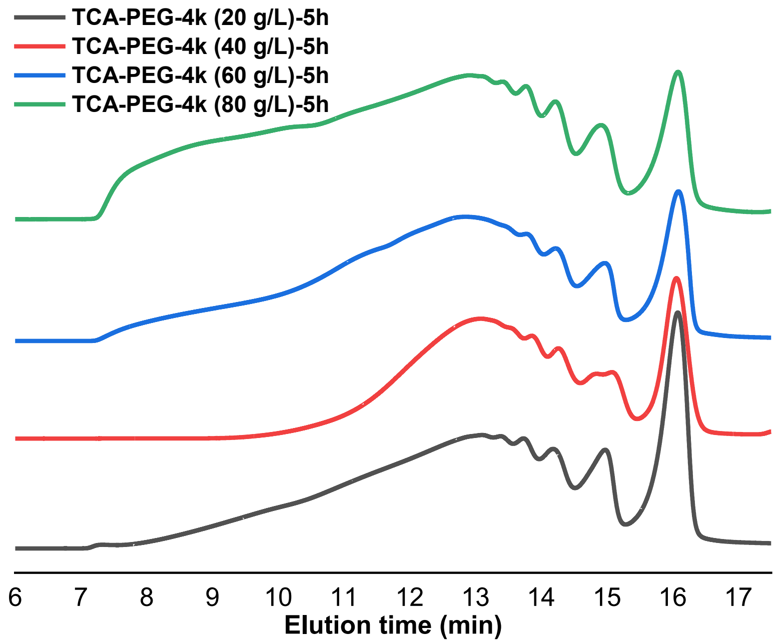

Figure 2-23. GPC charts of solution of **TCA-PEG-4k** ([**TCA-PEG-4k**] = 20 ~ 80 g/L) after 5 h irradiation, eluent: chloroform.

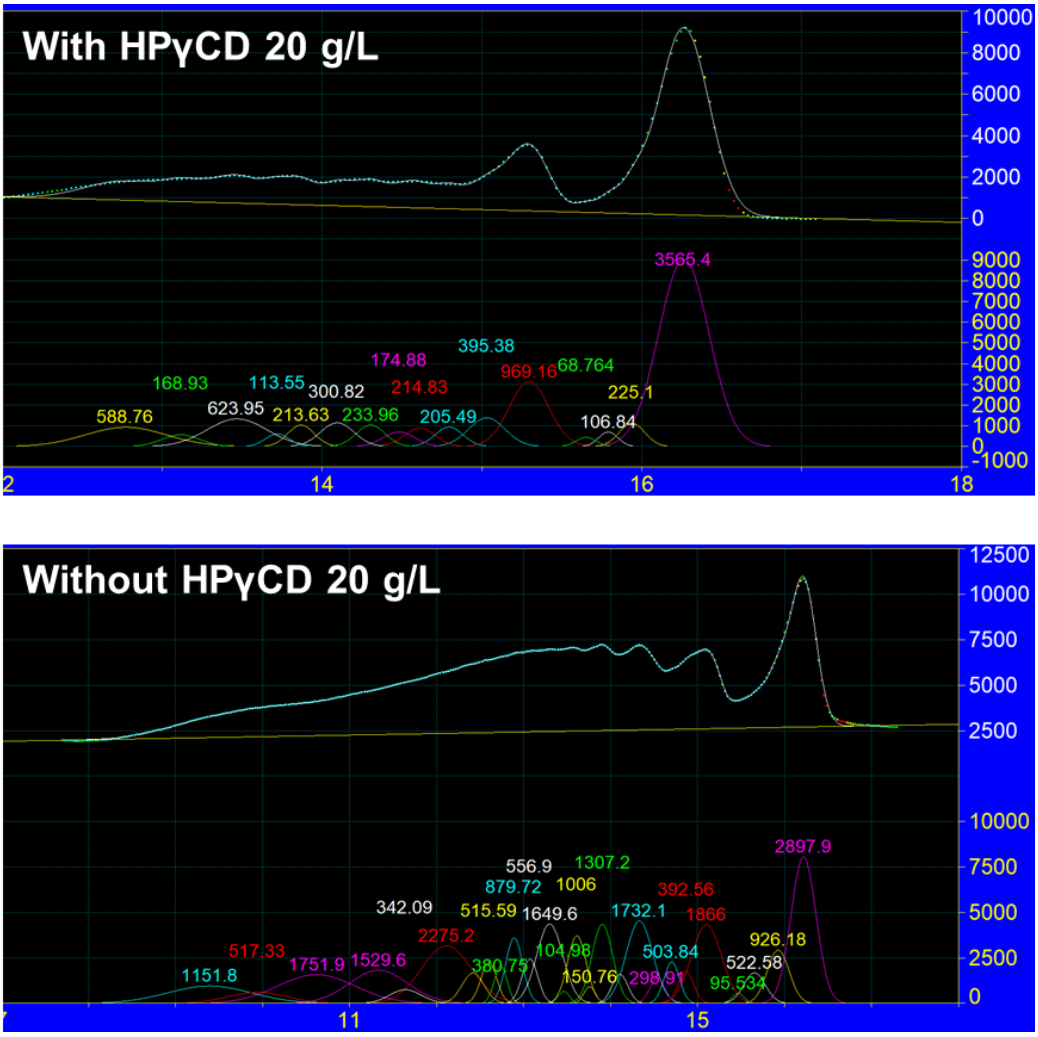

Figure 2-24. Curve fitting using the nonlinear least-squares method for GPC profiles of products of irradiating **TCA-PEG-4k** ([**TCA-PEG-4k**] = 20 g/L) in the presence and absence of HPγCD. Ratio of **C-1mer** in the obtained product is calculated from the integral ratio of the peaks. GPC profiles are shown as the signal intensity (differential refractive index) vs elution time.

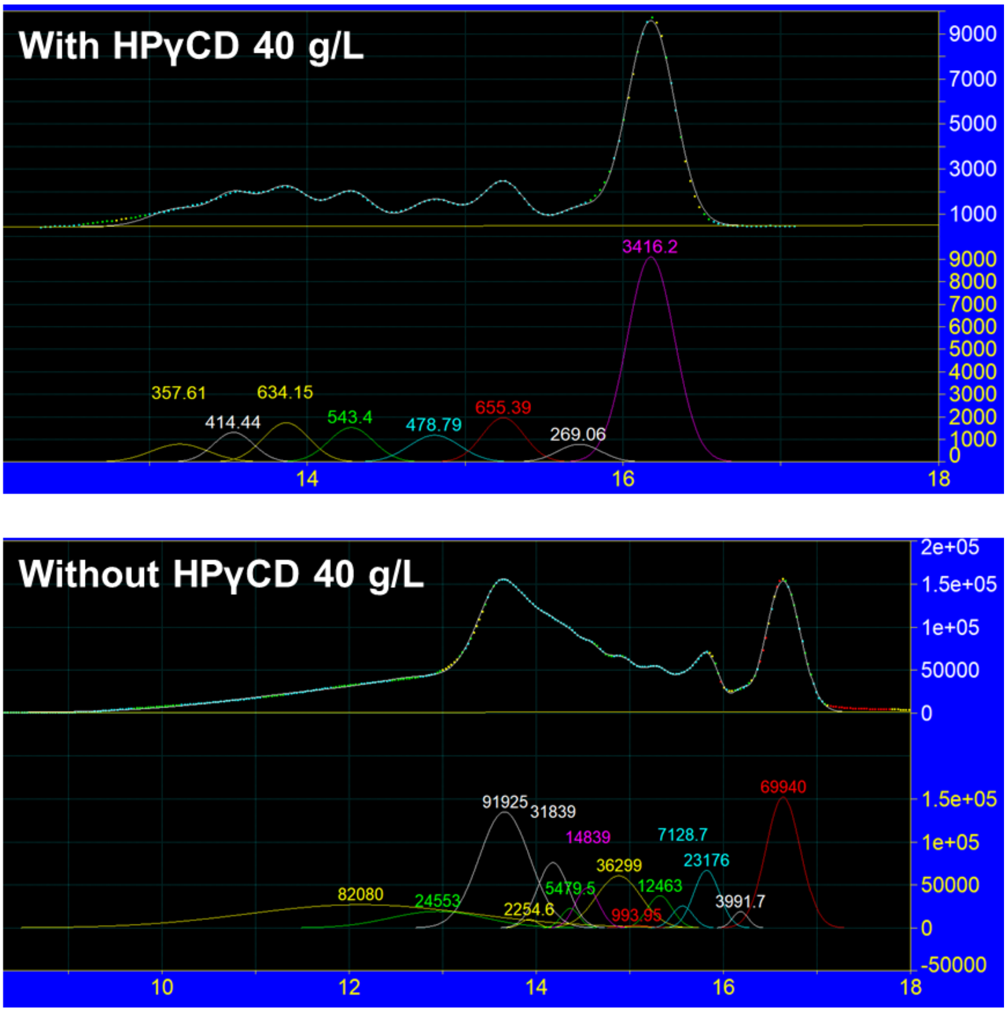

Figure 2-25. Curve fitting using the nonlinear least-squares method for GPC profiles of products of irradiating **TCA-PEG-4k** ([**TCA-PEG-4k**] = 40 g/L) in the presence and absence of HPγCD. Ratio of **C-1mer** in the obtained product is calculated from the integral ratio of the peaks. GPC profiles are shown as the signal intensity (differential refractive index) vs elution time.

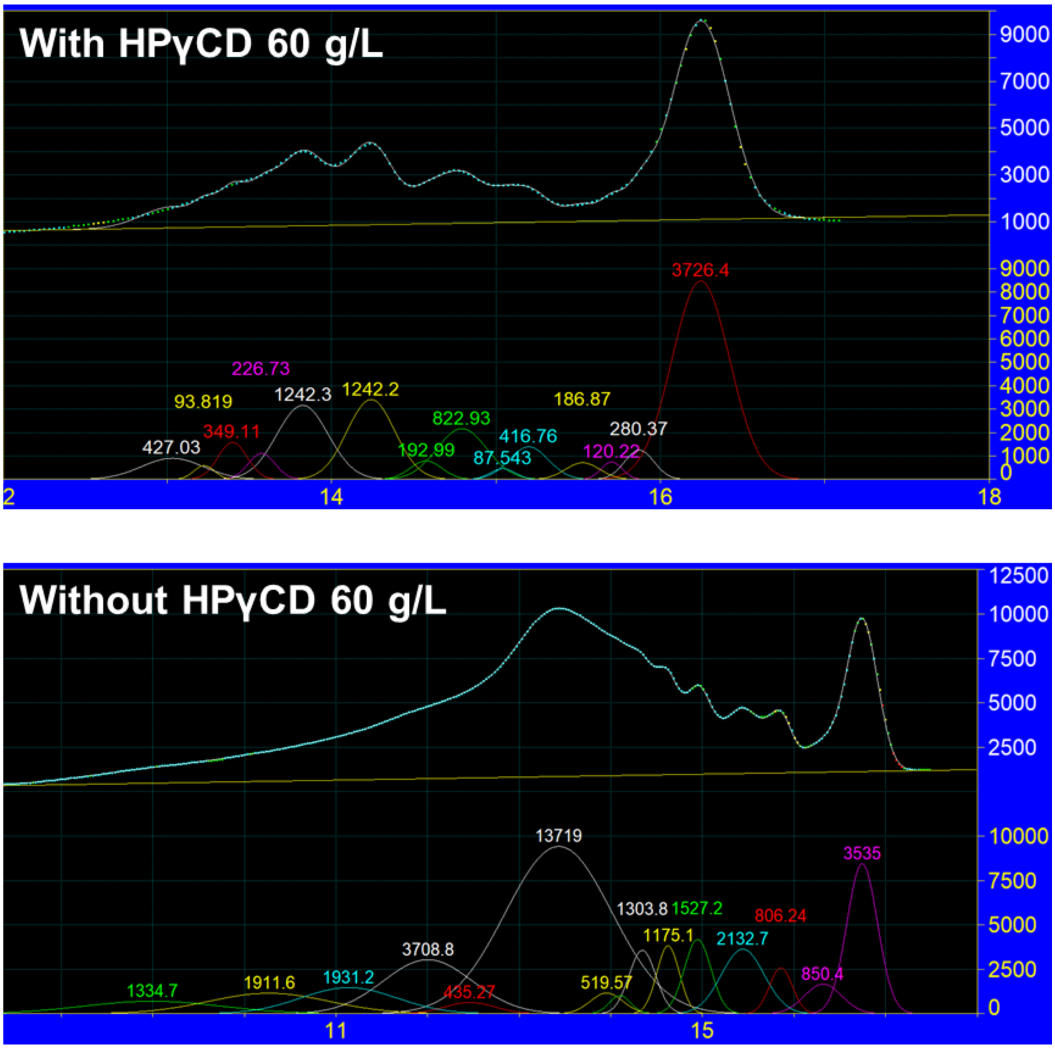

Figure 2-26. Curve fitting using the nonlinear least-squares method for GPC profiles of products of irradiating **TCA-PEG-4k** ([**TCA-PEG-4k**] = 60 g/L) in the presence and absence of HPγCD. Ratio of **C-1mer** in the obtained product is calculated from the integral ratio of the peaks. GPC profiles are shown as the signal intensity (differential refractive index) vs elution time.

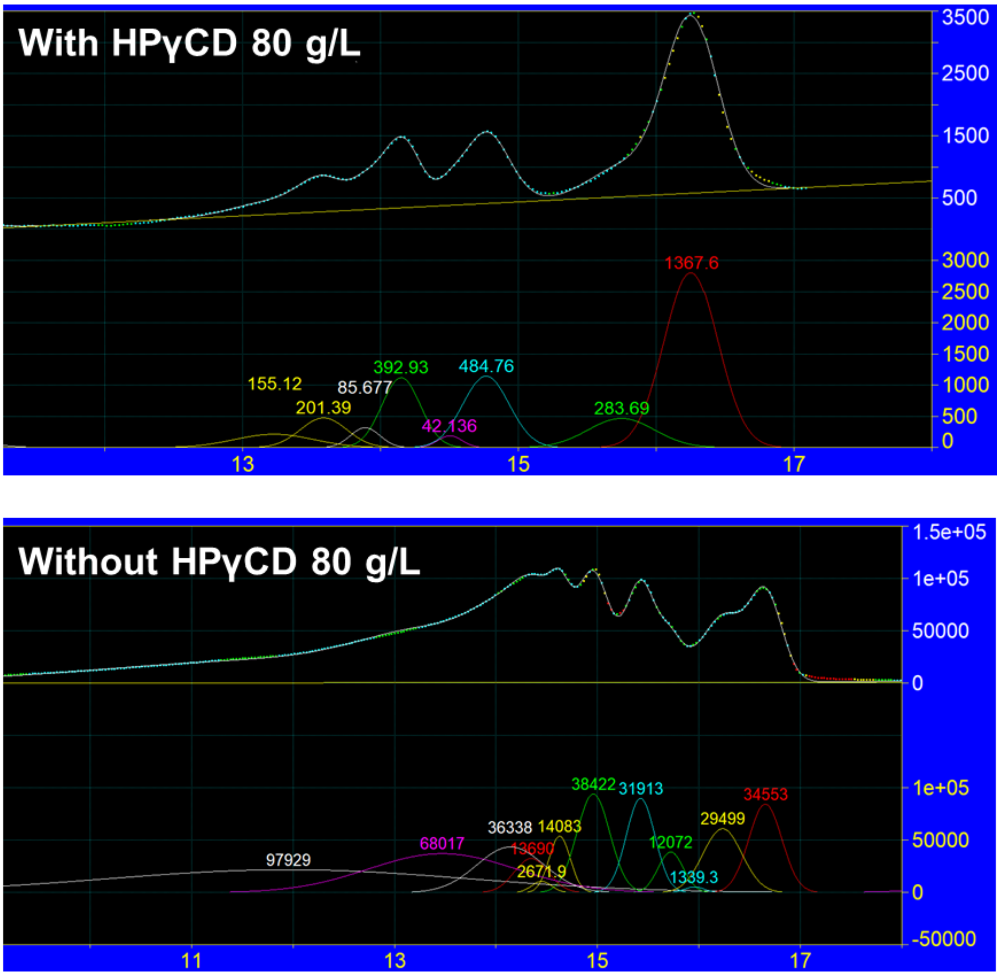

Figure 2-27. Curve fitting using the nonlinear least-squares method for GPC profiles of products of irradiating **TCA-PEG-4k** ([**TCA-PEG-4k**] = 80 g/L) in the presence and absence of HPγCD. Ratio of **C-1mer** in the obtained product is calculated from the integral ratio of the peaks. GPC profiles are shown as the signal intensity (differential refractive index) vs elution time.

2-3 Conclusion

In conclusion, the pPRx-assisted strategy achieved an efficient synthesis for CPs in high concentration (80 g/L). pPRx formed by end-group-modified PEG and HPγCD was prepared via an inclusion motif, which regulated the structure to a U-like-shape due to the steric effect of the bulky **TCA** groups as terminals of PEG chain. By irradiating the solution of pPRx, the cyclization of PEG in high concentration was accessible through the [2+2] photocycloaddition of the cinnamoyl moieties. The cyclization of **TCA-PEG-2k** gives cyclic monomer as major products with yield of 66% at a concentration of 80 g/L. This cyclization method is also appliable for PEG with higher MW. The cyclization of **TCA-PEG-4k** gives **C-1mer** with yield of 45% at 80 g/L.[19] Overall, by defining a supramolecular confinement that realizes an efficient synthesis of CPs in high concentration, this methodology can be applied to prepare various special polymer bearing ring-like structure such as cyclic polymer brush.[20,21]

References

1. Haque, F.; Grayson, S. M. *Nat. Chem.* **2020**, *12*, 433–444.
2. Roland, C. D.; Li, H.; Abboud, K. A.; Wagener, K. B.; Veige, A. S. *Nat. Chem.* **2016**, *8*, 791–796.
3. Hoskins, J. N.; Grayson, S. M. *Polym. Chem.* **2011**, *2*, 289–299.
4. Khanna, K.; Varshney, S.; Kakkar, A. K. *Polym. Chem.* **2010**, *1*, 1171–1185.
5. Wu, W.; Wang, W.; Li, J. *Prog. Polym. Sci.* **2015**, *46*, 55–85.
6. Geiser, D.; Hocker, H. *Macromolecules* **1980**, *13*, 653–656.
7. Oike, H.; Imaizumi, H.; Mouri, T.; Yoshioka, Y.; Uchibori, A.; Tezuka, Y. *J. Am. Chem. Soc.* **2000**, *122*, 9592–9599.
8. Zhao, Y.; Zhu, S.; Liao, C.; Wang, Y.; Lam, J.; Zhou, X.; Wang, X.; Xie, X.; Tang, B. Z. *Angew. Chem. Int. Ed.* **2021**, *60*, 16974–16979.
9. Zhu, W.; Li, Z.; Zhao, Y.; Zhang, K. *Macromol. Rapid Commun.* **2015**, *36*, 1987–1993.
10. Hild, G.; Kohler, A.; Rempp, P. *Eur. Polym. J.* **1980**, *16*, 525–527.
11. Josse, T.; De Winter, J.; Gerbaux, P.; Coulembier, O. *Angew. Chem. Int. Ed.* **2016**, *55*, 13944–13958.
12. Chang, Y. A.; Waymouth, R. M. *J. Polym. Sci., Part A: Polym. Chem.* **2017**, *55*, 2892–2902.
13. Xue, Y.; Jiang, S.; Zhong, H.; Chen, Z.; Wang, F. *Angew. Chem. Int. Ed.* **2022**, *61*.
14. Chen, L.; Wang, X.; Hou, R.; Lu, H.; He, Z.; Zhou, X.; Wang, X. *Polym. Chem.* **2023**, *14*, 4659–4670.
15. Ji, Z.; Li, Y.; Ding, Y.; Chen, G.; Jiang, M. *Polym. Chem.* **2015**, *6*, 6880–6884.
16. Tsuji, Y.; Kobayashi, Y.; Xiao, C.; Harada, A.; Yamaguchi, H. *Chem. Lett.* **2023**, *52*, 1–4.
17. Harada, A.; Li, J.; Kamachi, M. *Nature* **1994**, *370*, 126–128.

18. Karpkird, T.; Wanichweacharungruang, S. *J. Photochem. Photobiol., A* **2010**, *212*, 56–61.
19. Xiao, C. L.; Kobayashi, Y.; Tsuji, Y.; Harada, A.; Yamaguchi, H. *ACS Macro Lett.* **2023**, *12*, 1498–1502.
20. Isono, T.; Sasamori, T.; Honda, K.; Mato, Y.; Yamamoto, T.; Tajima, K.; Satoh, T. *Macromolecules* **2018**, *51*, 3855–3864.
21. Morgese, G.; Trachsel, L.; Romio, M.; Divandari, M.; Ramakrishna, S.; Benetti, E. M. *Angew. Chem. Int. Ed.* **2016**, *55*, 15583–15588.

Chapter 3

Reversible mechanical interlocking via stimuli-triggered non-homeomorphic topology transformation enables highly efficient rotaxane synthesis

3-1 Introduction

Mechanically interlocked molecules (MIMs) are molecular architectures in which the components are not connected via conventional covalent bonds but are interlocked through their topological arrangement. Rotaxanes, one of the most fundamental MIMs, have demonstrated tremendous potential in fields including molecular machines,[1,2,3,4] molecular recognition,[5,6,7] and supramolecular materials.[8,9,10,11] However, convenient (fewer reagents, reaction and purification steps), efficient (high conversion and yield) and functional (reversibility, various topologies or higher order structures) synthesis of rotaxanes remains challenging. Since the first statistical synthesis of rotaxane reported by Harrison,[12] some strategies such as threaded-and-stoppering, clipping and active template synthesis have been established and widely used.[13,14,15,16,17,18] However, aside from the axle and wheel molecules that comprise rotaxanes, these methods typically require addition of auxiliary reagents such as large excesses of stoppers, metal ions, or catalysts, thereby complicating both reaction and purification. Other than these methods, without extra addition, Chiu et al. reported the threaded-and-shrinking and threaded-and-swelling protocols to obtain rotaxane with isolated yields of 28% and 86% respectively, where the rotaxanes form via the irreversible transition of homeomorphic topology (rings with different cavities).[19,20] Leigh's group first reported the synthesis of [2]rotaxanes driven by stabilization of the axle-forming transition state with isolated yield of 50%.[21] Although these reagent-free methods rely solely on the axle and wheel molecules, the yields in most cases remain low to moderate. Moreover, expanding these methods to achieve “high-value-added” rotaxanes—such as those featuring various topologies, higher-order structures ([n]rotaxanes) or reversible mechanical interlocks—is particularly challenging due to the specific molecular structure imposed on the macrocycles and irreversible change on system’s potential energy surface during rotaxanation. Therefore, a refined strategy that reconciles the convenient, efficient, and functional synthesis of rotaxanes is still lacking.

This chapter focus on the investigation of the threaded-and-topology-transformation strategy for the one-pot synthesis of [2]- and [3]rotaxanes containing diverse topologies with excellent efficiency (up to 99% conversion and 92% isolated yield for [2]rotaxane; up to 96% conversion and 80% isolated yield for [3]rotaxane), in which mechanical interlock is reversible under heating (Figure 3-1). Aside from the wheel and axle molecules, no additional reagents such as stoppers or catalysts are required. First, we design a series of macrocycles incorporating cyano-stilbene moieties and crown ether fragments in their backbones. The cyano-stilbene moieties undergo intramolecular [2+2] photocycloaddition upon 365 nm UV irradiation. This photoreaction transforms the macrocycles’ topology from regular ring into the figure-eight structure containing two smaller rings fused by cyano-substituted cyclobutane, where two rings are fused in chair-like or orthogonal conformation. Upon dissolving dibenzylammonium-containing molecules and the macrocycles in solution, *pseudo*-rotaxane complexes form wherein the macrocycles act as wheels and the cationic guests as axles. Under 365 nm UV irradiation, the photoreaction of the cyano-stilbene moieties transforms the complexes from pseudo-rotaxanes with regular macrocycles into rotaxanes containing chair-like or orthogonal wheels. Moreover, rotaxanes with chair-like or orthogonal topologies exhibit totally different mechanical interlocked properties: under heating, chair-like rotaxanes convert back to *pseudo*-rotaxane, while orthogonal rotaxanes maintain their mechanical interlock. Additionally, the rate of this heat-triggered mechanical unlocking is controllable by adjusting the macrocycle structure. Notably, this approach represents the first demonstration of employing a reversible transformation between non-homeomorphic topologies (one-hole-ring versus two-holes-figure-eight structure) to synthesize rotaxanes and tune their mechanical states. The processes of mechanical interlocking and unlocking proceed through a reconstruction of the system's potential energy surface, wherein an insurmountable energy barrier is introduced or removed via the topology transformation. Accordingly, this strategy operates as an energy-ratchet-like mechanism, differing conceptually from interlocking by ring contraction or slipping, and from unlocking by kinetic dethreading (Scheme 2).[3,22,23] By strategically leveraging the molecular topologies, this work may provide new insight into the synthesis of MIMs with higher-order mechanical interlocks and to the design of thermally or photochemically gated units in molecular machines.

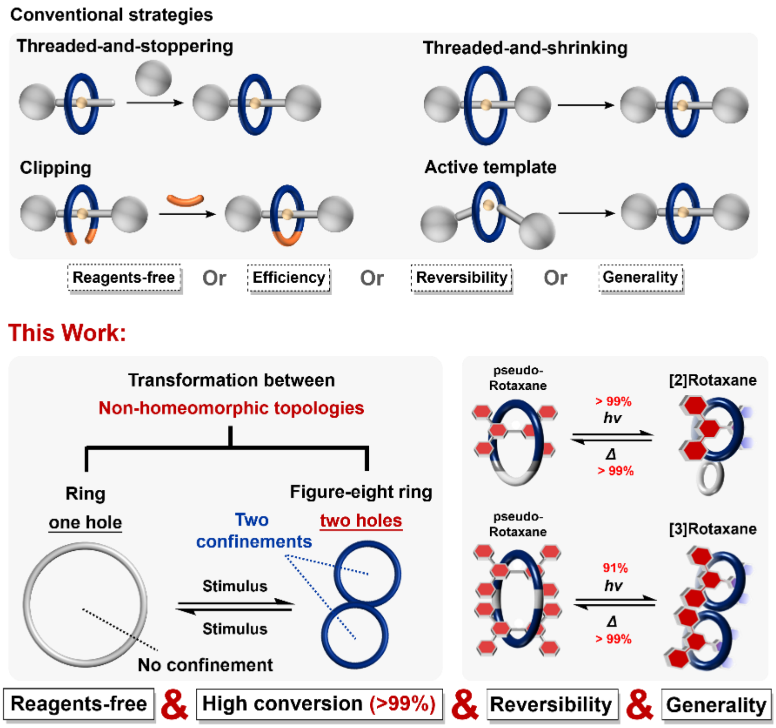

Figure 3-1. Conventional strategies for rotaxane synthesis (top), and reversible synthesis of rotaxane via non-homeomorphic topology transformation in this work (bottom)

3-2 Materials and Methods

Materials

All solvents for synthesis and reactions were purchased from TCI. All other chemicals were purchased from TCI and Nacalai Tesque and used without further purification.

Methods

The NMR spectra were obtained using a JEOL JNM-ECS 400 and 500 MHz NMR spectrometer. All ROESY spectra were obtained using an Agilent VNS 600 MHz NMR spectrometer. All NMR spectra were processed by MestReNova software. MALDI–TOF MS was measured by mass spectrometer BRUKER DALTONICS, Ultraflex III and autoflex maX MALDI TOF-TOF spectrometers. 2,5-Dihydroxybenzoic acid was used as a matrix. The UV irradiation was performed by using PER-365, Techno Sigma Co., Ltd.

Synthetic work

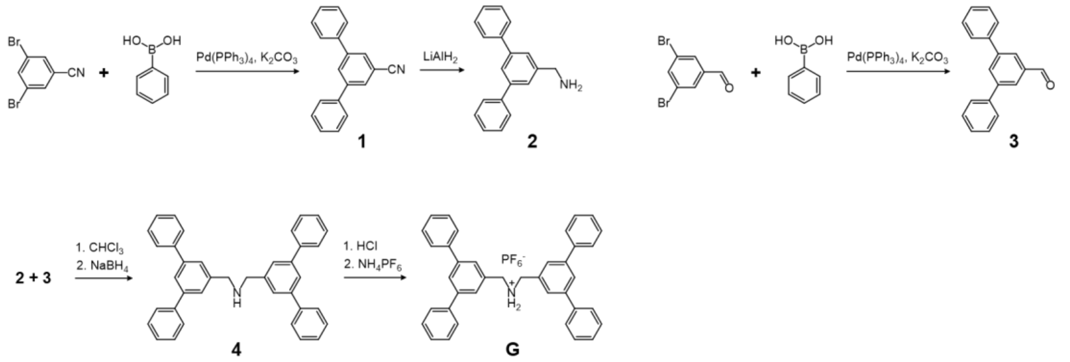

Scheme 3-1. Synthetic route of axle molecule **G**

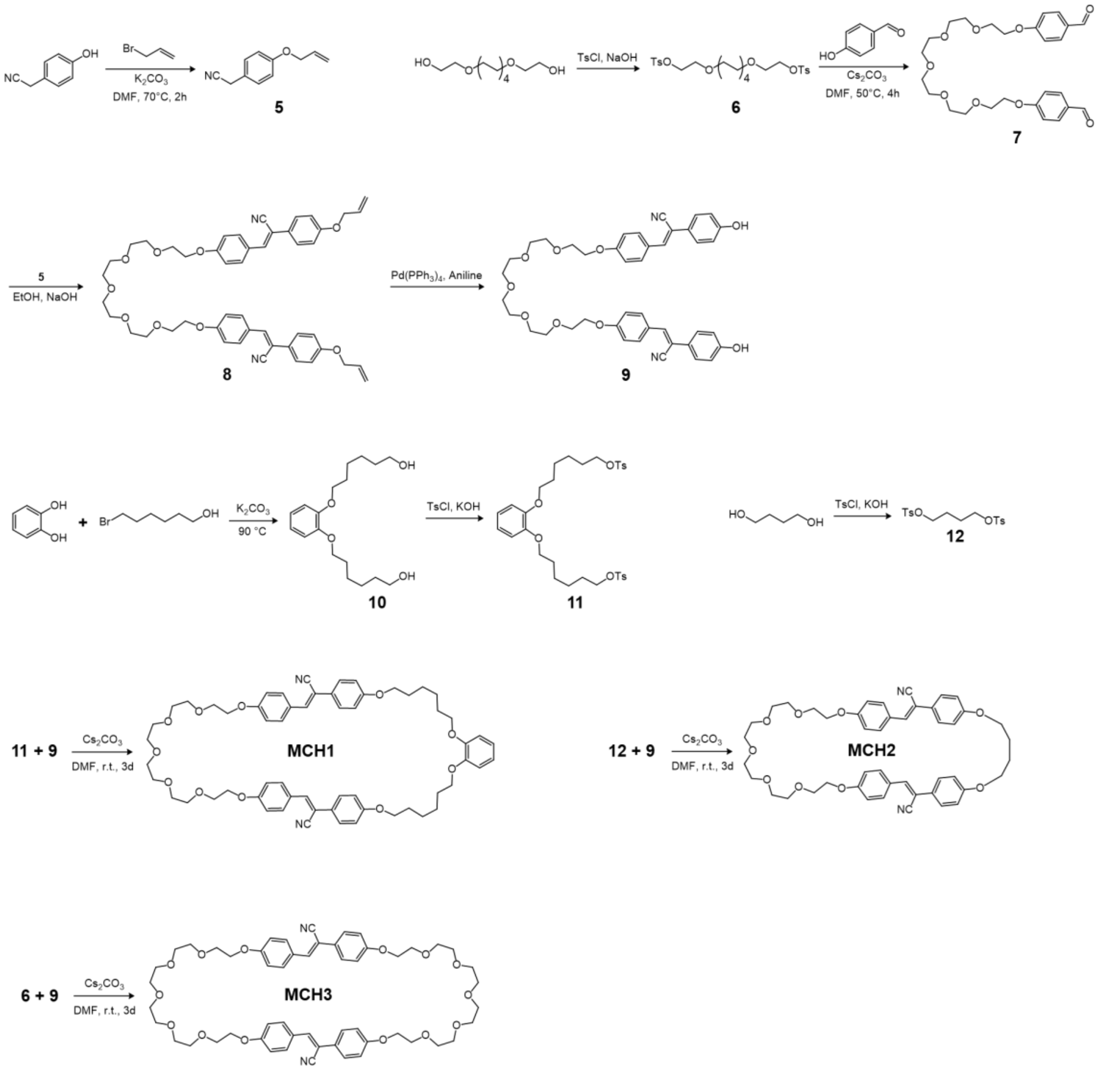

Scheme 3-2. Synthetic routes of **MCH1**, **MCH2** and **MCH3**

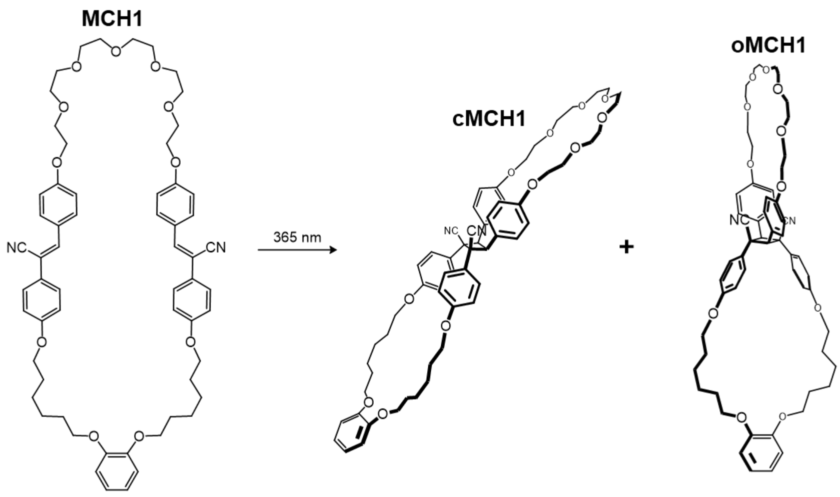

Scheme 3-3. Photoreaction of **MCH1** to produce **cMCH1** and **oMCH1**

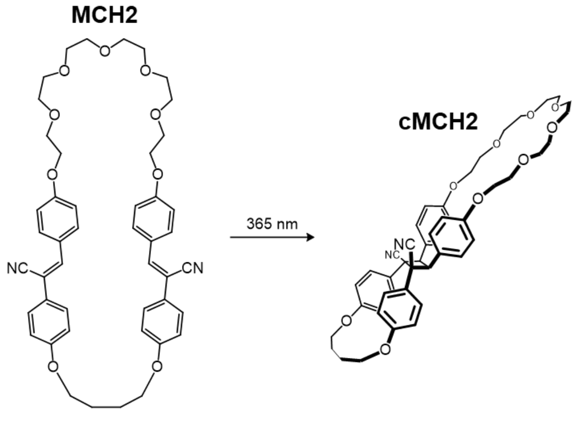

Scheme 3-4. Photoreaction of **MCH2** to produce **cMCH2**

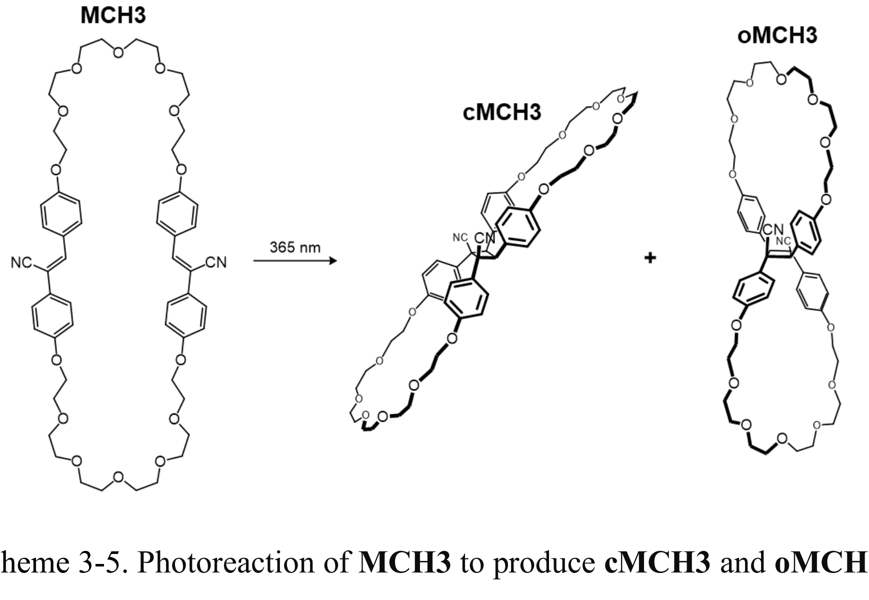

Scheme 3-5. Photoreaction of **MCH3** to produce **cMCH3** and **oMCH3**

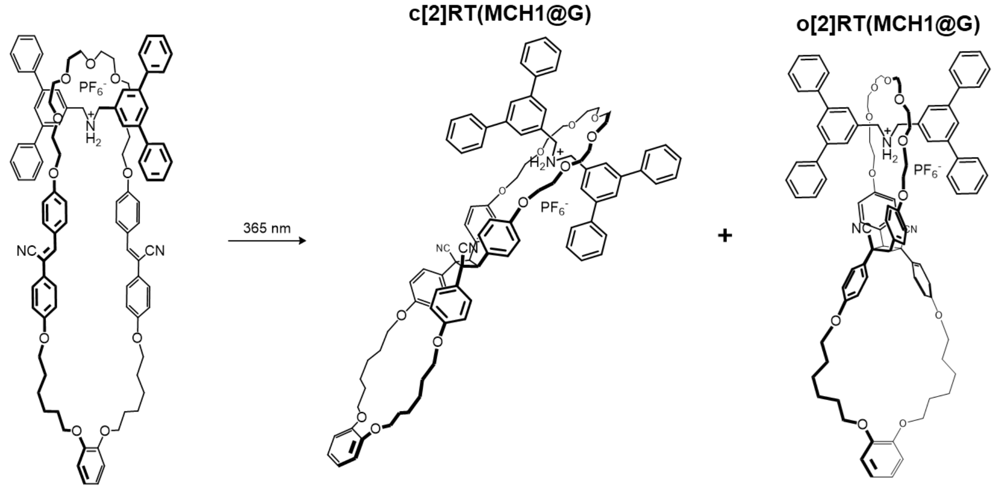

Scheme 3-6. Synthesis of **c[2]RT(cMCH1@G)** and **o[2]RT(oMCH1@G)**

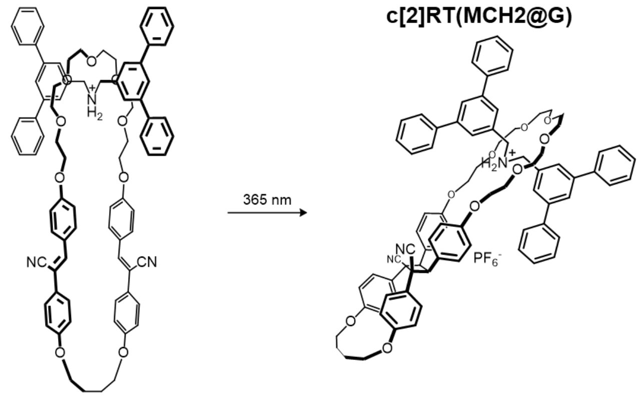

Scheme 3-7.Synthesis of **c[2]RT(cMCH2@G)**

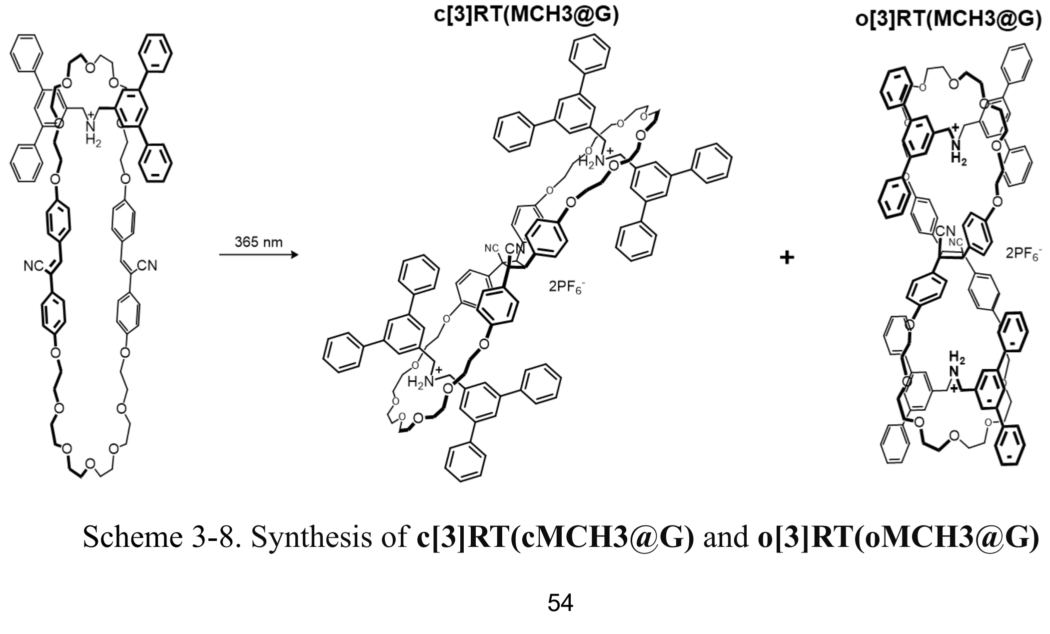

Scheme 3-8. Synthesis of **c[3]RT(cMCH3@G)** and **o[3]RT(oMCH3@G)**

Synthesis of 1

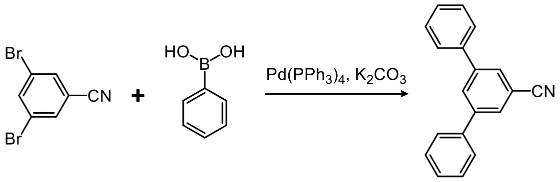

3,5-Dibromobenzonitrile (1.5 g, 5.7 mmol), phenylboronic acid (1.75 g, 14.4 mmol) were dissolved in a mixture solvent of 1,2-dimethoxyethane and water (70 mL, v/v = 5/1). $Pd(PPh_3)_4$ (664 mg, 0.57 mmol) and Na_2CO_3 (1.83 g, 17.3 mmol)were added to the mixture under bubbling by N_2. The mixture was reflux at 90 °C overnight. After cooling to room temperature, CH_2Cl_2 was added to the mixture and washed by water and then brine. The organic phase was separated, dried over Na_2SO_4 and evaporated to remove solvents under reduced pressure. The crude was purified through silica column chromatography (Hexane/Ethyl acetate) to give **1** as a white solid (Yield: 1.23 g, 84%). ^{1}H NMR (396 MHz, CHLOROFORM-*D*) ^{1}H NMR (396 MHz, CHLOROFORM-*D*) δ 7.99 (t, J = 1.8 Hz, 1H), 7.82 (d, J = 1.8 Hz, 2H), 7.66 – 7.56 (m, 4H), 7.52 – 7.46 (m, 4H), 7.45 – 7.39 (m, 2H).

Data was consistent with those reported in the literature [26].

^{1}H NMR (400 MHz, $CDCl_3$) spectrum of **1**

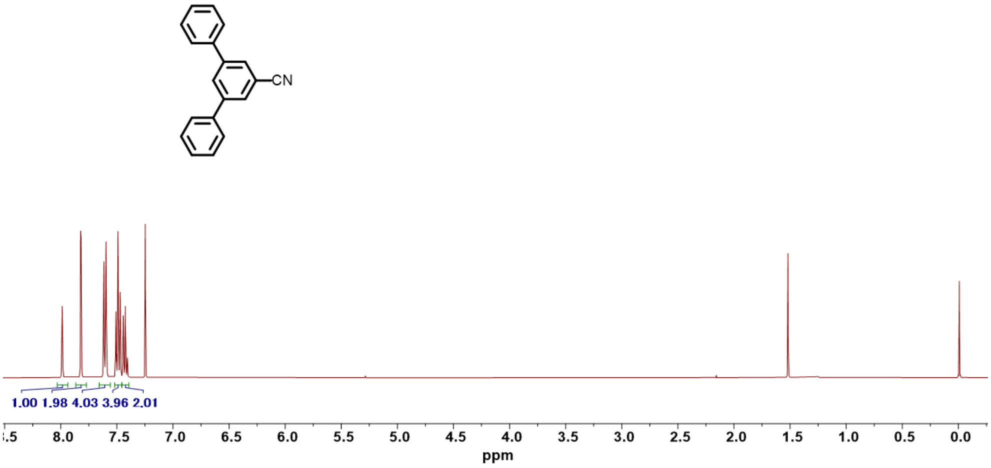

Synthesis of 2

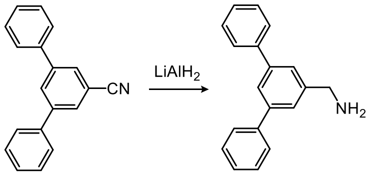

1 (1 g, 3.9 mmol) was dissolved in dry THF (20 mL). $LiAlH_4$ (0.59 g, 15.7 mmol) was added to the solution in portions under ice bath. The reaction mixture was stirred at room temperature for 4 h. The reaction was quenched by dropwise addition of water under ice cooling until gas evolution ceased. The resulting mixture was diluted with CH_2Cl_2 (60 mL) and filtered. The filtrate was dried over Na_2SO_4, filtered, and concentrated under reduced pressure to give **2** as a white solid (0.94 g, 94%).^{1}H NMR (400 MHz, CHLOROFORM-D) δ 7.69 (t, J = 1.7 Hz, 1H), 7.68 – 7.62 (m, 4H), 7.53 (dt, J = 1.7, 0.6 Hz, 2H), 7.49 – 7.42 (m, 4H), 7.40 – 7.33 (m, 2H), 4.01 (s, 2H). ^{13}C NMR (126 MHz, CHLOROFORM-*D*) δ 144.49, 142.22, 141.25, 128.89, 127.52, 127.39, 125.06, 124.84, 46.76. HR-MS (ESI): calcd for , $[C_{19}H_{17}N+H]^+$, m/z = 260.1434, found m/z = 260.1436.

^{1}H NMR (400 MHz, $CDCl_3$) spectrum of **2**

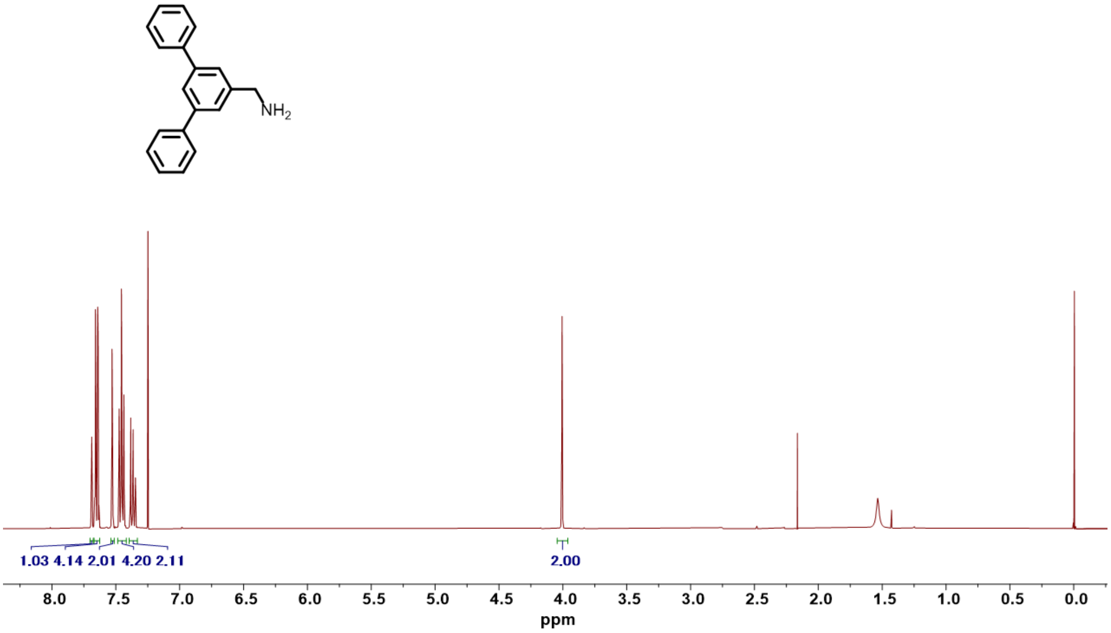

^{13}C NMR (125 MHz, $CDCl_3$) spectrum of **2**

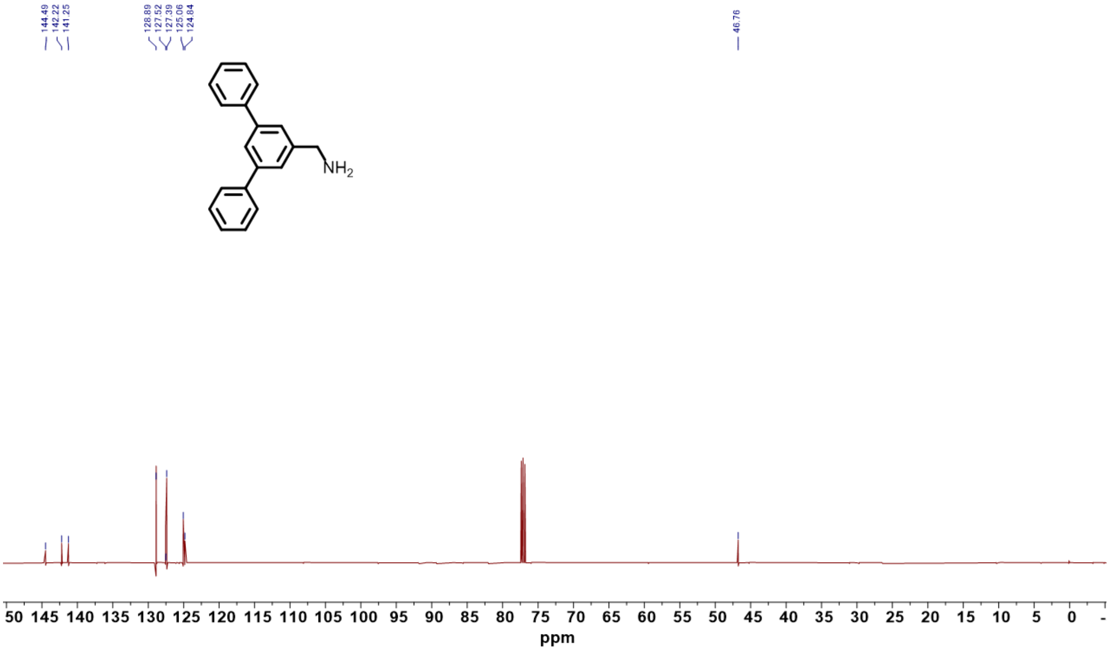

Synthesis of 3

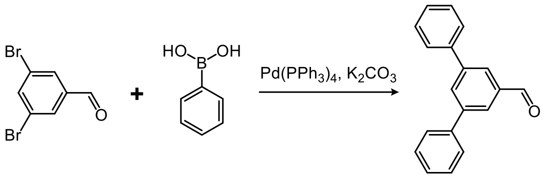

3,5-Dibromobenzaldehyde (1.5 g, 5.7 mmol), phenylboronic acid (1.75 g, 14.4 mmol) were dissolved in a mixture solvent of 1,2-dimethoxyethane and water (v/v = 5/1). $Pd(PPh_3)_4$ (664 mg, 0.57 mmol) and Na_2CO_3 (1.83 g, 17.3 mmol)were added to the mixture under bubbling by N_2. The mixture was reflux at 90 °C overnight. After cooling to room temperature, dichloromethane was added to the mixture and washed by water and then brine. The organic phase was separated, dried over Na_2SO_4, filtered and evaporated to remove solvents under reduced pressure. The crude was purified through silica column chromatography (Hexane/Ethyl acetate) to give **3** as a white solid (Yield: 1.23 g, 89%). ^1H NMR (500 MHz, CHLOROFORM-*D*) δ 10.15 (s, 1H), 8.14 – 7.95 (m, 3H), 7.72 – 7.61 (m, 4H), 7.57 – 7.45 (m, 4H), 7.45 – 7.37 (m, 2H).

Data was consistent with those reported in the literature [27].

^1H NMR (500 MHz, $CDCl_3$) spectrum of **3**

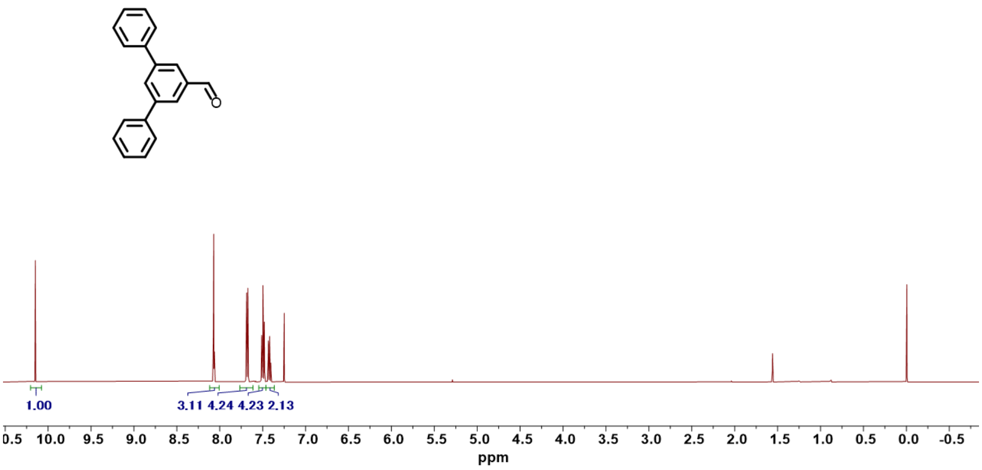

Synthesis of 4

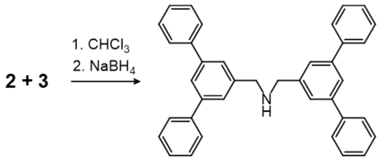

2 (0.7 g, 2.7 mmol) and **3** (0.697 g, 2.7 mmol) were dissolved in dry $CHCl_3$ (20 mL) and stirred at room temperature overnight. The solvent was removed under reduced pressure, and the residue was redissolved in a mixture solvent of THF and MeOH (30 mL, v/v = 2/1). $NaBH_4$ (0.41 g, 10.8 mmol) was added to the solution in portions, and the mixture was stirred at room temperature for 3 h. The reaction was quenched by addition of water, followed by extraction with CH_2Cl_2 and washing with water and the brine. The organic layer was separated, dried over Na_2SO_4, filtered, and concentrated under reduced pressure to give compound **4** as a white solid (Yield: 1.21 g, 90%). ^{1}H NMR (400 MHz, CHLOROFORM-*D*) δ 7.70 (t, *J* = 1.8 Hz, 2H), 7.67 – 7.64 (m, 8H), 7.59 (d, *J* = 1.8 Hz, 4H), 7.49 – 7.39 (m, 8H), 7.36 (m, 4H), 4.00 (s, 4H). ^{13}C NMR (126 MHz, CHLOROFORM-*D*) δ 142.05, 141.42, 141.21, 128.89, 127.52, 127.40, 126.20, 125.00, 53.25. HR-MS (ESI): calcd for , $[C_{38}H_{32}N+H]^+$, m/z = 502.2530, found m/z =502.2534.

^{1}H NMR (400 MHz, $CDCl_3$) spectrum of **4**

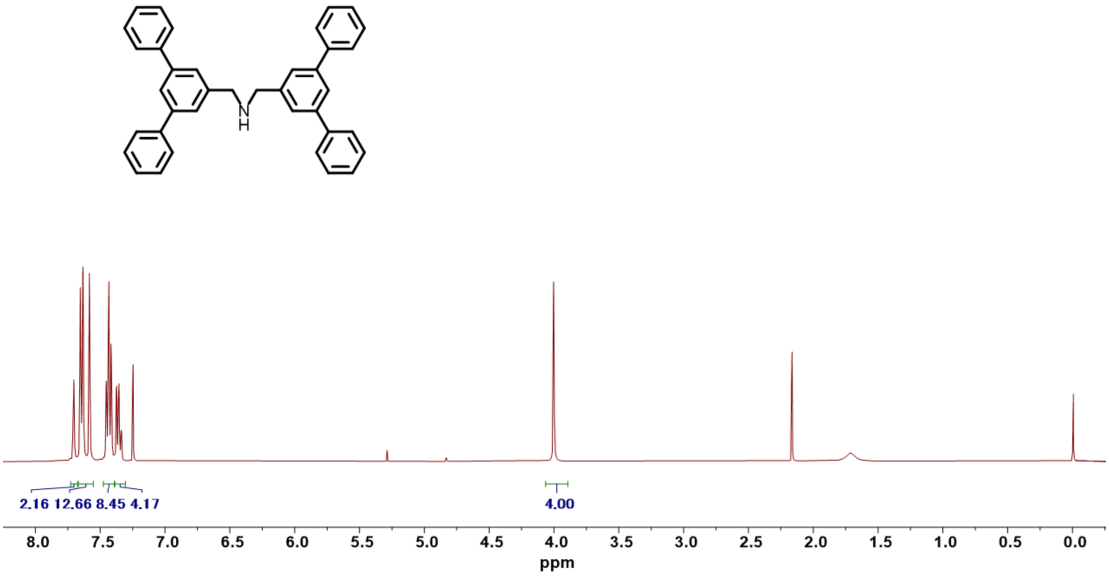

^{13}C NMR (125 MHz, $CDCl_3$) spectrum of **4**

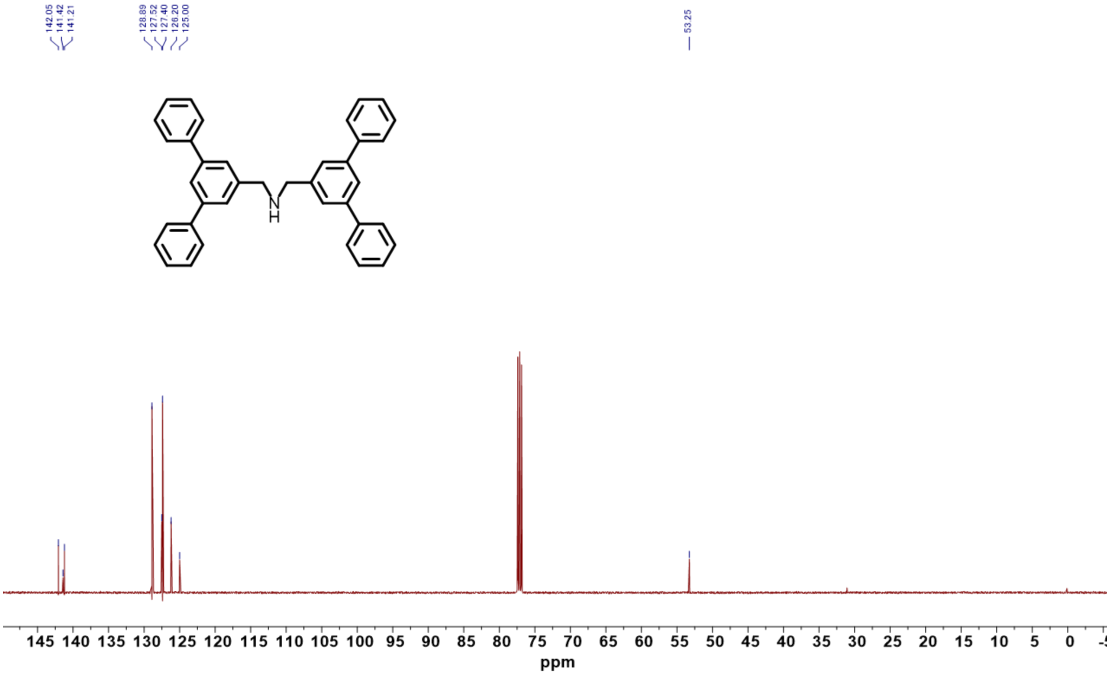

Synthesis of G

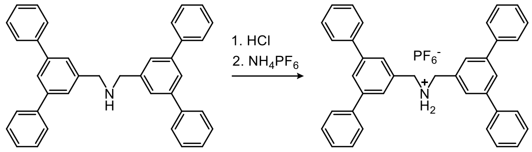

4 (1 g, 2 mmol) was dissolved in a mixture solvent of CH_2Cl_2 (40 mL). 3 mL concentrated HCl was added to the solution and stirred at room temperature overnight. The mixture was diluted with CH_2Cl_2 (60 mL), water (10 mL) and brine (100 mL). The biphasic mixture was centrifuged, and the organic layer was collected and concentrated under reduced pressure. The resulting residue was dispersed in acetone (50 mL), followed by addition of saturated aqueous solution of NH_4PF_6 (10 mL). The mixture was stirred at room temperature overnight and then concentrated under reduced pressure without heating to remove the acetone. The resulting suspension was diluted with deionized water and filtered by suction filtration. The solid was collected and dried under reduced pressure to obtain **G** as a white solid (Yield: 0.92 g, 71%). ^{1}H NMR (400 MHz, ACETONE-D_6) δ 8.85 (s, 2H), 8.00 (t, J = 1.7 Hz, 2H), 7.90 (d, J = 1.7 Hz, 4H), 7.80 – 7.67 (m, 8H), 7.51 – 7.44 (m, 8H), 7.43 – 7.37 (m, 4H), 4.92 (s, 4H). ^{13}C NMR (126 MHz, ACETONE-D_6) δ 142.57, 140.00, 132.53, 129.10, 128.09, 127.80, 127.13, 126.59, 52.05. HR-MS (ESI): calcd for , $[C_{38}H_{33}N]^+$, m/z = 502.2530, found m/z =502.2531.

^{1}H NMR (400 MHz, Acetone-d$_6$) spectrum of **G**

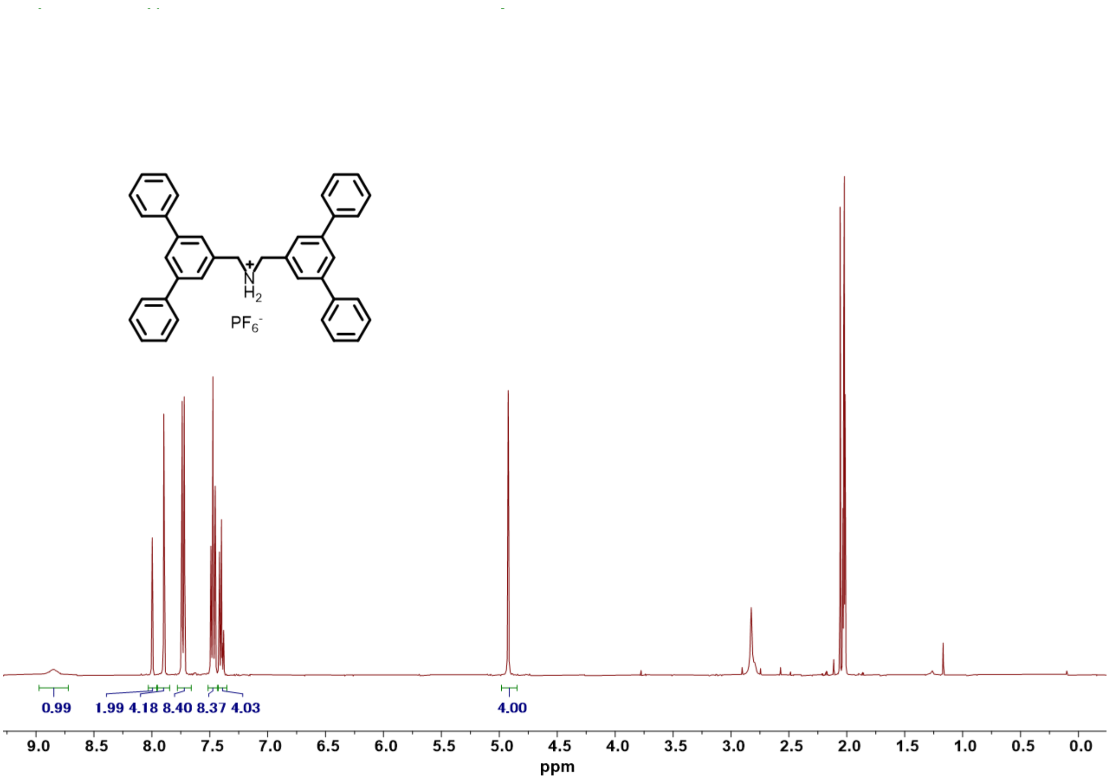

^{13}C NMR (125 MHz, Acetone-d$_6$) spectrum of **2**

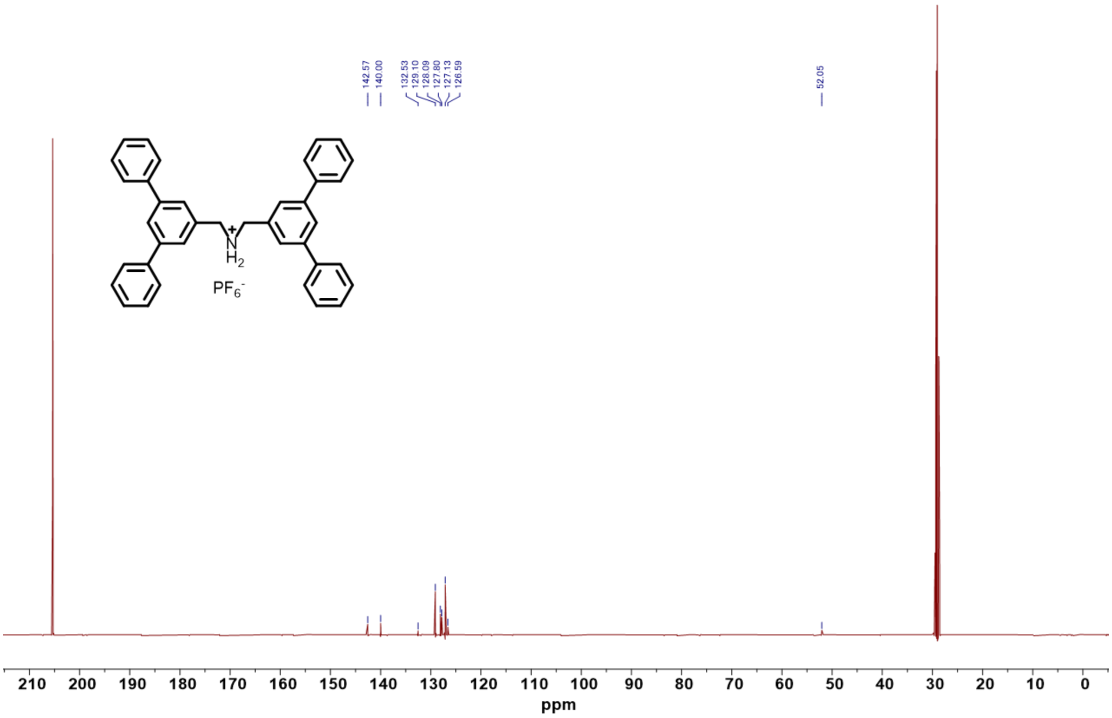

Synthesis of 5

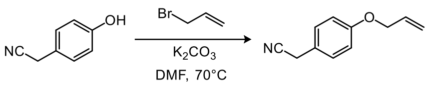

To a solution of 4-hydroxybenzyl cyanide (1 g, 7.51 mmol) and allyl bromide (0.91 g, 7.51 mmol) in DMF (30 mL) was added K_2CO_3 (2.07 g, 15.02 mmol). After bubbling by N_2 for 10 minutes, the mixture was stirred at 70 °C for 2 hours. The reaction mixture was poured into water and extracted with diethyl ether. The organic phase was washed with water (2x) and brine (1x), dried over $MgSO_4$ and evaporated. **26** was obtained as orange oil without further purification (Yield: 1.21 g, 93%). ^{1}H NMR (500 MHz, CHLOROFORM-*D*) δ 7.21 (d, *J* = 8.6, 2H), 6.90 (d, *J* = 8.6, 2H), 6.03 (m, 1H), 5.40 (dp, *J* = 17.2, 1.5 Hz, 1H), 5.29 (dp, *J* = 10.4, 1.3 Hz, 1H), 4.53 (dq, *J* = 5.4, 1.4 Hz, 2H), 3.67 (s, 2H).

Data was consistent with those reported in the literature [28].

^{1}H NMR (500 MHz, $CDCl_3$) spectrum of **5**

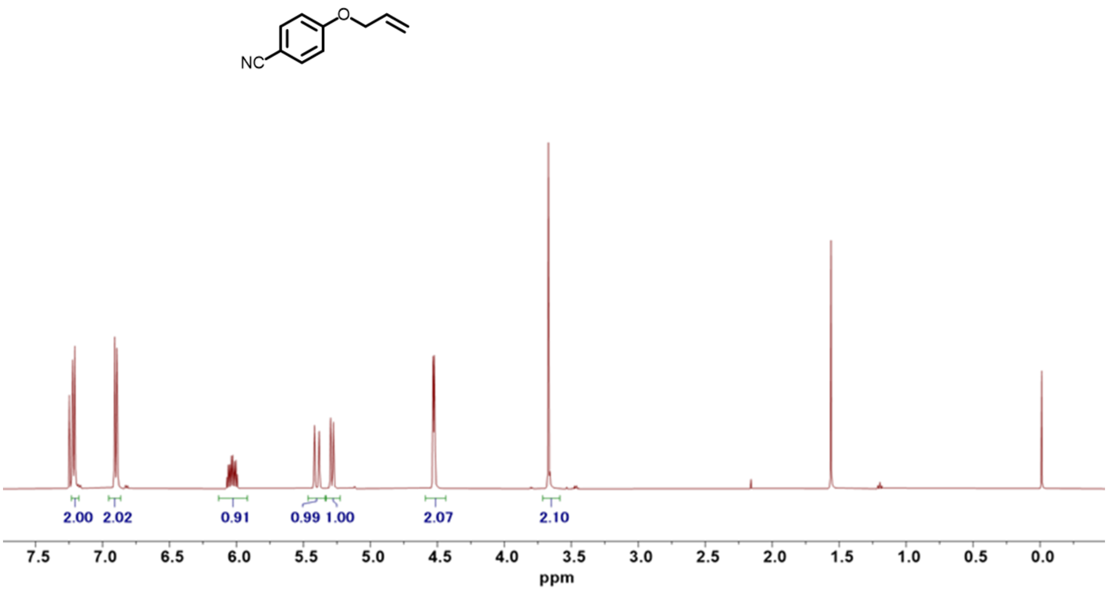

Synthesis of 6

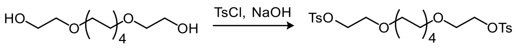

Hexaethylene glycol (3 g, 10.6 mmol) and p-toluenesulfonyl chloride (4.25 g, 22.3 mmol) were dissolved in DCM (30 mL). KOH (4.76 g, 85 mmol) was added into the solution under ice bath in portions over 1 h. The ice bath was removed after addition and the mixture was stirred at room temperature overnight. Then the reaction mixture was poured into water and extracted with CH_2Cl_2 (3x). The combined organic phase was washed with water (2x) and brine (1x), dried over Na_2SO_4 and evaporated. **6** was obtained as a colorless oil without further purification (Yield: 5.65 g, 90%). ^1H NMR (500 MHz, CHLOROFORM-*D*) δ 7.78 (d, *J* = 8.3 Hz, 4H), 7.33 (d, *J* = 8.3 Hz, 4H), 4.14 (t, *J* = 9.7 Hz, 4H), 3.67 (t, *J* = 9.7 Hz, 4H), 3.60 (s, 8H), 3.57 (s, 8H), 2.43 (s, 6H). Data was consistent with those reported in the literature [29].

^1H NMR (500 MHz, $CDCl_3$) spectrum of **6**

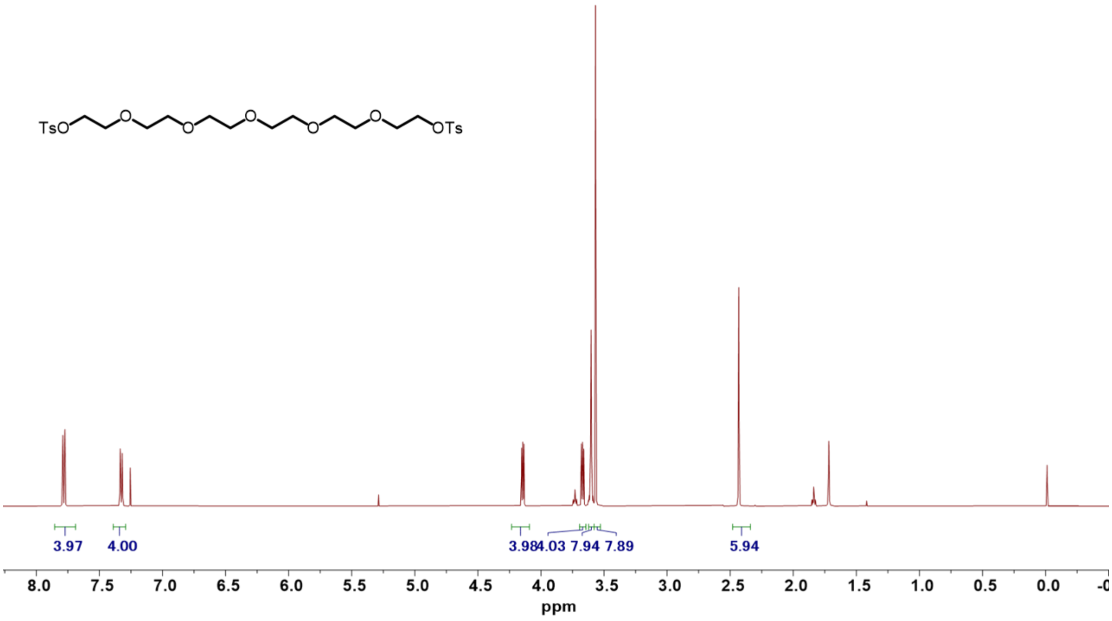

Synthesis of 7

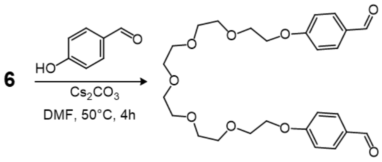

To a solution of **6** (1 g, 1.69 mmol) and 4-hydroxybenzaldehyde (0.41 g, 3.39 mmol) in DMF (40 mL) was added Cs_2CO_3 (1.65 g, 5.08 mmol). After stirring at 50 °C for 2 h, the reaction mixture was poured into water and extracted with ethyl acetate. The organic phase was washed with water (2x) and brine (1x), dried over $MgSO_4$ and evaporated. **7** was obtained as a light-yellow oil without further purification (Yield: 0.83 g, 93%). ^{1}H NMR (500 MHz, CHLOROFORM-*D*) δ 9.86 (s, 2H), 7.81 (d, *J* = 8.8 Hz, 4H), 7.00 (d, *J* = 8.8 Hz, 4H), 4.28 – 4.08 (m, 4H), 3.91 – 3.81 (m, 4H), 3.76 – 3.52 (m, 16H). Data was consistent with those reported in the literature [30].

^{1}H NMR (500 MHz, $CDCl_3$) spectrum of **7**

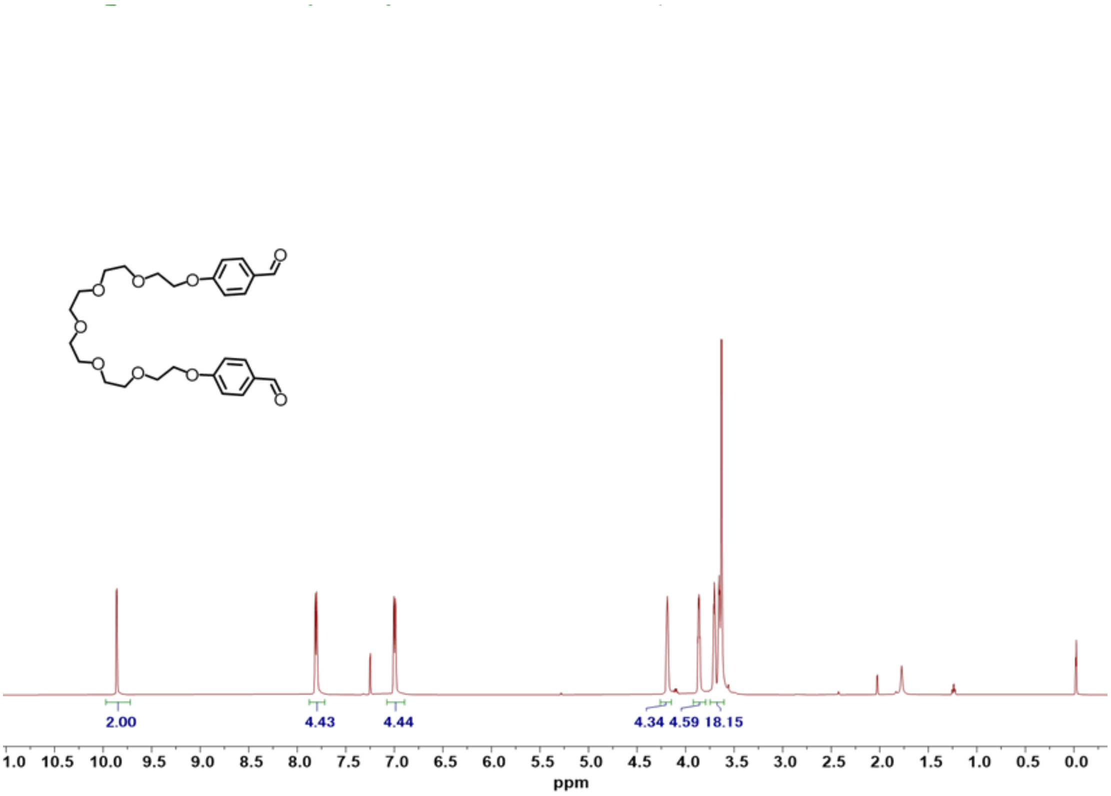

Synthesis of 8

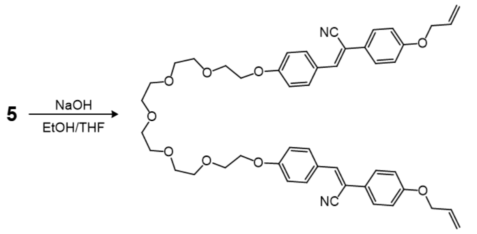

To a solution of **5** (1.23 g, 7.1 mmol) and **7** (1.66 g, 3.38 mmol) in dry ethanol (20 mL) and dry THF (15 mL) was added NaOH (0.14 g, 1.69 mmol) under N_2 atmosphere. After stirring at room temperature overnight, the reaction mixture was poured into water and extracted with ethyl acetate. The organic phase was washed with water (1x) and brine (1x), dried over $MgSO_4$ and evaporated. The crude was purified via the silica column chromatography (CH_2Cl_2/Ethyl acetate). **8** was obtained as yellow oil (Yield: 0.96 g, 70%). ^{1}H NMR (500 MHz, CHLOROFORM-*D*) δ 7.82 (d, *J* = 8.9 Hz, 4H), 7.55 (d, *J* = 8.8 Hz, 4H), 7.33 (s, 2H), 6.96 (m, 8H), 6.05 (m, 2H), 5.42 (dq, *J* = 17.2, 1.6 Hz, 1H), 5.30 (dq, *J* = 10.5, 1.4 Hz, 1H), 4.57 (dt, *J* = 5.3, 1.5 Hz, 2H), 4.17 (t, *J* = 9.7 Hz, 4H), 3.86 (t, *J* = 9.7 Hz, 4H), 3.73 – 3.63 (m, 16H). ^{13}C NMR (101 MHz, CHLOROFORM-D) δ 160.39, 159.16, 140.03, 132.92, 130.95, 127.55, 127.13, 126.93, 118.75, 118.11, 115.23, 115.01, 108.39, 70.96, 70.72, 70.67, 69.66, 68.99, 68.07, 67.62. HR-MS (ESI): calcd for , $[C_{48}H_{52}N_2O_9+Na]^+$, m/z = 823.3571, found m/z = 823.3578.

^{1}H NMR (500 MHz, CDCl$_3$) spectrum of **8**

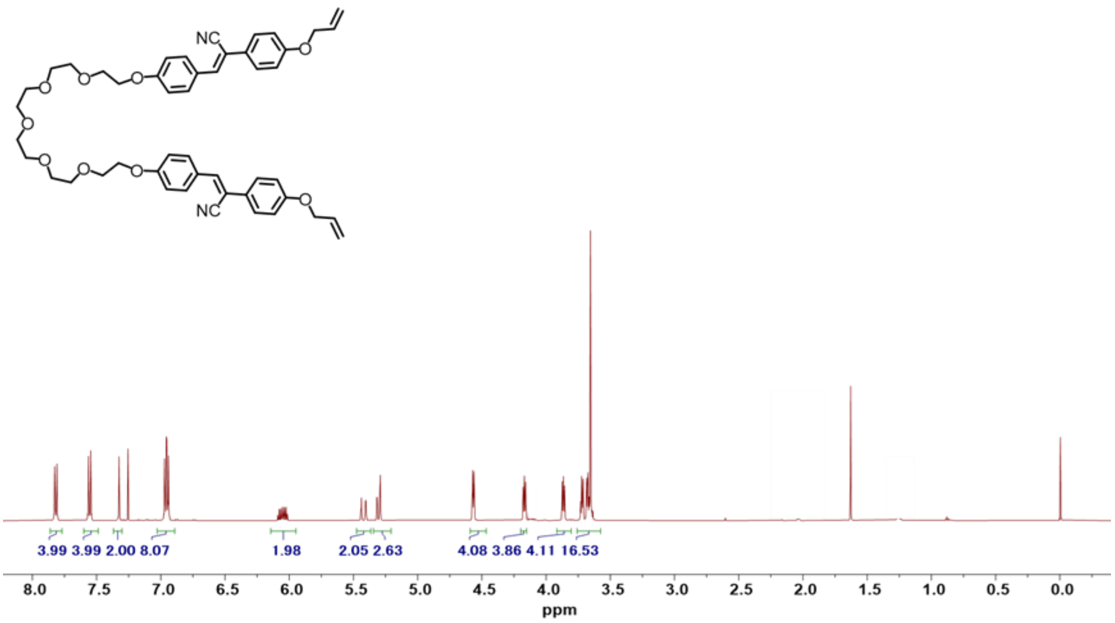

^{13}C NMR (125 MHz, CDCl$_3$) spectrum of **8**

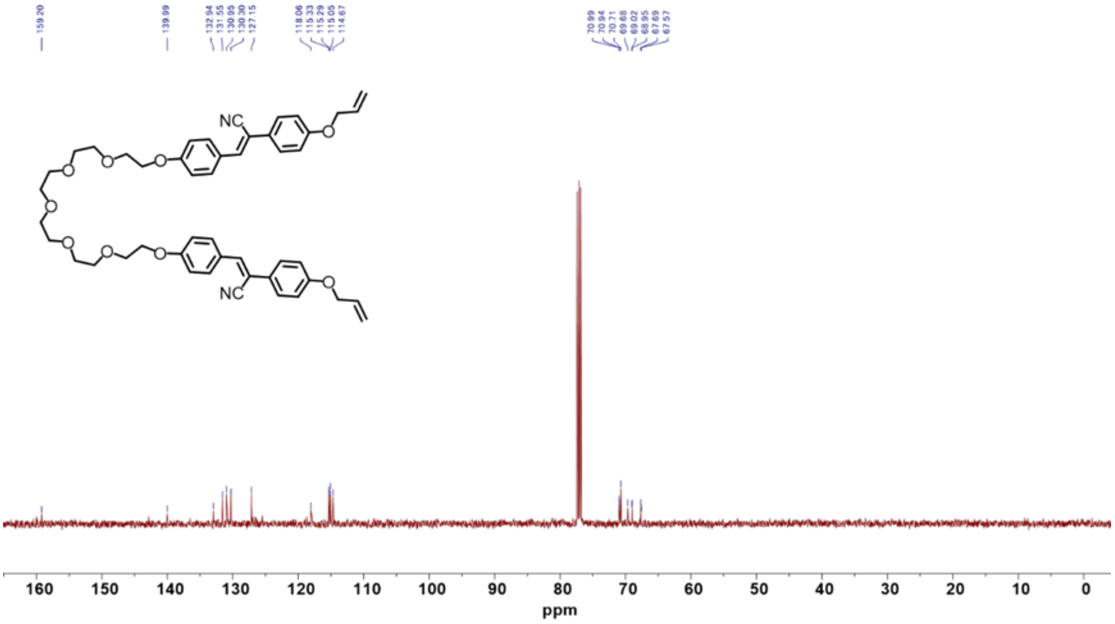

Synthesis of 9

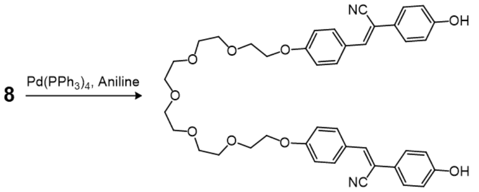

To a solution of **8** (0.96 g, 1.20 mmol) and aniline (126 mg, 1.32 mmol) in dry THF (10 mL) was added Pd(PPh$_3$)$_4$ (72 mg, 0.06 mmol) under N$_2$ atmosphere. After stirring at room temperature overnight, the reaction mixture was poured into water and extracted with CH$_2$Cl$_2$. The organic phase was washed with water (1x), brine (1x), dried over MgSO$_4$ and evaporated. The crude was purified via the silica column chromatography (CH$_2$Cl$_2$/Ethyl acetate). **9** was obtained as a light-yellow oil (Yield: 0.55 g, 64%). ^{1}H NMR (500 MHz, CHLOROFORM-*D*) δ 7.67 (d, *J* = 8.8 Hz, 4H), 7.32 (d, *J* = 8.7 Hz, 4H), 7.12 (s, 2H), 6.83 (d, *J* = 8.8, 4H), 6.74 (d, *J* = 8.9 Hz, 4H), 3.99 (t, *J* = 9.6, 4H), 3.80 (t, *J* = 9.6, 5H), 3.72 – 3.63 (m, 16H). ^{13}C NMR (101 MHz, CHLOROFORM-D) δ 160.07, 157.20, 139.41, 130.82, 127.05, 126.75, 126.45, 118.83, 116.16, 114.74, 108.11, 70.71, 70.65, 70.55, 70.48, 69.67, 67.26. HR-MS (ESI): calcd for , [C$_{42}$H$_{44}$N$_2$O$_9$+Na]$^+$, m/z = 743.2945, found m/z = 743.2947.

^{1}H NMR (500 MHz, CDCl$_3$) spectrum of **9**

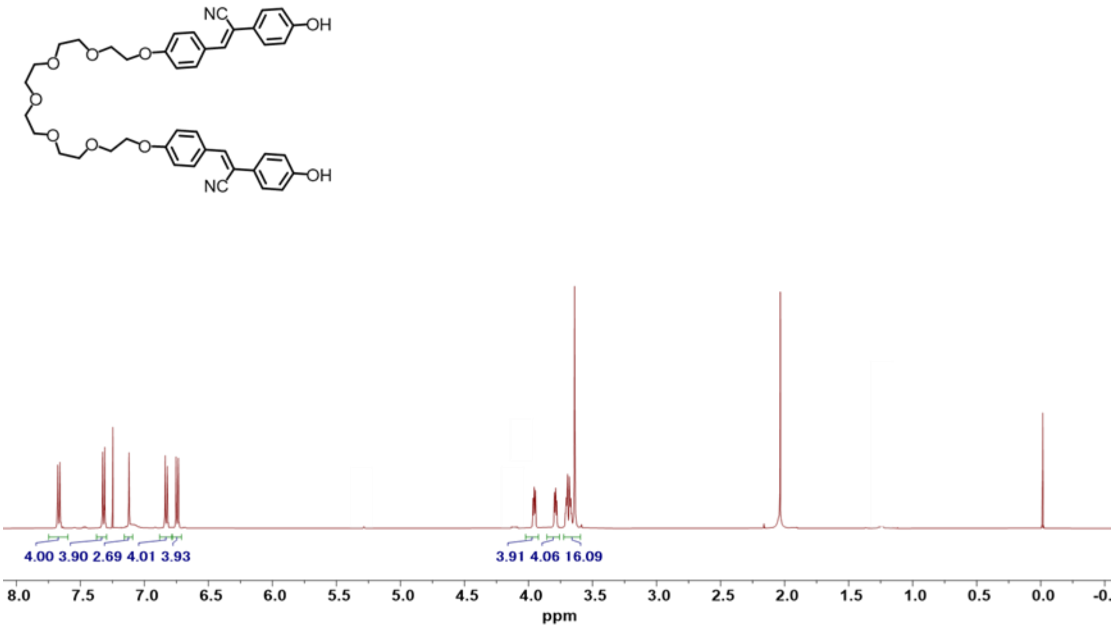

^{13}C NMR (400 MHz, CDCl$_3$) spectrum of **9**

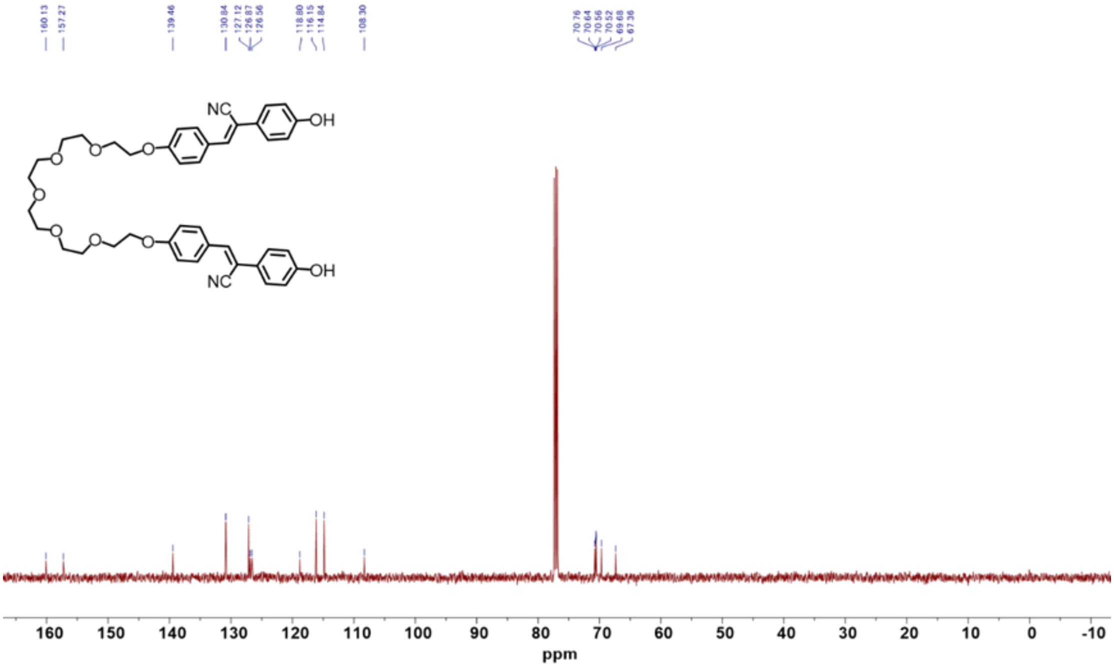

Synthesis of 10

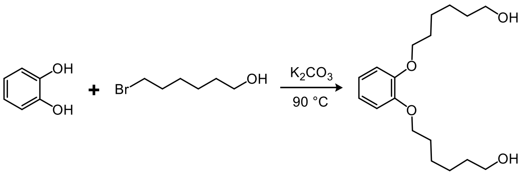

To a solution of catechol (2 g, 18.2 mmol) and 6-bromohexan-1-ol (14.1 g, 45.4 mmol) in DMF was added K_2CO_3 under N_2 atmosphere. After stirring at 90 °C overnight, the reaction mixture was poured into water and extracted with ethyl acetate. The organic phase was washed with water (3 x) and brine (1x), dried over $MgSO_4$ and evaporated. The crude was purified via silica column chromatography (CH_2Cl_2/Ethyl acetate). **10** were obtained as white solid (Yield: 2.93 g, 52%). ^{1}H NMR (396 MHz, CHLOROFORM-*D*) δ 6.87 (s, 4H), 3.98 (t, *J* = 6.4 Hz, 4H), 3.63 (t, *J* = 6.6 Hz, 4H), 1.89 – 1.75 (m, 4H), 1.61 – 1.33 (m, 12H).

Data was consistent with those reported in the literature [31].

^{1}H NMR (400 MHz, $CDCl_3$) spectrum of **10**

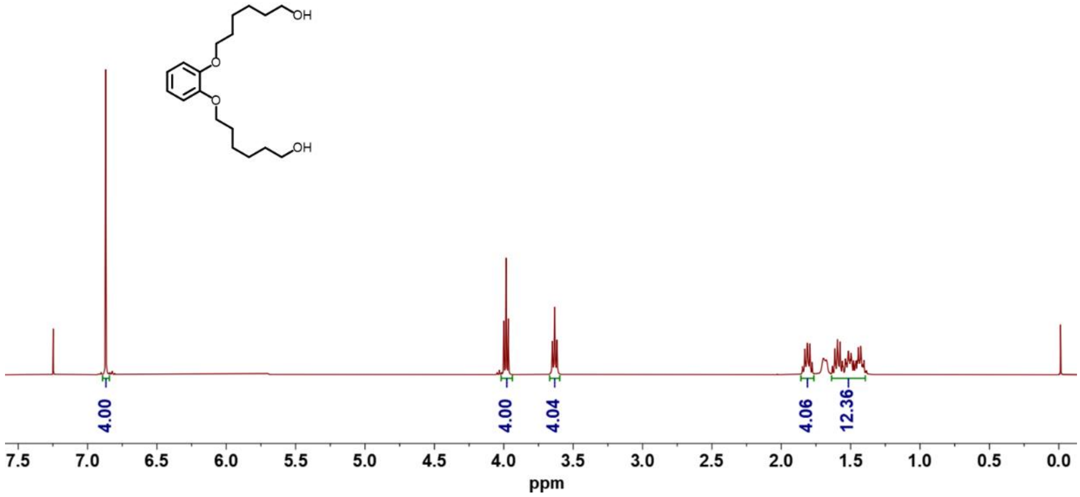

Synthesis of 11

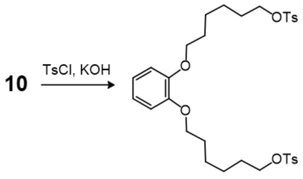

10 (1 g, 3.2 mmol) and p-toluenesulfonyl chloride (1.79 g, 6.75 mmol) were dissolved in diethyl ether (40 mL). KOH (1.45 g, 25.8 mmol) was added into the solution under ice bath in portions over 1 h. The ice bath was removed after addition and the mixture was stirred at room temperature overnight. Then the reaction mixture was poured into water and extracted with CH_2Cl_2 (3x). The combined organic phase was washed with water (2x) and brine (1x), dried over Na_2SO_4 and evaporated. **6** was obtained as a colorless oil without further purification (Yield: 4.07 g, 86%). ^{1}H NMR (500 MHz, CHLOROFORM-*D*) δ 7.77 (d, *J* = 8.3 Hz, 4H), 7.32 (d, *J* = 7.9, 0.6 Hz, 4H), 6.93 – 6.78 (m, 4H), 4.01 (t, *J* = 6.4 Hz, 4H), 3.92 (t, *J* = 6.5 Hz, 4H), 1.78 – 1.72 (m, 4H), 1.68 – 1.63 (m, 4H), 1.45 – 1.32 (m, 8H). ^{13}C NMR (126 MHz, CHLOROFORM-*D*) δ 149.19, 144.75, 133.37, 129.91, 127.96, 121.27, 114.28, 70.60, 69.02, 29.17, 28.91, 25.54, 25.26, 21.69. HR-MS (ESI): calcd for , $[C_{32}H_{42}O_8S_2+Na]^+$, m/z = 641.2219, found m/z = 641.2219.

^{1}H NMR (500 MHz, $CDCl_3$) spectrum of **11**

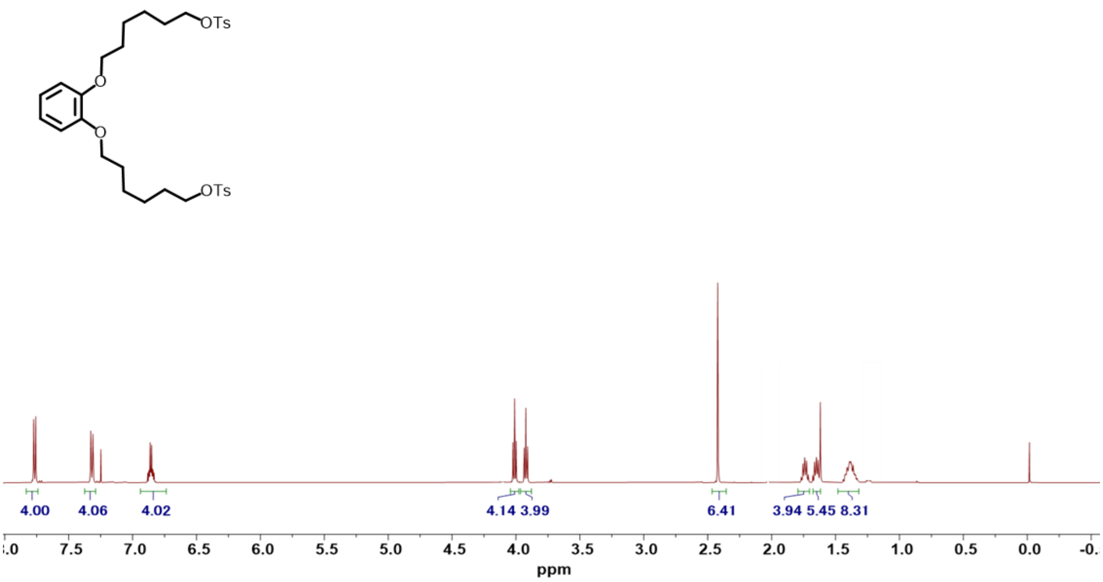

^{13}C NMR (125 MHz, $CDCl_3$) spectrum of **11**

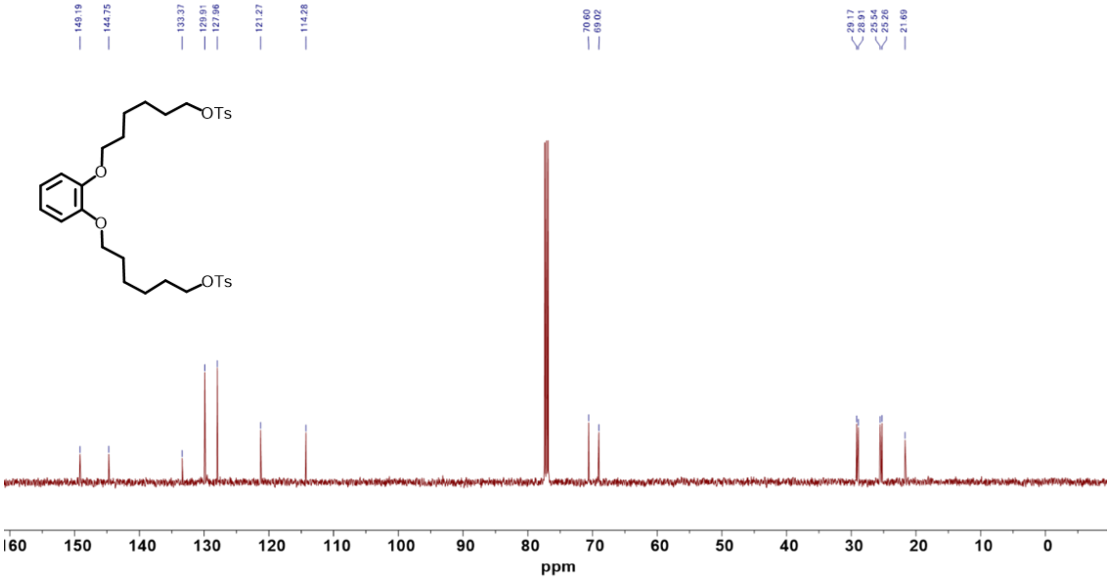

Synthesis of 12

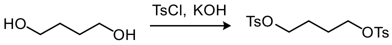

Butane-1,4-diol (2 g, 22.2 mmol) and p-toluenesulfonyl chloride (8.88 g, 46.6 mmol) were dissolved in CH_2Cl_2 (60 mL). KOH (9.94 g, 17.8 mmol) was added into the solution under ice bath in portions over 1 h. The ice bath was removed after addition and the mixture was stirred at room temperature overnight. Then the reaction mixture was poured into water and extracted with CH_2Cl_2 (3x). The combined organic phase was washed with water (2x) and brine (1x), dried over Na_2SO_4 and evaporated. **6** was obtained as a white solid without further purification (Yield: 3.43 g, 86%). ^{1}H NMR (396 MHz, CHLOROFORM-*D*) δ 7.82 – 7.68 (d, *J* = 6.5 Hz, 4H), 7.38 – 7.29 (d, *J* = 6.5 Hz, 4H), 3.99 – 3.96 (m, 4H), 2.44 (s, 6H), 1.70 – 1.67 (m, 4H).

Data was consistent with those reported in the literature.[32]

^{1}H NMR (400 MHz, CDCl$_3$) spectrum of **12**

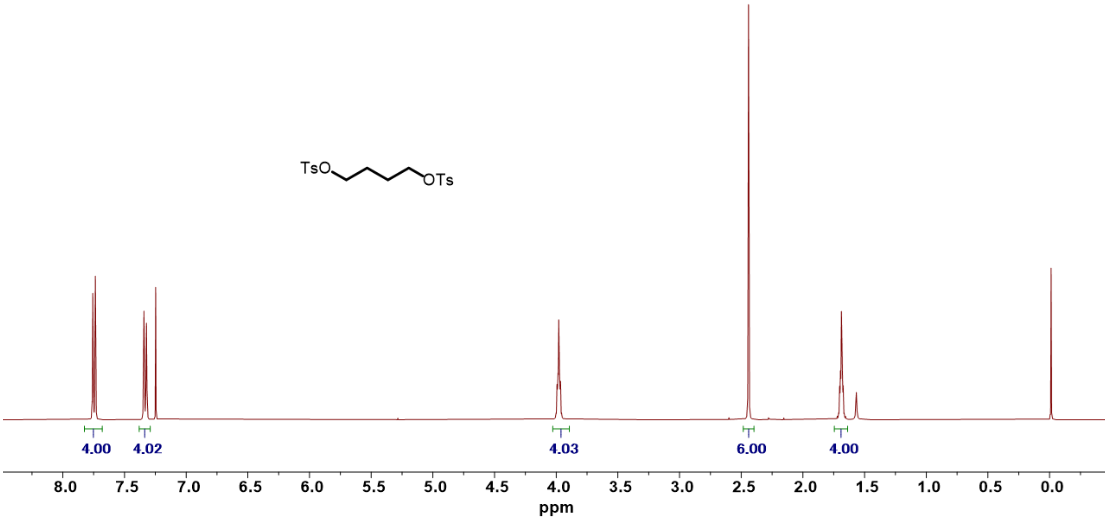

Synthesis of MCH1

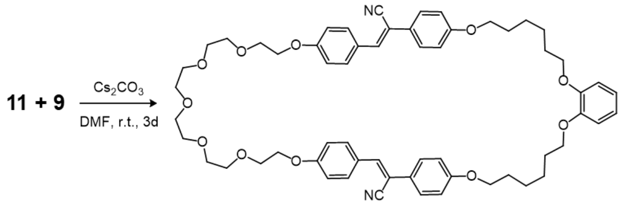

To a solution of **11** (0.6 g, 0.97 mmol) and **9** (0.7 g, 0.97 mmol) in DMF (80 mL) was added Cs_2CO_3 (1.89 g, 5.82 mmol). The mixture was stirred at room temperature for 3 days. Then the reaction mixture was poured into water and extracted with ethyl acetate. The organic phase was dried over $MgSO_4$ and evaporated. The crude was purified via the silica column chromatography (CH_2Cl_2/ Ethyl acetate). **MCH1** was obtained as a yellow solid (Yield: 0.31 g, 32%). ^{1}H NMR (500 MHz, CHLOROFORM-*D*) δ 7.68(d, *J* = 8.8 Hz, 4H), 7.39 (d, *J* = 8.8 Hz, 4H), 7.13 (s, 2H), 6.89 (s, 4H), 6.84 (d, *J* = 8.8 Hz, 4H), 6.78 (d, *J* = 8.8 Hz, 4H), 4.10 – 4.05 (t, *J* = 9.5 Hz, 4H), 4.01 (t, *J* = 11.9 Hz, 4H), 3.89 – 3.81 (m, 8H), 3.75 – 3.59 (m, 16H), 1.81 (m, 8H), 1.64 – 1.46 (m, 8H). ^{13}C NMR (101 MHz, CHLOROFORM-*D*) δ 160.29, 159.63, 149.31, 139.57, 130.94, 126.95, 126.81, 121.20, 118.77, 114.81, 114.04, 108.09, 71.04, 70.86, 70.83, 69.65, 69.08, 68.08, 29.47, 26.36, 26.01. HR-MS (ESI): calcd for , $[C_{60}H_{70}N_2O_{11}+Na]^+$, m/z = 1017.4877, found m/z = 1017.4883.

^{1}H NMR (500 MHz, $CDCl_3$) spectrum of **MCH1**

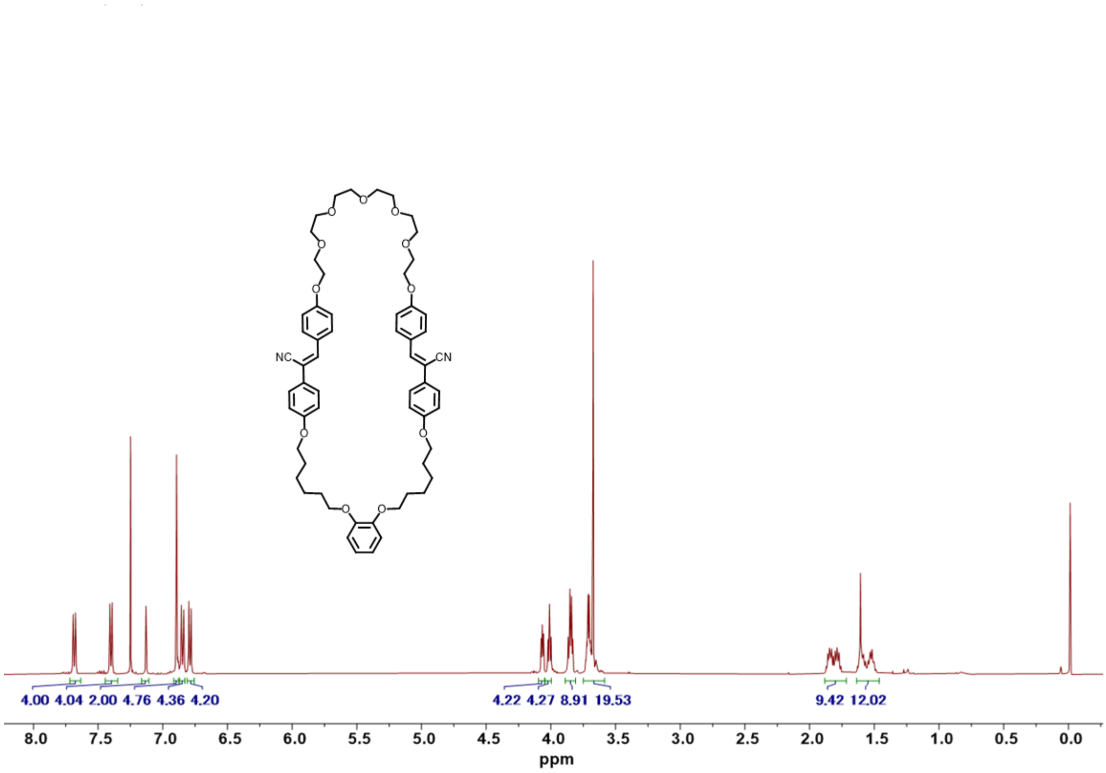

^{13}C NMR (100 MHz, $CDCl_3$) spectrum of **MCH1**

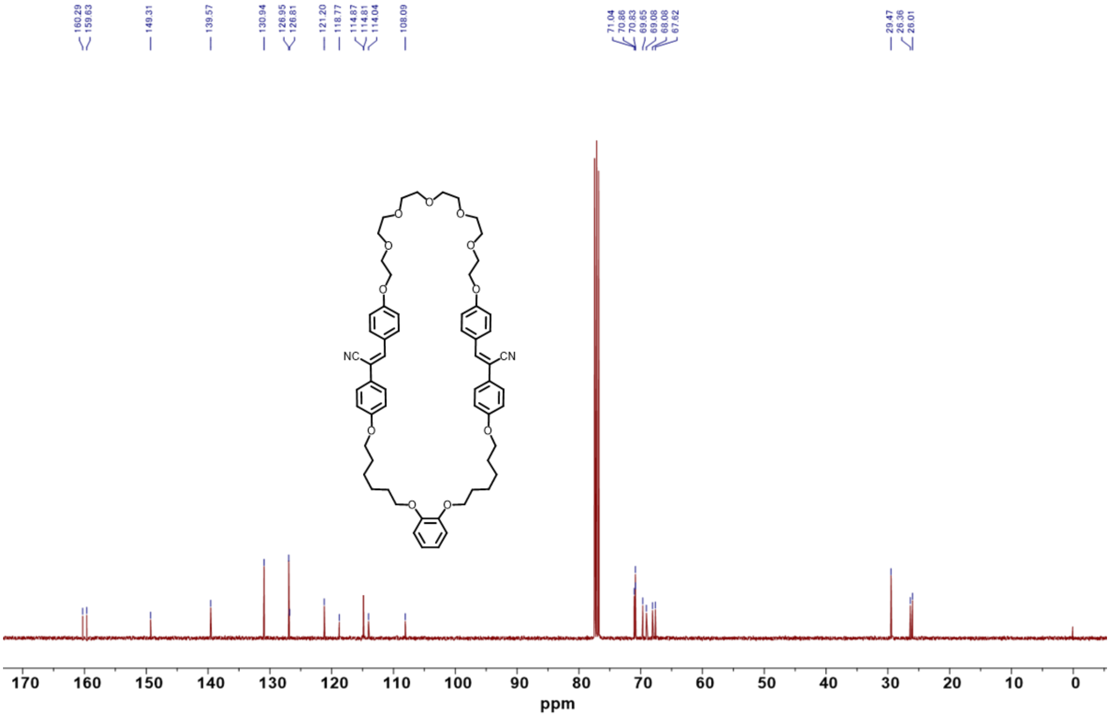

Synthesis of MCH2

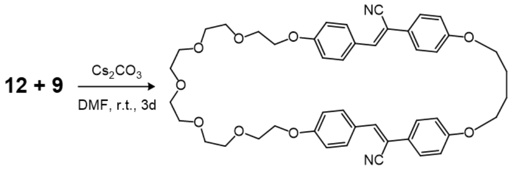

To a solution of **12** (0.386 g, 0.97 mmol) and **9** (0.7 g, 0.97 mmol) in DMF (80 mL) was added Cs_2CO_3 (1.89 g, 5.82 mmol). The mixture was stirred at room temperature for 3 days. Then the reaction mixture was poured into water and extracted with ethyl acetate. The organic phase was dried over $MgSO_4$ and evaporated. The crude was purified via the silica column chromatography (CH_2Cl_2/ Ethyl acetate). **MCH2** was obtained as a yellow solid (Yield: 0.26 g, 35%). ^{1}H NMR (500 MHz, CHLOROFORM-*D*) δ 7.70 (d, *J* = 8.7 Hz, 4H), 7.35 (d, *J* = 8.7 Hz, 4H), 7.19 (s, 2H), 6.84 (d, *J* = 8.7 Hz, 4H), 6.65 (d, *J* = 8.7 Hz, 4H), 4.23 – 4.06 (m, 8H), 3.88 (t, *J* = 9.5 Hz, 4H), 3.77 – 3.61 (m, 16H), 1.99 (br t, *J* = 8.3 Hz, 4H). ^{13}C NMR (101 MHz, CHLOROFORM-*D*) δ 160.30, 158.93, 139.79, 130.97, 127.05, 126.80, 118.81, 115.14, 114.92, 108.05, 70.89, 70.86, 70.81, 69.67, 67.69, 67.47, 24.87. HR-MS (ESI): calcd for , $[C_{16}H_{50}N_2O_9+Na]^+$, m/z = 797.3414, found m/z = 797.3410.

^{1}H NMR (500 MHz, CDCl$_3$) spectrum of **MCH2**

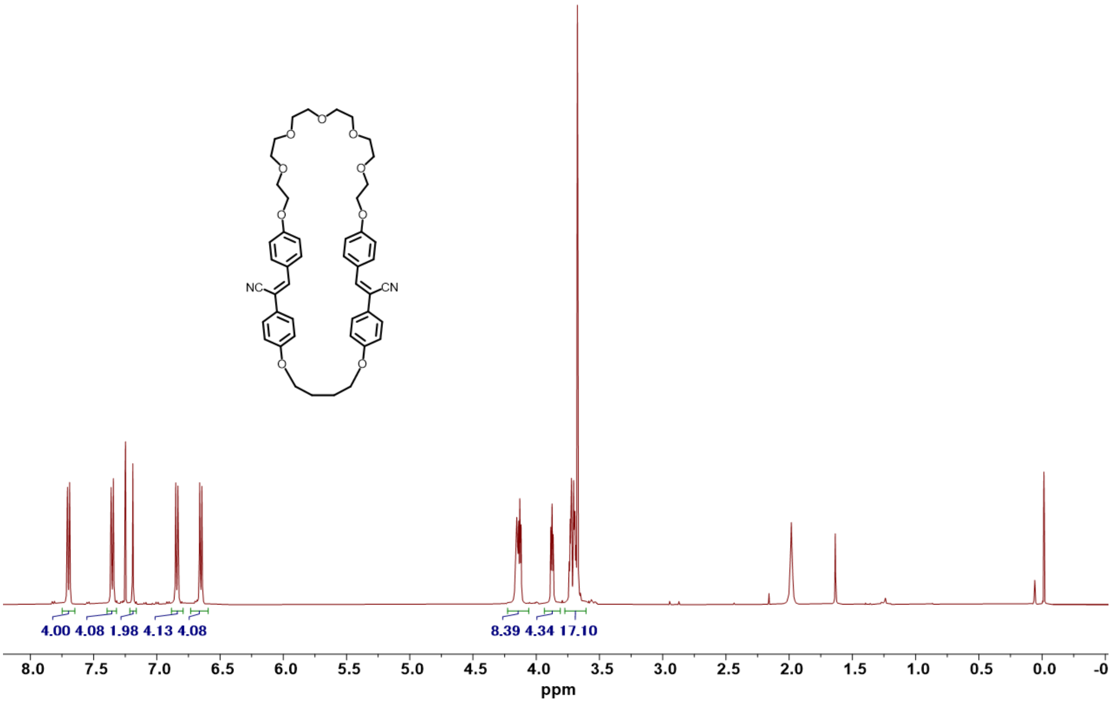

^{13}C NMR (100 MHz, CDCl$_3$) spectrum of **MCH2**

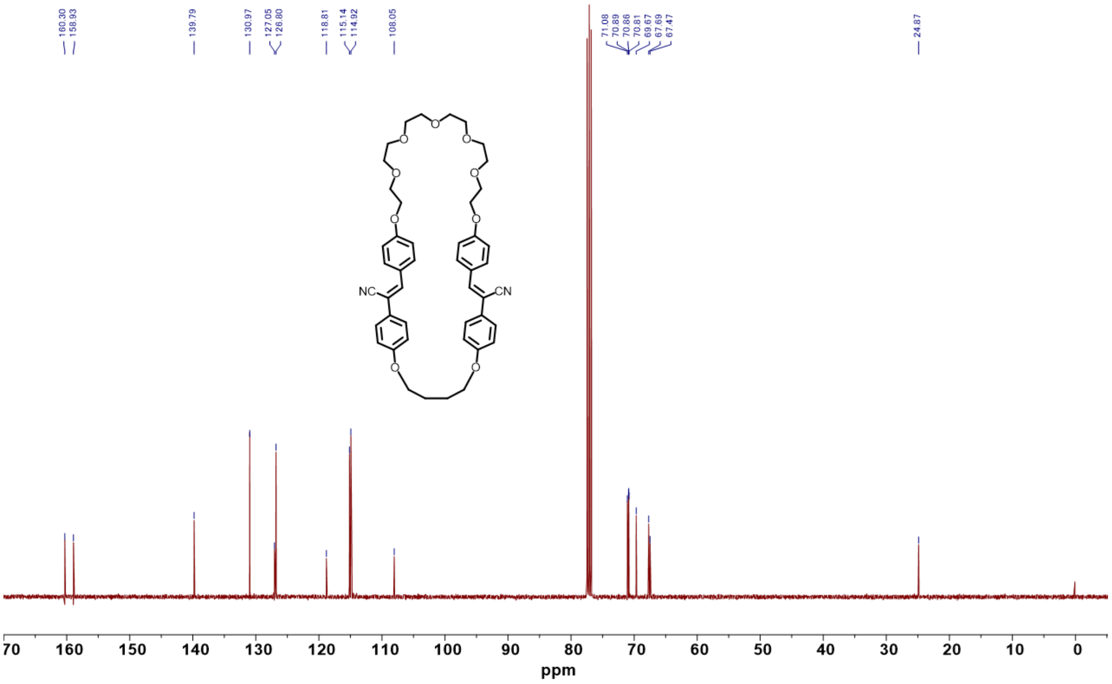

Synthesis of MCH3

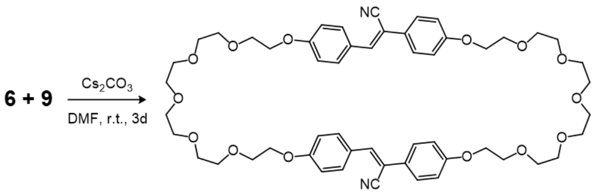

To a solution of **6** (0.573 g, 0.97 mmol) and **9** (0.7 g, 0.97 mmol) in DMF (80 mL) was added Cs_2CO_3 (1.89 g, 5.82 mmol). The mixture was stirred at room temperature for 3 days. Then the reaction mixture was poured into water and extracted with ethyl acetate. The organic phase was dried over $MgSO_4$ and evaporated. The crude was purified via the silica column chromatography (CH_2Cl_2/ Ethyl acetate). **MCH3** was obtained as a yellow solid (Yield: 0.24 g, 26%). ^1H NMR (400 MHz, CHLOROFORM-*D*) δ 7.72 (d, *J* = 8.8, 4H), 7.45 (d, *J* = 8.3, 4H), 7.19 (s, 2H), 6.88 (m, 8H), 4.12 – 4.04 (m, 8H), 3.83 (m, 8H), 3.74 – 3.59 (m, 32H). ^{13}C NMR (101 MHz, CHLOROFORM-*D*) δ 160.35, 159.34, 139.84, 130.96, 127.39, 127.03, 126.82, 118.74, 115.04, 114.93, 108.11, 71.00, 70.79, 70.78, 69.70, 69.63, 67.66, 67.63. HR-MS (ESI): calcd for , $[C_{60}H_{70}N_2O_{11}+Na]^+$, m/z = 989.4412, found m/z = 989.4411.

^{1}H NMR (400 MHz, $CDCl_3$) spectrum of **MCH3**

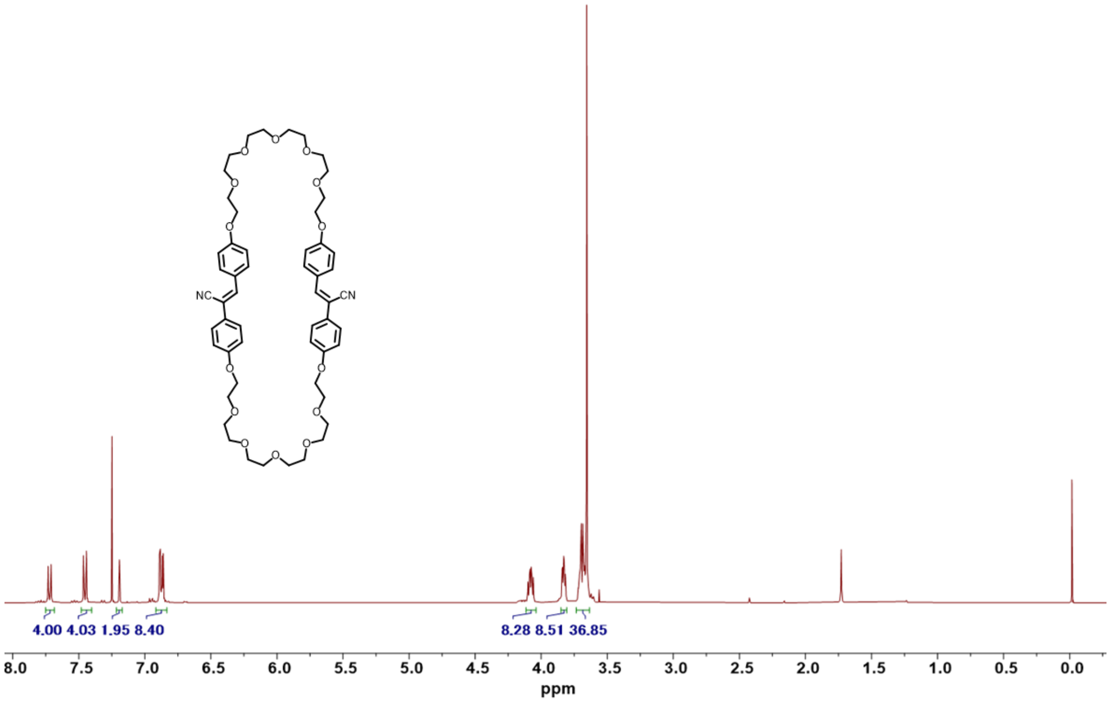

^{13}C NMR (100 MHz, $CDCl_3$) spectrum of **MCH3**

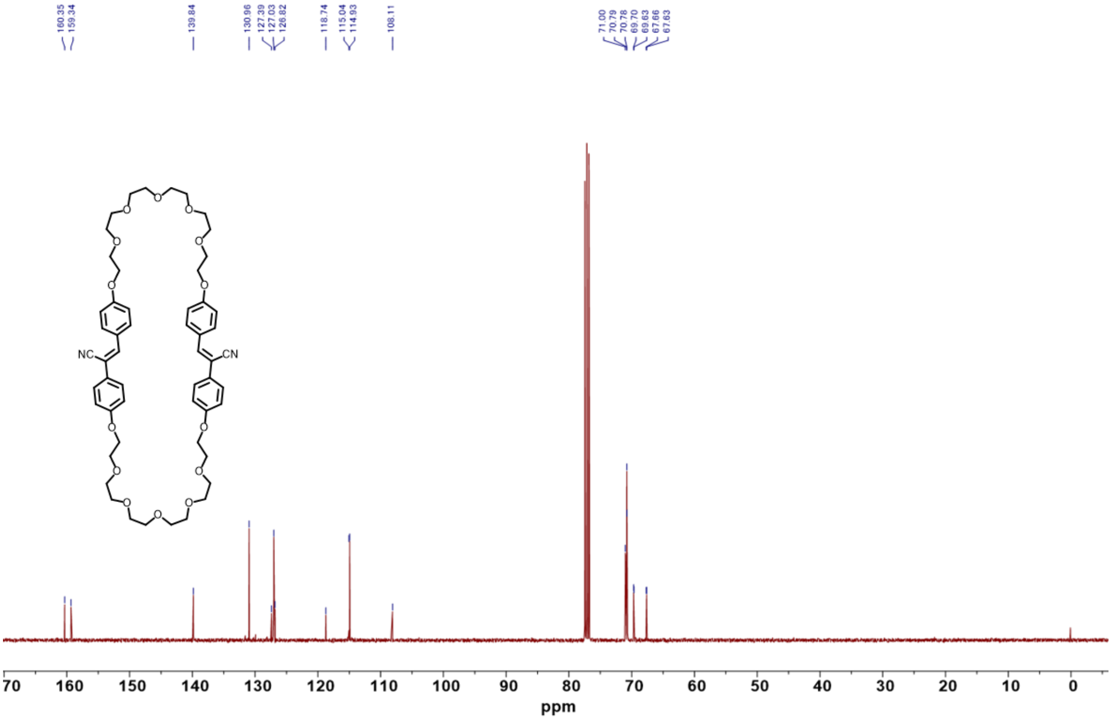

Synthesis of cMCH1 and oMCH1 by intramolecular [2+2] photocycloaddition and growth of their single crystal

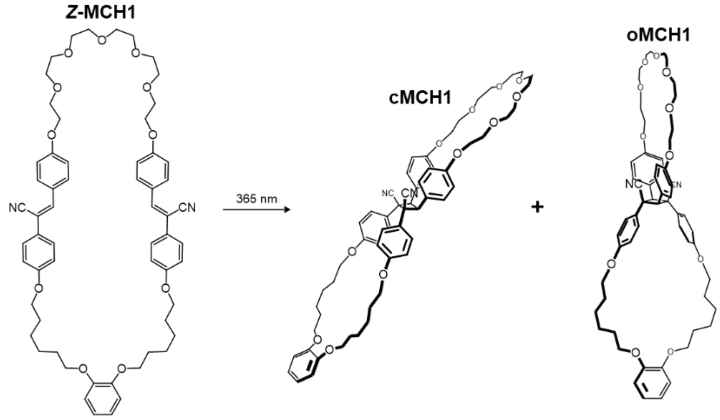

Synthesis: **MCH1** (100 mg, 25 mM) was dissolved in $CHCl_3$ (4.2 mL) and degassed by bubbling with N_2. The solution was then cooled to -78 °C using a low temperature reactor and irradiated with 365 nm UV light overnight. After irradiation, the solution was directly subjected to silica column chromatography for isolation (CH_2Cl_2/Ethyl acetate = 100/0 – 60/40, gradient elution). **cMCH1** and **oMCH1** were isolated as white solid (**cMCH1**: 72 mg, 72%; **oMCH1**: 4.3 mg, 4.3%, Mixture: 19.1 mg, 19.1%; In total: 95%).

*Note: Partial overlap of **cMCH1** and **oMCH1** during column elution led to loss in yield of pure compounds.*

cMCH1: ^{1}H NMR (500 MHz, CHLOROFORM-*D*) δ 7.15 (d, *J* = 8.8 Hz, 4H), 7.12 (d, *J* = 8.8 Hz, 4H), 6.90 (s, 4H), 6.82 (d, *J* = 8.8 Hz, 4H), 6.64 (d, *J* = 8.8 Hz, 4H), 4.91 (s, 2H), 4.16 – 4.06 (m, 4H), 4.00 (t, *J* = 6.1 Hz, 1H), 3.87 (t, *J* = 6.6 Hz, 1H), 3.82 (t, *J* = 4.7 Hz, 4H), 3.71 – 3.60 (m, 16H), 1.82 (p, *J* = 6.3 Hz, 4H), 1.71 (m, 4H), 1.54 (m, 4H), 1.46 (m, 4H). ^{13}C NMR (101 MHz, CHLOROFORM-*D*) δ 159.29, 158.10, 149.43, 130.65, 128.84, 126.63, 125.54, 121.42, 119.48, 114.64, 114.62, 71.07, 70.91, 70.73, 69.71, 69.20, 68.06, 67.56, 54.92, 46.34, 29.40, 28.87, 25.87, 25.66. HR-MS (ESI): calcd for , $[C_{60}H_{70}N_2O_{11}+Na]^+$, m/z = 1017.4877, found m/z = 1017.4880.

oMCH1: ^{1}H NMR (500 MHz, CHLOROFORM-*D*) δ 7.69 (d, *J* = 8.8 Hz, 4H), 7.23 – 7.20 (m, 8H), 6.87 – 6.83 (m, 8H), 4.37 (t, *J* = 3.5 Hz, 4H), 4.28 (s, 2H), 4.13 (t, *J* = 6.3

Hz, 4H), 3.94 (t, *J* = 7.3 Hz, 4H), 3.83 – 3.77 (t, *J* = 8.6 Hz, 4H), 3.70 (m, 4H), 3.64 – 3.51 (m, 12H), 1.78 (m, 4H), 1.71 (m, 4H), 1.43 (m, 8H). ^{13}C NMR (126 MHz, CHLOROFORM-*D*) δ 159.80, 158.55, 148.66, 132.88, 130.20, 126.77, 126.43, 120.87, 119.34, 116.63, 115.86, 113.08, 71.11, 70.62, 70.49, 69.90, 69.09, 68.88, 67.70, 54.89, 50.53, 29.77, 29.11, 28.26, 25.68, 25.53. HR-MS (ESI): calcd for , $[C_{60}H_{70}N_2O_{11}+Na]^+$, m/z = 1017.4877, found m/z = 1017.4885.

Single crystal growth: single crystal of **cMCH1** and **oMCH1** were growth by the by vapor diffusion of hexane into their $CHCl_3$ solutions at 4 °C.

^{1}H NMR (500 MHz, $CDCl_3$) spectrum of **cMCH1**

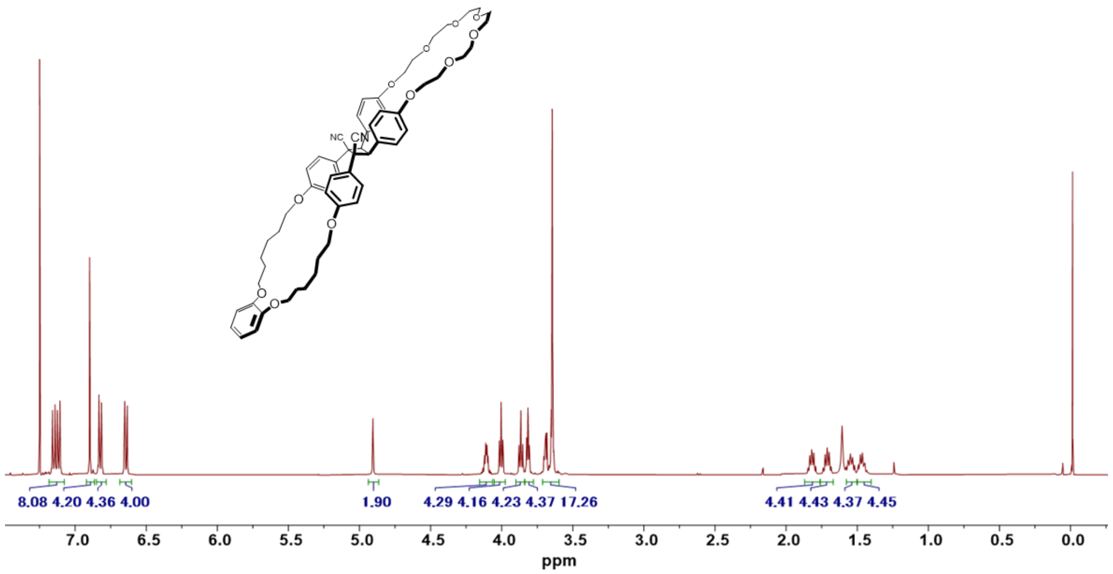

^{13}C NMR (100 MHz, $CDCl_3$) spectrum of **cMCH1**

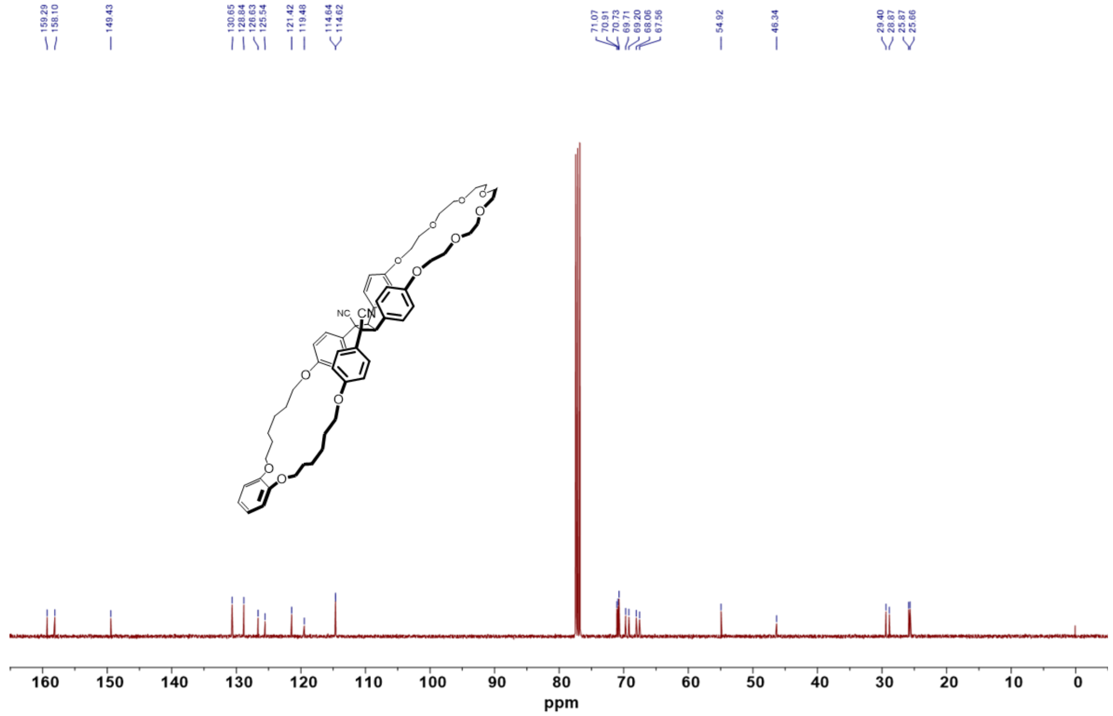

^{1}H NMR (500 MHz, $CDCl_3$) spectrum of **oMCH1**

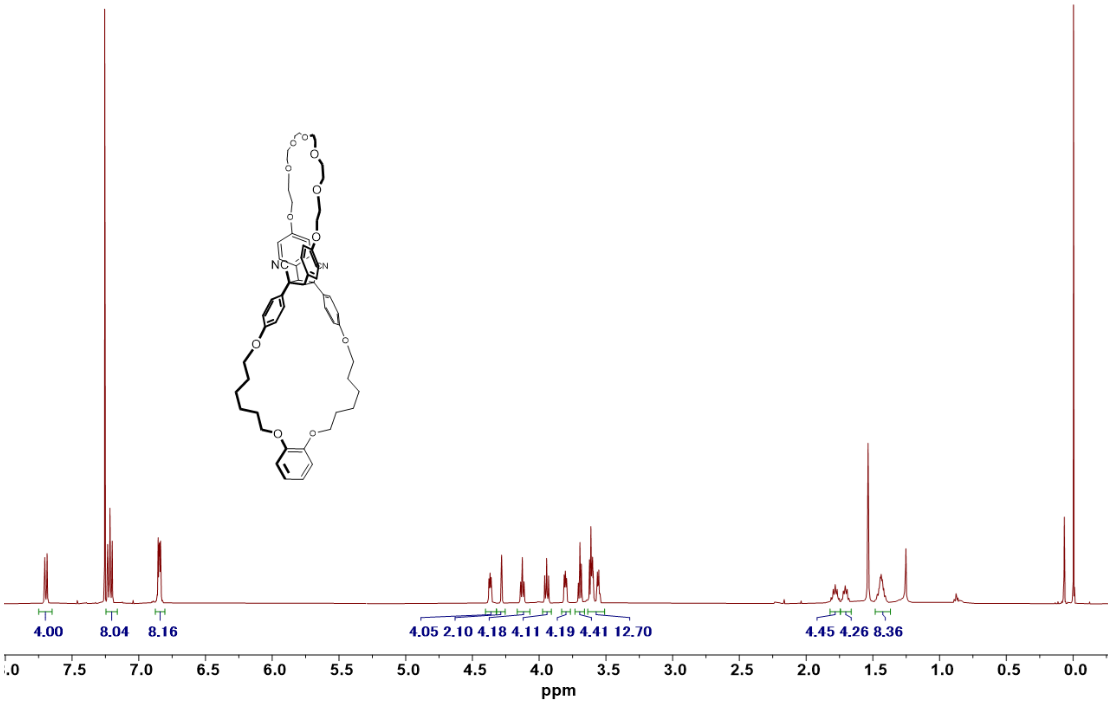

^{13}C NMR (125 MHz, $CDCl_3$) spectrum of **oMCH1**

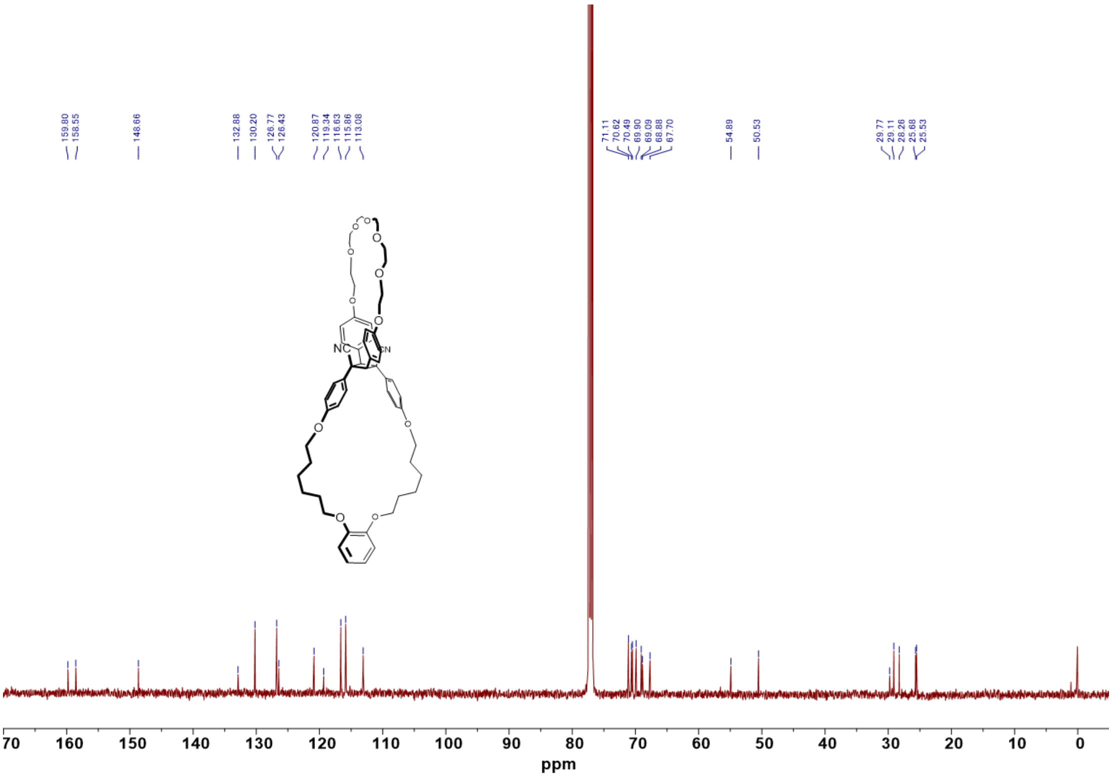

Details of Single-Crystal X-ray Structure Determinations

cMCH1: Single crystal X-ray diffraction data were collected at 223.15 K on a Rigaku XtaLAB Synergy-R four-circle diffractometer using Mo Kα radiation ($\lambda = 0.71073$ Å) from a rotating-anode X-ray tube (Rigaku (Mo) X-ray Source). Cell refinement, data collection, and reduction were performed with CrysAlisPro version 1.171.41.122a (Rigaku OD, 2021), and an empirical multi-scan absorption correction was applied.[33] Reflections were merged by SHELXL according to the crystal class to ensure robust statistical treatment for subsequent refinement. The structure was solved using SHELXT 2018/2 (Sheldrick, 2018) and refined by full-matrix least-squares on F^2 with SHELXL 2018/3 (Sheldrick, 2015), where hydrogen atoms were placed in idealized positions and constrained to ride on their parent atoms. Molecular graphics and publication materials were prepared using Olex2 version 1.5.[34-36] See Tables S1 for a summary of data collection, solution and refinement details. Complete details of the structures can be obtained from the Cambridge Crystallographic Data Centre at www.ccdc.cam.ac.uk for CCDC accession numbers 2443528.

oMCH1: Single crystal X-ray diffraction data were collected at 120.15 K on a Rigaku XtaLAB Synergy-R four-circle diffractometer using Mo Kα radiation ($\lambda = 0.71073$ Å) from a rotating-anode X-ray tube (Rigaku (Mo) X-ray Source). Data collection, cell refinement, and integration were performed with CrysAlisPro version 1.171.41.122a (Rigaku Oxford Diffraction, 2021).[33] An empirical multi-scan absorption correction was applied using spherical harmonics as implemented in the SCALE3 ABSPACK scaling algorithm. Reflection merging was carried out by SHELXL according to the crystal class, and structure factors included contributions from the .fab file. The structure was solved with SHELXT 2018/2 (Sheldrick, 2018) and refined by full-matrix least-squares on F^2 with SHELXL 2019/3 (Sheldrick, 2015), employing riding constraints for the hydrogen atoms. Molecular graphics and publication materials were prepared using Olex2 version 1.5.[34-36] See Tables S1 for a summary of data collection, solution and refinement details. Complete details of the structures can be obtained from the Cambridge Crystallographic Data Centre at www.ccdc.cam.ac.uk for CCDC accession numbers 2443529.

Table 1 X-ray experimental details for **cMCH1** and **oMCH1**.

Compound	**cMCH1**	**oMCH1**
CCDC No.	2443528	2443529
Empirical formula	$C_{62}H_{72}Cl_6N_2O_{11}$	$C_{63}H_{72}Cl_9N_2O_{11}$
Formula weight	1233.91	1352.27
Temperature/K	223.15	120.15
Crystal system	triclinic	triclinic
Space group	P-1	P-1
a/Å	12.8790(3)	10.4396(3)
b/Å	13.7920(3)	13.9469(4)
c/Å	18.8490(4)	23.7674(6)
α/°	85.565(2)	78.125(2)
β/°	77.924(2)	78.429(2)
γ/°	73.013(2)	79.111(2)
Volume/Å^3	3130.69(13)	3278.08(16)
Z	2	2
ρ_{calc}g/cm^3	1.309	1.370
μ/mm^{-1}	0.334	0.443
F(000)	1296.0	1410.0
Crystal size/mm^3	0.4 × 0.25 × 0.1	0.3 × 0.04 × 0.03
Radiation	Mo Kα (λ = 0.71073)	Mo Kα (λ = 0.71073)
2Θ range for data collection/°	3.088 to 62.364	3.02 to 59.842
Reflections collected	72299	32513
Independent reflections	16551	14894
Data/restraints/parameters	16552/2575/1315	14894/4/768
Goodness-of-fit on F^2	1.034	1.047
R_1 [I>=2σ (I)]	0.0972	0.0820
R_1 (all data)	0.1360	0.1137
wR_2 [I>=2σ (I)]	0.2876	0.1957
wR_2 (all data)	0.3202	0.2127
Largest diff. peak/hole / e Å^{-3}	0.74/-0.48	1.18/-0.63

Synthesis of cMCH2 by intramolecular [2+2] photocycloaddition

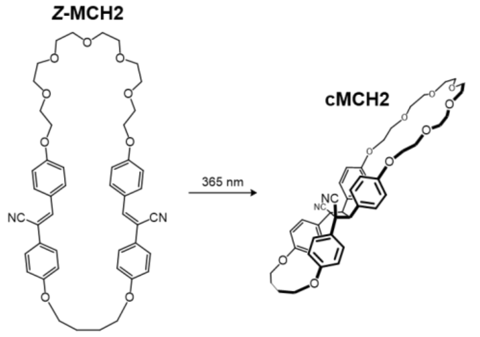

MCH2 (78 mg, 25 mM) was dissolved in $CHCl_3$ (4.2 mL) and degassed by bubbling with N_2. The solution was then cooled to -78 °C using a low temperature reactor and irradiated with 365 nm UV light overnight. After irradiation, the solvent was removed under reduced pressure to give **cMCH2** as a white solid quantitatively. ^{1}H NMR (500 MHz, CHLOROFORM-*D*) δ 7.21 (dd, *J* = 8.6, 2.6 Hz, 2H), 7.18 – 7.12 (d, 4H), 7.00 (dd, *J* = 8.7, 2.6 Hz, 2H), 6.88 – 6.79 (d, 4H), 6.62 (m, *J* = 15.8, 8.6, 2.7 Hz, 4H), 4.93 (s, 2H), 4.23 (t, 4H), 4.15 – 4.08 (m, 4H), 3.82 (t, *J* = 4.7 Hz, 4H), 3.72 – 3.60 (m, 16H), 1.58 (m, 4H). ^{13}C NMR (126 MHz, CHLOROFORM-*D*) δ 158.18, 156.87, 131.13, 130.64, 126.75, 126.53, 125.67, 119.12, 117.33, 116.56, 114.71, 71.08, 70.93, 70.75, 69.73, 67.62, 66.19, 55.73, 44.89, 21.31. HR-MS (ESI): calcd for , $[C_{16}H_{50}N_2O_9+Na]^+$, m/z = 797.3414, found m/z = 797.3420.

^{1}H NMR (500 MHz, $CDCl_3$) spectrum of **cMCH1**

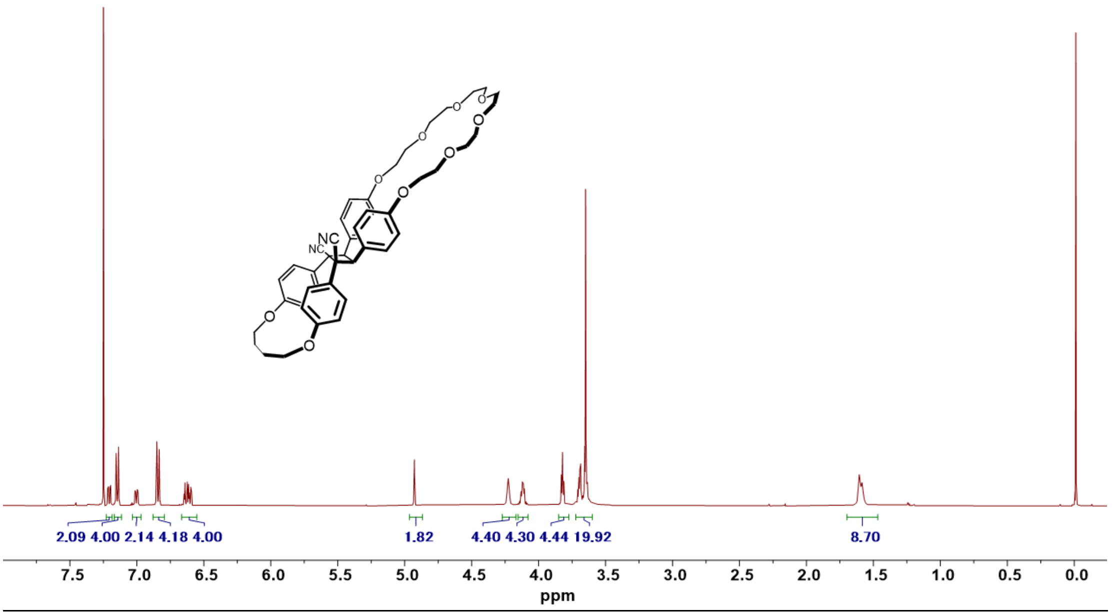

^{13}C NMR (125 MHz, $CDCl_3$) spectrum of **cMCH1**

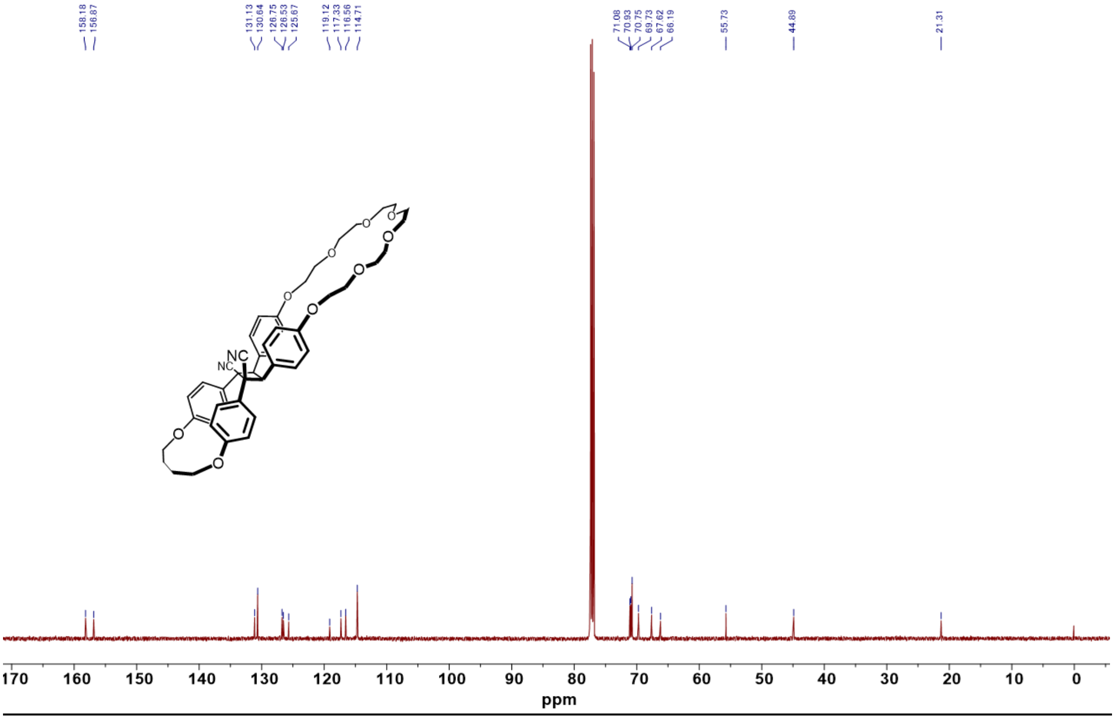

Synthesis of cMCH3 and oMCH3 by intramolecular [2+2] photocycloaddition

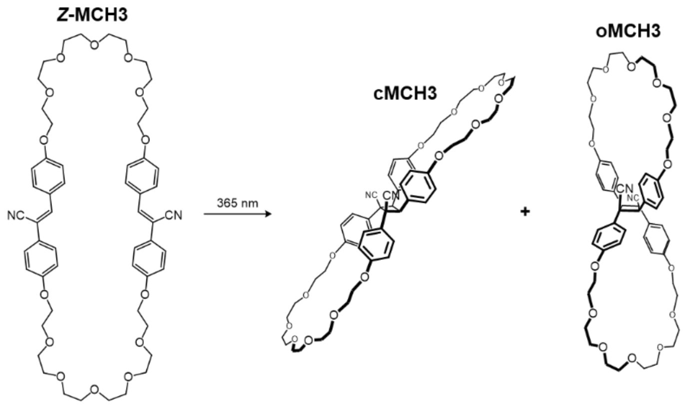

MCH3 (97 mg, 25 mM) was dissolved in $CHCl_3$ (4.2 mL) and degassed by bubbling with N_2. The solution was then cooled to -78 °C using a low temperature reactor and irradiated with 365 nm UV light for 2 days. After irradiation, the solution was directly subjected to silica column chromatography for isolation (Ethyl acetate/MeOH = 100/0 – 92/8, gradient elution). **cMCH3** and **oMCH3** were isolated as white solid (**cMCH3**: 70 mg, 72%; **oMCH3**: 4.3 mg, 4.4%; Mixture: 11.6 mg, 12%; In total: 88%).

*Note: Partial overlap of **cMCH3** and **oMCH3** during column elution led to loss in yield of pure compounds.*

cMCH3: ^{1}H NMR (400 MHz, CHLOROFORM-D) δ 7.21 (d, *J* = 8.9 Hz, 4H), 7.10 (d, *J* = 8.9 Hz, 4H), 6.81 (d, *J* = 8.9 Hz, 4H), 6.72 (d, *J* = 8.9 Hz, 4H), 4.90 (s, 2H), 4.15 – 4.07 (m, 4H), 4.07 – 4.00 (m, 4H), 3.80 (m, 8H), 3.72 – 3.57 (m, 32H). ^{13}C NMR (101 MHz, CHLOROFORM-*D*) δ 158.99, 158.10, 130.65, 128.80, 126.59, 126.03, 119.54, 114.86, 114.60, 71.10, 71.06, 70.93, 70.90, 70.88, 70.86, 70.73, 69.71, 69.64, 67.55, 54.60, 47.08. HR-MS (ESI): calcd for , $[C_{60}H_{70}N_2O_{11}+Na]^+$, m/z = 989.4412, found m/z = 989.4412.

oMCH3: ^{1}H NMR (500 MHz, CHLOROFORM-*D*) δ 7.56 (d, *J* = 8.9 Hz, 4H), 7.29 (d, *J* = 8.9 Hz, 4H), 7.17 (d, *J* = 8.9 Hz, 4H), 7.98 (d, *J* = 8.9 Hz, 4H), 4.37 – 4.31 (m, 4H), 4.25 (s, 2H), 4.24 – 4.19 (m, 4H), 3.83 – 3.75 (m, 8H), 3.67 – 3.41 (m, 32H). ^{13}C NMR (126 MHz, CHLOROFORM-*D*) δ 159.64, 159.17, 132.56, 129.74, 126.65, 126.35, 119.14, 116.51, 116.36, 71.10, 71.00, 70.74, 70.59, 70.57, 70.53, 70.46, 70.02, 69.84, 68.75, 68.26, 55.81. HR-MS (ESI): calcd for , $[C_{60}H_{70}N_2O_{11}+Na]^+$, m/z = 989.4412, found m/z = 989.4416.

^{1}H NMR (400 MHz, CDCl$_3$) spectrum of **cMCH3**

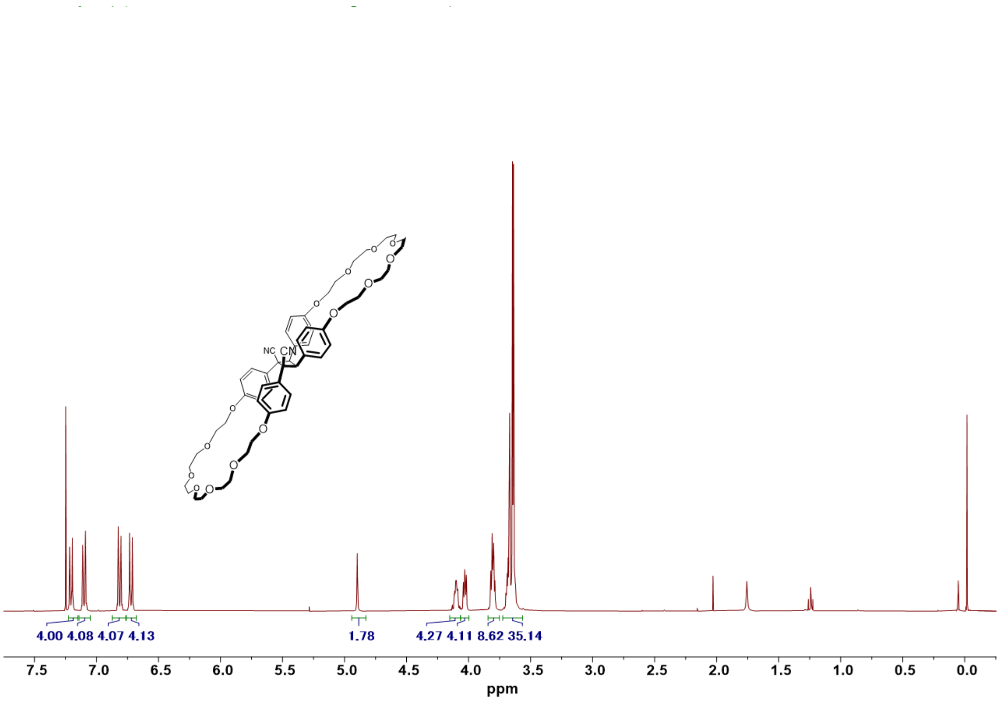

^{13}C NMR (100 MHz, CDCl$_3$) spectrum of **cMCH3**

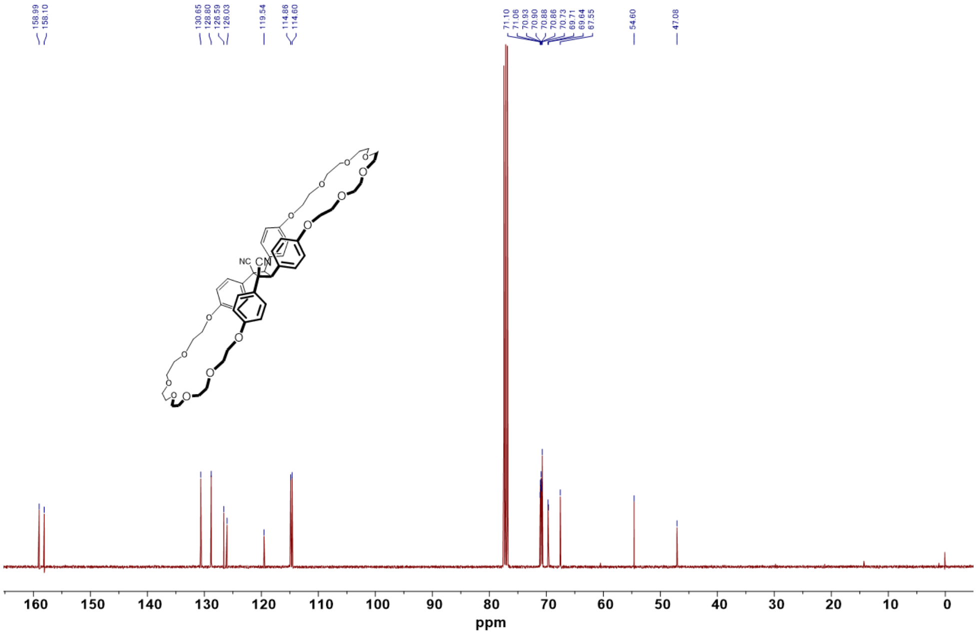

^{1}H NMR (500 MHz, CDCl$_3$) spectrum of **oMCH3**

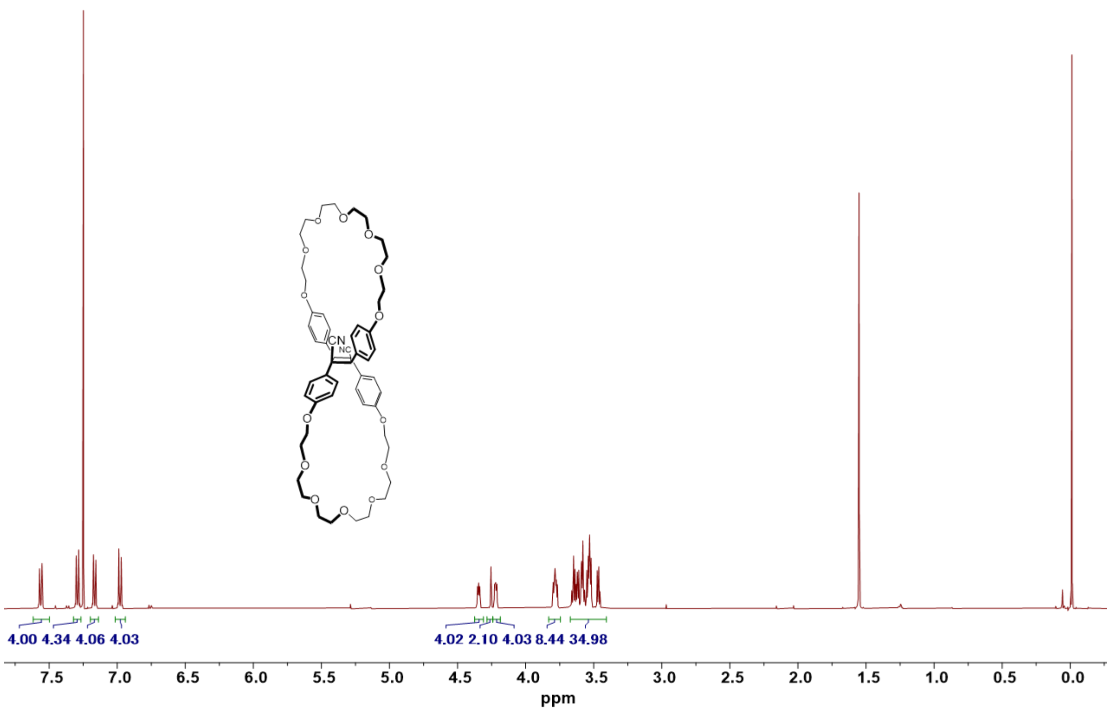

^{13}C NMR (125 MHz, CDCl$_3$) spectrum of **oMCH3**

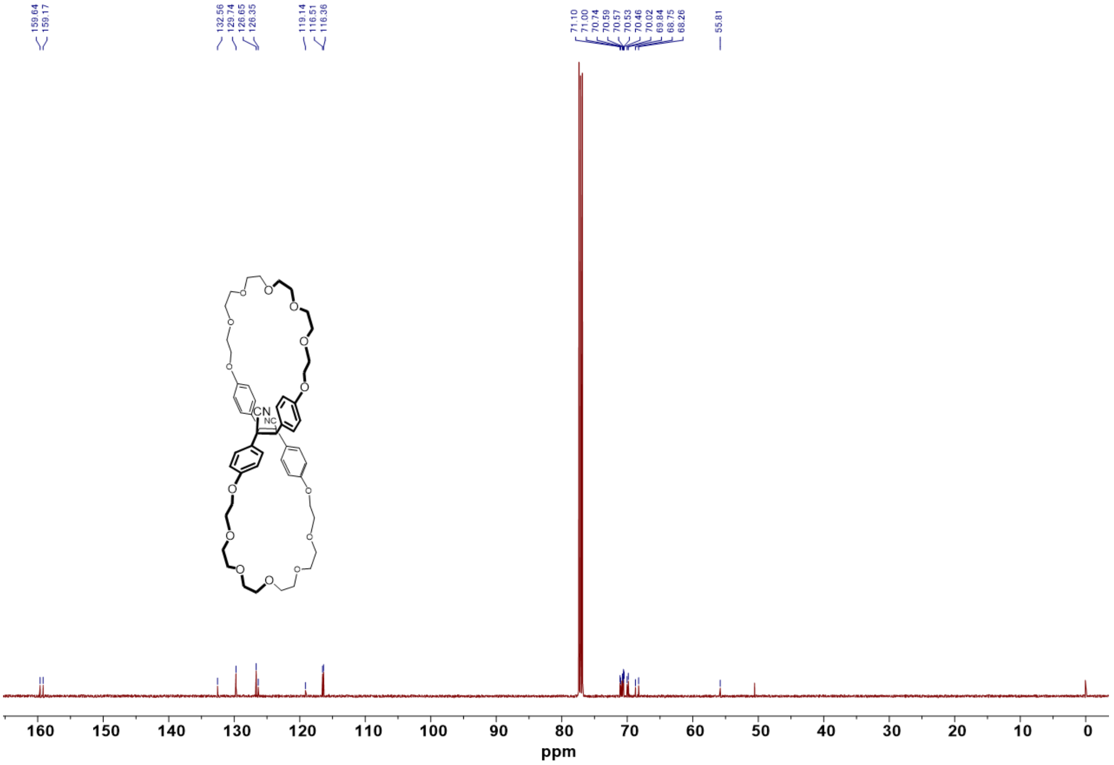

Synthesis of c[2]RT(cMCH1@G) and of o[2]RT(oMCH1@G)

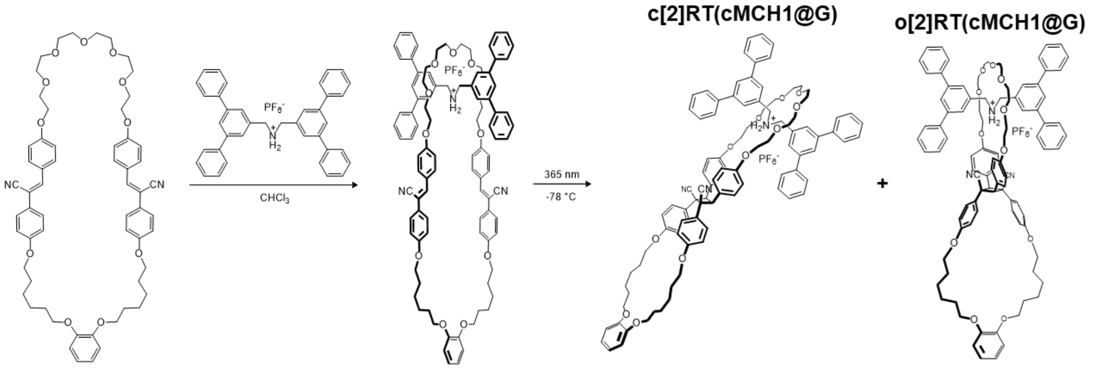

MCH1 (100 mg, 0.1 mmol, 50 mM) and **G** (195 mg, 0.3 mmol) were dissolved in acetone (2 mL) and degassed by bubbling with N_2. The solution was then cooled to -78 °C using a low temperature reactor and irradiated with 365 nm UV light overnight. After irradiation, the solution was removed under reduced pressure without heating directly. The resulting residue was purified by silica column chromatography (CH_2Cl_2/Ethyl acetate = 100/0 – 88/12, gradient elution). **c[2]RT(cMCH1@G)** and **o[2]RT(oMCH1@G)** were isolated as white solid (**c[2]RT(cMCH1@G)**: 134 mg, 79%; **o[2]RT(oMCH1@G)**: 10.1 mg, 6.1%; Mixture: 11.2 mg, 6.8%; In total: 92%).

*Note: Partial overlap of **c[2]RT(cMCH1@G)** and **o[2]RT(oMCH1@G)** during column elution led to little loss in yield of pure compounds.*

c[2]RT(cMCH1@G): ^{1}H NMR (600 MHz, ACETONE-D_6) δ 8.22 (br s, 2H), 8.11 (br t, J = 1.7 Hz, 1H), 8.08 (br t, J = 1.7 Hz, 1H), 7.94 (d, J = 1.7 Hz, 2H), 7.87 (d, J = 1.7 Hz, 2H), 7.86 – 7.83 (m, 8H), 7.56 (m, 8H), 7.49 – 7.42 (m, 4H), 7.31 (d, J = 8.8 Hz, 4H), 7.13 (d, J = 8.8 Hz, 4H), 6.96 (dd, J = 5.9, 3.6 Hz, 2H), 6.88 (dd, J = 6.0, 3.6 Hz, 2H), 6.78 (d, J = 8.8 Hz, 4H), 6.66 (d, J = 8.8 Hz, 4H), 5.17 (s, 2H), 4.78 (t, J = 6.3, 3.3 Hz, 2H), 4.68 – 4.63 (t, 2H), 4.01 (m, 8H), 3.97 (t, J = 6.6 Hz, 4H), 3.79 (m, 2H), 3.73 (m, 2H), 3.69 – 3.64 (m, 4H), 3.63 – 3.59 (m, 2H), 3.52 (m, 2H), 3.46 (m, 4H), 3.37 (m, 4H), 1.83 – 1.78 (m, 4H), 1.73 (m, 4H), 1.62 – 1.56 (m, 4H), 1.51 (m, 4H). ^{13}C NMR (101 MHz, ACETONE-D_6) δ 159.47, 157.61, 149.78, 142.50, 142.29, 140.02, 139.90, 132.56, 131.21, 130.97, 129.23, 129.08, 128.91, 128.19, 128.12, 127.93, 127.86, 127.46, 127.21, 127.15, 126.89, 126.82, 126.57, 125.77, 121.32, 119.76, 114.92, 114.67, 113.67, 70.97, 70.44, 70.18, 70.05, 69.93, 68.93, 67.85, 67.23, 59.72, 54.59, 46.16, 25.74, 25.47, 20.01, 13.68. HR-MS (ESI): calcd for $[M - PF_6]^+$, $[C_{98}H_{102}N_3O_{11}]^+$, m/z = 1497.7543, found m/z = 1496.7538.

o[2]RT(oMCH1@G): ^{1}H NMR (600 MHz, ACETONE-D_6) δ 8.05 (br t, *J* = 1.7 Hz, 2H), 7.86 – 7.83 (m, 8H), 7.81 (d, *J* = 1.7 Hz, 4H), 7.72 (d, *J* = 8.9 Hz, 4H), 7.53 – 7.55 (m, 8H), 7.47 – 7.41 (m, 8H), 7.13 – 7.07 (m, 8H), 6.90 (dd, *J* = 6.0, 3.6 Hz, 2H), 6.79 (dd, *J* = 6.0, 3.5 Hz, 2H), 4.84 (s, 2H), 4.43 – 4.37 (m, 4H), 4.26 (t, *J* = 7.0 Hz, 4H), 4.06 (m, 4H), 3.93 (t, *J* = 7.2 Hz, 4H), 3.87 – 3.81 (br, 4H), 3.54 – 3.51 (br, 4H), 3.48 – 3.43 (m, 4H), 3.24 – 3.27 (m, 4H), 2.97 – 2.91 (m, 4H), 1.78 (m, 8H), 1.50 (m, 8H). ^{13}C NMR (101 MHz, ACETONE-D_6) δ 205.35, 159.13, 158.65, 148.93, 142.18, 140.06, 132.46, 130.31, 129.21, 128.91, 128.43, 128.11, 128.07, 128.03, 127.54, 127.15, 126.53, 120.67, 120.34, 116.13, 116.01, 113.13, 71.09, 70.23, 70.16, 69.91, 68.94, 68.58, 67.63, 67.57, 55.70, 52.37, 50.63, 27.80, 25.13. HR-MS (ESI): calcd for $[M - PF_6]^+$, $[C_{98}H_{102}N_3O_{11}]^+$, m/z = 1497.7543, found m/z = 1497.7546.

^{1}H NMR (600 MHz, acetone-d6) spectrum of **c[2]RT(cMCH1@G)**

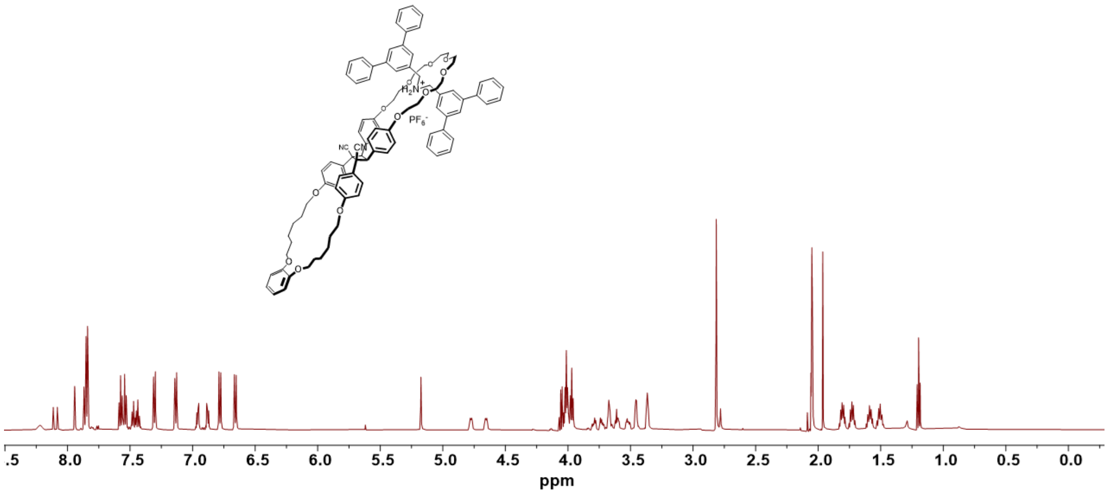

^{13}C NMR (100 MHz, acetone-d6) spectrum of **o[2]RT(oMCH1@G)**

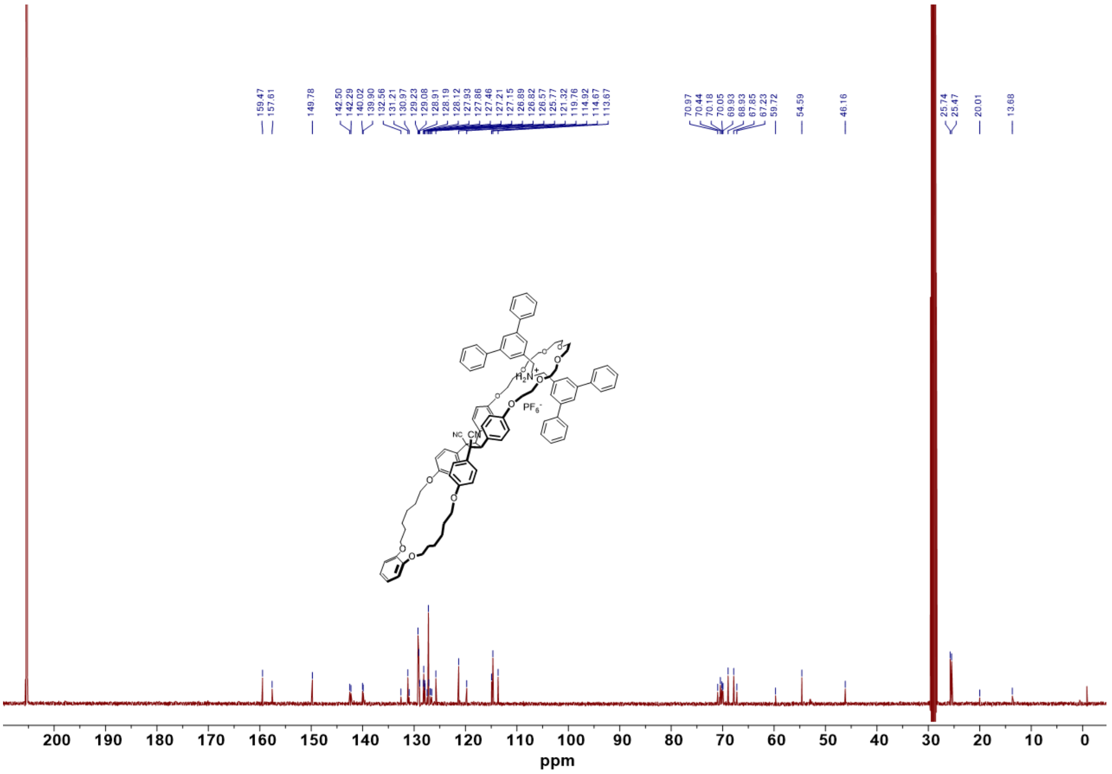

^{1}H NMR (500 MHz, acetone-d6) spectrum of **o[2]RT(cMCH1@G)**

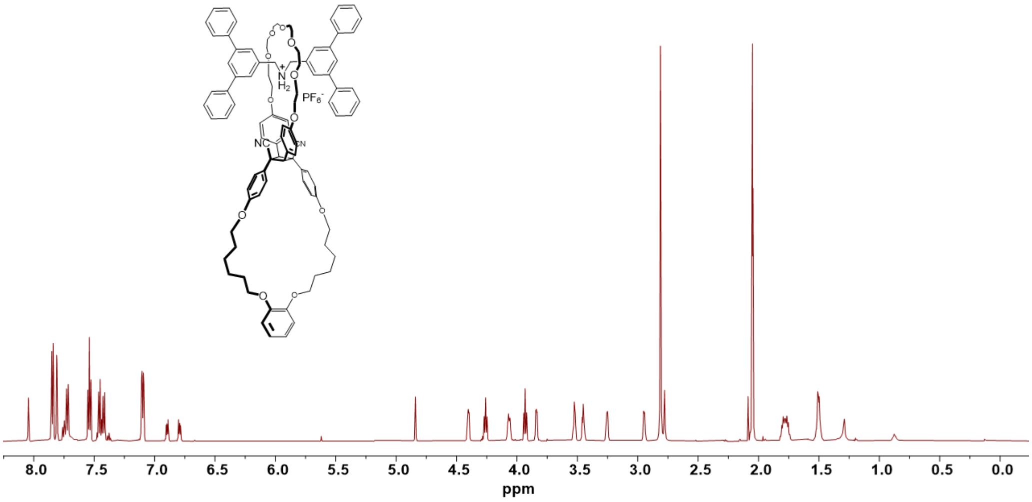

^{13}C NMR (100 MHz, acetone-d6) spectrum of **o[2]RT(oMCH1@G)**

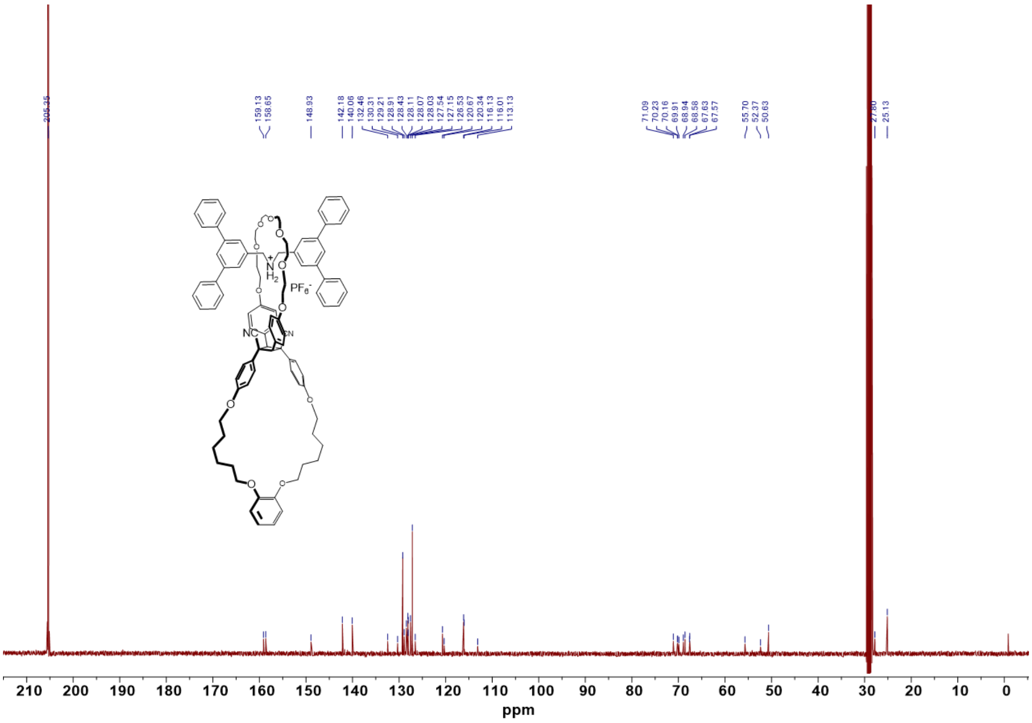

Synthesis of c[2]RT(cMCH2@G)

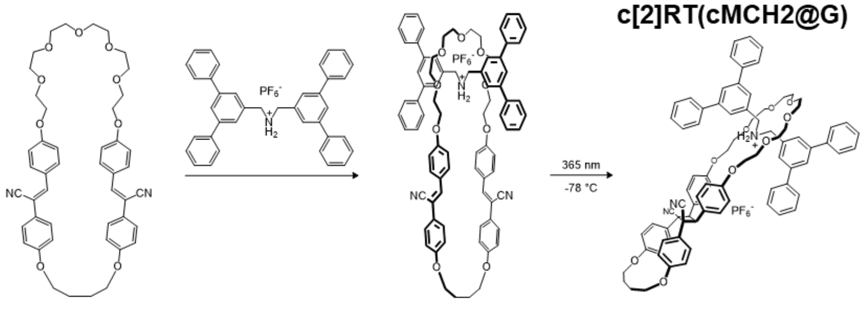

MCH2 (78 mg, 0.1 mmol, 50 mM) and **G** (195 mg, 0.3 mmol) were dissolved in acetone (2 mL) and degassed by bubbling with N_2. The solution was then cooled to -78 °C using a low temperature reactor and irradiated with 365 nm UV light overnight. After irradiation, the solution was removed under reduced pressure without heating directly. The resulting residue was purified by silica column chromatography (CH_2Cl_2/Ethyl acetate = 100/0 – 88/12, gradient elution). **c[2]RT(cMCH1@G)** was isolated as white solid (132 mg, 92%). ^{1}H NMR (600 MHz, ACETONE-D_6) δ 8.23 (br s, 2H), 8.08 (t, *J* = 1.7 Hz, 1H), 7.94 (d, *J* = 1.7 Hz, 2H), 7.87 (d, *J* = 1.7 Hz, 2H), 7.30 (dd, *J* = 8.8, 2.6 Hz, 2H), 7.86 – 7.82 (m, 8H), 7.61 – 7.51 (m, 8H), 7.49 – 7.39 (m, 4H), 7.30 (dd, *J* = 8.8, 2.6 Hz, 2H), 7.18 (dd, *J* = 8.7, 2.6 Hz, 2H), 7.15 (d, *J* = 8.8 Hz, 4H), 6.77 (dd, *J* = 8.7, 2.8 Hz, 2H), 6.71 (dd, *J* = 8.7, 2.7 Hz, 2H), 6.66 (d, *J* = 1.7 Hz, 4H), 5.20 (s, 2H), 4.76 – 4.80 (br, 2H), 4.67 – 4.63 (br, 2H), 4.27 (s, 4H), 3.96 – 4.05 (m, 4H), 3.80 –3.76 (br, 2H), 3.74 – 3.69 (br, 2H), 3.69 – 3.63 (m, 4H), 3.62 – 3.58 (br, 2H), 3.53 – 3.48 (br, 2H), 3.47 – 3.42 (m, 4H), 3.37 – 3.34 (m, 4H), 1.63 (br, 4H). ^{13}C NMR (126 MHz, ACETONE-D_6) δ 170.09, 157.23, 142.51, 142.29, 140.02, 139.90, 131.20, 130.69, 129.24, 128.15, 128.12, 127.93, 127.86, 127.56, 127.21, 126.82, 126.58, 125.59, 119.55, 117.29, 116.79, 113.70, 70.97, 70.44, 70.18, 70.05, 69.93, 67.24, 65.89, 59.71, 55.38, 53.06, 52.95, 44.61, 21.12, 13.67. HR-MS (ESI): calcd for $[M - PF_6]^+$, $[C_{84}H_{82}N_3O_9]^+$, m/z = 1276.6046, found m/z = 1276.5996.

^{1}H NMR (600 MHz, acetone-d6) spectrum of **c[2]RT(cMCH2@G)**

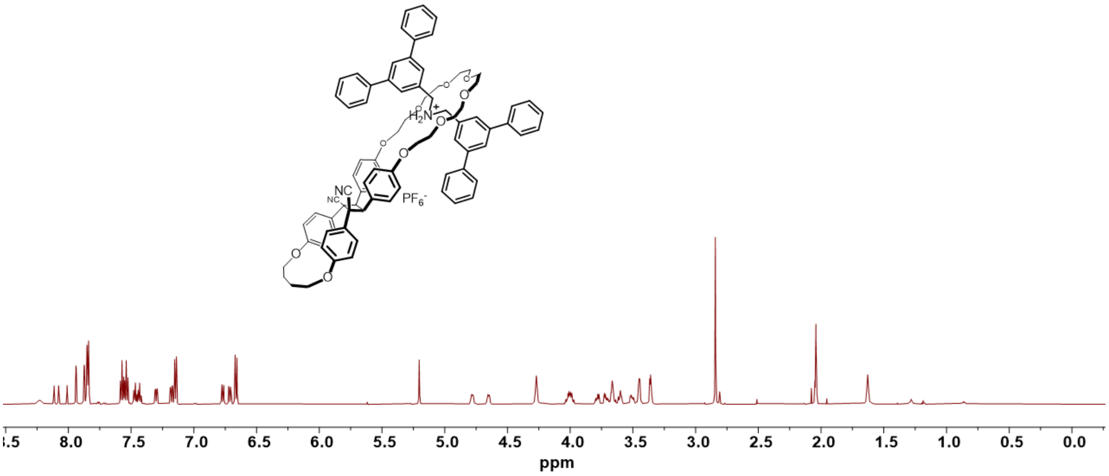

^{13}C NMR (125 MHz, acetone-d6) spectrum of **c[2]RT(cMCH2@G)**

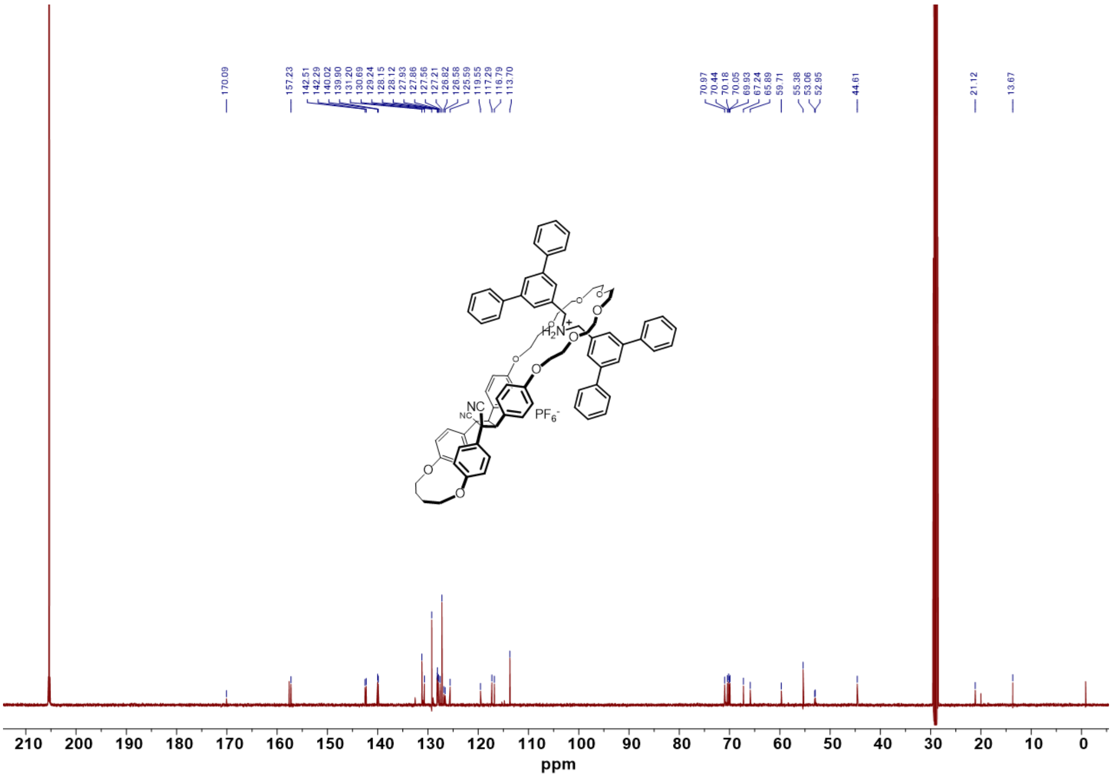

Synthesis of c[3]RT(cMCH3@G) and of o[3]RT(oMCH3@G)

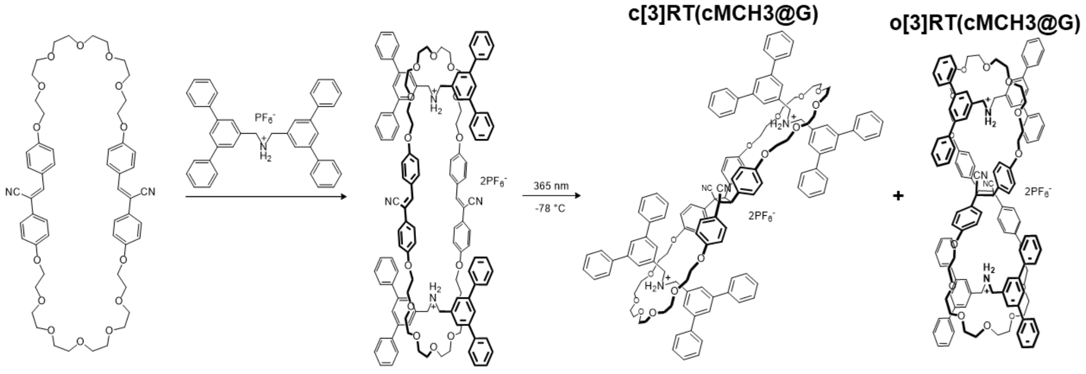

MCH1 (97 mg, 0.1 mmol, 50 mM) and **G** (227.4 mg, 0.35 mmol) were dissolved in acetone (2 mL) and degassed by bubbling with N_2. The solution was then cooled to -78 °C using a low temperature reactor and irradiated with 365 nm UV light for 3 days. After irradiation, the solution was removed under reduced pressure without heating directly. The resulting residue was purified by silica column chromatography (CH_2Cl_2/Ethyl acetate = 100/0 – 88/12, gradient elution). **c[3]RT(cMCH3@G)** and **o[3]RT(oMCH3@G)** were isolated as white solid (**c[3]RT(cMCH3@G)**: 156 mg, 69%; **o[2]RT(oMCH1@G)**: 5.3 mg, 2.3%; Mixture: 19.7 mg, 8.7%; In total: 80%).

Note: Partial overlap of ***c[3]RT(cMCH3@G)*** *and* ***o[3]RT(oMCH3@G)*** *during column elution led to little loss in yield of pure compounds.*

c[3]RT(cMCH3@G): ^{1}H NMR (600 MHz, ACETONE-*D*$_6$) δ 8.19 (br s, 2H), 8.15 – 8.06 (m, 4H), 7.95 – 7.82 (m, 24H), 7.61 – 7.52 (m, 16H), 7.50 – 7.45 (m, 4H), 7.45 – 7.40 (m, 4H), 7.14 (d, *J* = 8.9 Hz, 1H), 7.07 (d, *J* = 8.8 Hz, 1H), 6.64 (d, *J* = 8.8 Hz, 1H), 6.55 (d, *J* = 8.9 Hz, 1H), 5.02 (s, 2H), 4.78 – 4.74 (br, 2H), 4.66 – 4.62 (br, 2H), 4.60 – 4.57 (br, 2H), 4.05 – 3.97 (m, 8H), 3.91 – 3.87 (m, 4H), 3.80 – 3.72 (m, 8H), 3.69 – 3.58 (m, 12H), 3.54 – 3.42 (m, 10H), 3.37 – 3.33 (m, 4H), 3.31 – 3.27 (m, 4H). ^{13}C NMR (101 MHz, ACETONE-*D*$_6$) δ 158.77, 157.65, 142.50, 142.42, 142.30, 142.27, 140.03, 140.01, 139.89, 132.55, 131.12, 129.26, 129.23, 129.11, 128.24, 128.19, 128.17, 128.11, 127.96, 127.93, 127.59, 127.25, 127.22, 127.20, 126.82, 126.56, 126.53, 119.56, 114.43, 113.67, 70.96, 70.82, 70.54, 70.50, 70.41, 70.17, 70.05, 69.94, 67.65, 67.23, 59.72, 54.12, 46.55, 20.01, 13.67. HR-MS (ESI): calcd for $[M - 2PF_6]^+$, $[C_{130}H_{130}N_4O_{14}]^{2+}$, m/z = 985.9803, found m/z = 985.9810.

o[3]RT(oMCH3@G): ^{1}H NMR (600 MHz, ACETONE-D_6) δ 8.33 (br s, 2H), 8.04 – 8.00 (m, 4H), 7.83 (m, 8H), 7.80 (m, 8H), 7.76 (m, 8H), 7.53 (m, 8H), 7.45 (m, 16H), 7.33 (d, *J* = 8.4 Hz, 4H), 7.30 (d, *J* = 8.6 Hz, 4H), 7.06 (d, *J* = 8.7 Hz, 4H), 6.99 (d, *J* = 8.6 Hz, 4H), 4.61 – 4.56 (br, 4H), 4.40 – 4.37 (br, 4H), 4.31 (s, 2H), 4.21 – 4.18 (m, 4H), 4.08 – 4.04 (br, 4H), 3.88 – 3.85 (m, 4H), 3.85 – 3.81 (m, 4H), 3.76 (m, 4H), 3.64 (m, 4H), 3.53 (t, *J* = 5.3 Hz, 4H), 3.45 (m, 8H), 3.26 (m, 4H), 3.22 (m, 4H), 2.98 (m, 4H). HR-MS (ESI): calcd for $[M - 2PF_6]^+$, $[C_{130}H_{130}N_4O_{14}]^+$, m/z = 985.9803, found m/z = 985.9805.

^{1}H NMR (600 MHz, acetone-d6) spectrum of **c[3]RT(cMCH3@G)**

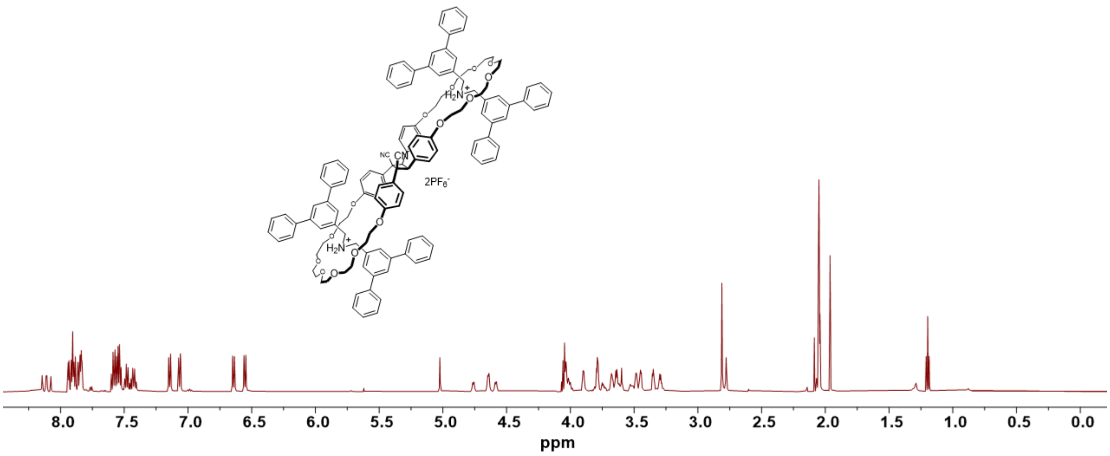

^{1}H NMR (100 MHz, acetone-d6) spectrum of **c[3]RT(cMCH3@G)**

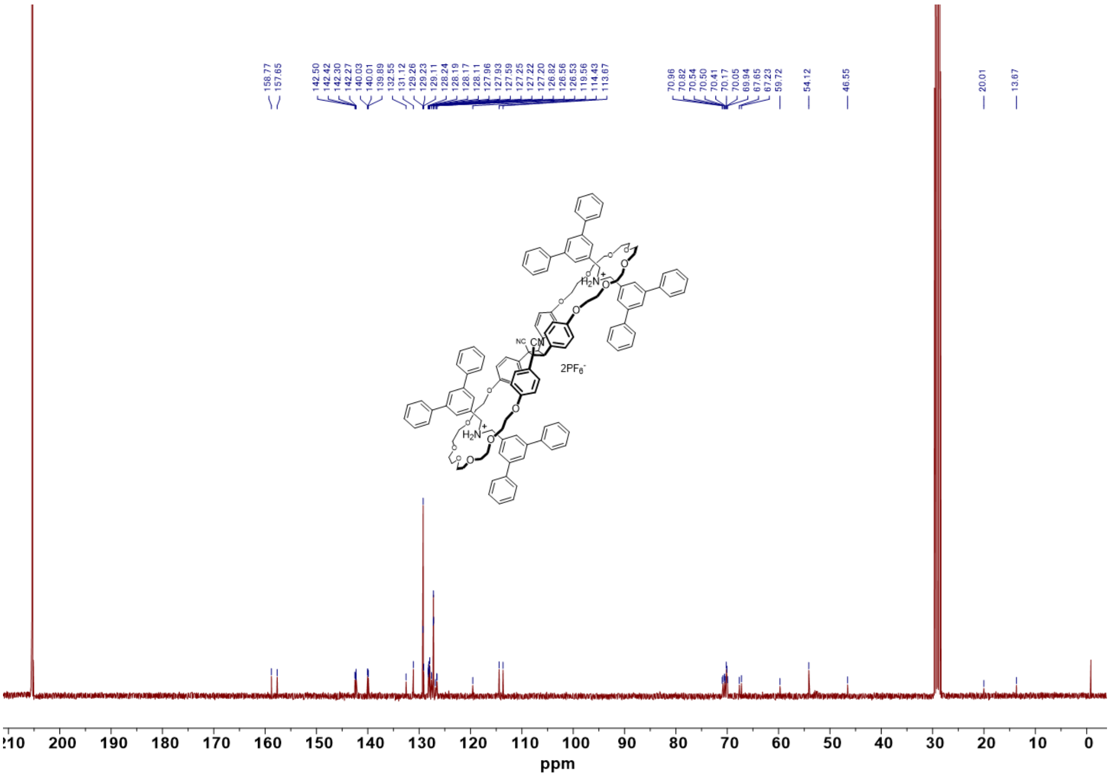

^{1}H NMR (600 MHz, acetone-d6) spectrum of **c[3]RT(oMCH3@G)**

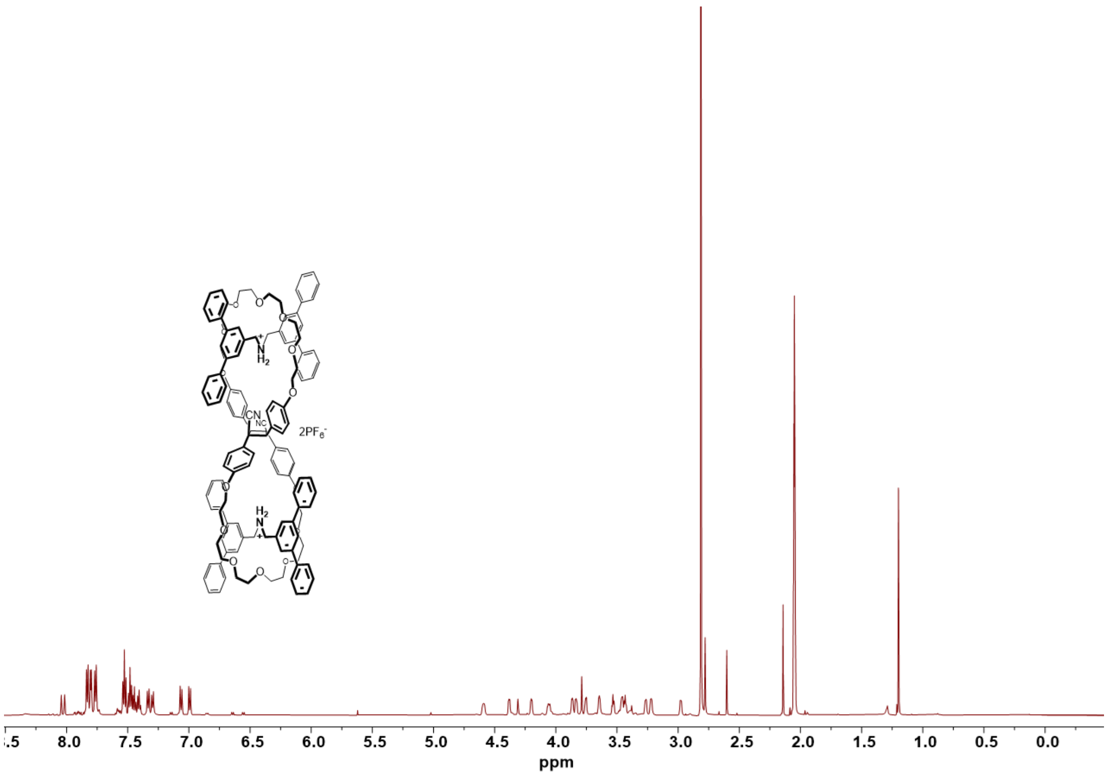

^{1}H NMR (100 MHz, acetone-d6) spectrum of **o[3]RT(oMCH3@G)**

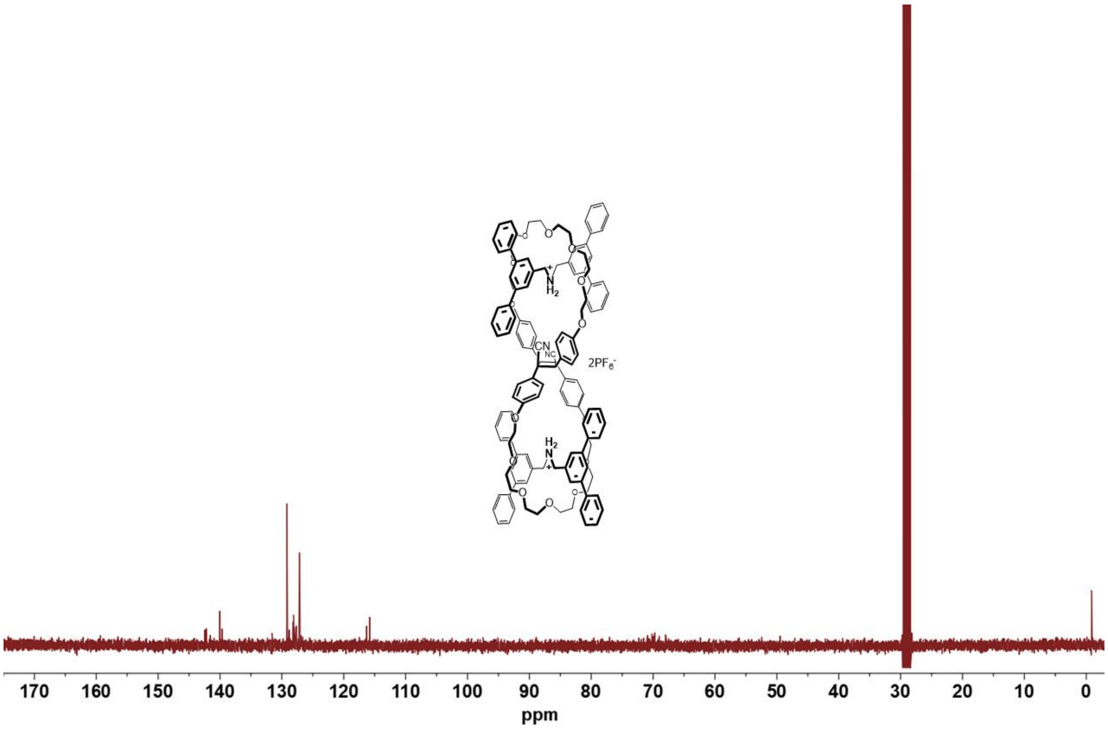

3-2 Results and discussion

3-2-1 Reversible topology transformation between macrocycles and figure-eight ring structures

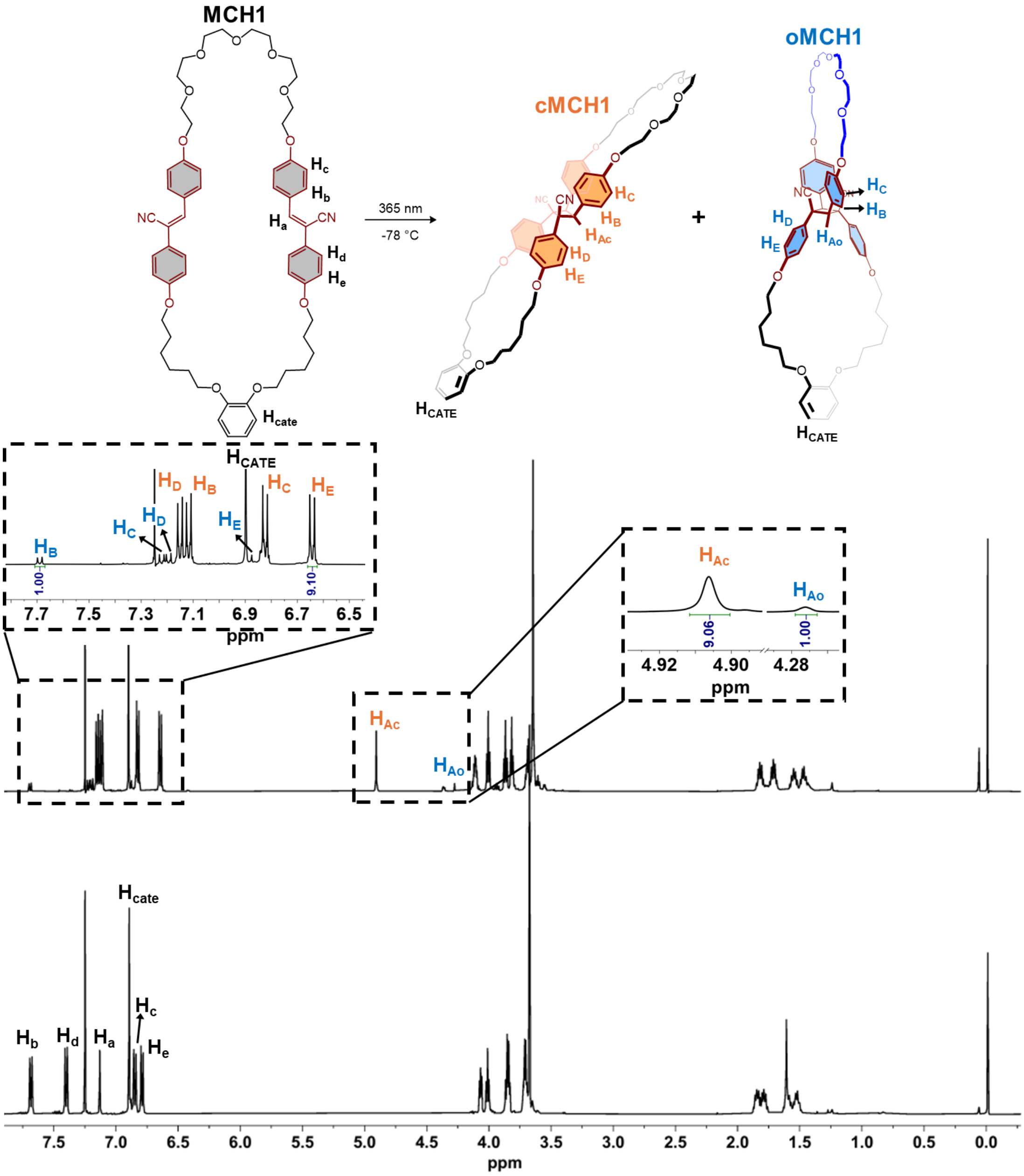

Figure 3-2. Photoisomerization and intramolecular [2+2] photocycloaddition of **MCH1**. ^{1}H NMR spectrum of **MCH1** (bottom) and **MCH1** after irradiation by 365 nm UV light at -78 °C overnight (above); 298 K, $CHCl_3$-d.

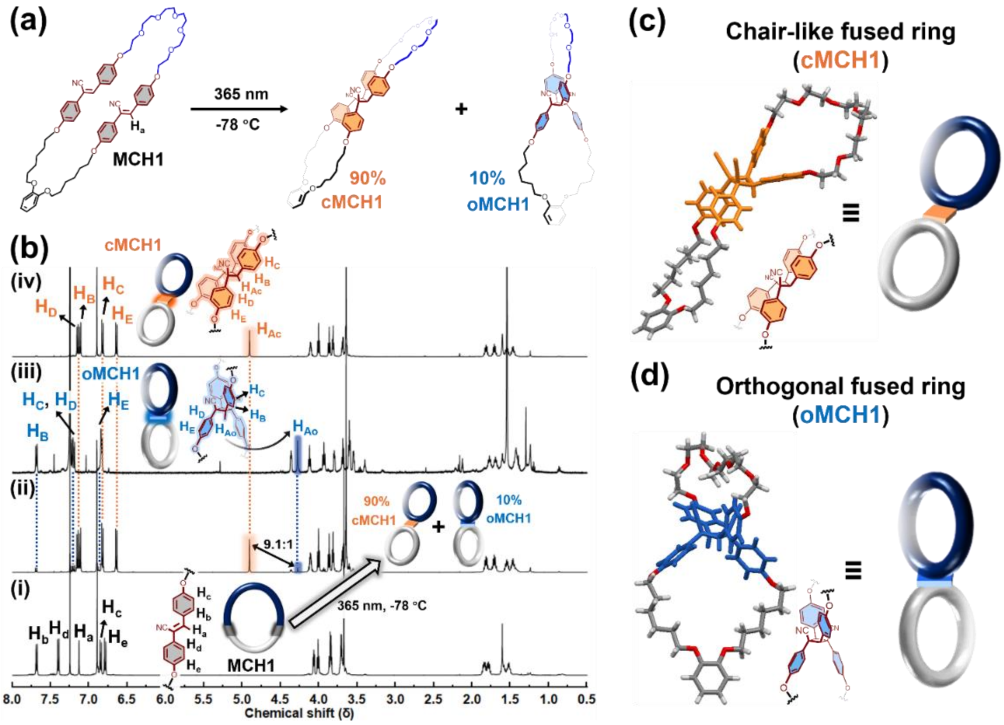

Figure 3-3. Topology transformation of **MCH1** from a regular macrocyclic structure to a figure-eight fused ring: (a) Photo-induced topology transformation of **MCH1**. (b) ^{1}H NMR spectra of **MCH1** (i), mixture after irradiating **MCH1** (ii), isolated **oMCH1** (iii) and isolated **cMCH1** (iv). The structures of (c) **cMCH1** and (d) **oMCH1** determined by single-crystal X-ray diffraction.

Three macrocycles (**MCHn**, **n = 1-3**) were synthesized, each incorporating the same hexaethylene glycol as the crown ether fragment and cyano-stilbene moiety as the switch for topology transformation, but differing in the structure of the other half of the ring (Scheme 3-2). In **MCH1**, the macrocycle transforms to the two smaller rings fused via cyano-substituted cyclobutene (Figures 3-2, 3-3a, and 3-3b). The topology transformation from **MCH1** to the figure-eight fused ring structures proceeds quantitatively without any side products. Notably, two distinct fused-ring products were obtained: **cMCH1** as the major product and **oMCH1** as the minor product, with a diastereomeric ratio (d.r.) of 9.1, determined by ^{1}H NMR integration (Figures 3-2). **cMCH1** and **oMCH1** were both isolated via chromatography. Single crystal X-ray diffraction analysis revealed these two fused-ring products exhibit completely different topologies: in **cMCH1**, the two small rings adopt a chair-like geometry, whereas in **oMCH1**, they are arranged in an orthogonal manner (Figures 3-3c, and 3-3d). This isomerism of products is attributed to the different arrangement of two cyano-stilbene moieties in **MCH1** during photoreaction. The parallel head-to-head arrangement of two cyano-stilbene moieties leads to the formation of a chair-like fused-ring after [2+2] photocycloaddition, while the antiparallel head-to-tail arrangement leads to the formation of an orthogonal fused-ring (Scheme 3-9). The ^{1}H NMR spectrum of **MCH1** shows single set of proton signals of cyano-stilbene moiety, indicating the exchange of their arrangement in solution is transient on the NMR time scale (Figure 3-2). Therefore, the distribution of products may arise from the differences in the efficiency of the [2+2] photocycloaddition of the two cyano-stilbene moieties in the different arrangements. The detailed structure analysis and assignment of proton signals are shown as figures 3-4 to 3-7 (^{1}H NMR and COSY spectra).

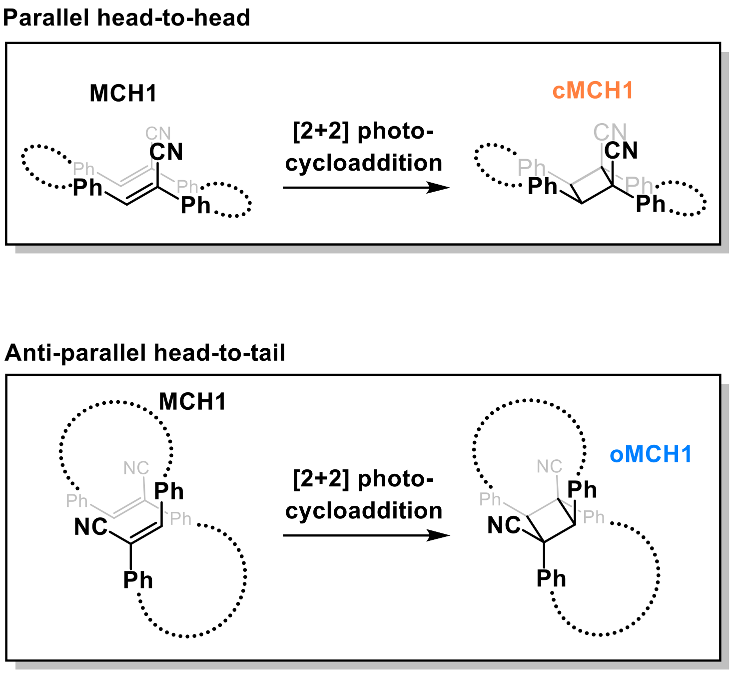

Scheme 3-9. intramolecular [2+2] photocycloaddition of cyano-stilbene in a parallel head-to-head arrangement affords **cMCH1** (above) and intramolecular [2+2] photocycloaddition of cyano-stilbene in an anti-parallel head-to-tail arrangement affords **oMCH1** (bottom).

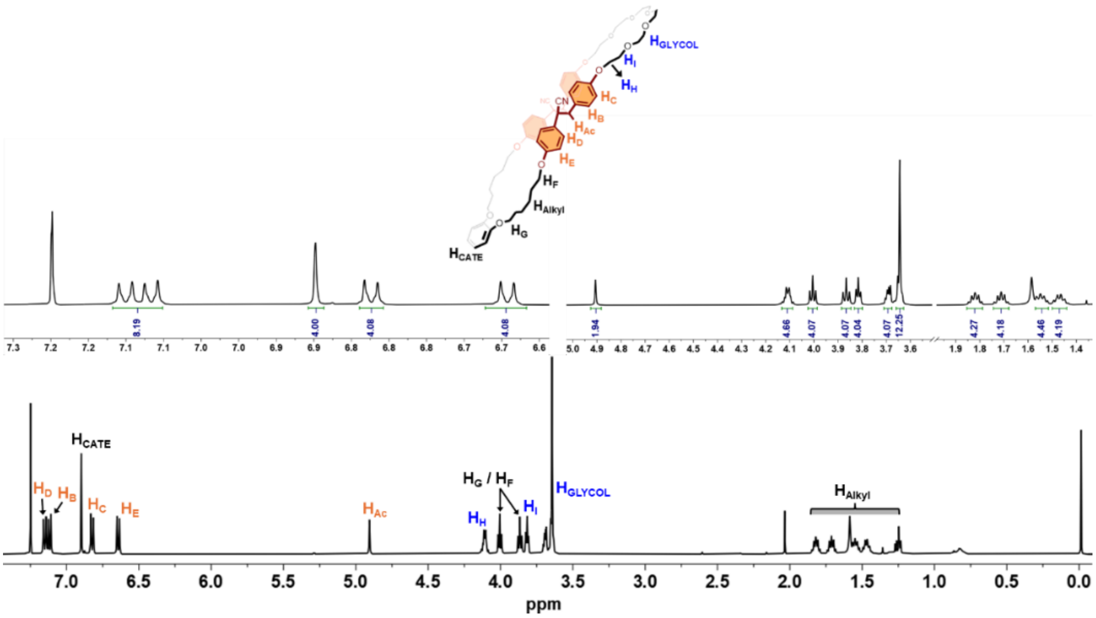

Figure 3-4. ^{1}H NMR spectrum of **cMCH1**; 298 K, $CHCl_3$-d.

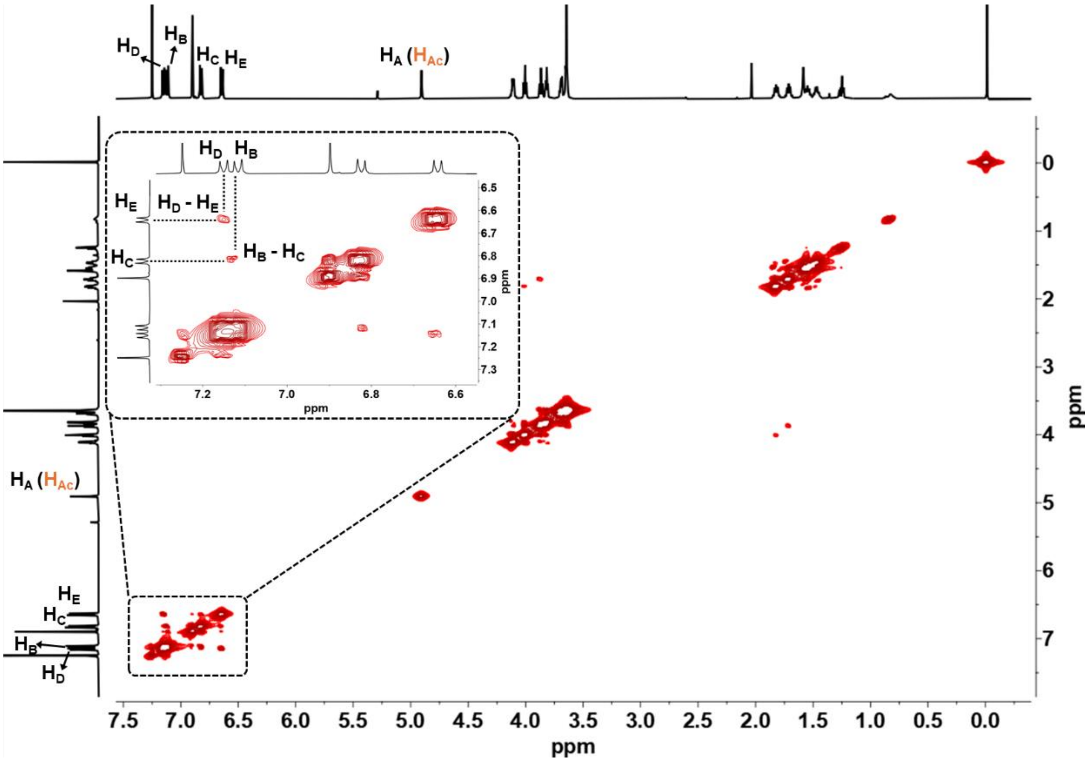

Figure 3-5. COSY spectrum of **cMCH1**; 298 K, CHCl$_3$-d.

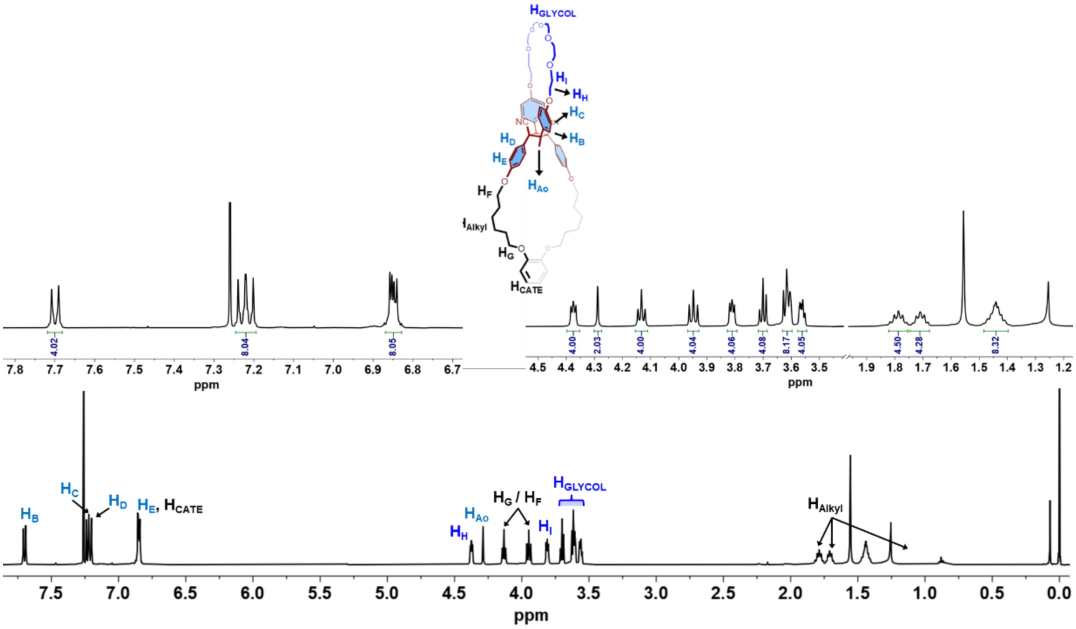

Figure 3-6. ^{1}H NMR spectrum of **oMCH1**; 298 K, CHCl$_3$-d.

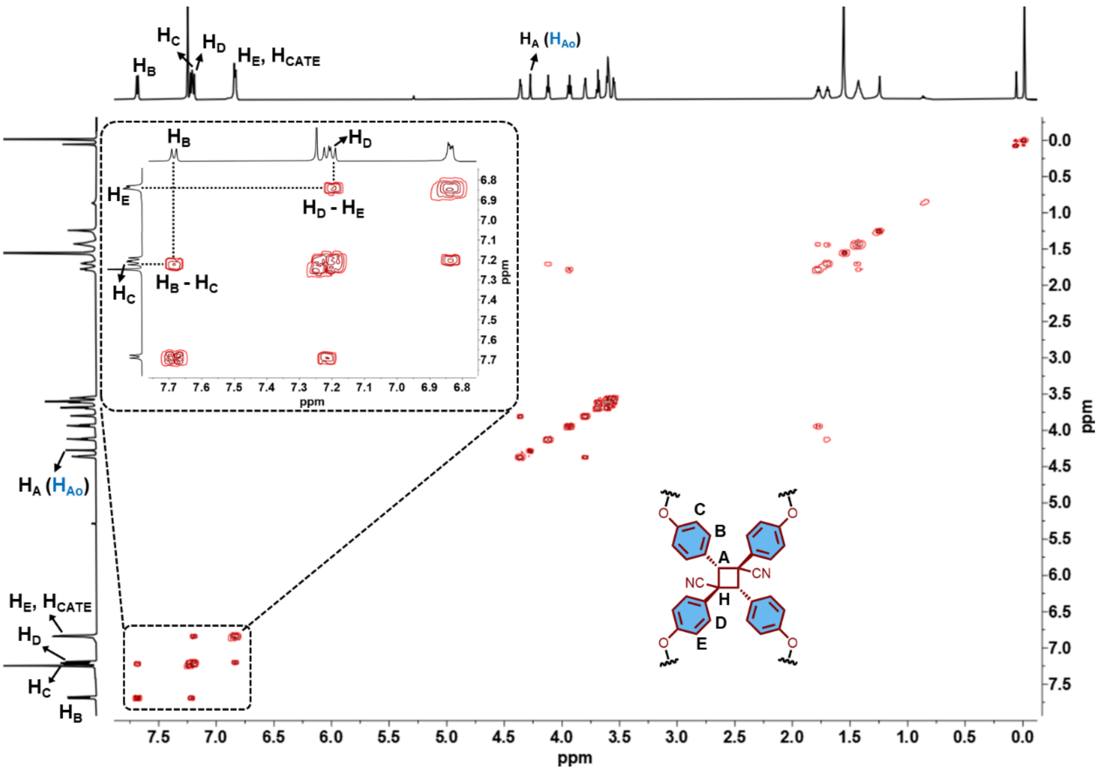

Figure 3-7. COSY spectrum of **oMCH1**; 298 K, $CHCl_3$-d.

For **MCH2**, topology transformation resulted in no orthogonal fused-ring compound and 100% conversion to the chair-like fused-ring as the only product (Figure 3-8). This exclusive product distribution is due to the small ring-size of **MCH2**. In other words, the four-carbon-atoms alkyl chain is too short to allow the two cyano-stilbene moieties to arrange in an antiparallel heat-to-tail manner, preventing the formation of the orthogonal fused-ring structure via [2+2] photocycloaddition. The detailed structure analysis and assignment of proton signals are shown as figures 3-9 and 3-10 (^1H NMR and COSY spectra).

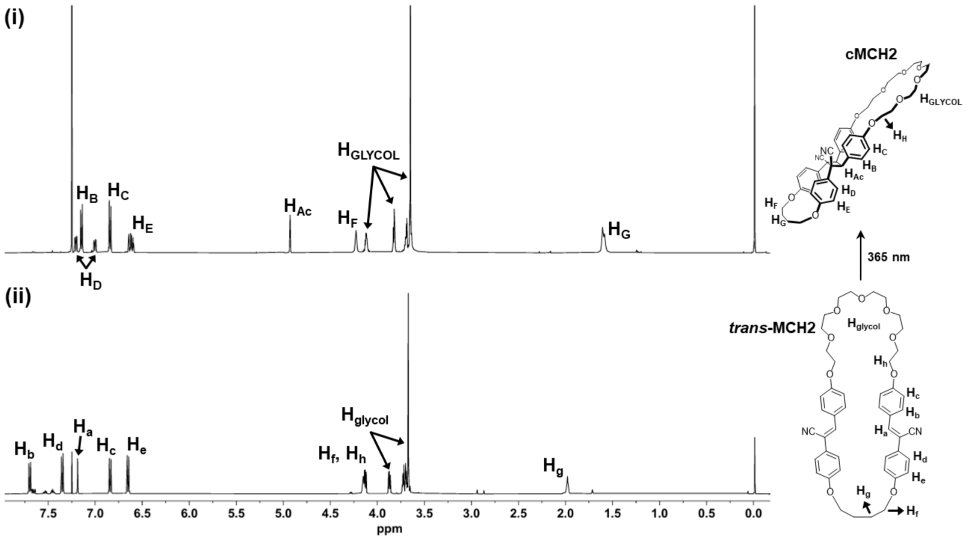

Figure 3-8. ^{1}H NMR spectra of **MCH2** (i) and **MCH2** after irradiation by 365 nm UV light at -78 °C overnight (ii); 298 K, CHCl$_3$-d.

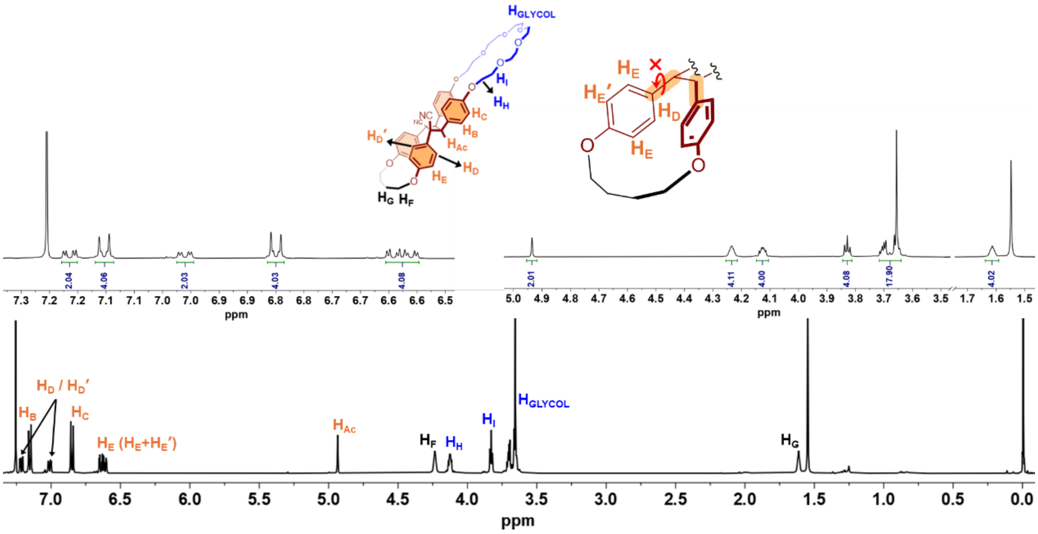

Figure 3-9. ^{1}H NMR spectrum of **cMCH2**; 298 K, CHCl$_3$-d.

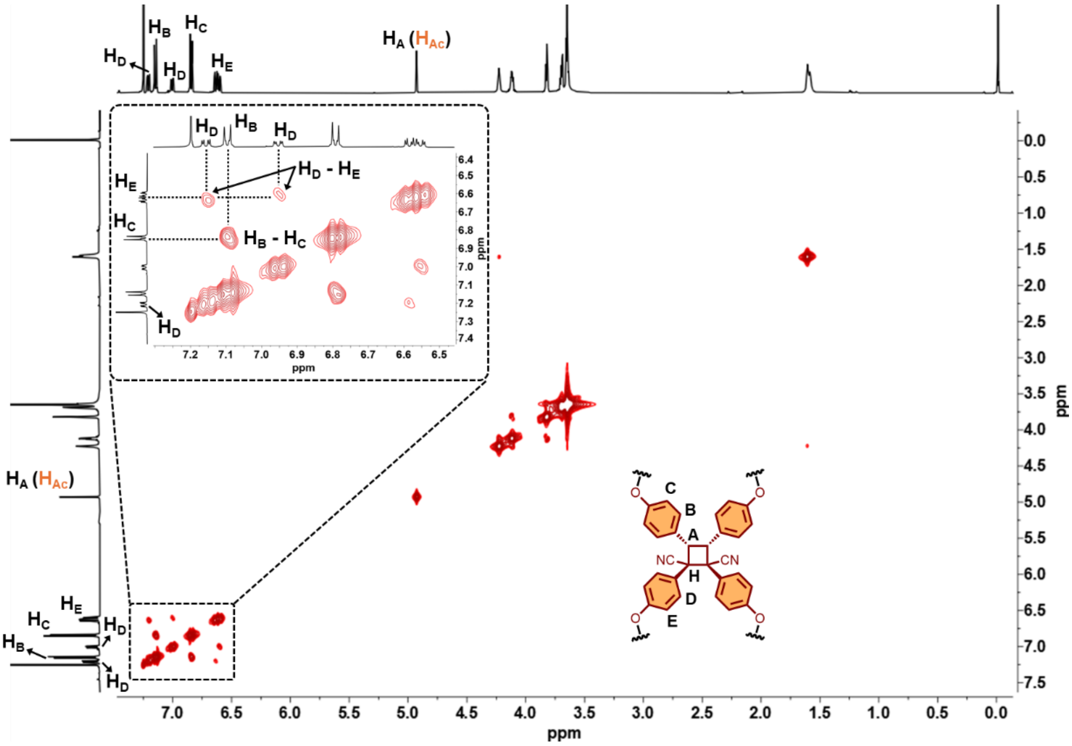

Figure 3-10. COSY spectrum of **cMCH2**; 500 MHz, 298 K, CHCl3-d.

In contrast to **MCH1** and **MCH2**, another half of the ring structure in **MCH3** is hexaethylene glycol rather than the alkyl chains, providing highest flexibility to the macrocycle framework to allow an easier arrangement of the two cyano-stilbene moieties in an antiparallel heat-to-tail manner. As a result, the topology transformation of **MCH3** produced more orthogonal fused-ring product, with a d.r. of 5.0 (Figure 3-11). The detailed structure analysis and assignment of proton signals are shown as figures 3-12 to 3-15 (^{1}H NMR and COSY spectra).

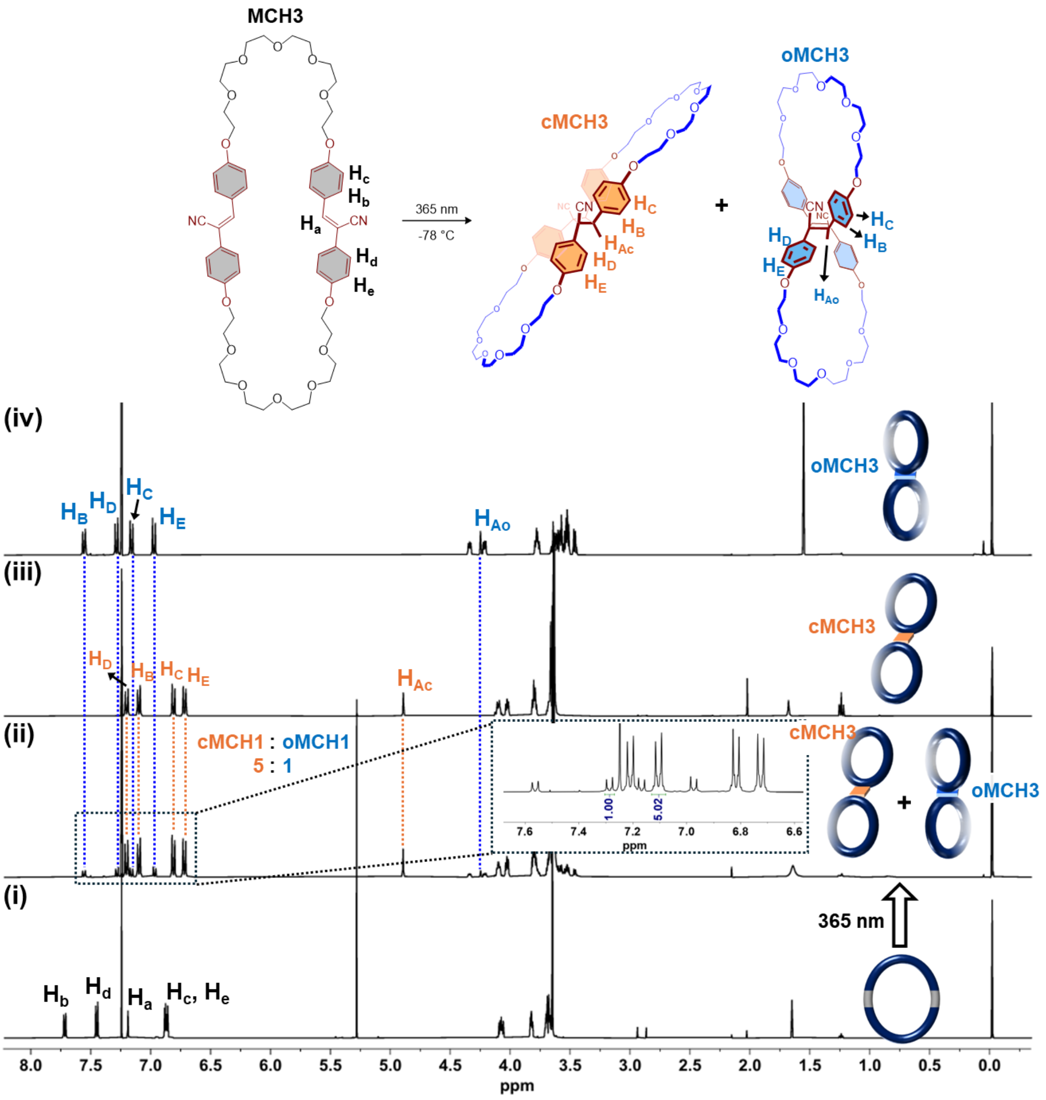

Figure 3-11. ^{1}H NMR spectra of **MCH3** (i), **MCH3** after irradiation by 365 nm UV light at -78 °C overnight (ii), isolated **cMCH3** (iii) and isolated **oMCH3** (iv); 298 K, $CHCl_3$-d.

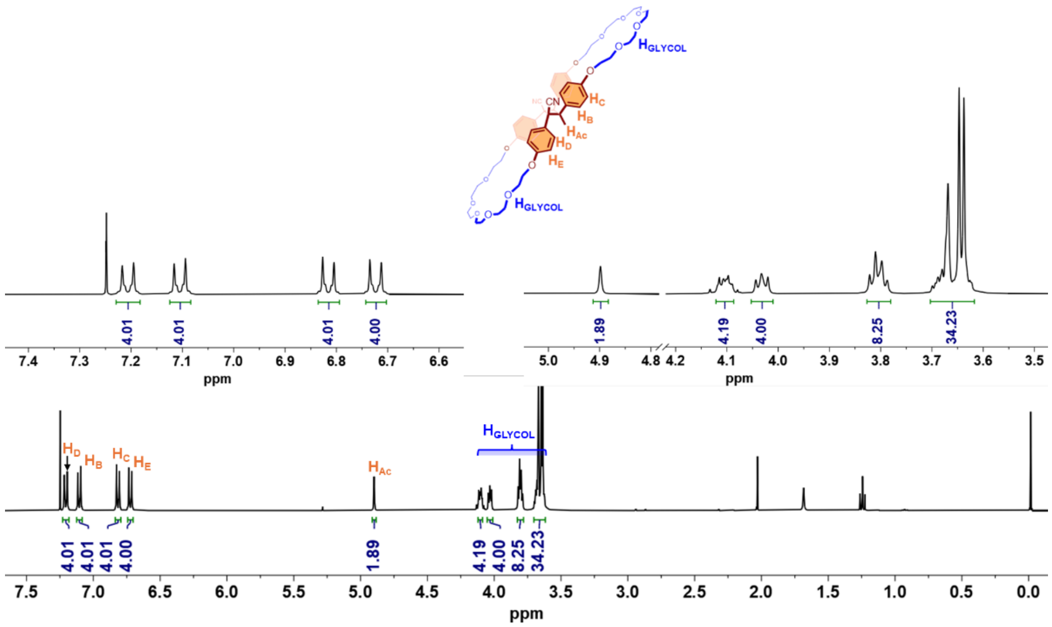

Figure 3-12. ^{1}H NMR spectrum of **cMCH3**; 298 K, $CHCl_3$-d.

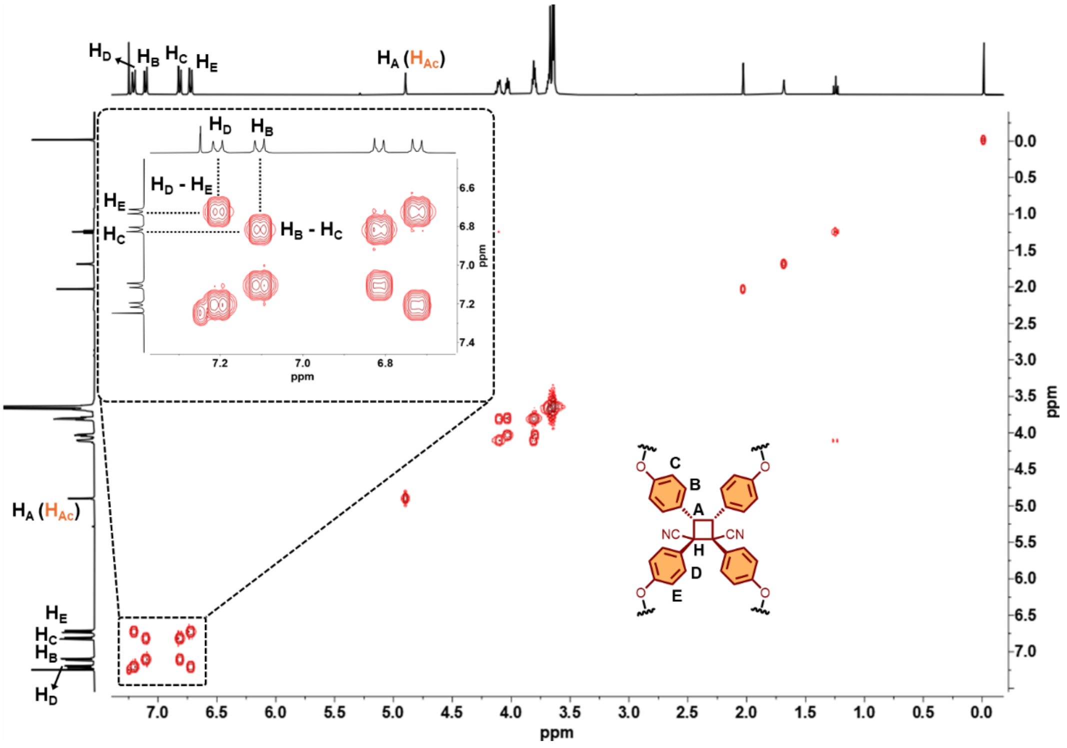

Figure 3-13. COSY spectrum of **cMCH3**; 298 K, $CHCl_3$-d.

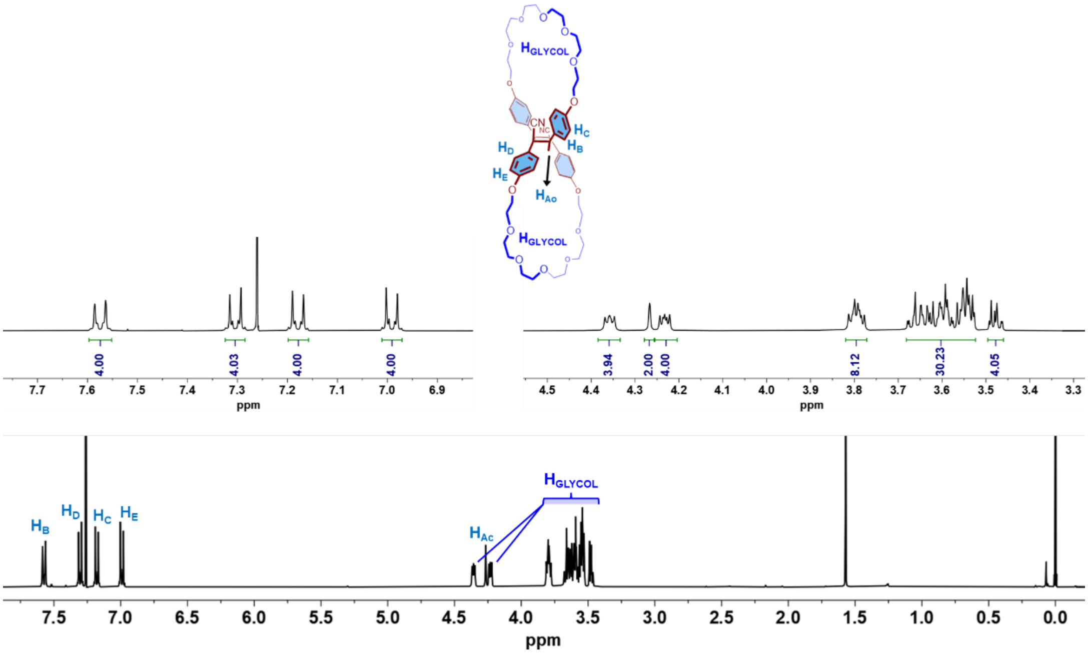

Figure 3-14. ^{1}H NMR spectrum of **oMCH3**; 298 K, $CHCl_3$-d.

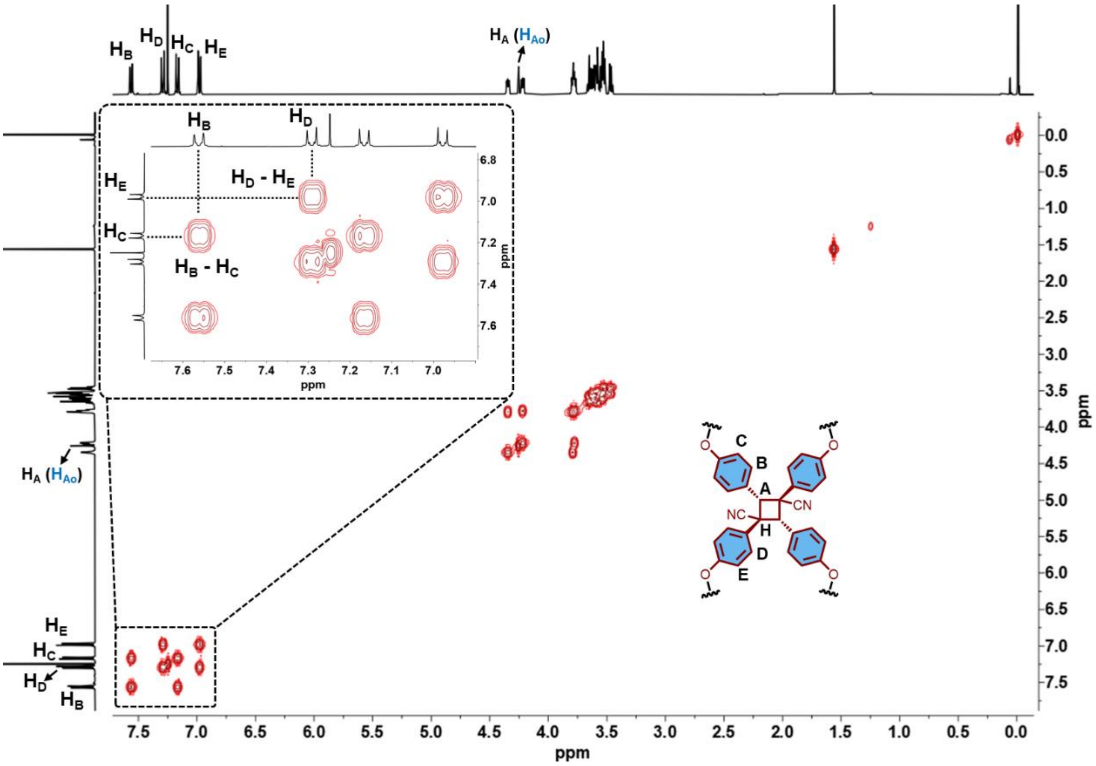

Figure 3-15. COSY spectrum of **oMCH3**

Additionally, all chair-like fused-ring products (**cMCH1**, **2**, and **3**) exhibit topological reversibility upon heating, quantitatively converting back to their corresponding macrocycles (**MCH1**, **2**, and **3**). According to the ^{1}H NMR spectra recorded at different heating time, the intensity of the cyclobutane proton signals decreased when a chloroform solution of **cMCH1–3** was heated at 80 °C under a nitrogen atmosphere (Figures 3-16, 3-17 and 3-18). Concurrently, signals corresponding to the cyano-stilbene moieties reappeared, indicating a topology transformation from a chair-like figure-eight structure to a regular macrocyclic structure. Among the three compounds, **cMCH1** showed the fastest transformation rate, suggesting that its cyclobutane unit is the most thermally labile. **cMCH3** converted slightly more slowly than **cMCH1**, while **cMCH2** transformed much more slowly than both.

In contrast, both orthogonally fused-ring compounds (**oMCH1** and **oMCH3**) retained their structural integrity, showing no cyclobutane cleavage under heating at 80 °C (Figures 3-19 and 3-20).

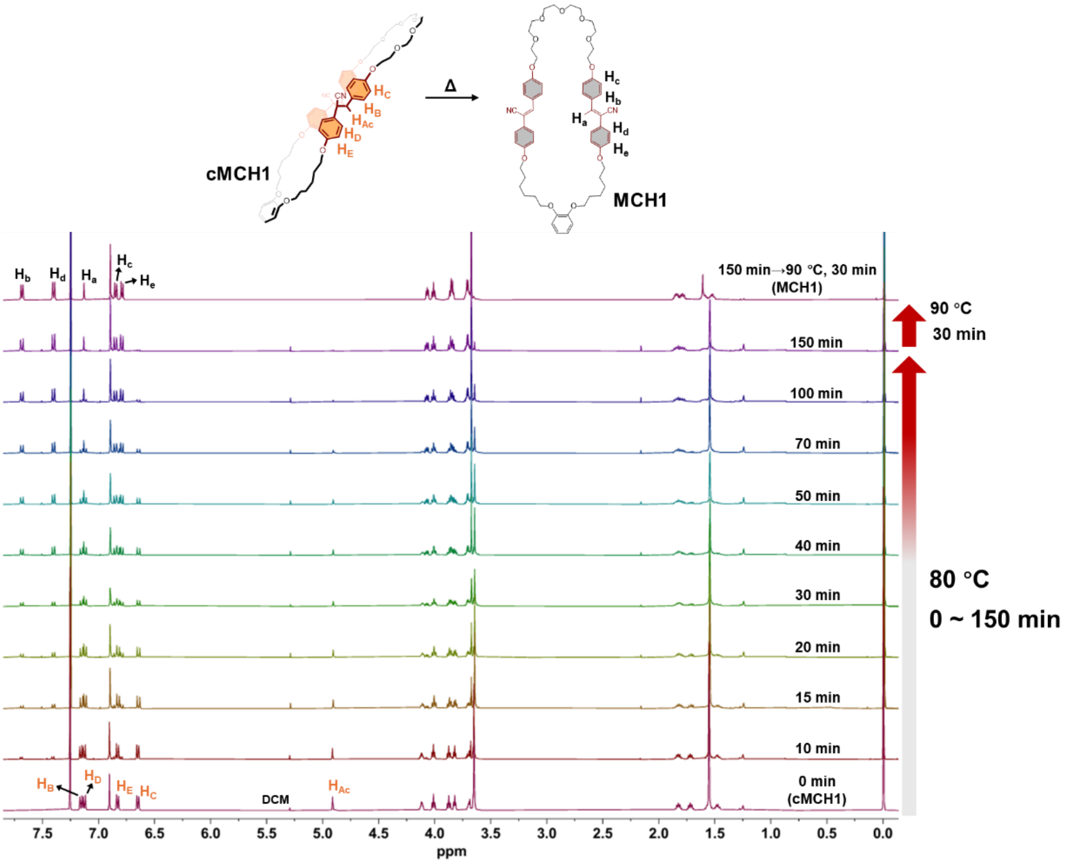

Figure 3-16. ^{1}H NMR spectra of sealed $CHCl_3$ solution of **cMCH1** after heating in oil bath at 80 °C for 150 minutes, followed by heating in oil bath at 90 °C for 30 minutes in the solid state; 298 K, $CHCl_3$-d.

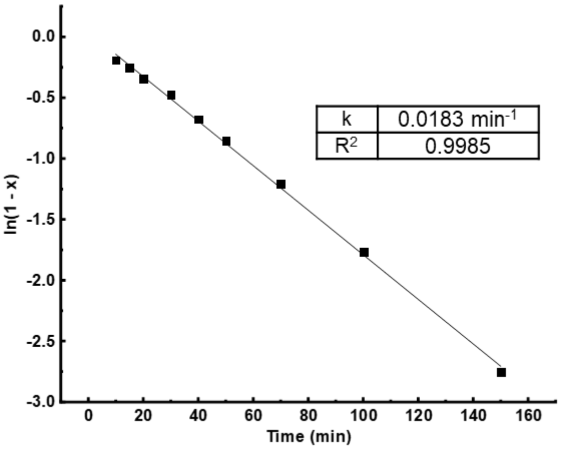

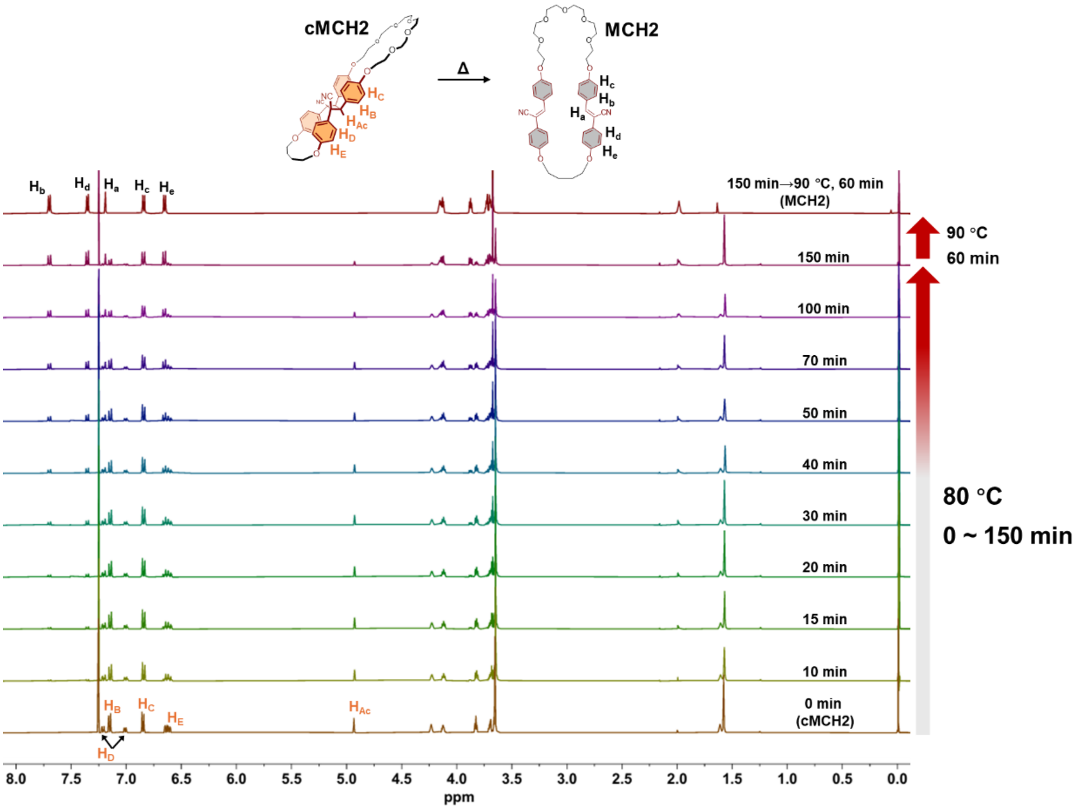

Figure 3-17. ^{1}H NMR spectra of sealed $CHCl_3$ solution of **cMCH2** after heating in oil bath at 80 °C for 150 minutes, followed by heating at 90 °C for 60 minutes in the solid state; 298 K, $CHCl_3$-d.

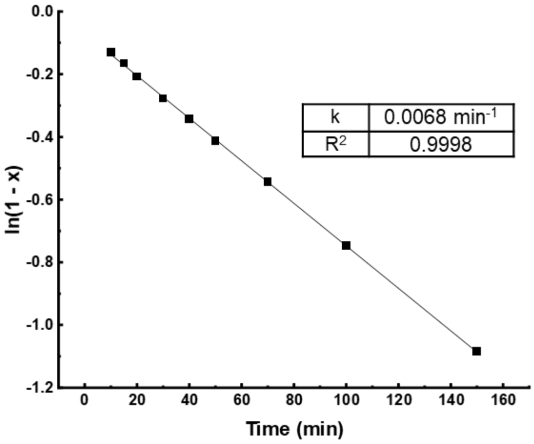

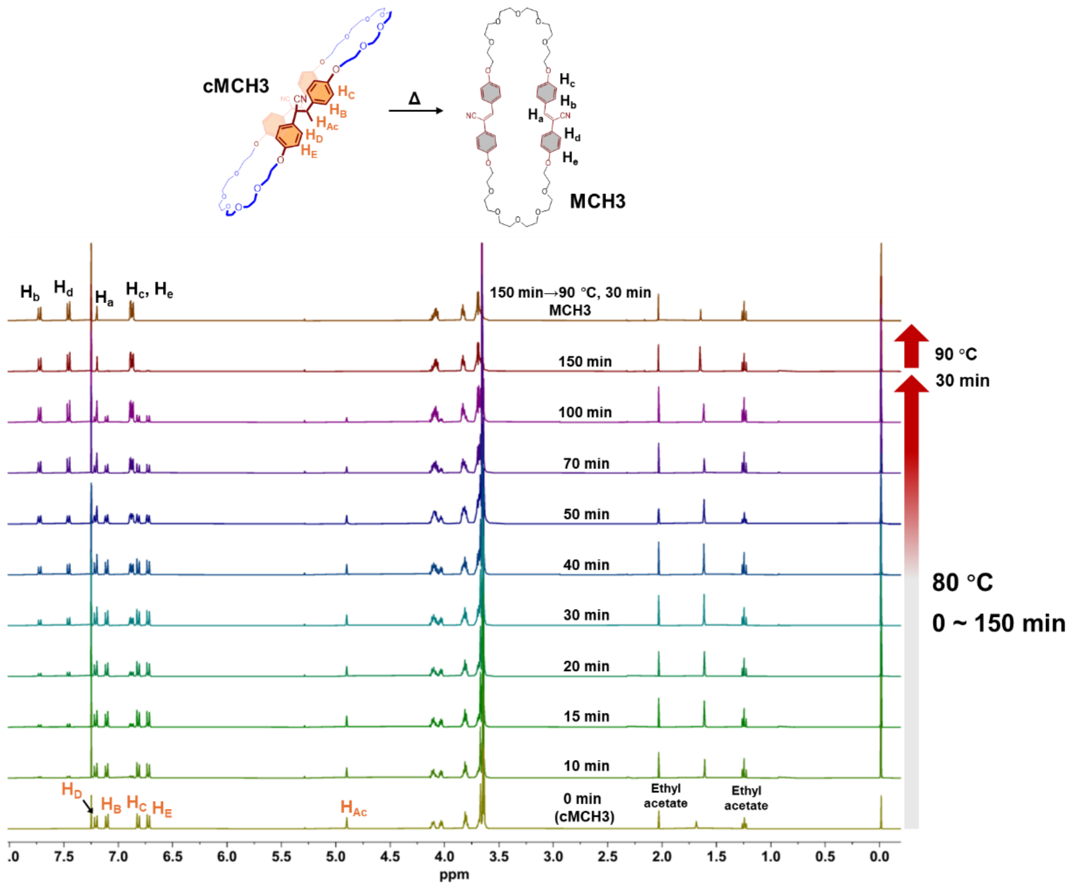

Figure 3-18. ^{1}H NMR spectra of sealed CHCl$_3$ solution of **cMCH3** after heating in oil bath at 80 °C for 150 minutes, followed by heating at 90 °C for 30 minutes in the solid state; 298 K, CHCl$_3$-d.

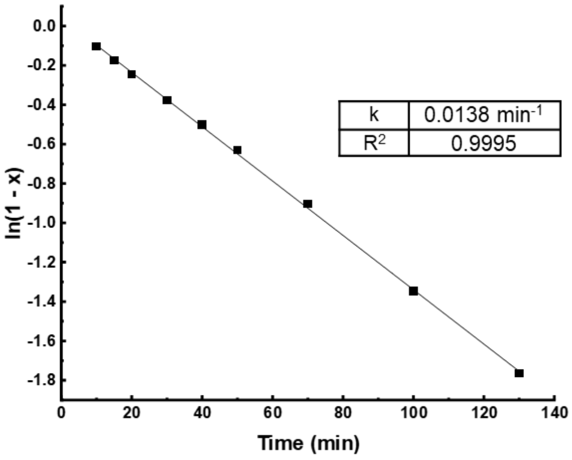

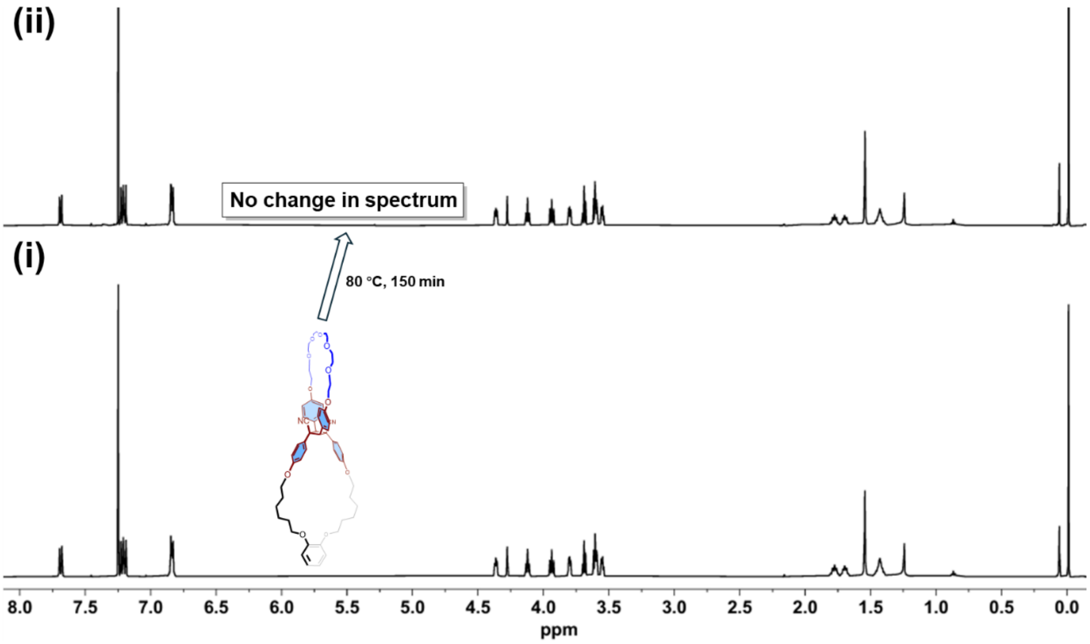

Figure 3-19. ^{1}H NMR spectra of **oMCH1** (i) and sealed CHCl$_3$ solution of **oMCH1** after heating in oil bath at 80 °C for 150 minutes (ii); 298 K, CHCl$_3$-d.

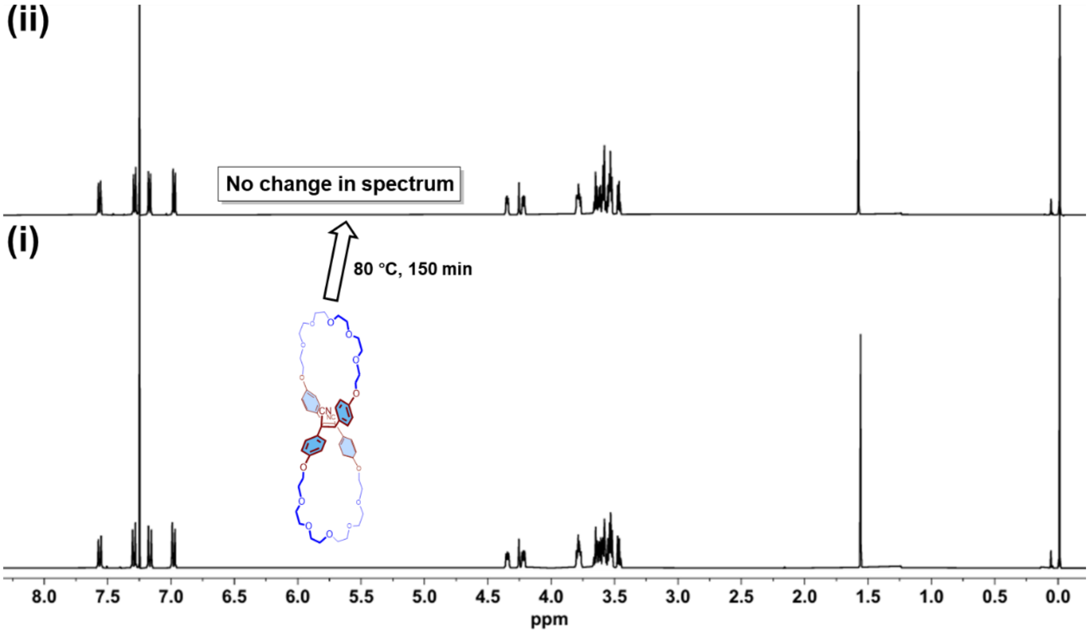

Figure 3-20. ^{1}H NMR spectra of **oMCH3** (i) and sealed CHCl$_3$ solution of **oMCH3** after heating at oil bath at 80 °C for 150 minutes (ii); 298 K, CHCl$_3$-d.

3-2-2 Rotaxanation via topology transformation from macrocycles to figure-eight ring structures

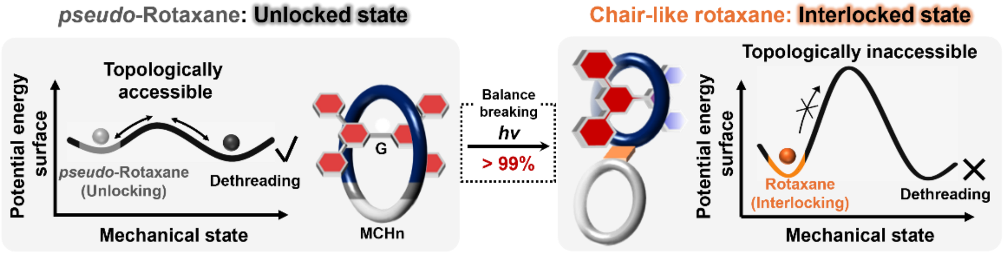

Scheme 3-10. Rotaxanation via the topology transformation between non-homeomorphic structures.

Subsequently, compound **G**, bearing a quaternary ammonium salt, was employed as the axle molecule to form complexes with each macrocycle in solution. Upon simple dissolution of **G** and the macrocycle in acetone, followed by UV irradiation at –78 °C, efficient rotaxanation occurred. It is important to note that although the formation of the mechanical bond between the wheel and axle directly arises from a decrease in ring size, this confinement is fundamentally driven by a topology transformation between non-homeomorphic structures (Scheme 3-10). During rotaxanation, the topology transformation breaks the balance in initial system (*pseudo*-rotaxane), accompanied by a restructuring of the potential energy surface into that of the rotaxane system. Consequently, a thermally inaccessible energy barrier is created, preventing dethreading and achieving the formation of rotaxanes. Additionally, as discussed above, the resulting chair-like figure-eight structure is topologically reversible, reverting to macrocyclic structure upon heating. This reverse transformation restores the potential energy surface to that of the *pseudo*-rotaxane system, thereby enabling reversible mechanical unlocking and allowing subsequent dynamic dethreading (vide infra).

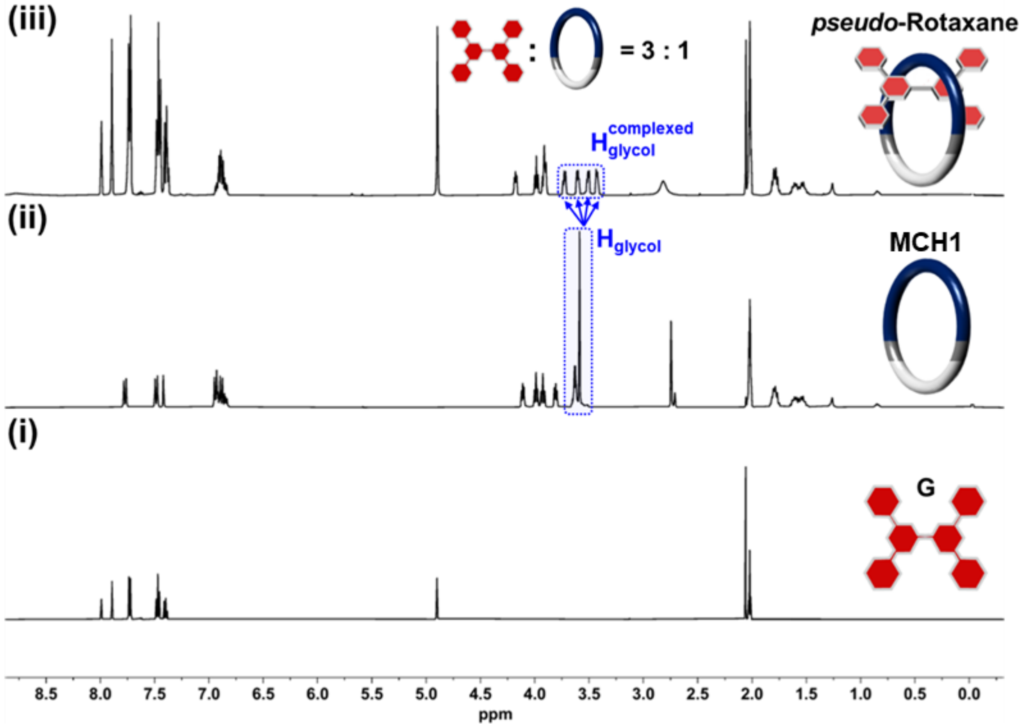

Figure 3-21. ^{1}H NMR spectra of **G** (i), **MCH1** (ii), and mixture of **G** and **MCH1** in a ratio of 3:1 (iii); 298 K, acetone-d6**.**

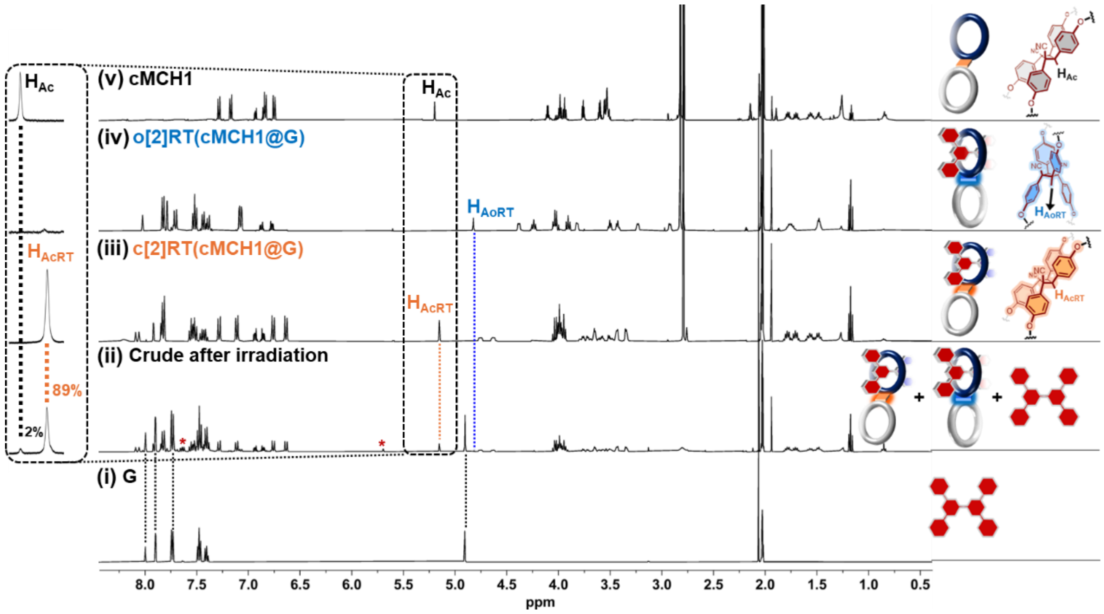

Figure 3-22. ^{1}H NMR spectra of **G** (i), crude after irradiating the mixture of **G** (3 eq) and **MCH1** (1 eq, 5 mM) by 365 nm UV light overnight at -78 °C (ii), isolated **c[2]RT(cMCH1@G)** (iii), isolated **o[2]RT(oMCH1@G)** (iv) and **cMCH1** (vi); 298 K,

acetone-d6. The asterisk "*" in spectrum (ii) marks an impurity generated from **G** after it was left standing in acetone solution (See figure 3-23).

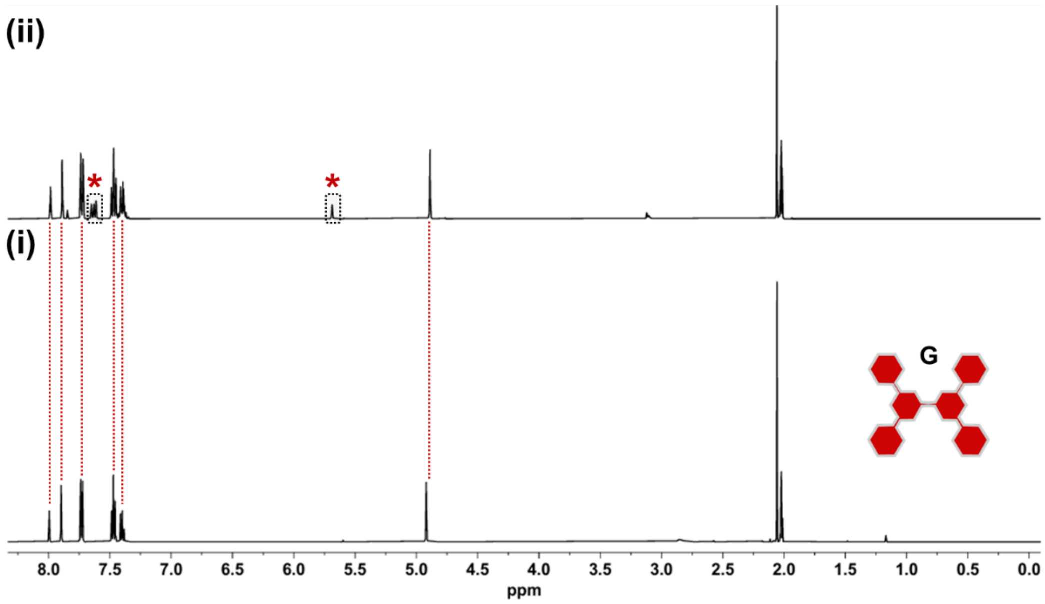

Figure 3-23. ^{1}H NMR spectra of **G** (i) and **G** after being left standing in acetone at -78 °C overnight (ii); 298 K, acetone-d6**.** The synthetic **G** occasionally generates an impurity when dissolved in acetone and left to stand overnight.

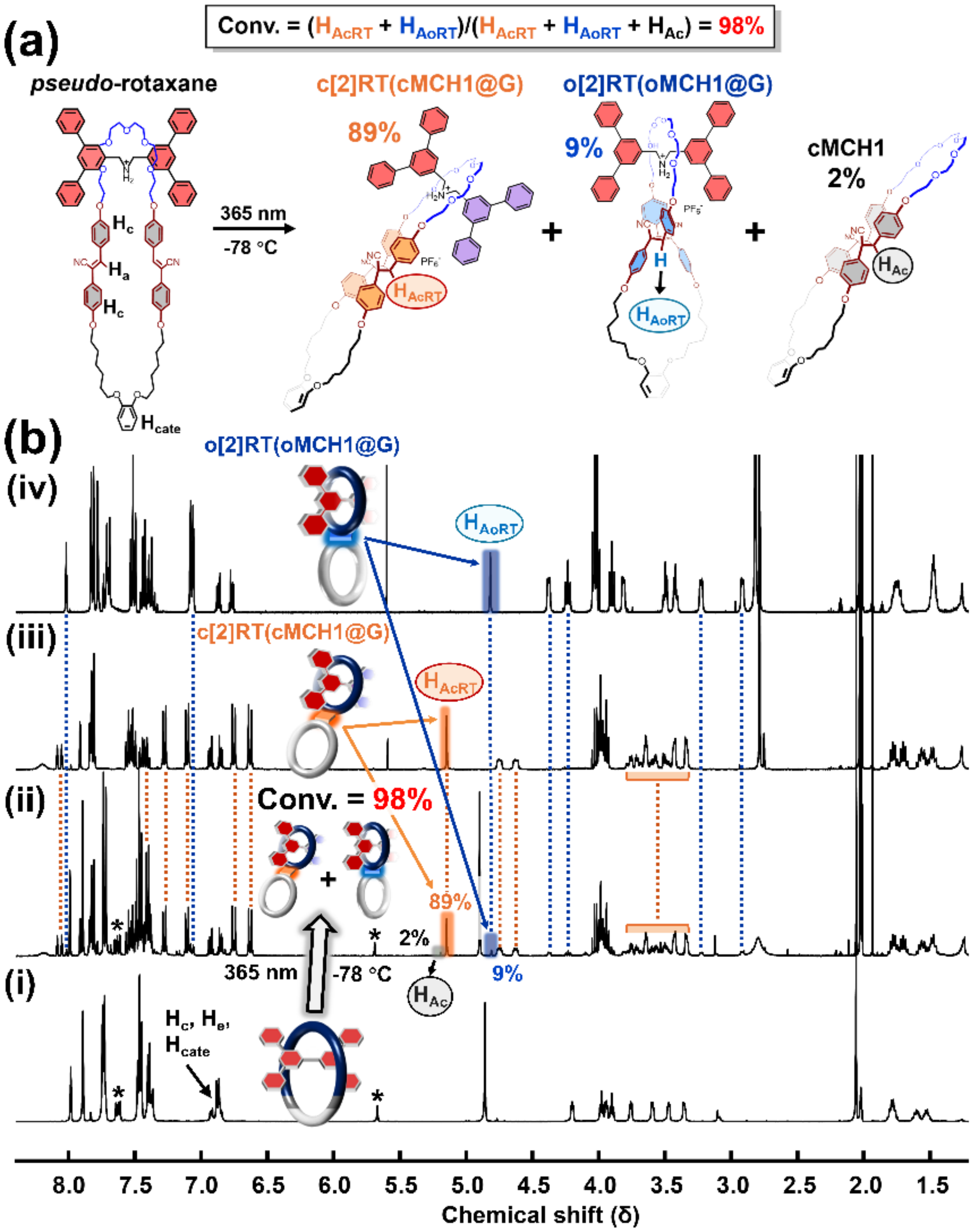

Figure 3-24. Synthesis of [2]rotaxanes via topology transformation of **MCH1**: (a) Photo-induced rotaxanation and molecular structures. (b) ^{1}H NMR spectra of mixture of **G** (3 eq) and **MCH1** (1 eq) (i), crude after irradiating the mixture solution (ii), isolated **c[2]RT(cMCH1@G)** (iii) and isolated **o[2]RT(oMCH1@G)** (iv). Note: the asterisks in spectra (i) and (ii) denote impurities derived from **G** (see figure 3-23).

First, we synthesized, isolated and characterized the rotaxanes using **MCH1** and **G**. According to ^{1}H NMR spectra, typical spliting of proton signals of glycol units are observed after mixing **MCH1** and **G**, indicating the formation of complex by recognition of hexaethtleneglycol fragment on cation guest molecule (Figure 3-21). A solution of **MCH1** (1 eq) and **G** (3 eq) in acetone was degassed with N_2, followed by irradiation with 365 nm UV light at –78 °C overnight. As shown in the ^{1}H NMR spectra (Figures 3-22 and 3-24b), all proton signals of cyano-stilbene moieties disappeared, and new signals corresponding to the cyclobutane rings were observed. Similar to the topology transformation of **MCH1** in the absence of an axle molecule, two types of cyclobutane with chair-like or orthogonal geometry were produced in a d.r. of 9.9:1, as determined by ^{1}H NMR integration. The observation of two types of cyclobutane indicates the presence of topological isomerism in the obtained rotaxanes. Importantly, based on the integration of cyclobutane signals, 98% of the macrocycles were converted into rotaxanes, with only a small portion forming free **cMCH1**. In agreement with the NMR spectra, we successfully isolated two distinct rotaxanes. One is **c[2]RT(cMCH1@G)**, which exhibits a chair-like geometry, and the other is **o[2]RT(oMCH1@G)**, exhibiting an orthogonal geometry. The isolated yield of rotaxanes is 92% and the isolated d.r. was determined to be 13:1.

The topological difference between **c[2]RT(cMCH1@G)** and **o[2]RT(oMCH1@G)** is clearly revealed by their ^{1}H NMR spectra. According to the ^{1}H NMR spectra, protons H_1, H_2, and H_6 of axle G become spectroscopically non-equivalent in the chair-like rotaxane, each exhibiting distinct splitting into two sets of signals (H_1/H_1', H_2/H_2', and H_6/H_6') (Figures 3-25 to 3-28). In contrast, all protons of axle G remain chemically equivalent in **o[2]RT(oMCH1@G)**, showing no unexpected splitting (Figures 3-29 to 3-32). This spectral difference arises from the distinct topological environments of the axle in the two rotaxanes. In **c[2]RT(cMCH1@G)**, the two cyano groups are located on the same face of the cyclobutane ring (and thus on the same face of the crown ether), which may form weak hydrogen bonds with nearby aromatic protons ($H_2/H_3/H_4\cdots NC$), in a manner analogous to the intermolecular hydrogen bonding observed in the single-crystal structure of **cMCH1**. In contrast, the orthogonal geometry of **o[2]RT(oMCH1@G)** leads to a symmetric spatial arrangement, with the two cyano groups symmetrically located on opposite sides of the crown ether plane. This spatial symmetry preserves the chemical equivalence of all axle protons, resulting in no observable splitting.

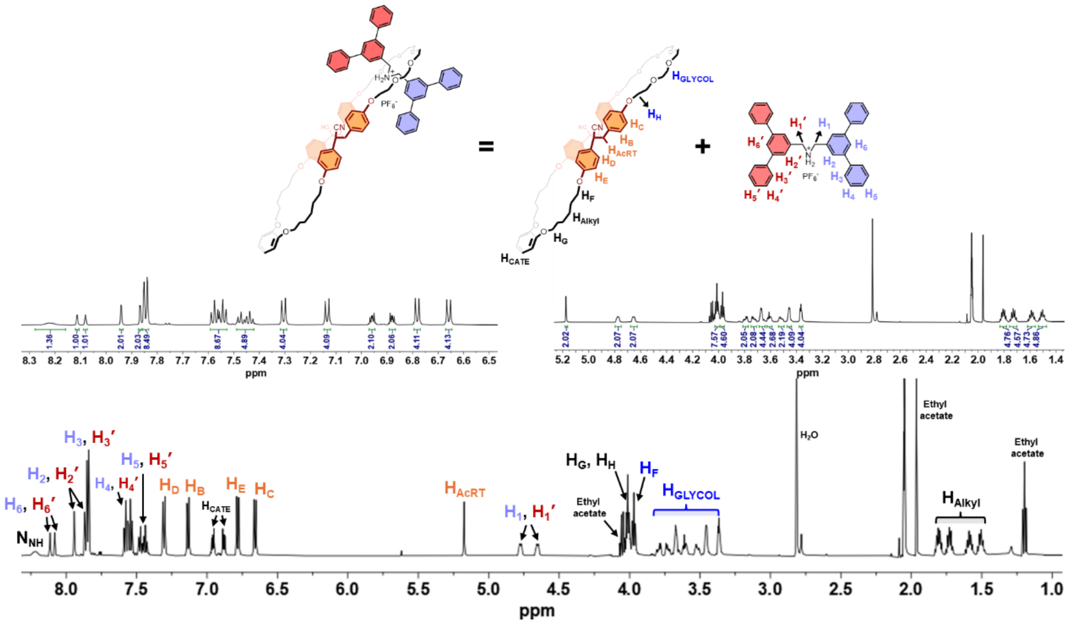

Figure 3-25. ^{1}H NMR spectrum of **c[2]RT(cMCH1@G)**; 298 K, acetone-d6.

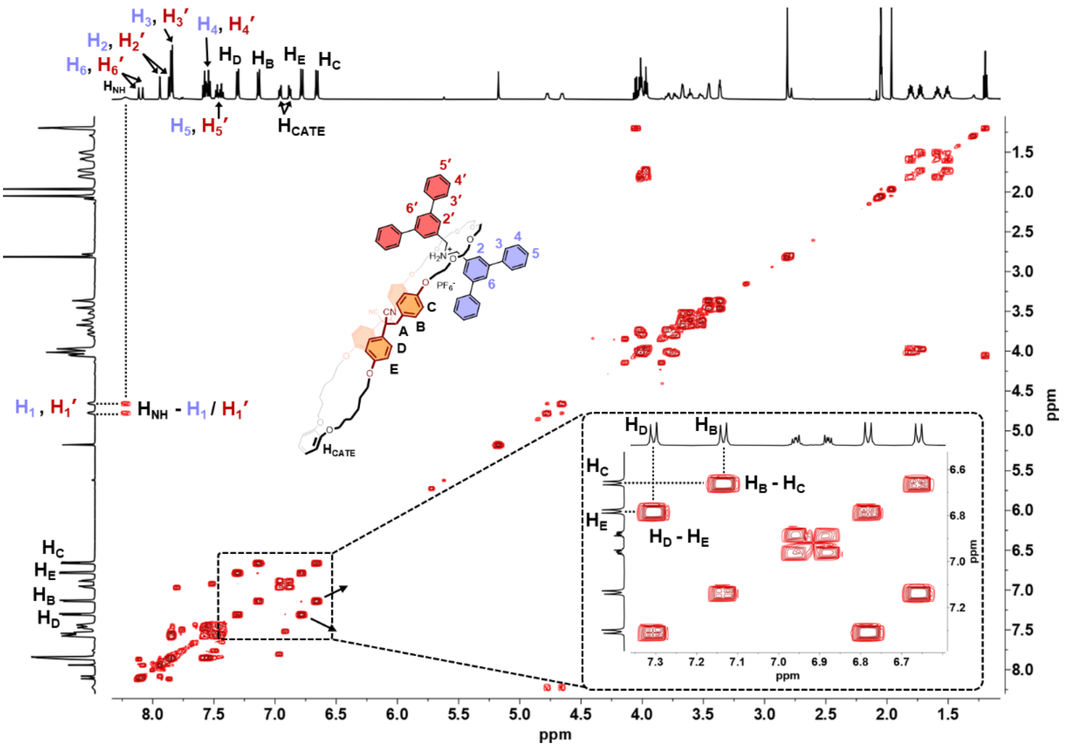

Figure 3-26. COSY spectrum of **c[2]RT(cMCH1@G)**; 298 K, acetone-d6.

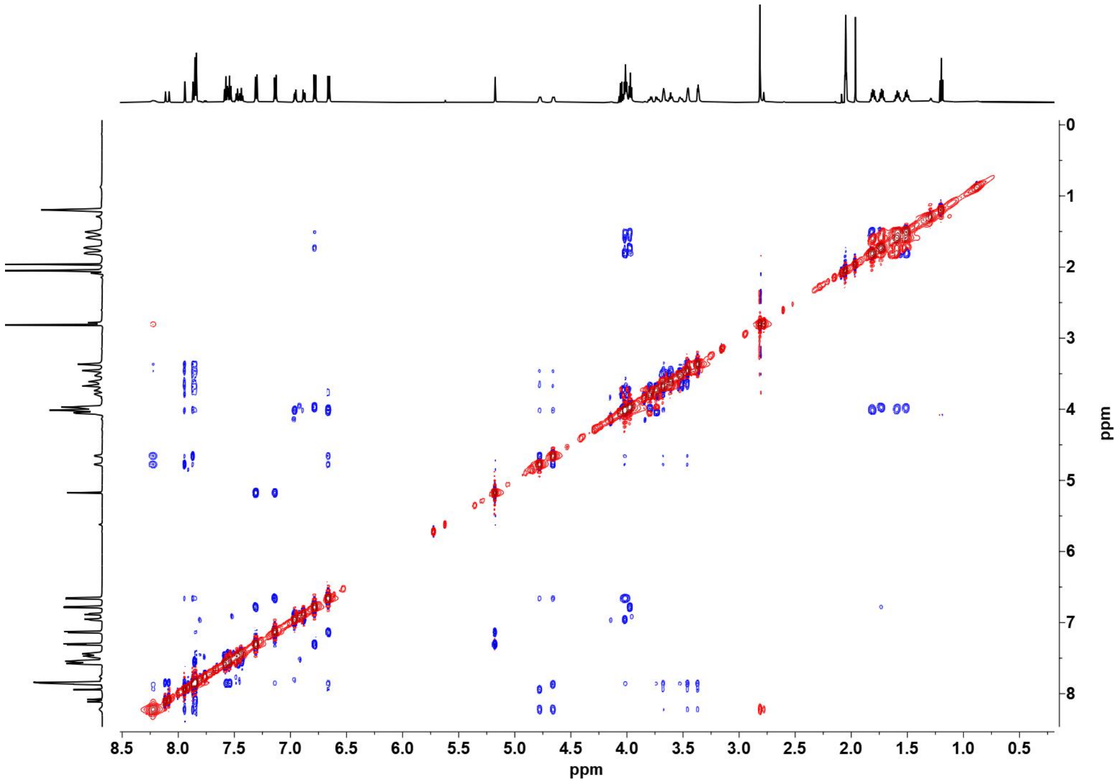

Figure 3-27. ROESY spectrum of **c[2]RT(cMCH1@G)**; 298 K, acetone-d6.

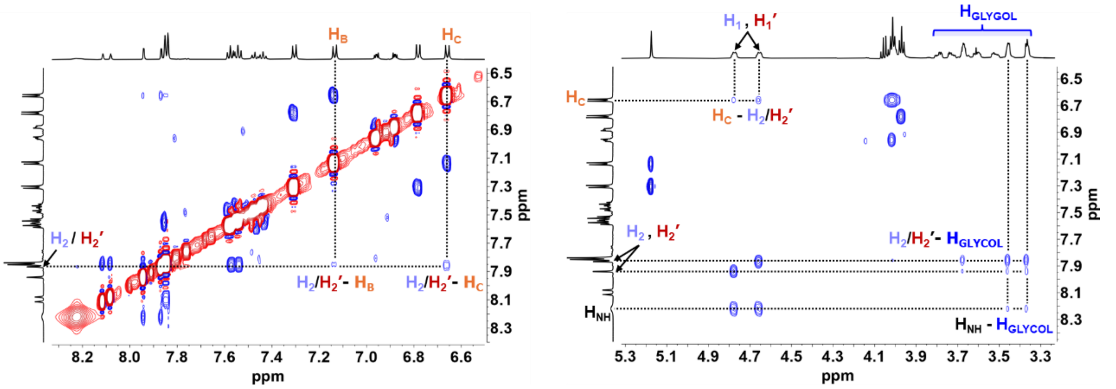

Figure 3-28. Patial ROESY spectra of **c[2]RT(cMCH1@G)**; 298 K, acetone-d6.

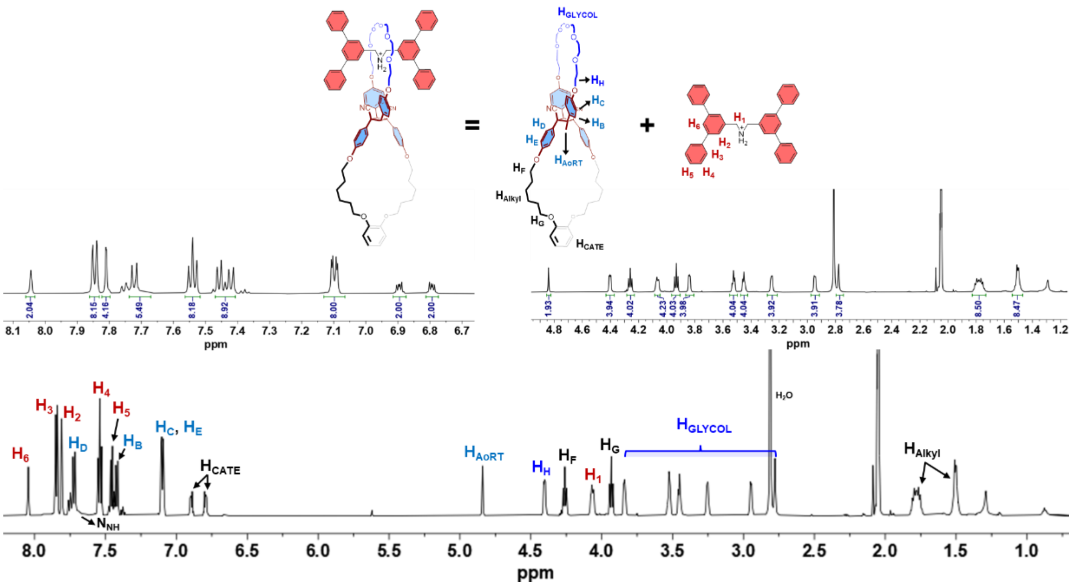

Figure 3-29. ^{1}H NMR spectrum of **o[2]RT(oMCH1@G)**; 298 K, acetone-d6.

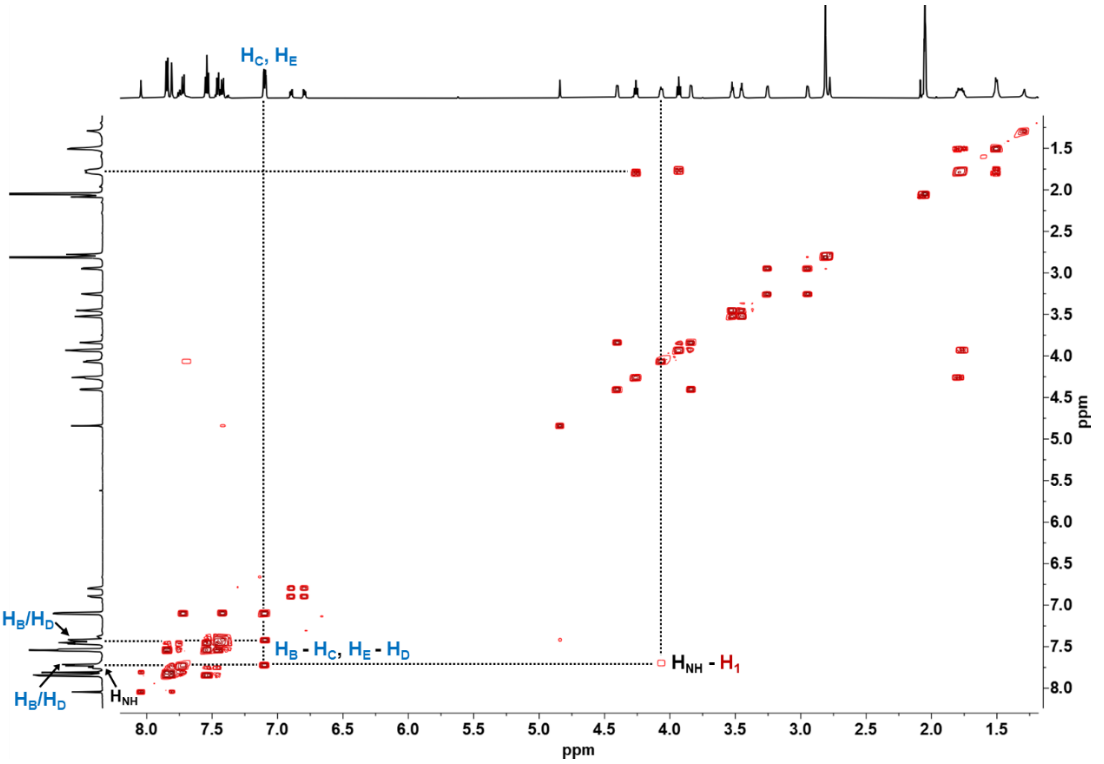

Figure 3-30. COSY spectrum of **o[2]RT(oMCH1@G)**; 298 K, acetone-d6.

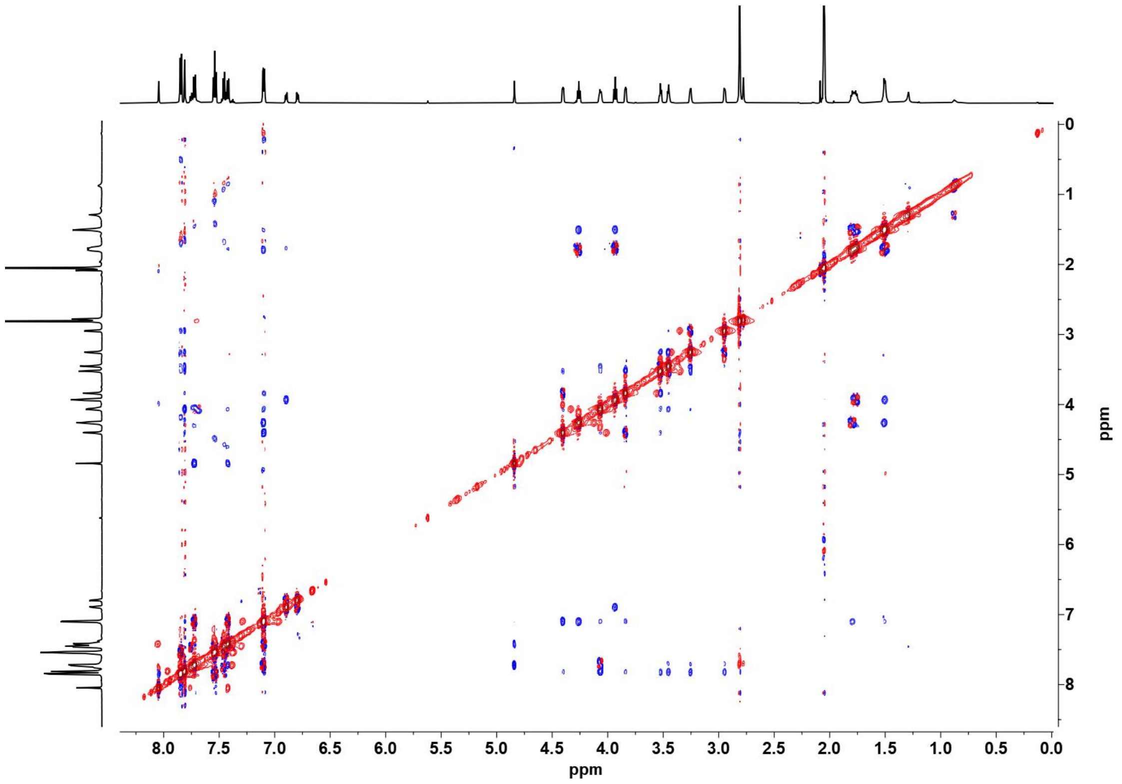

Figure 3-31. ROESY spectrum of **o[2]RT(oMCH1@G)**; 298 K, acetone-d6.

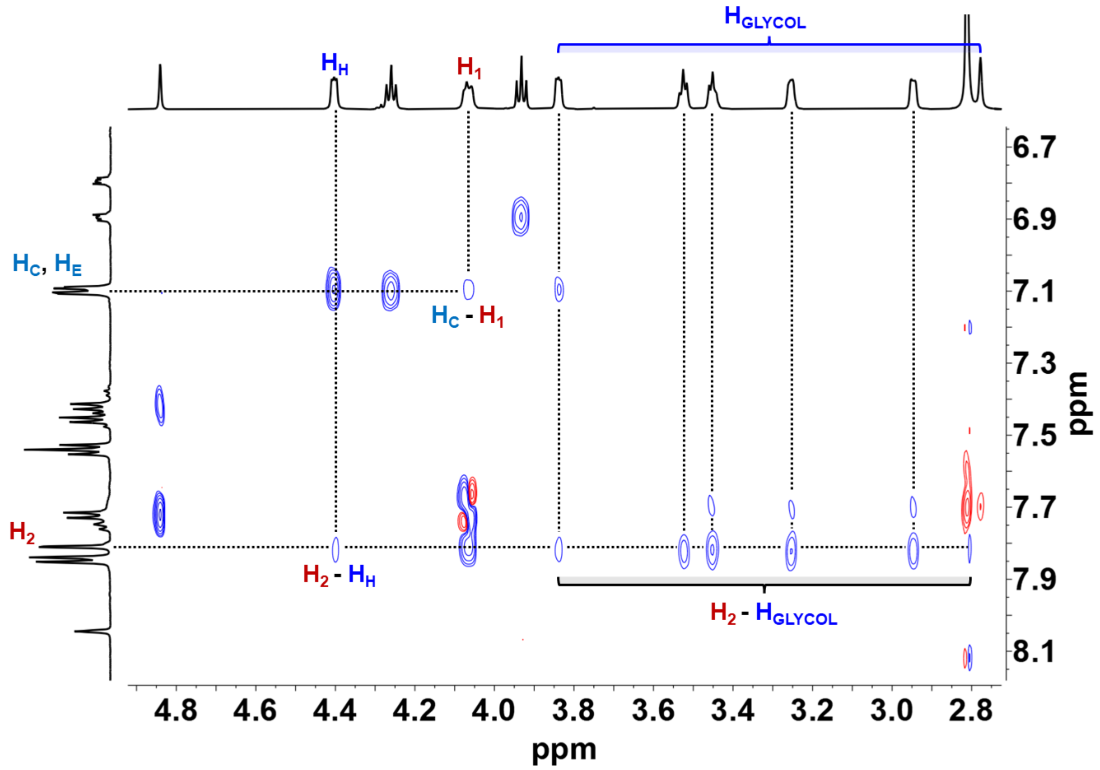

Figure 3-32. Patial ROESY spectrum of **o[2]RT(oMCH1@G)**; 298 K, acetone-d6.

Following the successful synthesis of rotaxanes from **MCH1** and **G**, we applied the same strategy to **MCH2**. Effectvie complexation between **MCH2** and **G** was confirmed by ^{1}H NMR spectra (Figure 3-33). As shown in the figure 3-34, all proton signals of the cyano-stilbene moieties in **MCH2** disappeared upon 365 nm UV irradiation, and only signals corresponding to the chair-like cyclobutane ring were observed, indicating the exclusive formation of a single topological product. This outcome is consistent with the behavior of **MCH2** in the absence of axle molecules. Remarkably, the rotaxanation proceeded with nearly quantitative efficiency, with the conversion of macrocycles to rotaxanes exceeding 99%. According to the ^{1}H NMR spectrum of the product mixture, only excess **G** and the rotaxane product were observed, which was further confirmed by comparison with the spectra of **cMCH2** and isolated **c[2]RT(cMCH2@G)** (Figures 3-34 and 3-35b). The isolated yield of **c[2]RT(cMCH2@G)** is 92%.

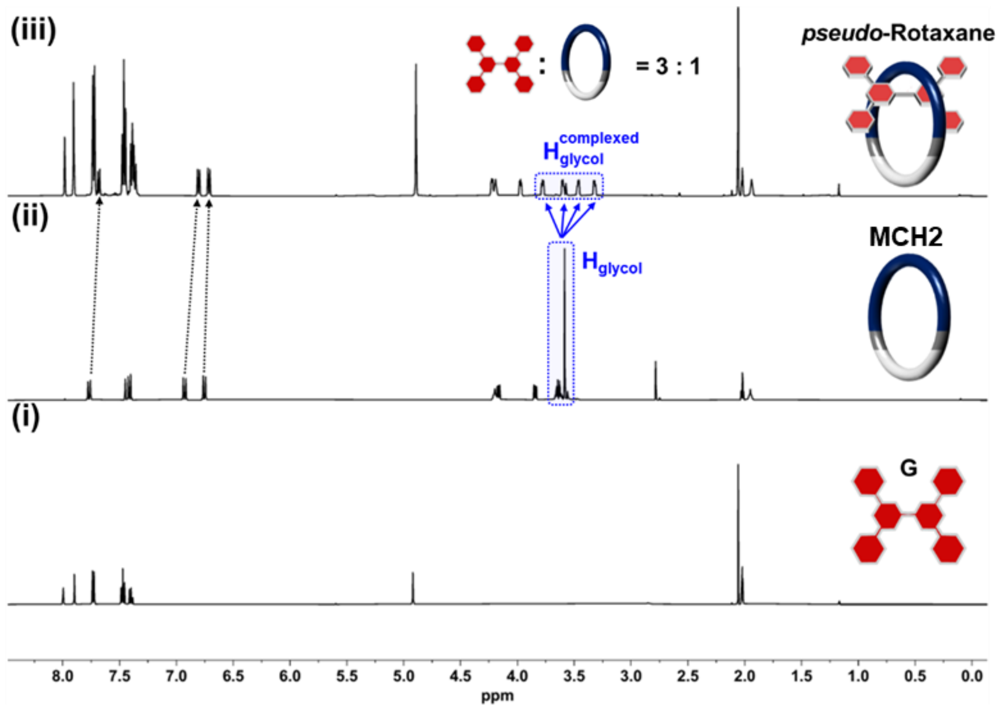

Figure 3-33. ^{1}H NMR spectra of **G** (i), **MCH2** (ii), and mixture of **G** and **MCH2** in a ratio of 3:1 (iii); 298 K, acetone-d6**.**

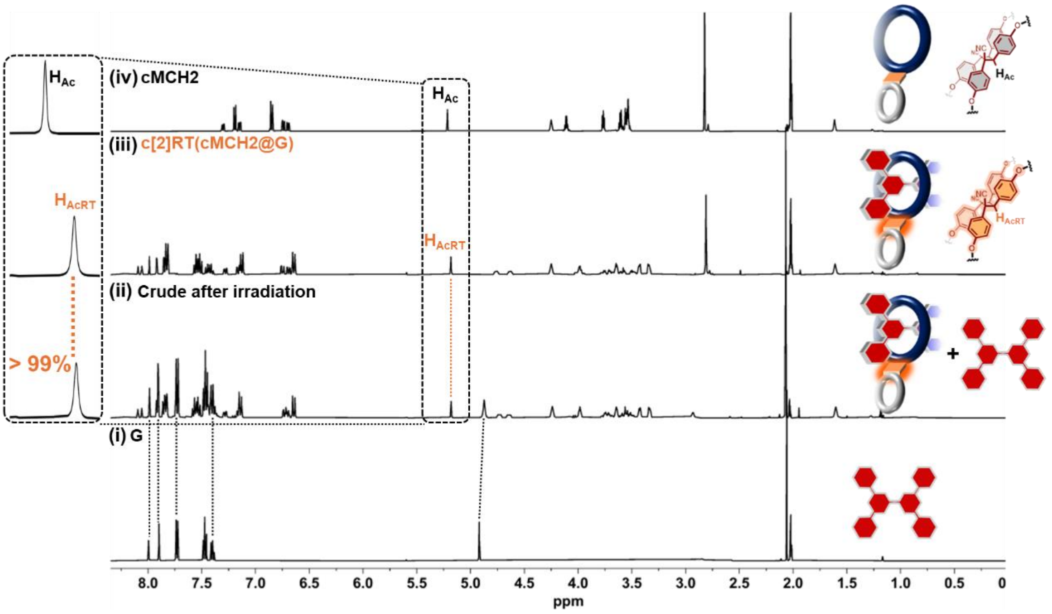

Figure 3-34. ^{1}H NMR spectra of **G** (i), crude after irradiating the mixture of **G** (3 eq) and **MCH2** (1 eq, 5 mM) by 365 nm UV light overnight at -78 °C (ii), isolated **c[2]RT(cMCH2@G)** (iii), and **cMCH2** (iv); 298 K, acetone-d6**.**

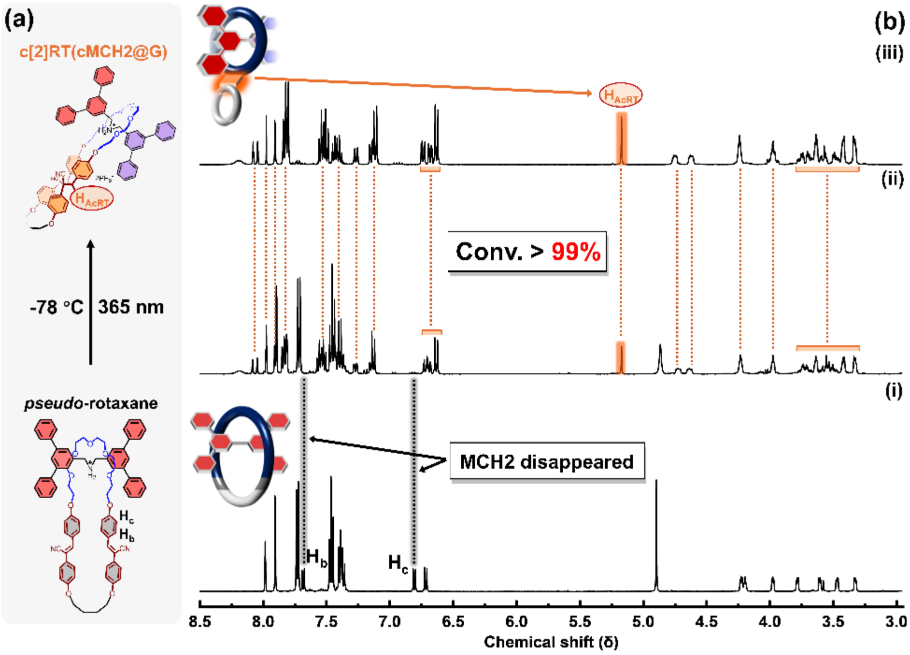

Figure 3-35. Synthesis of [2]rotaxanes via topology transformation of **MCH2**: (a) Photo-induced rotaxanation and molecular structures. (b) ^{1}H NMR spectra of mixture of **G** (3 eq) and **MCH2** (1 eq) (i), crude after irradiating the mixture solution (ii) and isolated **c[2]RT(cMCH2@G)** (iii).

The ^{1}H NMR spectrum shows that the proton signals of axles in **c[2]RT(cMCH2@G)** split in the same way as in **c[2]RT(cMCH1@G)**, indicating a similar chair-like geometry (Fig. S33). Moreover, in the smallest fused ring formed by a four-carbon chain, the aromatic protons appear as two distinct sets of signals ($H_{D1,2}$ and $H_{E1,2}$) (Figures 3-9, 3-36, and 3-37). This splitting is attributed to restricted rotation of the phenyl groups, which is likely caused by the limited conformational freedom imposed by the compact fused ring structure.

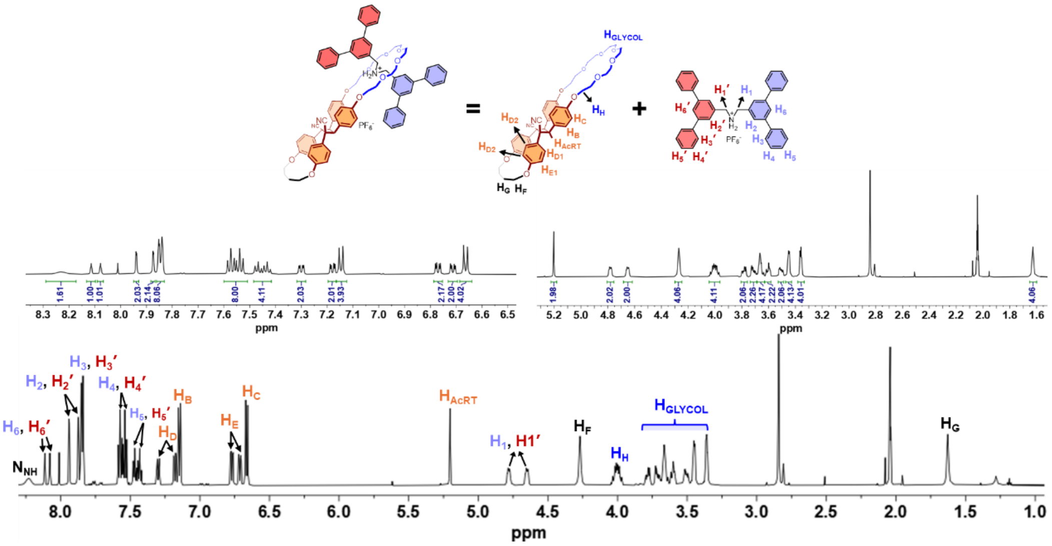

Figure 3-36. ^{1}H NMR spectrum of **c[2]RT(cMCH2@G)**; 298 K, acetone-d6.

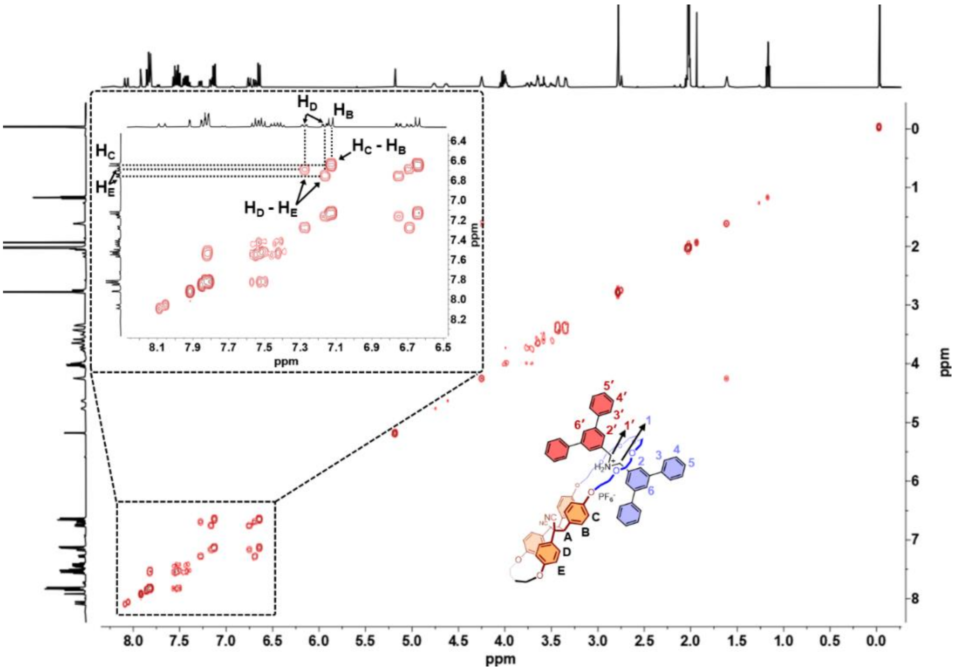

Figure 3-37. COSY spectrum of c[2]RT(cMCH2@G); 298 K, acetone-d6.

Subsequently, we extended this strategy to the synthesis of MIMs with more complex mechanical interlocks, namely [3]rotaxanes, in which one macrocycle is mechanically interlocked with two axles. Using **MCH3** (a macrocycle bearing two hexaethylene glycol fragments as recognition sites) and **G**, we obtained two types of [3]rotaxanes with chair-like or orthogonal topologies, similar to the topological transformation observed for **MCH3** in the absence of axle molecules (Figure 3-40a).

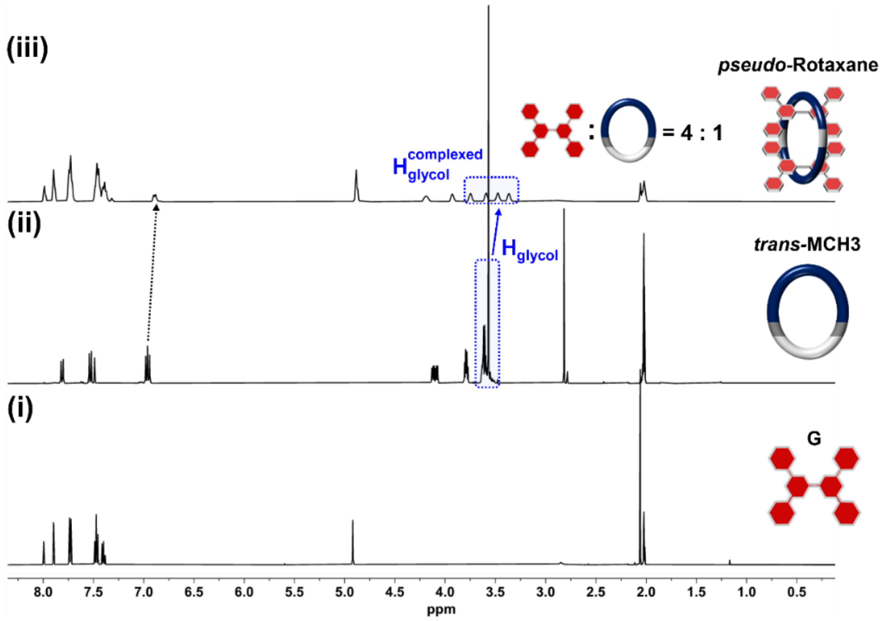

Figure 3-38. ^{1}H NMR spectra of **G** (i), **MCH3** (ii), and mixture of **G** and **MCH3** in a ratio of 4:1 (iii); 298 K, acetone-d6**.**

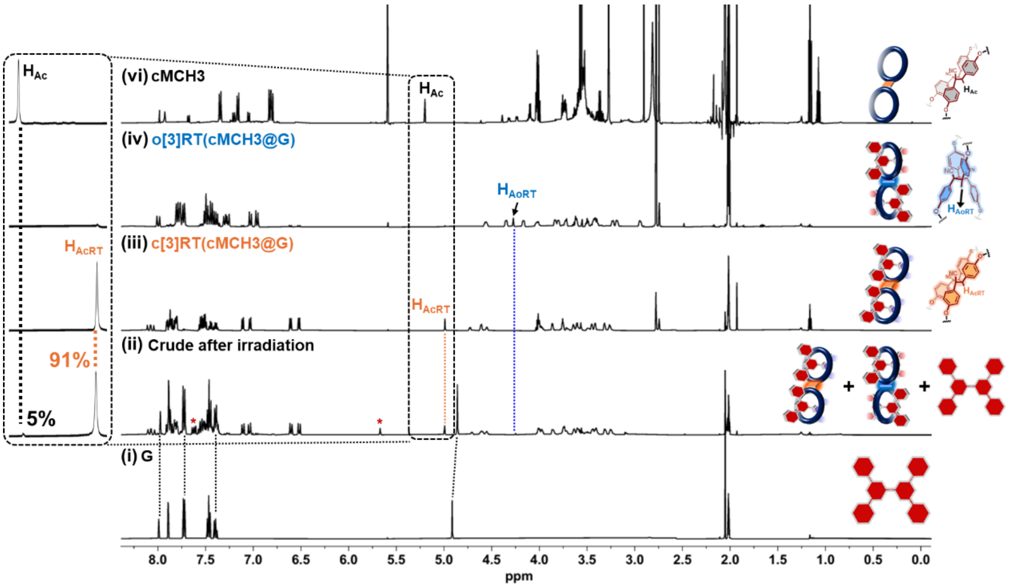

Figure 3-39. ^{1}H NMR spectra of **G** (i), crude after irradiating the mixture of **G** (4 eq) and **MCH3** (1 eq, 5 mM) by 365 nm UV light overnight at -78 °C (ii), isolated **c[3]RT(cMCH3@G)** (iii), isolated **o[3]RT(oMCH3@G)** (iv) and **cMCH3** (vi); 298 K, acetone-d6**.** The asterisk "*" in spectrum (ii) marks an impurity generated from **G** after it was left standing in acetone solution (See Figure S22).

Rotaxane formation was confirmed by ^{1}H NMR spectra, which showed trends consistent with those of former systems (Figure 3-38). The conversion of macrocycles to [3]rotaxanes reached 96%, with a diastereomeric ratio (d.r.) of 18:1 (chair-like **c[3]RT(cMCH3@G)** vs. orthogonal **o[3]RT(oMCH3@G)**). Both [3]rotaxanes were successfully isolated by chromatography, with an overall yield of 80% and an isolated d.r. of 30:1 (Figures 3-39 and 3-40).

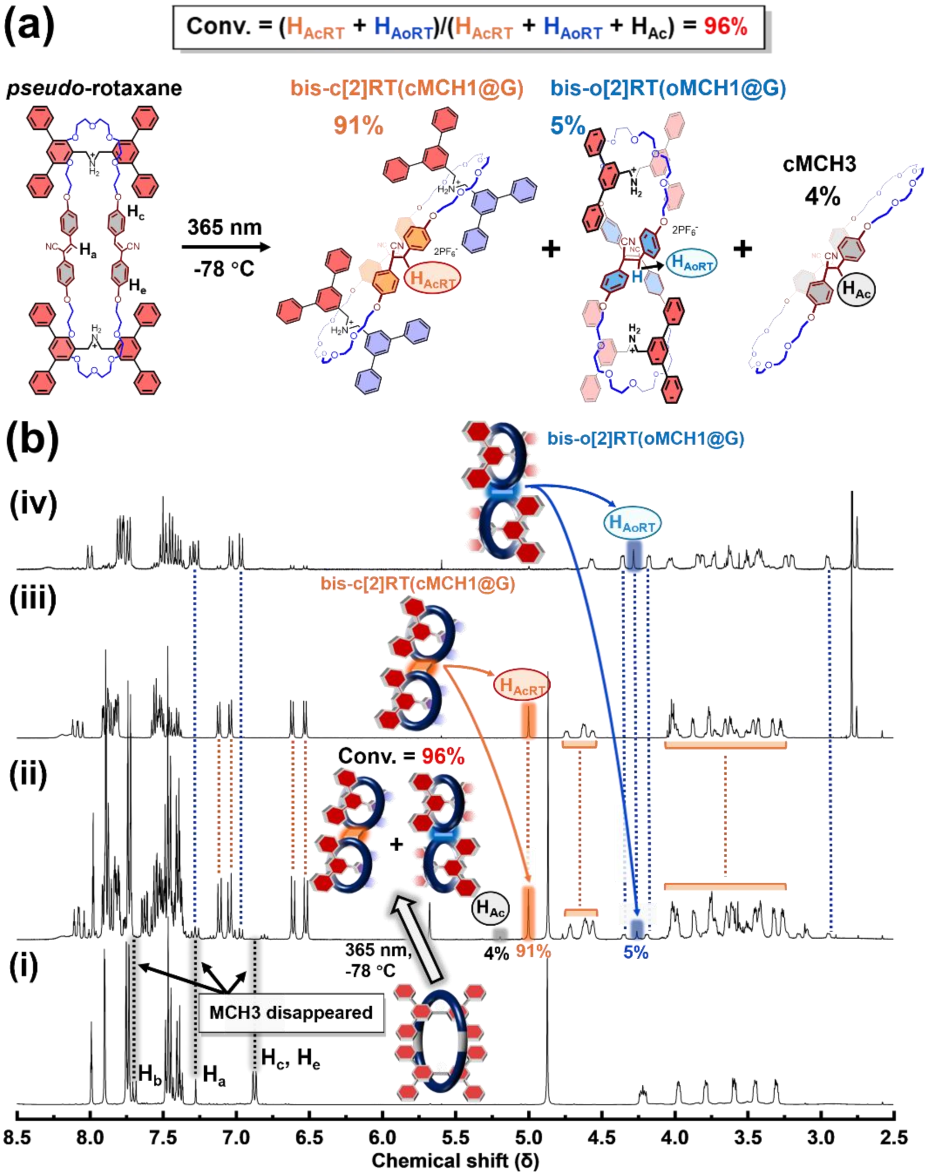

Figure 3-40. Synthesis of [3]rotaxanes via topology transformation of **MCH3**: (a) Photo-induced rotaxanation and molecular structures. (b) ^{1}H NMR spectra of mixture of **G** (4 eq) and **MCH3** (1 eq) (i), crude after irradiating the mixture solution (ii), isolated **c[3]RT(cMCH3@G)** (iii) and isolated **o[3]RT(oMCH3@G)** (iv).

According to the ^{1}H NMR spectra, **c[3]RT(cMCH3@G)** exhibits the same splitting pattern of axle protons as the previous two chair-like rotaxanes, indicating that the two axles adopt a parallel arrangement within the interlocked architecture (Figures 3-41 to 3-44). In contrast, the NMR spectrum of **o[3]RT(oMCH3@G)** reflects the same spatial symmetry observed in **o[2]RT(oMCH1@G)**, suggesting that the two axles are arranged in an orthogonal fashion (Figures 3-45 to 3-48). In this orthogonal [3]rotaxane, both the two axles and the two macrocyclic components adopt mutually orthogonal orientations, forming a unique geometry in which each structural element, whether axle or ring, is oriented orthogonally to its immediate neighbors. This spatial arrangement gives rise to a highly ordered interlocked architecture.

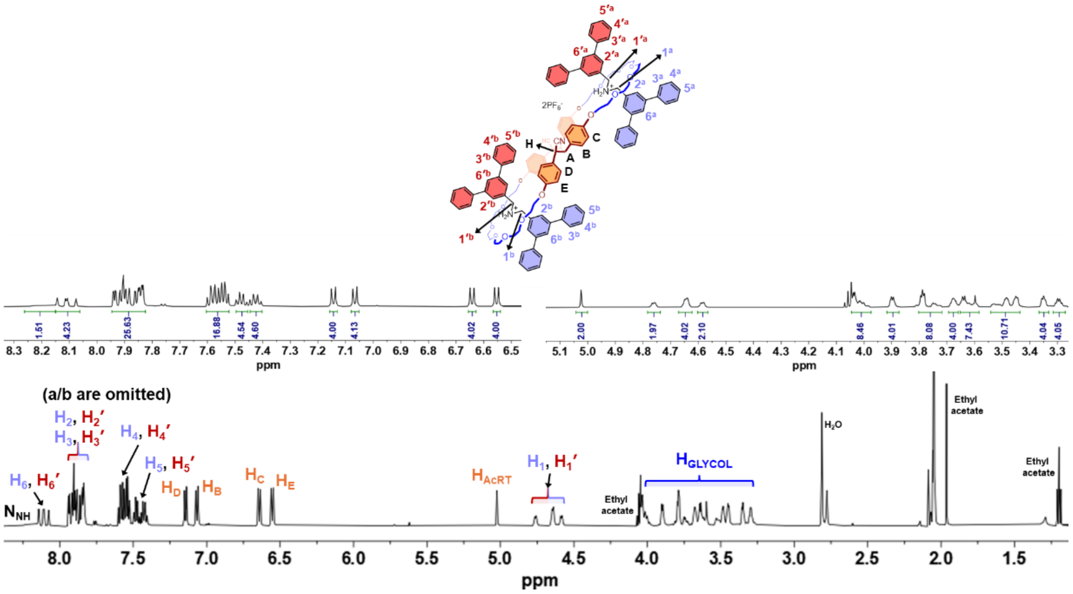

Figure 3-41. ^{1}H NMR spectrum of **c[3]RT(cMCH3@G)**; 298 K, acetone-d6**.**

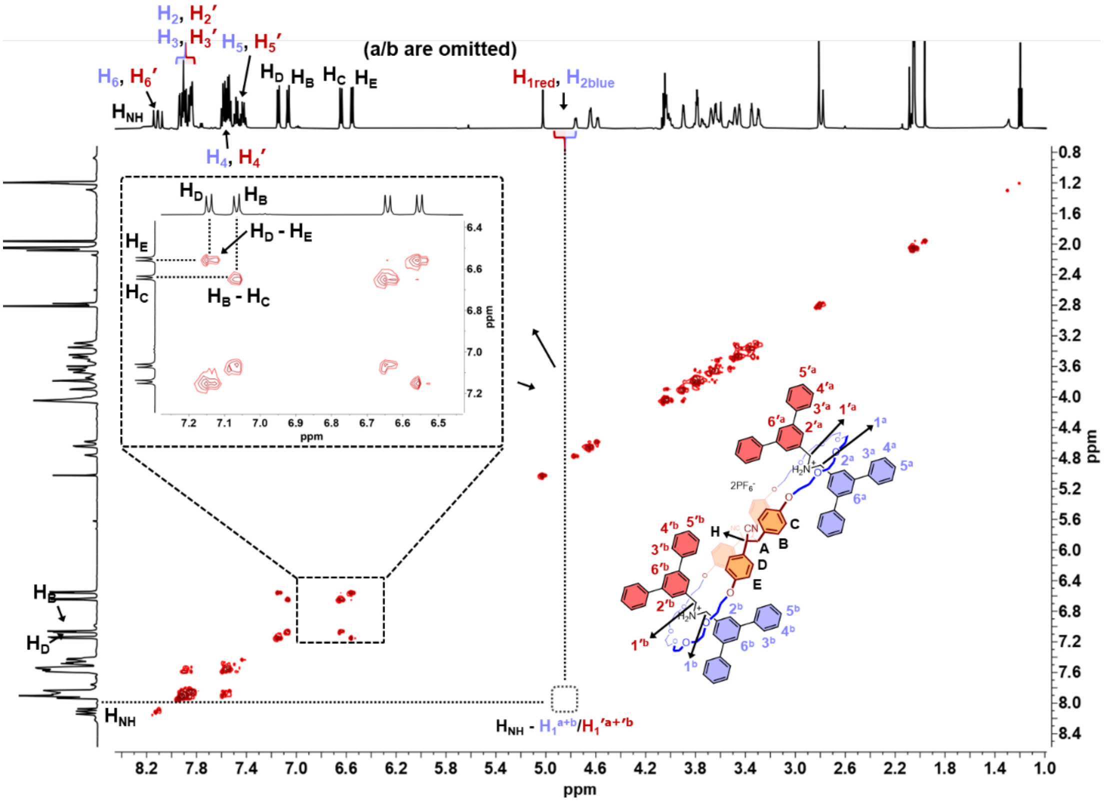

Figure 3-42. COSY spectrum of **c[3]RT(cMCH3@G)**; 298 K, acetone-d6**.**

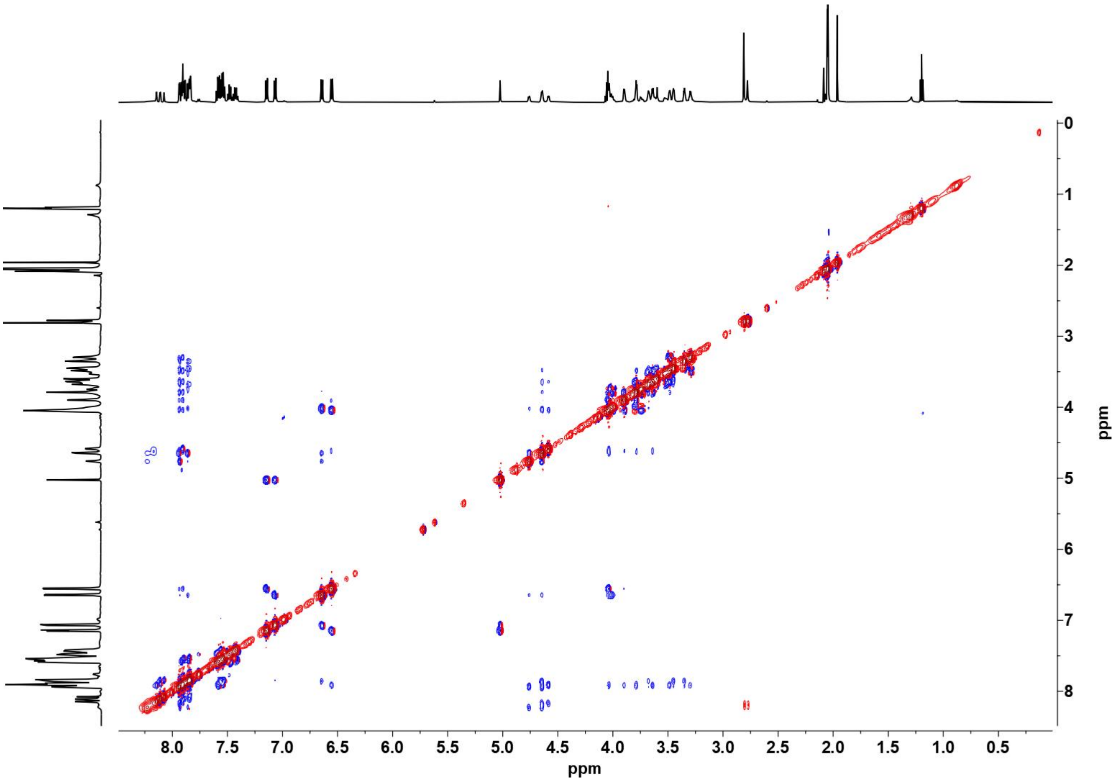

Figure 3-43. ROESY spectrum of **c[3]RT(cMCH3@G)**; 298 K, acetone-d6**.**

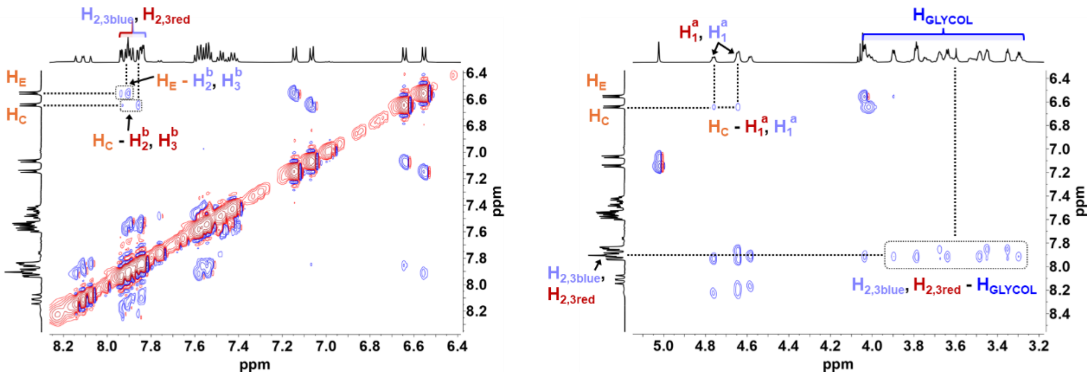

Figure 3-44. Patial ROESY spectra of **c[3]RT(cMCH3@G)**; 298 K, acetone-d6**.**

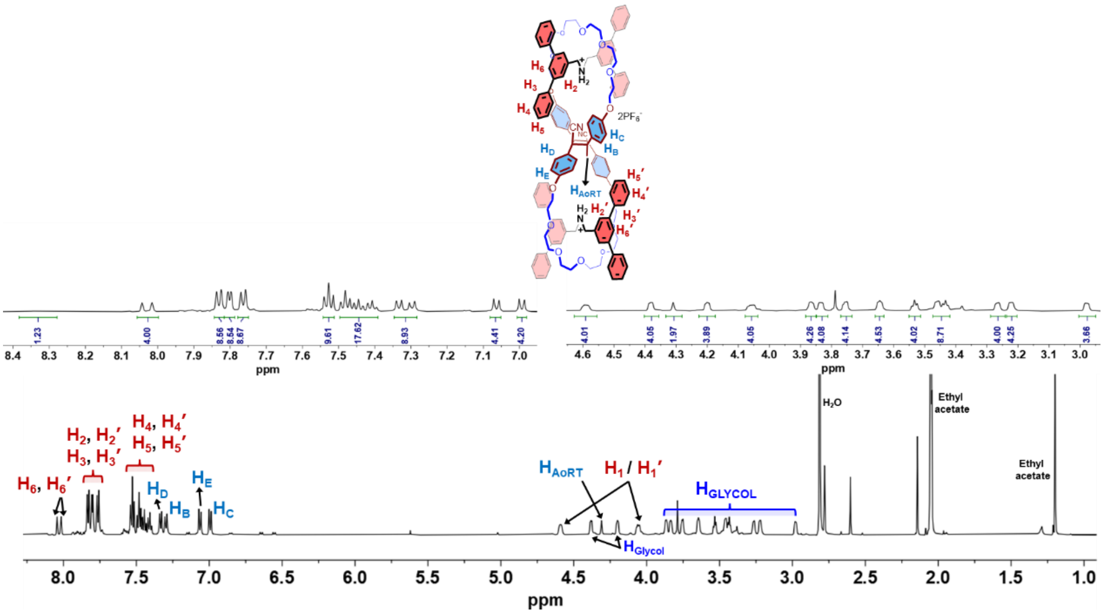

Figure 3-45. ^{1}H NMR spectrum of **o[3]RT(oMCH3@G)**; 298 K, acetone-d6**.**

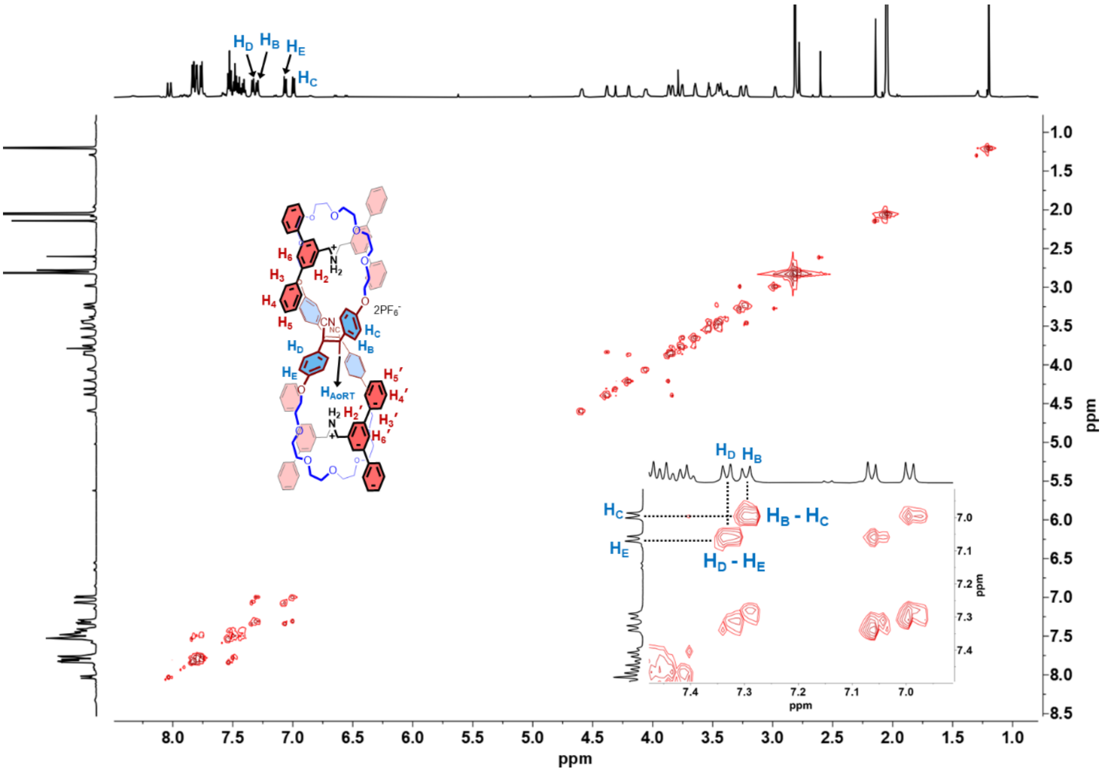

Figure 3-46. COSY spectrum of **o[3]RT(oMCH3@G)**; 298 K, acetone-d6**.**

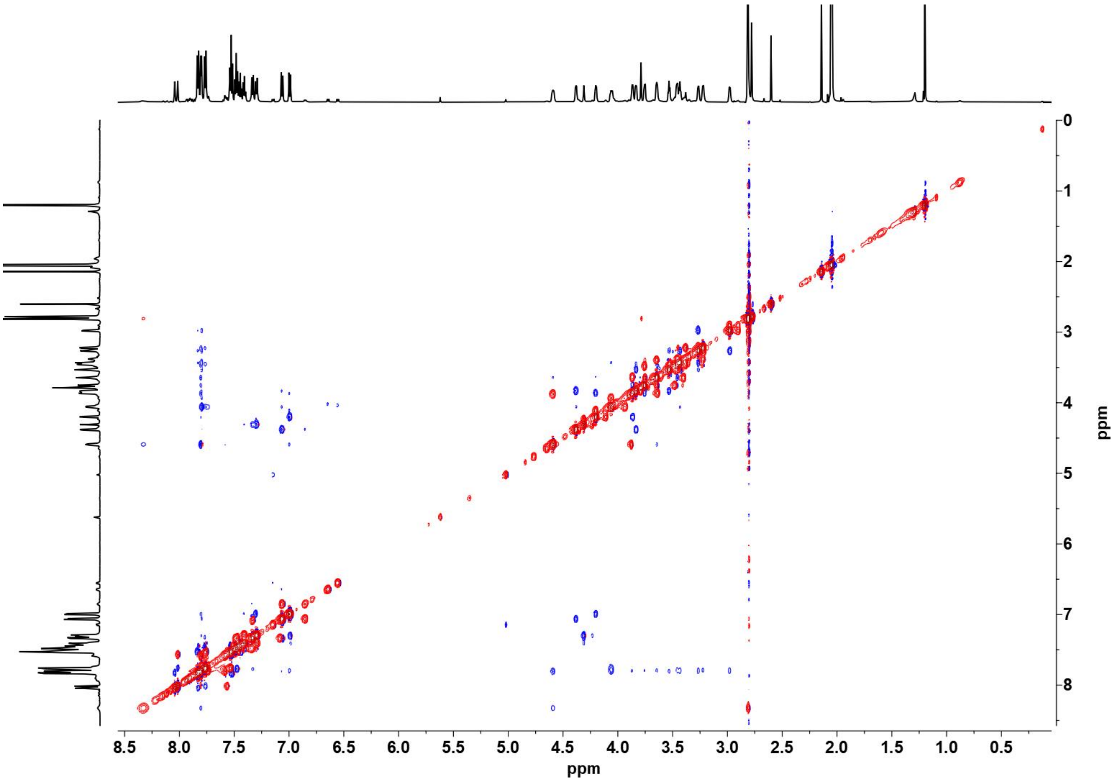

Figure 3-47. ROESY spectrum of **o[3]RT(oMCH3@G)**; 298 K, acetone-d6**.**

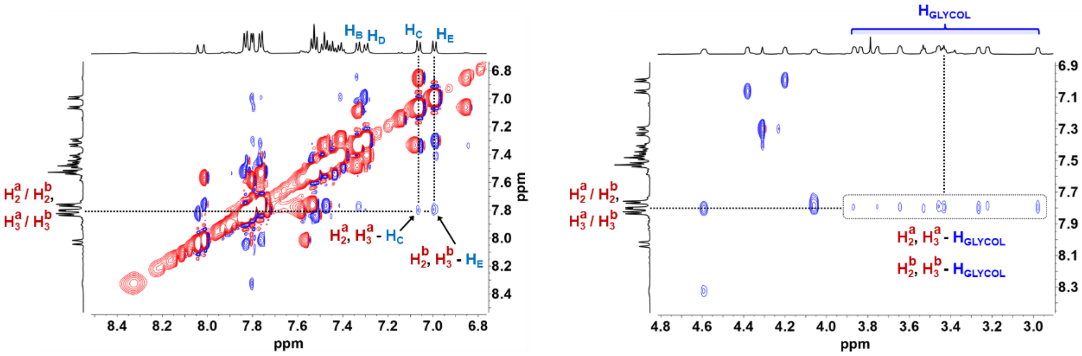

Figure 3-48. Patial ROESY spectra of **o[3]RT(cMCH2@G)**; 298 K, acetone-d6**.**

3-2-3 Derotaxanation via reverse topology transformation from figure-eight ring structures to macrocycles

By showing rotaxanation relying on topology transformation of three distinct macrocycles, we demonstrated the convenient, efficient, and structurally versatile synthesis of rotaxanes with diverse topologies and complex mechanical interlocks. Remarkably, the topological reversibility of the chair-like fused rings endows the resulting rotaxanes with mechanical unlocking capabilities

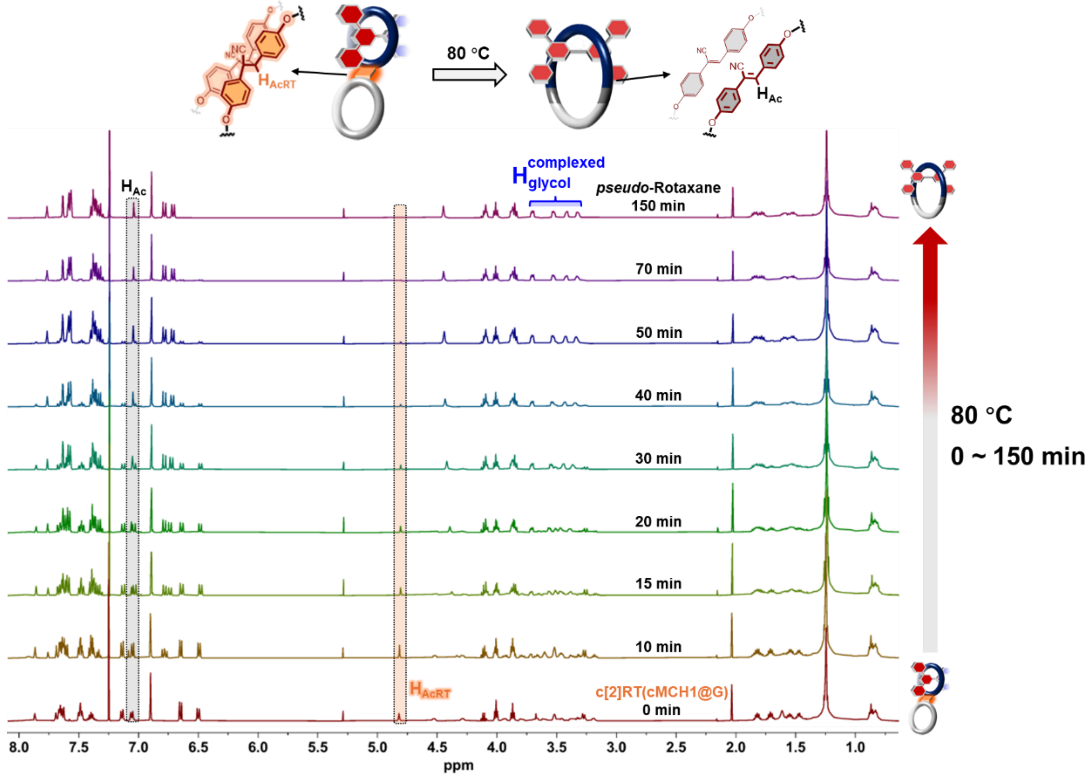

Figure 3-49. ^{1}H NMR spectra of sealed $CHCl_3$ solution of **c[2]RT(cMCH1@G)** after heating in oil bath at 80 °C for 150 minutes in $CHCl_3$ solution; 298 K, $CHCl_3$-d.

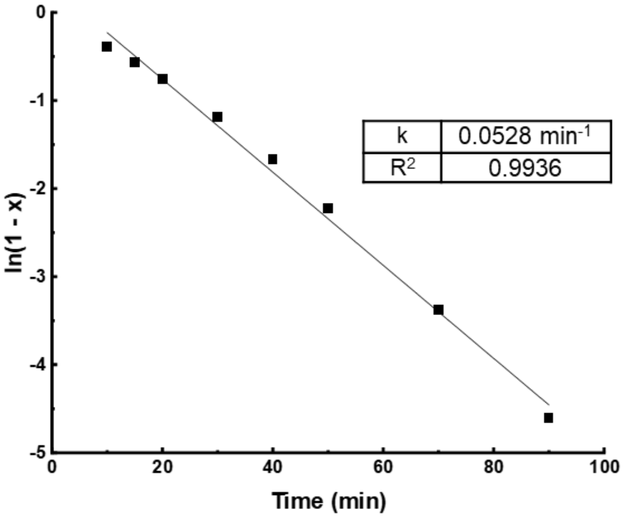

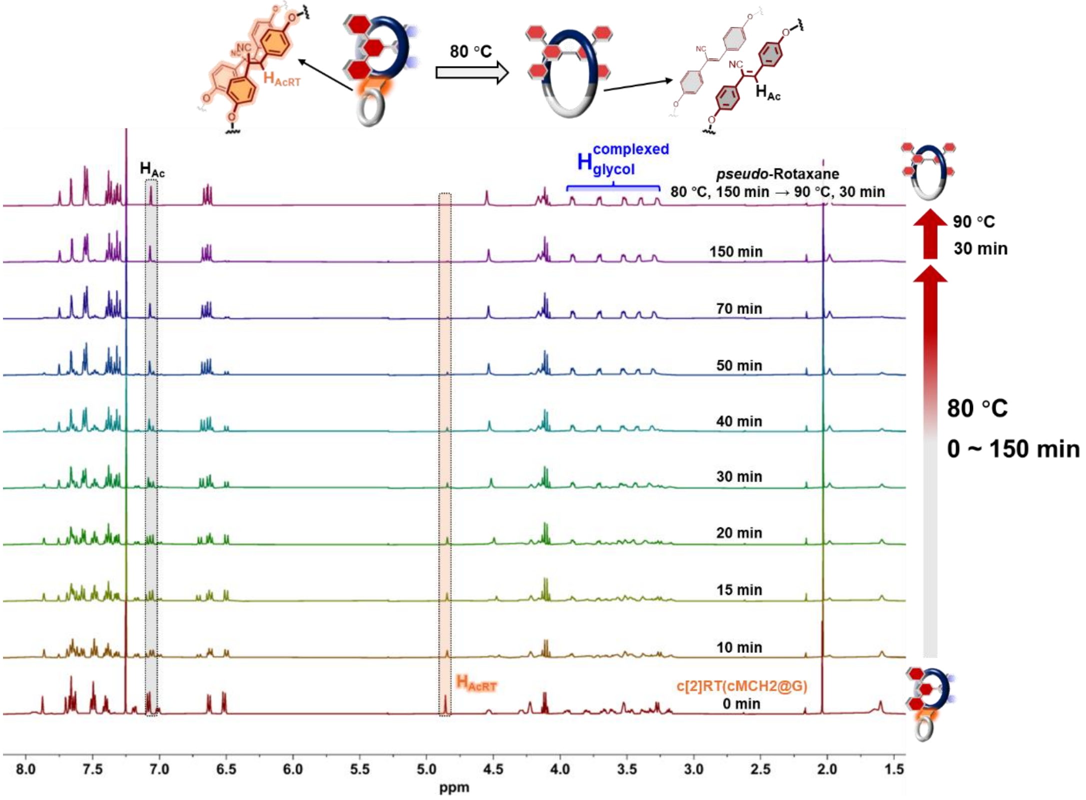

Figure 3-50. ^{1}H NMR spectra of sealed $CHCl_3$ solution of **c[2]RT(cMCH2@G)** after heating at 80 °C for 150 minutes, followed by heating in 90 °C bath for additional 30 minutes; 298 K, $CHCl_3$-d.

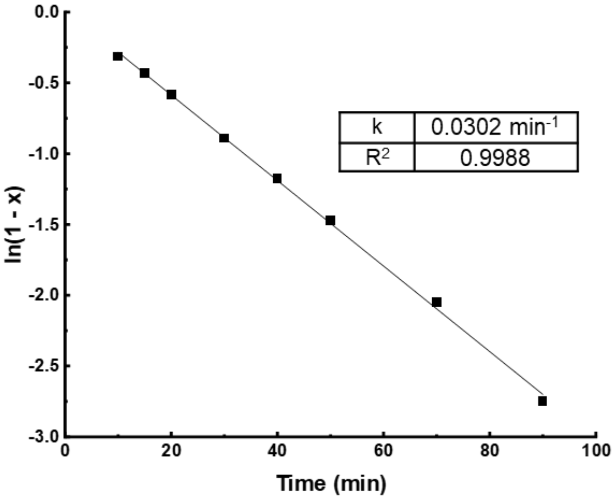

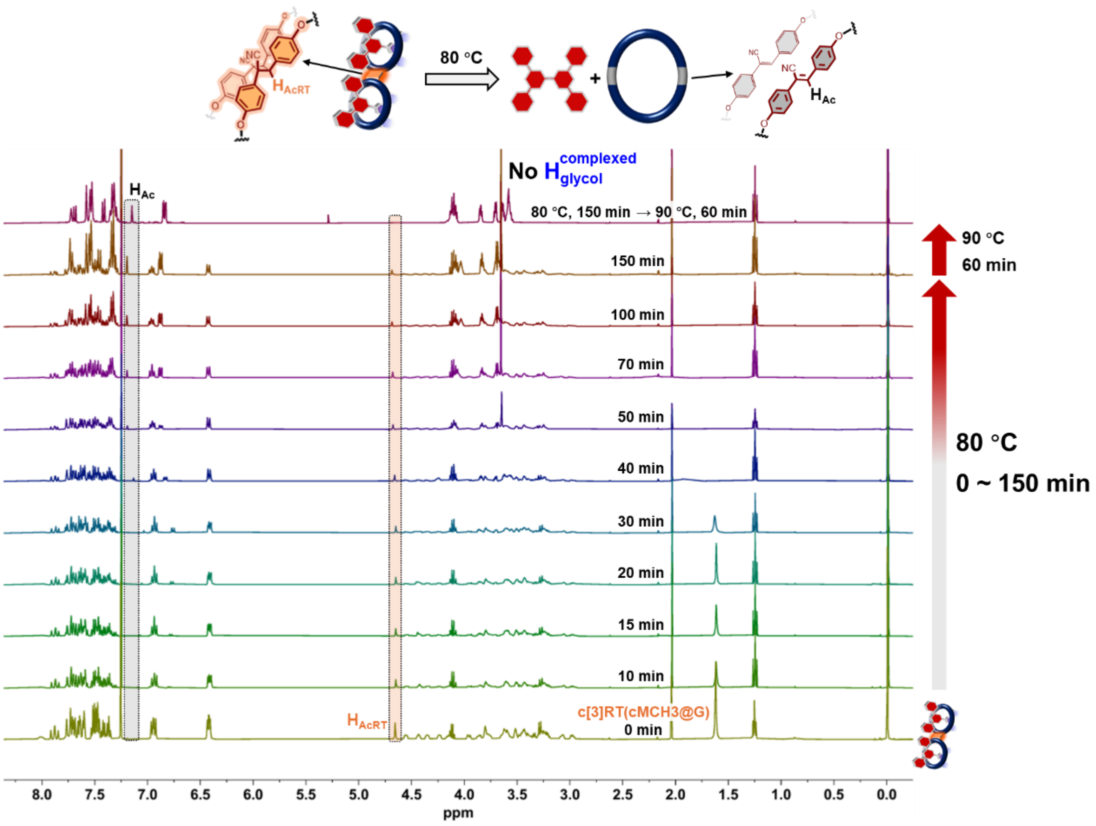

Figure 3-51. ^{1}H NMR spectra of sealed $CHCl_3$ solution of **c[3]RT(cMCH3@G)** after heating at 80 °C for 150 minutes, followed by heating at 90 °C bath for additional 60 minutes; 298 K, $CHCl_3$-d.

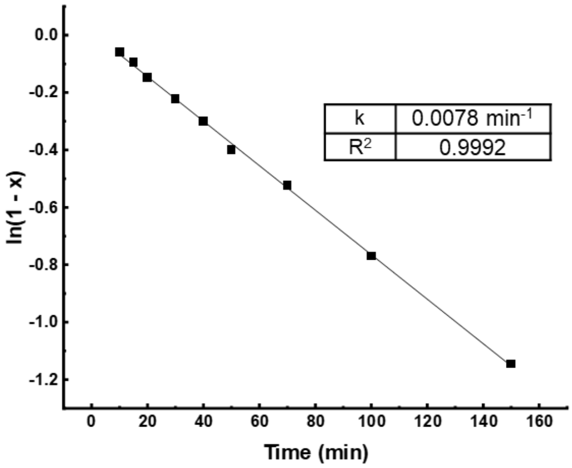

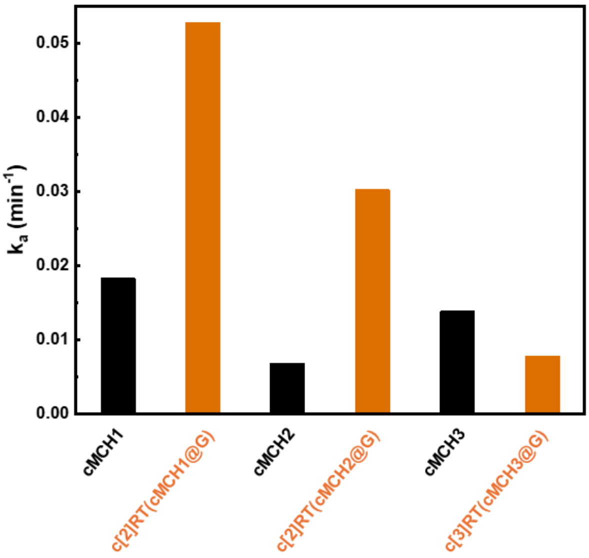

Figure 3-52. k of all chair-like compounds

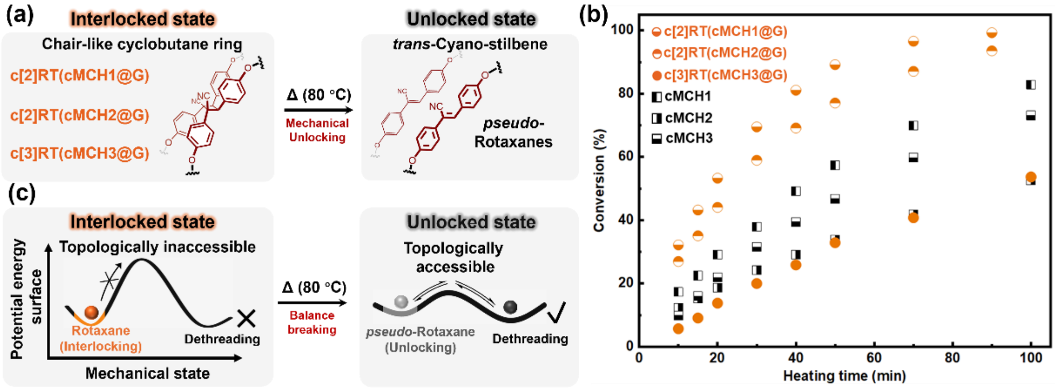

Figure 3-53. Mechanical unlocking of chair-like rotaxanes via reverse topology transformation between non-homeomorphic structures: (a) Thermal-induced transition from rotaxanes to *pseudo*-rotaxanes. (b) Conversion vs. heating time curve for the reverse topology transformation of chair-like figure-eight structures**.** (c) Schematic illustration of the variation in the system's potential energy surface.

. In the cases of three chair-like rotaxanes, according to ^{1}H NMR spectra at different heating time, the cyclobutane proton signals (H_{AcRT}) progressively decreased upon heating, while the characteristic signals of the *trans*–cyano–stilbene moieties reappeared (Figures 3-49 to 3-52). This spectral evolution indicates that the wheel components of the rotaxanes undergo a topology transition back to their original large-cavity ring forms. As a result, the steric barrier imposed by the figure-eight structure is eliminated, leading to mechanical unlocking and the conversion of rotaxanes into *pseudo*-rotaxanes. Differing from the conversion rate of **cMCH1-3**, the trend in across the three chair-like rotaxanes follows as: **c[2]RT(cMCH1@G) > c[2]RT(cMCH2@G) > c[3]RT(cMCH3@G)** (Figure 3-53b). Upon heating at 80 °C for 70 minutes, the conversion of three rotaxanes reached 97%, 87%, 41%. Complete conversion was achieved after elongating the heating time or temperature. Unexpectedly, the significant differences in thermal conversion were observed between non-interlocked fused ring structure and their corresponding rotaxanes. For example, the conversion of **c[2]RT(cMCH1@G)** proceeds much faster than that of **cMCH1** and similarly, **c[2]RT(cMCH2@G)** converts more readily than **cMCH2**. These results suggest that the mechanical interlock in [2]rotaxanes destabilizes the covalent cyclobutane linkage. In contrast, **c[3]RT(cMCH3@G)** shows a slower conversion than **cMCH3**, indicating that a more complex mechanical interlock can, counterintuitively, stabilize the covalent linkage. This unexpected trend implies a unique mechanism at the molecular level. We speculate that in [2]rotaxanes, the asymmetric mechanical constraint may induce an uneven distribution of stress in molecular architecture upon heating, thereby facilitating the activation of covalent linkage. In contrast, the more symmetric interlocked structure of the [3]rotaxane may help distribute internal stress more evenly, thus stabilizing the architecture.[24,25]

Notably, the mechanical unlocking process differs from the dethreading of wheel over the axle ends in kinetically stable rotaxane, but rather by an energy ratchet-like mechanism (Figure 3-53c). The thermodynamically driven topological reconfiguration between non-homeomorphic structures is accompanied by a restructuring of the system's potential energy surface. This transformation allows the loss of mechanical interlock and enables subsequent dethreading of the resulting *pseudo*-rotaxanes. This clean, efficient, and fully reversible transformation, triggered solely by heat or light and requiring no additional reagents, could serve as a conceptually useful framework for constructing thermally or photochemically gated units in molecular machines.

3-3 Conclusion

In summary, we have developed an energy ratchet-like strategy to achieve reversible mechanical interlocking and unlocking in rotaxanes through a stimuli-triggered topology transformation between non-homeomorphic structures. Upon UV irradiation, the macrocycle in a *pseudo*-rotaxane undergoes a topological transition from a regular ring to a figure-eight fused ring with a chair-like conformation. The resulting smaller cavities prevent the ring from slipping over the axle termini, thereby locking the axle and forming a rotaxane. This one-pot rotaxanation proceeds without the addition of external reagents such as catalysts or stoppers, achieving up to ~100%

conversion and 92% isolated yield. Conversely, the heat-triggered reverse topology transformation enlarges the macrocycle cavity, thus triggering mechanical unlocking and converting the rotaxane back to a *pseudo*-rotaxane. Both interlocking and unlocking are driven by a reversible restructuring of the system's potential energy surface. This topology-transformation-based mechanism also enables the synthesis of rotaxanes with diverse geometries and complex mechanical interlocks. Orthogonal rotaxanes, in which the fused rings adopt a mutually orthogonal arrangement, were also synthesized and isolated with tunable diastereomeric ratios under different macrocyclic designs. In addition, [3]rotaxanes consisting of one macrocycle and two axles, featuring both chair-like and orthogonal topologies, were also efficiently synthesized with a total conversion of 96% and isolated yield of 80%. This topology-transformation-based strategy for modulating mechanical interlocks in rotaxanes may provide a new insight for constructing complex mechanical interlocks in supramolecular architecture and thermally or photochemically gated units in molecular machines.

References

1. Bissell, R. A.; Córdova, E.; Kaifer, A. E.; Stoddart, J. F. *Nature* **1994**, *369*, 133–137.
2. Canton, M.; Groppi, J.; Casimiro, L.; Corra, S.; Baroncini, M.; Silvi, S.; Credi, A. *J. Am. Chem. Soc.* **2021**, *143*, 10890–10894.
3. Kay, E. R.; Leigh, D. A.; Zerbetto, F. *Angew. Chem. Int. Ed.* **2007**, *46*, 72–191.
4. Borsley, S.; Leigh, D. A.; Roberts, B. M. *Angew. Chem. Int. Ed.* **2024**, *63*, e202400495.

5. Gilday, L. C.; Robinson, S. W.; Barendt, T. A.; Langton, M. J.; Mullaney, B. R.; Beer, P. D. *Chem. Rev.* **2015**, *115*, 7118–7195.
6. Langton, M. J.; Beer, P. D. *Acc. Chem. Res.* **2014**, *47*, 1935–1949.
7. Tse, Y. C.; Docker, A.; Marques, I.; Félix, V.; Beer, P. D. *Nat. Chem.* **2025**, *in press*, 1–9.
8. Harada, A.; Li, J.; Kamachi, M. *Nature* **1992**, *356*, 325–327.
9. Okumura, Y.; Ito, K. *Adv. Mater.* **2001**, *13*, 485–487.
10. Kim, K. *Chem. Soc. Rev.* **2002**, *31*, 96–107.
11. Sagara, Y.; Karman, M.; Verde-Sesto, E.; Matsuo, K.; Kim, Y.; Tamaoki, N.; Weder, C. *J. Am. Chem. Soc.* **2018**, *140*, 1584–1587.
12. Harrison, I. T.; Harrison, S. *J. Am. Chem. Soc.* **1967**, *89*, 5723–5724.
13. Wu, C.; Lecavalier, P. R.; Shen, Y. X.; Gibson, H. W. *Chem. Mater.* **1991**, *3*, 569–572.
14. Mobian, P.; Collin, J. P.; Sauvage, J. P. *Tetrahedron Lett.* **2006**, *47*, 4907–4909.
15. Glink, P. T.; Oliva, A. I.; Stoddart, J. F.; White, A. J.; Williams, D. J. *Angew. Chem. Int. Ed.* **2001**, *40*, 1870–1875.
16. Wu, J.; Leung, K. C. F.; Stoddart, J. F. *Proc. Natl. Acad. Sci. U.S.A.* **2007**, *104*, 17266–17271.
17. Crowley, J. D.; Goldup, S. M.; Lee, A. L.; Leigh, D. A.; McBurney, R. T. *Chem. Soc. Rev.* **2009**, *38*, 1530–1541.
18. Jamagne, R.; Power, M. J.; Zhang, Z. H.; Zango, G.; Gibber, B.; Leigh, D. A. *Chem. Soc. Rev.* **2024**, *in press*, 1–10.
19. Hsueh, S. Y.; Ko, J. L.; Lai, C. C.; Liu, Y. H.; Peng, S. M.; Chiu, S. H. *Angew. Chem.* **2011**, *123*, 6773–6776.
20. Chiu, C. W.; Lai, C. C.; Chiu, S. H. *J. Am. Chem. Soc.* **2007**, *129*, 3500–3501.
21. De Bo, G.; Dolphijn, G.; McTernan, C. T.; Leigh, D. A. *J. Am. Chem. Soc.* **2017**, *139*, 8455–8457.
22. Masai, H.; Terao, J.; Fujihara, T.; Tsuji, Y. *Chem. Eur. J.* **2016**, *22*, 6624–6630.

23. Ashton, P. R.; Baxter, I.; Fyfe, M. C.; Raymo, F. M.; Spencer, N.; Stoddart, J. F.; et al. *J. Am. Chem. Soc.* **1998**, *120*, 2297–2307.
24. Zhang, M.; De Bo, G. *J. Am. Chem. Soc.* **2019**, *141*, 15879–15883.
25. Zhang, M.; De Bo, G. *J. Am. Chem. Soc.* **2018**, *140*, 12724–12727.
26. Liu, Y.; Li, X.; Liu, Q.; Li, X.; Liu, H. *Org. Lett.* **2022**, *24*, 6604–6608.
27. Kokkala, P.; Mpakali, A.; Mauvais, F. X.; Papakyriakou, A.; Daskalaki, I.; Petropoulou, I.; Georgiadis, D. *J. Med. Chem.* **2016**, *59*, 9107–9123.
28. Kong, W. G.; An, H. J.; Song, Q. L. *Chem. Commun.* **2017**, *53*, 8968–8971.
29. Palmquist, M. S.; Gruschka, M. C.; Dorsainvil, J. M.; Delawder, A. O.; Saak, T. M.; Danielson, M. K.; Barnes, J. C. *Polym. Chem.* **2022**, *13*, 2115–2122.
30. Balamurugan, A.; Reddy, M. L. P.; Jayakannan, M. *J. Mater. Chem. A* **2013**, *1*, 2256–2266.
31. Jamdade, A. B.; Sutar, D. V.; Gnanaprakasam, B. *Org. Lett.* **2023**, *25*, 9058–9063.
32. Shan, M.; Carlson, K. E.; Bujotzek, A.; Wellner, A.; Gust, R.; Weber, M.; Haag, R. *ACS Chem. Biol.* **2013**, *8*, 707–715.
33. *CrysAlisPro*, Version 1.171.41.122, Rigaku OD **2021**.
34. Sheldrick, G. M. *Acta Crystallogr., Sect. A* **2015**, *71*, 3–8.
35. Sheldrick, G. M. *Acta Crystallogr., Sect. C* **2015**, *71*, 3–8.
36. Dolomanov, O. V.; Bourhis, L. J.; Gildea, R. J.; Howard, J. A. K.; Puschmann, H. *J. Appl. Crystallogr.* **2009**, *42*, 339–341.

Chapter 4

Summary and Conclusions

In this thesis the author focuses on tuning the topology of molecules by supramolecular strategies.

Chapter 2 focuses on the preparation of cyclic polymers by assistance of pseudo-polyrotaxane. This novel approach enables cyclization at significantly higher concentrations, approximately 800 times greater than those used in conventional methods, while maintaining high efficiency and selectivity toward the cyclized polymer products.

Chapter 3 focuses on tuning the topology of macrocycles and applying this topology transformation to the synthesis of rotaxanes. At the molecular level, a reversible and stimuli-triggered transformation between non-homeomorphic topologies, specifically between a simple ring and a figure-eight structure, was successfully achieved. This strategy was then employed in rotaxane synthesis, enabling quantitative conversion in both the formation and dissociation of [2]rotaxanes. Furthermore, higher-order mechanically interlocked molecules (MIMs), such as [3]rotaxanes, were also synthesized with high conversion.

In conclusion, this thesis has investigated the control of topology at a molecular level. Chapters 2 and 3 have highlighted topology transformation on polymer system and MIMs system, respectively. These findings provide valuable insights into the rational design of complex molecular architectures and offer potential for broader applications in related fields.

List of Publication

1. Xiao, C. L.; Kobayashi, Y.; Tsuji, Y.; Harada, A.; Yamaguchi, H. Efficient Synthesis of Cyclic Poly (ethylene glycol) s under High Concentration Conditions by the Assistance of Pseudopolyrotaxane with Cyclodextrin Derivatives. *ACS Macro Lett.* **2023**, *12*, 1498–1502. (Chapter 2)

2. Xiao, C.; Li, X.; Okamoto, N.; Kobayashi, Y.; Nishiuchi, T.; Tani, Y.; Yamaguchi, H. Reversible Mechanical Interlocking via Stimuli-triggered Non-homeomorphic Topology Transformation Enables Highly Efficient Rotaxane Synthesis. *Angew. Chem. Int. Ed.* e202513783. (Chapter 3)